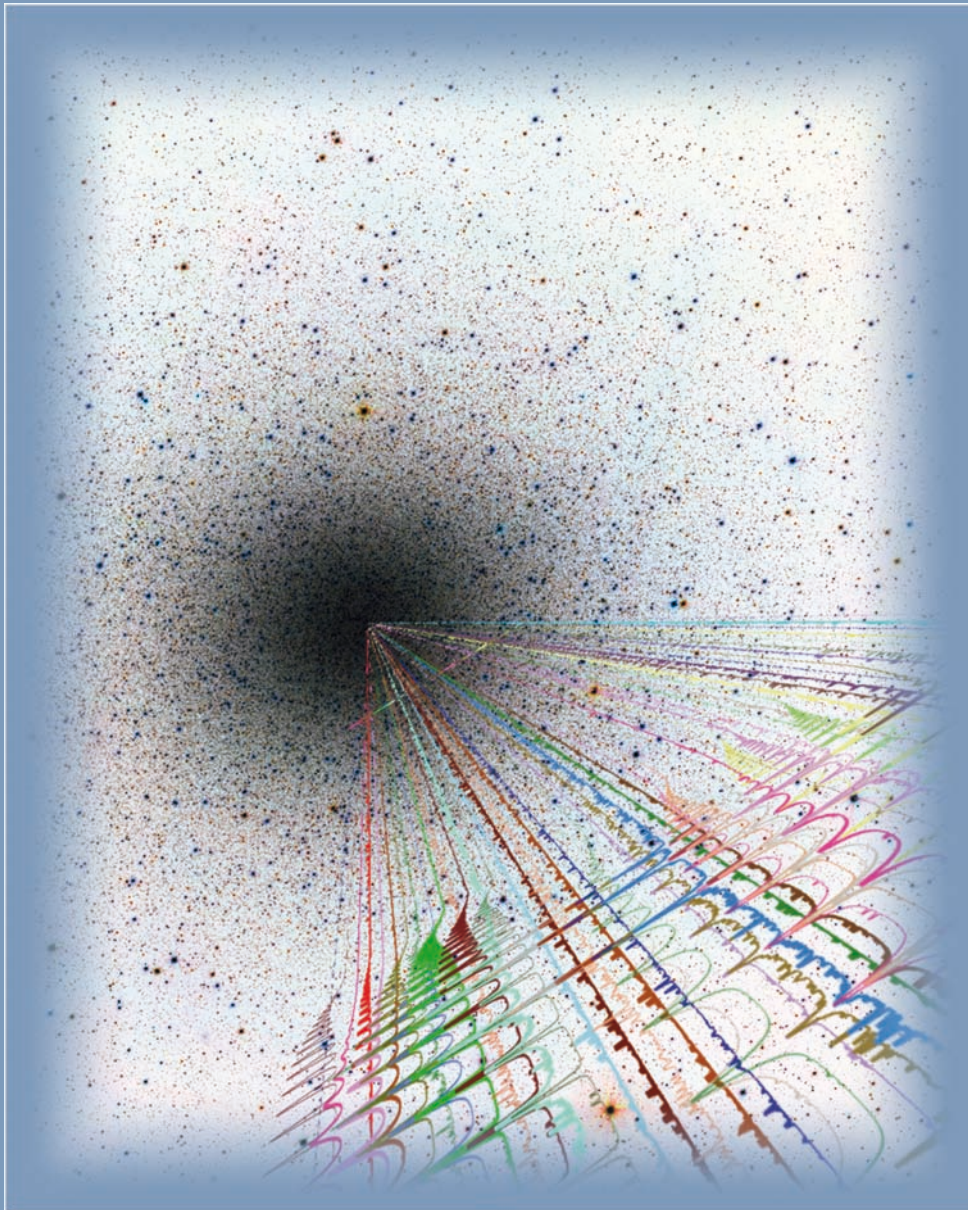


Tim-Oliver Husser

# 3D-Spectroscopy of Dense Stellar Populations



Universitätsverlag Göttingen



Tim-Oliver Husser  
3D-Spectroscopy of Dense Stellar Populations

This work is licensed under the [Creative Commons](#) License 3.0 “by-nd”, allowing you to download, distribute and print the document in a few copies for private or educational use, given that the document stays unchanged and the creator is mentioned. You are not allowed to sell copies of the free version.



erschienen im Universitätsverlag Göttingen 2012

---

Tim-Oliver Husser

# 3D-Spectroscopy of Dense Stellar Populations



Universitätsverlag Göttingen  
2012

## Bibliographische Information der Deutschen Nationalbibliothek

Die Deutsche Nationalbibliothek verzeichnet diese Publikation in der Deutschen Nationalbibliographie; detaillierte bibliographische Daten sind im Internet über <http://dnb.ddb.de> abrufbar.

### *Anschrift des Autors*

Tim-Oliver Husser  
e-mail: [husser@astro.physik.uni-goettingen.de](mailto:husser@astro.physik.uni-goettingen.de)

### Dissertation

zur Erlangung des mathematisch-naturwissenschaftlichen Doktorgrades  
"Doctor rerum naturalium"  
an der Georg-August-Universität Göttingen  
vorgelegt von  
Tim-Oliver Husser aus Melle

Referent: Prof. Dr. Stefan Dreizler  
Korreferent: Prof. Dr. Martin M. Roth  
Tag der mündlichen Prüfung: 12. Juli 2012

This work is protected by German Intellectual Property Right Law.  
It is also available as an Open Access version through the publisher's homepage and the Online Catalogue of the State and University Library of Goettingen (<http://www.sub.uni-goettingen.de>). Users of the free online version are invited to read, download and distribute it. Users may also print a small number for educational or private use. However they may not sell print versions of the online book.

Satz und Layout: Tim-Oliver Husser  
Umschlaggestaltung: Jutta Pabst  
Titelabbildung: Colour-inverted image of the globular cluster  $\omega$  Centauri with some stellar spectra. The picture of  $\omega$  Centauri has been taken with OmegaCAM at the VST, ESO/INAF-VST/OmegaCAM.  
Acknowledgement: A. Grado/INAF-Capodimonte Observatory

© 2012 Universitätsverlag Göttingen  
<http://univerlag.uni-goettingen.de>  
ISBN: 978-3-86395-092-7

*I have spent my entire life, trying to bring order into the Universe.*  
Sheldon Cooper





# Abstract

The aim of this work is to prepare observations of globular clusters with the upcoming second-generation *VLT* instrument *MUSE*, which is an integral-field unit (IFU) with an outstanding combination of a  $1 \times 1$  arcmin<sup>2</sup> field of view and a 0.2 arcsec spatial resolution, covering the wavelength range from 4 650 to 9 300 Å at a spectral resolution of 2.6 Å (FWHM).

I present the current state of research on globular clusters, which have long been assumed to be very simple structures composed of stars that were all formed in a single burst of star formation. Thus, they should all have the same age and chemical composition. Observations during the last decades have shown that this is not the case and that, in fact, all globular clusters seem to consist of multiple generations of stars. A fundamental role in the evolution of clusters is played by their binary stars. Unfortunately, it is still unclear why we see a much smaller binary fraction in globular clusters than in field stars in the solar neighbourhood, so it is important to gain a better understanding of the current number and distribution of binary systems. For some globular clusters, evidence has been found for the existence of intermediate-mass black holes in their centres, which would fill the gap between the low-mass stellar black holes and the super-massive ones located in the centres of galaxies.

The major part of the work for this thesis consisted of evaluating, creating and testing methods for the analysis of *MUSE* spectra. Since we expect to obtain a couple of thousands of stellar spectra from a single exposure, automatic methods are required to process them, i. e. determine their radial velocity  $v_{\text{rad}}$  and atmospheric parameters like effective temperature  $T_{\text{eff}}$ , surface gravity  $\log(g)$ , metallicity  $[Fe/H]$  and alpha element abundance  $[\alpha/Fe]$ . Tests have been performed to estimate the accuracy of the methods and we conducted a first *dry run* in which we tried to simulate real *MUSE* data. Furthermore, the methods have been used on real data. I will finish this topic with making suggestions and recommendations for real *MUSE* observations.

For analyzing *MUSE* data, a comprehensive library of stellar spectra is required. Since none could be found that met our requirements, I created a new library of high-resolution synthetic spectra based on the stellar atmosphere code *PHOENIX*. Its spherical symmetric mode was used to compute model atmospheres and to synthesize detailed synthetic stellar spectra. A new self-consistent way of describing microturbulence for the model atmospheres has been developed. The synthetic spectra

cover the wavelength range from  $500\text{\AA}$  to  $5.5\mu\text{m}$  with resolutions of  $R = 500\,000$  in the optical and near IR,  $R = 100\,000$  in the IR and  $\Delta\lambda = 0.1\text{\AA}$  in the UV. The parameter space covers  $2300\text{K} \leq T_{\text{eff}} \leq 8000\text{K}$ ,  $0.0 \leq \log(g) \leq +6.0$ ,  $-4.0 \leq [Fe/H] \leq +1.0$  and  $-0.3 \leq [\alpha/M] \leq +0.8$ . With its high spectral resolution and broad wavelength range, the spectra can be used not only for the analysis of *MUSE* data but for a wide range of applications of spectral analysis and stellar parameter synthesis.

# Contents

<b>List of Figures</b>	<b>xiii</b>
<b>List of Tables</b>	<b>xvii</b>
<b>1 Introduction</b>	<b>1</b>
<b>2 Globular Clusters</b>	<b>9</b>
2.1 Positions and shapes . . . . .	10
2.2 Ages . . . . .	13
2.3 Time scales . . . . .	15
2.4 Binaries and core collapse . . . . .	17
2.5 Blue stragglers . . . . .	19
2.6 Kinematics and black holes . . . . .	20
2.7 Multiple populations . . . . .	23
2.8 Science goals with <i>MUSE</i> . . . . .	26
<b>3 A new library of PHOENIX stellar atmospheres and synthetic spectra</b>	<b>27</b>
3.1 The library . . . . .	28
3.1.1 Dimensions and resolution . . . . .	28
3.1.2 Calculation of model atmospheres and synthetic spectra . . . . .	29
3.1.3 Input parameters for <i>PHOENIX</i> . . . . .	30
3.1.3.1 Mass . . . . .	31
3.1.3.2 Convection . . . . .	31
3.1.3.3 Micro-turbulence . . . . .	32
3.1.3.4 Equation of state . . . . .	34
3.1.3.5 Element abundances . . . . .	34
3.1.4 Comparison with previous <i>PHOENIX</i> models . . . . .	35
3.1.5 Vacuum wavelengths . . . . .	36
3.2 The <i>PHOENIX</i> pipeline . . . . .	36
3.2.1 The MySQL database . . . . .	37
3.2.2 The job manager . . . . .	39

3.2.3	Exporting the database . . . . .	40
3.2.4	Other command-line tools . . . . .	41
3.2.5	Files created by <i>PHOENIX</i> and the pipeline . . . . .	41
3.3	Processing the <i>PHOENIX</i> spectra . . . . .	42
3.3.1	Converting to FITS files . . . . .	42
3.3.2	Interpolating missing spectra . . . . .	44
3.3.3	Extracting subgrids . . . . .	44
3.3.4	Convoluting and resampling the spectra . . . . .	46
3.3.5	Calculating 2nd derivatives . . . . .	48
3.3.6	Final script . . . . .	48
3.4	Limb Darkening . . . . .	48
3.5	Synspec . . . . .	50
<b>4</b>	<b>Analyzing <i>MUSE</i> data</b>	<b>53</b>
4.1	Extraction of spectra from a <i>MUSE</i> cube . . . . .	53
4.2	Telluric line correction . . . . .	54
4.3	Parameter estimation using isochrones . . . . .	59
4.4	Interpolator for the grid of spectra . . . . .	60
4.4.1	Linear interpolation . . . . .	60
4.4.2	Spline interpolation . . . . .	62
4.5	Rebinning spectra . . . . .	66
4.6	Radial velocities and line broadening . . . . .	68
4.7	Line spread function . . . . .	70
4.8	Multiple components . . . . .	71
4.9	Spectral continuum . . . . .	72
4.9.1	Stellar continuum . . . . .	73
4.9.2	Extinction . . . . .	75
4.9.3	Normalizing with a polynomial . . . . .	76
4.9.4	Using a template spectrum . . . . .	78
4.9.5	Maximum values in bins of spectrum . . . . .	80
4.9.6	Applying correction to both the model and the observation . . . . .	80
4.9.7	Fitting continuum difference only . . . . .	81
4.10	Fitting stellar parameters . . . . .	83
4.10.1	Method 1 . . . . .	84
4.10.2	Method 2 . . . . .	85
4.11	Fitting single alpha element abundances . . . . .	86
<b>5</b>	<b>Results</b>	<b>91</b>
5.1	Quality of fits varying with temperature . . . . .	91
5.2	Impact of noise on fitting parameters . . . . .	92
5.3	Line broadening . . . . .	93
5.4	Resolution of model spectra . . . . .	94

5.5	Neglecting the alpha element abundance . . . . .	95
5.6	Problems with the calibration . . . . .	96
5.6.1	Wavelength calibration . . . . .	96
5.6.2	Flux calibration . . . . .	97
5.7	Binaries . . . . .	98
5.8	Single alpha element abundances . . . . .	100
5.9	Isochrone fit . . . . .	102
5.10	Problems with the <i>PHOENIX</i> spectra . . . . .	102
5.11	MUSE dry run . . . . .	104
5.11.1	The simulated <i>MUSE</i> cube . . . . .	104
5.11.2	Extraction of spectra . . . . .	106
5.11.3	Noise . . . . .	106
5.11.4	Radial velocities . . . . .	108
5.11.5	Stellar parameters . . . . .	109
5.11.6	Alpha element abundances . . . . .	111
5.12	Miles library . . . . .	111
5.12.1	Wavelength calibration . . . . .	112
5.12.2	Atmospheric parameters and radial velocities . . . . .	113
5.13	PMAS data of M13 and M92 . . . . .	115
5.13.1	Radial velocities . . . . .	117
5.13.2	Effective temperatures and colours . . . . .	118
5.13.3	Metallicities . . . . .	119
5.13.4	Comparison of results for multiple visits . . . . .	120
<b>6</b>	<b>A proposal for <i>MUSE</i> observations</b>	<b>121</b>
6.1	Selection of globular clusters . . . . .	121
6.2	Exposure times . . . . .	121
6.3	Intermediate-mass black holes . . . . .	124
6.4	Multiple populations . . . . .	126
6.5	Binaries . . . . .	126
6.6	Example pointings for 47 Tuc . . . . .	129
<b>7</b>	<b>Conclusions and outlook</b>	<b>131</b>
	<b>Bibliography</b>	<b>135</b>
<b>A</b>	<b>List of galactic globular clusters</b>	<b>155</b>
<b>B</b>	<b>Tools in the <i>pyphoenix</i> package</b>	<b>161</b>
B.1	phxadd . . . . .	161
B.2	phxaddextra . . . . .	161
B.3	phxch . . . . .	162
B.4	phxstatus . . . . .	162

---

<b>C</b>	<b>Tools in the <i>spexxy</i> package</b>	<b>163</b>
C.1	<code>spexxyCheckGrid</code>	163
C.2	<code>spexxyConvertPhxGrid</code>	163
C.3	<code>spexxyConvolveGrid</code>	164
C.4	<code>spexxyExtractGrid</code>	164
C.5	<code>spexxyFillGridHoles</code>	165
C.6	<code>spexxyFitBinary</code>	165
C.7	<code>spexxyFitElements</code>	166
C.8	<code>spexxyFitLosvd</code>	166
C.9	<code>spexxyFitParams</code>	166
C.10	<code>spexxyGridDerivs</code>	167
C.11	<code>spexxyImportIsochroneCMD</code>	167
C.12	<code>spexxyInterpolate</code>	168
C.13	<code>spexxyIsoFit</code>	168
C.14	<code>spexxyLSF</code>	169
C.15	<code>spexxyTellurics</code>	169

# List of Figures

1.1	Image of the globular cluster $\omega$ Centauri. . . . .	2
1.2	Computer generated picture of <i>MUSE</i> . . . . .	3
1.3	Picture of <i>MUSE</i> in its integration hall in Lyon. . . . .	4
1.4	Picture of <i>MUSE</i> 's field slicer currently being assembled. . . . .	5
2.1	Positions of all known Galactic globular clusters . . . . .	10
2.2	Distances of Galactic globular clusters from the sun and from the Galactic centre. . . . .	10
2.3	Distribution of radii in Galactic globular clusters. . . . .	11
2.4	Distribution of stellar densities in a few selected globular clusters. . . . .	12
2.5	King models for different core concentrations. . . . .	12
2.6	Comparison of colour-magnitude diagrams of field stars and stars in M3. . . . .	13
2.7	Colour-magnitude diagram of M3 with various isochrones. . . . .	14
2.8	Illustration of vertical ( $\Delta V$ ) and horizontal ( $\Delta(B-V)$ ) methods for measuring GC ages. . . . .	14
2.9	Relaxation times of Galactic globular clusters. . . . .	16
2.10	Distribution of metallicities in Galactic globular clusters. . . . .	16
2.11	Plots of the surface luminosity curves for several non-core-collapsed and core-collapsed clusters and $\omega$ Cen as a special case. . . . .	19
2.12	$M_{\text{BH}}$ -bulge relations for galaxies and extrapolation to globular clusters. . . . .	21
2.13	Colour-magnitude diagrams of $\omega$ Cen in different filters. . . . .	24
2.14	Na-O anti-correlation in globular clusters. . . . .	24
3.1	Distribution of stellar masses for different effective temperatures and surface gravities. . . . .	32
3.2	Distribution of the mixing length parameter $\alpha$ in the <i>PHOENIX</i> grid. . . . .	32
3.3	Distribution of micro-turbulences for that part of the <i>PHOENIX</i> grid with solar element abundances. . . . .	33
3.4	TiO bands of new <i>PHOENIX</i> spectrum compared to one created using <i>AMES-cond-v2.6</i> . . . . .	36
3.5	The MySQL database schema used for storing information about the models for the <i>PHOENIX</i> pipeline. . . . .	37
3.6	The sqlite database schema used for storing information about the models. . . . .	40

3.7	Quality of interpolation for three different spectra. . . . .	45
3.8	Limb darkening curves and derived transit light curves. . . . .	49
3.9	Some example Synspec spectra. . . . .	50
4.1	Sequence of images illustrating the process of extracting spectra from a <i>MUSE</i> data cube. . . . .	54
4.2	The telluric spectrum in the wavelength range 3 700 - 55 000Å. . . . .	55
4.3	Night-sky emission spectrum from UVES observations . . . . .	56
4.4	Telluric absorption in an A0-type star. . . . .	58
4.5	Illustration of fitting $T_{\text{eff}}$ and $\log(g)$ using isochrones. . . . .	59
4.6	Illustration of problems of linear interpolation. . . . .	62
4.7	Labelling of points for the bilinear interpolation. . . . .	62
4.8	Illustration of the process of spline-interpolating spectra within a N- dimensional grid. . . . .	64
4.9	Quality of interpolation in $T_{\text{eff}}$ and $\log(g)$ for a sun-like star. . . . .	65
4.10	Comparison of resampling and rebinning. . . . .	66
4.11	Plot of the Hermite polynomials $H_3$ to $H_6$ in the range -2 to 2. . . . .	69
4.12	Plot of the summands of Eq. 4.24 with $\sigma = 0.5$ and $h_m = 0.5, 3 \leq m \leq 6$ . . .	69
4.13	<i>MUSE</i> LSF at 5 000 Å and a Gaussian with 2.6 Å FWHM. . . . .	69
4.14	Line broadenings of Gaussian LSF for several PMAS spectra. . . . .	69
4.15	Fitting the <i>MUSE</i> LSF with a model spectrum with 1 Å FWHM. . . . .	71
4.16	A spectrum for a sun-like star with $T_{\text{eff}} = 5800 \text{ K}$ , $\log(g) = 4.5$ synthesized with Synspec. . . . .	72
4.17	Illustration of a continuum change in a spectrum. . . . .	73
4.18	Comparison of a <i>PHOENIX</i> spectrum with a Planck spectrum of same temperature. . . . .	74
4.19	Spectra at <i>MUSE</i> resolution for three different stars. . . . .	75
4.20	Comparison of extinction laws for SMC, LMC and Milky Way. . . . .	76
4.21	Comparison of different methods for normalizing a spectrum. . . . .	77
4.22	Observed spectrum with matching template, residuals with best-fit poly- nomial and final normalized spectrum. . . . .	78
4.23	Observed spectrum with the regions containing the 15% largest values in each bin and estimated continuum points and normalized spectrum. . .	79
4.24	Observation and model, both normalized in the same way. . . . .	81
4.25	Legendre polynomials $P_0$ to $P_6$ . . . . .	82
4.26	Estimating the continuum difference using model spectra with incorrect stellar parameters. . . . .	84
4.27	Flow chart illustrating the complete fitting process. . . . .	86
4.28	Difference between two <i>PHOENIX</i> spectra with different Ca abundances. .	87
4.29	Same plots as in Fig. 4.28, but for variations of Mg and Ti in 4 000 K stars. .	87
4.30	Normalized spectrum of a star with $T_{\text{eff}}=6\,000 \text{ K}$ , $\log(g)=5.0$ and $[Fe/H]$ with alpha element masks. . . . .	88
5.1	Accuracy of parameter fits for different temperatures. . . . .	92



5.2	Impact of noise on the accuracy of the four fitted parameters $T_{\text{eff}}$ , $\log(g)$ , $[Fe/H]$ and $v_{\text{rad}}$ .	92
5.3	Accuracy of line broadening fits.	94
5.4	Impact of incorrect spectral resolution of model spectra.	94
5.5	Fitting stellar parameters with an alpha element abundance fixed to zero.	95
5.6	Accuracy of parameter fits with a random jitter in wavelengths caused by an incorrect calibration.	96
5.7	Accuracy of parameter fits with a stretched wavelength grid.	96
5.8	Systematic errors produced by an incorrect flux calibration.	98
5.9	Systematic errors produced by a discontinuity in the spectrum.	99
5.10	Line broadening in binaries with equal components.	99
5.11	Examples of how the quality of the fit results can be improved by fitting two components instead of one.	100
5.12	Results of single alpha element fits.	101
5.13	Difference between $V-I$ colours in the isochrone and in <i>PHOENIX</i> spectra.	101
5.14	Comparison of old and new <i>PHOENIX</i> spectra in one of the lines of the CaII triplet.	103
5.15	Distribution of stellar parameters for all stars in the simulated data cube.	104
5.16	Distribution of magnitudes in data cube.	105
5.17	Velocity dispersion in data cube.	105
5.18	Integrated white light image of the simulated <i>MUSE</i> data cube based on observations of 47 Tuc with the two analyzed sub-fields marked in red.	106
5.19	Colour-magnitude diagram of 47 Tuc.	106
5.20	Analysis of the noise on the spectra produced by the extraction process.	107
5.21	S/N ratio of extracted spectra over their magnitude.	107
5.22	Distribution of S/N ratios of extracted spectra.	107
5.23	Accuracy of radial velocity fits in the dry run.	108
5.24	Reconstruction of the velocity dispersion.	108
5.25	Accuracy of stellar parameter fits.	109
5.26	Fit of spectra with surface gravities fixed to the values from the input spectra and $[\alpha/Fe]$ fixed to 0 or 0.3.	110
5.27	Results of the fits with the alpha element abundance $[\alpha/Fe]$ as a free parameter.	110
5.28	Results of the abundance fits for Mg, Si, Ca and Ti.	111
5.29	Measured radial velocities at the blue and at the red end of the spectra in the Miles library.	112
5.30	Fit of the spectra from the Miles library against our <i>PHOENIX</i> grid.	113
5.31	Fit of the spectra from the Miles library against ELODIE spectra.	113
5.32	Fields in M13 observed with PMAS.	114
5.33	Fields in M92 observed with PMAS.	115
5.34	Colour-magnitude diagrams of the two globular clusters M13 and M92.	115
5.35	Some spectra from the M13 sample.	116
5.36	Comparison of the radial velocities fitted by S. Kamann and our results.	117

5.37	Some spectra from the M13 cube and their best fitting model spectra from the <i>cflib</i> library. The greyed out parts have been discarded from the analysis due to tellurics. . . . .	117
5.38	Colours determined from <i>PHOENIX</i> spectra with atmospheric parameter as given by the fits. . . . .	118
5.39	Comparison of the radial velocities fitted by S. Kamann and our results for M92. . . . .	118
5.40	Same plot as the left one in Fig. 5.38, but for M92. . . . .	118
5.41	Distribution of the fitted metallicities for both M13 and M92. . . . .	119
6.1	All spectra from the <i>MUSE</i> dry run co-added. . . . .	122
6.2	Correlation between absolute magnitude of GCs and their total mass and estimated IMBH masses. . . . .	124
6.3	Plot of velocity dispersion over absolute magnitude for globular clusters and a best-fitting function. . . . .	124
6.4	Distribution of estimated radii for the spheres of influences for galactic globular clusters. . . . .	124
6.5	Expected radial velocities in binary systems for four different types of companions. . . . .	127
6.6	Annual visibility of the globular clusters from Paranal. . . . .	128
6.7	Example pointings for 47 Tuc. . . . .	130

# List of Tables

1.1	Selection of currently available IFUs for the optical domain in comparison to <i>MUSE</i> . . . . .	6
2.1	Observed spread in metallicity for several massive globular clusters. . . .	25
3.1	Parameter space of the <i>PHOENIX</i> grid. . . . .	29
3.2	Sampling of the spectra in the <i>PHOENIX</i> grid. . . . .	29
3.3	Coefficients for calculating the mass in Eq. 3.6. . . . .	31
3.4	Element abundances used in the <i>PHOENIX</i> grid. . . . .	35
3.5	Keywords in the FITS headers of the files containing the spectra. . . . .	43
3.6	Parameter space of the Synspec grid. . . . .	50
4.1	Telluric regions that are currently considered in the correction. . . . .	58
4.2	Flux of a star calculated in different ways for a star with $T_{\text{eff}} = 5800\text{K}$ and $\log(g) = 4.5$ . . . . .	74
5.1	Fit results for spectra in Fig. 5.11. . . . .	100
5.2	Measured colours from <i>PHOENIX</i> spectra with solar parameters. . . . .	103
5.3	Measured wavelengths for lines of Balmer series in some spectra from the Miles library and in <i>PHOENIX</i> spectra. . . . .	111
5.4	Comparison of results from fits for spectra of the same star. . . . .	120
6.1	List of globular clusters proposed for observations with <i>MUSE</i> . . . . .	122
6.2	Crowding limits, background luminosities and estimated exposure times for three different pointings for each of the GCs from our sample. . . . .	123
6.3	Masses, radii of spheres of influence and crowding limits for some GCs. . . . .	125
6.4	Coordinates, distances to cluster centre, crowding limit, background luminosity and estimated exposure time for each sample pointing. . . . .	129
A.1	List of galactic globular clusters. . . . .	160



# Chapter 1

## Introduction

Almost two thousand years ago about 150 AD, a Greek-Roman citizen of Egypt named Claudius Ptolemy wrote a book about the apparent motions of stars and planets in the sky, which was later called the *Almagest*, from the Arabic word for *greater*. In his work, he included a list of 1022 stars that was mainly based on observations by Hipparchos from about 300 years earlier. One of the objects was also listed in a catalogue by Johann Bayer almost 1500 years later – in his *Uranometria* from 1603 it appeared under the name  $\omega$  Centauri, making it the 24th star in the constellation of Centaurus.

Thus, for about 2 millennia, this object was known as a star, before in 1677 Edmond Halley pointed a telescope at it from the island St Helena in the South Atlantic Ocean, seeing only a fuzzy blob, which he classified as a nebula, large as the full moon and visible to the naked eye. At the end of the 18th century, Charles Messier did not include  $\omega$  Centauri in his famous catalogue for the plain reason that with its declination of  $-47$  degrees it just was not visible from Paris. So it took some more decades, before John William Herschel in the 1830s observed  $\omega$  Centauri again. What he saw was a massive collection of stars (see Fig. 1.1) and therefore he reclassified it as what it is known today: a *globular cluster*.

Due to its brightness and size,  $\omega$  Centauri has since been an archetype for the analysis of globular clusters. Many of the fascinating discoveries from the last decades (see Chapter 2) have been studied in detail on  $\omega$  Centauri, like the finding of multiple populations we nowadays observe in clusters (see e. g. Bedin et al., 2004a; Bellini et al., 2010), which culminated in the discovery of several distinct main-sequences (see e. g. Bedin et al., 2004b; Piotto et al., 2005). Furthermore, dynamical studies of  $\omega$  Centauri have been conducted, resulting in evidence for mass segregation (Anderson, 1997) as well as for an intermediate-mass black hole in its centre (van der Marel & Anderson, 2010; Noyola et al., 2010). Most of those discoveries have been confirmed on other globular clusters, but in some points,  $\omega$  Centauri still seems to be unique, e. g. in its wide spread of metallicity (Piotto et al., 2005). There have been suggestions that it is not a normal cluster, but just the stripped remnants of a dwarf galaxy (Majewski et al., 2000; Gnedin

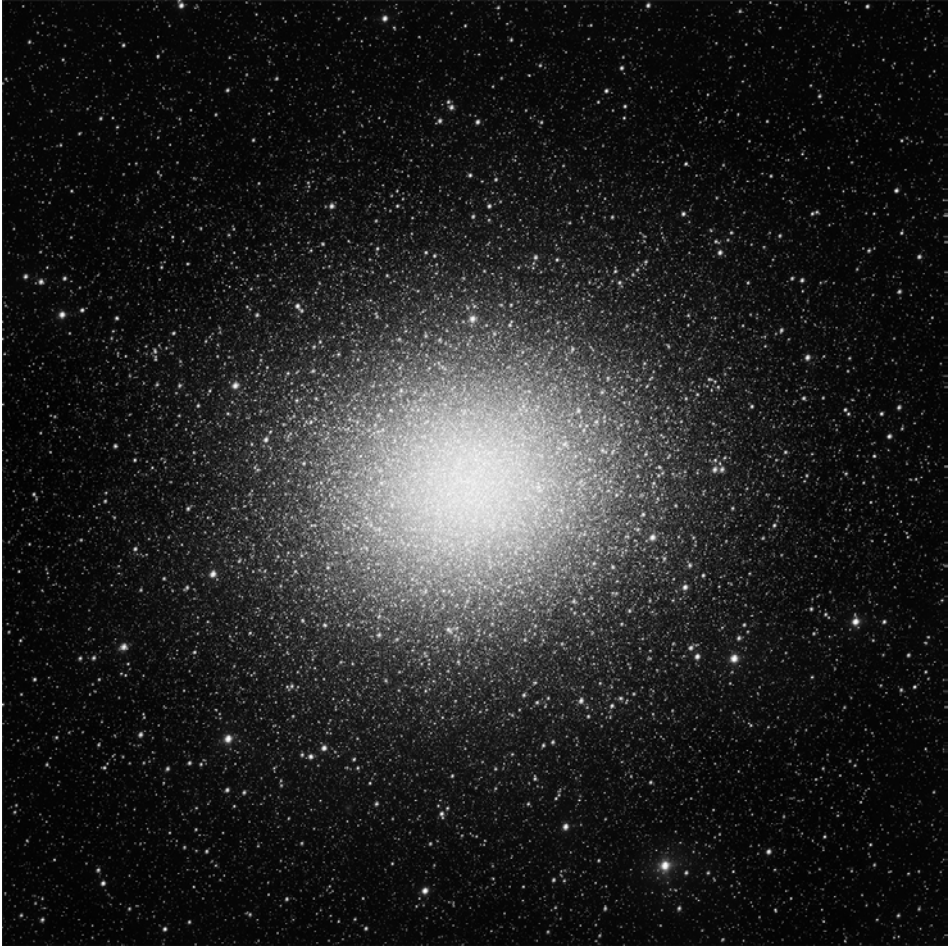


**Figure 1.1:** Image of  $\omega$  Centauri taken with OmegaCAM at the VST (Acknowledgement: A. Grado/INAF-Capodimonte Observatory, ESO/INAF-VST/OmegaCAM). The whole field is one degree across, showing the enormous size of the globular cluster ( $\sim 150$  ly across) and including about 300 000 stars.

et al., 2002).

Here the wheel has come full circle –  $\omega$  Centauri is not a single star as has been believed for thousands of years and as could still be expected from its Bayer designation. But despite all the similarities, is it really a globular cluster? And what exactly defines globular clusters – how are they formed and how do they evolve? Those are still open questions that we want to address with a new instrument for the VLT called MUSE.

The Multi Unit Spectroscopic Explorer (MUSE, see Bacon et al., 2010) is a second-generation instrument for the Very Large Telescope (VLT), which is located on the Cerro Paranal in Chile and operated by the European Southern Observatory (ESO). It

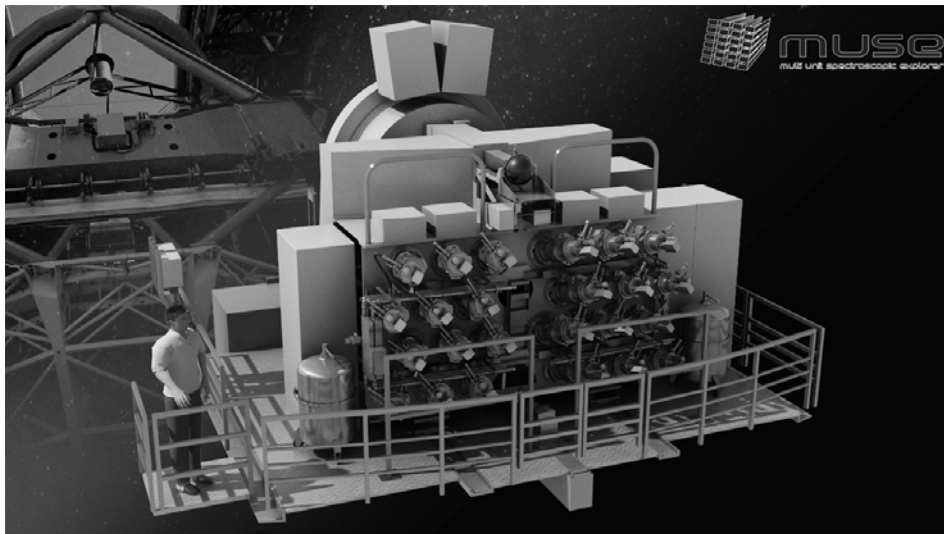


**Figure 1.2:** Computer generated picture of MUSE with its 24 IFUs standing on the Nasmyth platform B of the VLT-UT4 (©CRAL).

is currently built by a consortium of seven major European astronomical institutes, including the Institute for Astrophysics in Göttingen.

*MUSE* is an integral-field unit (*IFU*), which allows it to take images with full spectral information for each pixel. The result is usually a data cube (the reason for using the term *3D spectroscopy*) that is not so different to the data produced by series of Fabry-Pérot images. The main advantage of an *IFU* is that the observation is done in a single exposure, so there is no change in weather or seeing between the images at different wavelengths. Currently there are three technical approaches for *IFUs*:

**Lenslet array** : An array of micro-lenses splits up the image and the light from each is dispersed by a spectrograph (Bacon et al., 1995). An example for this kind of *IFU* is the *SAURON* instrument (Bacon et al., 2001) at the 4.2 m William Herschel Telescope on La Palma.

**Fibres** : The most common technique for *IFUs* uses a bundle of optical fibres in the image plane, which transfer the light to the spectrograph (Barden & Wade, 1988). A major problem of this kind of *IFUs* are the gaps between the fibres, i. e. the spatial coverage is not contiguous. This disadvantage can be overcome by using lenslets in front of the fibres, which focus all their light into the fibres (Allington-Smith et al., 1997). Examples are the *Potsdam Multi-Aperture Spectrophotometer (PMAS)*, see Roth et al., 2005) at the 3.5m telescope on Calar Alto, or two existing instrument at the *VLT*: *ARGUS* (Pasquini et al., 2002), the *IFU* mode of the *FLAMES+Giraffe* spectrograph, and the *Visual and IR Multi-Object Spectrograph (VIMOS)*, see Le Fèvre et al., 2003).

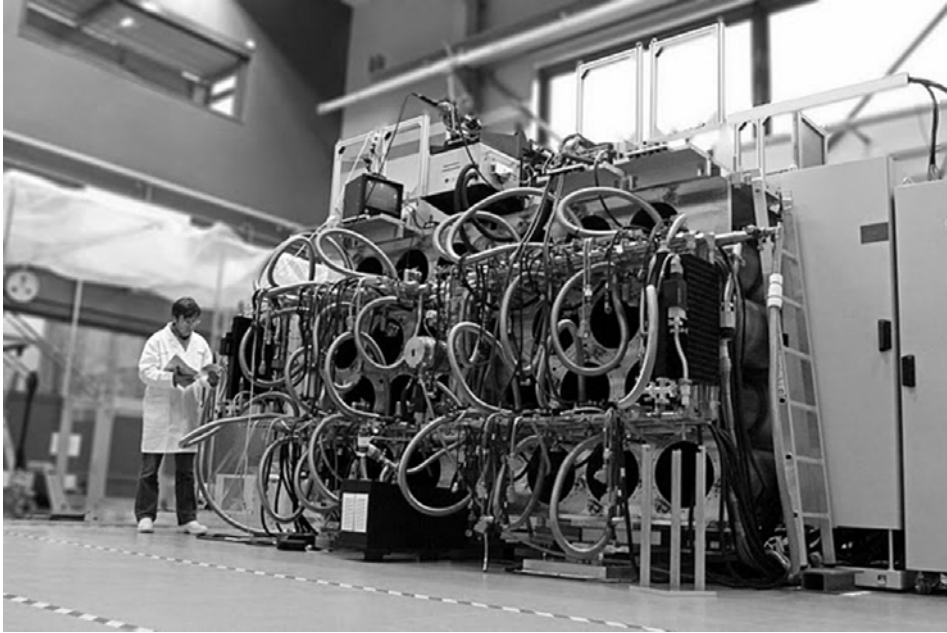


**Figure 1.3:** Picture of MUSE in its integration hall in Lyon. Shown are the holes in the structure that will hold the IFUs and the pipes for the cooling system (©CRAL).

**Image-slicer :** The need for fibres can be eliminated by using segmented mirrors, which divide the image into slices that are then laid out end to end and transferred to the spectrograph (Content, 1997). An IFU of this type called *SINFONI* (Eisenhauer et al., 2003) is already attached to one of the *VLT* telescopes.

*MUSE* (see Fig. 1.2) is an instrument of the third category: a field slicer divides the image into sub-fields that are sent to 24 identical IFUs (Laurent et al., 2010), where the image slicers split the image again, before the light reaches the spectrographs. Each of the 24 spectrographs has a detector containing a  $4k \times 4k$  CCD with  $15 \mu m$  pixels. The wavelength coverage will be  $4\,650 \text{ \AA}$  to  $9\,300 \text{ \AA}$  with a spectral resolution of  $\Delta\lambda = 2.6 \text{ \AA}$ , i. e.  $R = 1\,770$  at the blue end and  $R = 3\,590$  at the red end. Two different modes will be available: in the wide field mode (WFM), the field of view will be  $60'' \times 60''$  with a spatial resolution of  $0.2''$ , which is perfectly adjusted to the seeing on Paranal and equal to the resolution of FORS, while for the narrow field mode (NFM) it will be  $8'' \times 8''$  and  $0.025''$  respectively, requiring an adaptive optics system that will be available later on. For both modes, the number of spatial pixels is  $300 \times 300$ . A picture of *MUSE* in its integration hall in Lyon is shown in Fig. 1.3 and a part of the field slicer that is currently being assembled in Fig. 1.4.

Table 1.1 shows a list of currently available IFUs in the optical domain, collected



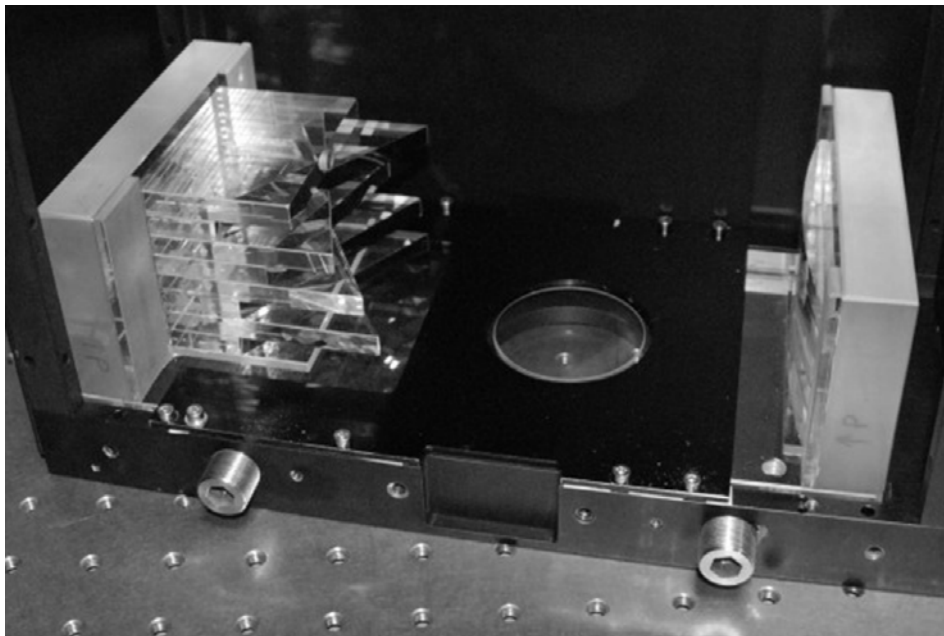


**Figure 1.4:** Picture of MUSE's field slicer currently being assembled. On the left, eight of the optical elements are already present, which will divide the image into sub-fields that are sent to the 24 IFUs, where the image slicers split the image again, before they reach the spectrographs (©CRAL).

from the *Integral Field Spectroscopy Wiki*<sup>1</sup>. With *Integral* (Arribas et al., 1998), *VIMOS*, *SAURON* and the two *VIRUS* IFUs there are only five instruments with a field of view comparable to that of *MUSE*, but for all of them the spatial sampling is coarser. On the other hand, there are some instruments that can compete with the spatial resolution of *MUSE*, but for those the field of view is significantly smaller.

Conveniently, the apparent radius of most galactic globular clusters is about 1 arcmin, so the field of view of *MUSE* has the perfect size for observing them – and with its high spatial resolution we will be able to identify a couple of thousands of stars in a typical *MUSE* field. Thus, with only a few pointings we can observe major parts of a single globular cluster, and using the narrow field mode, we can have a deep look at its very centre.

Previous spectroscopic observations of globular clusters used either long-slit or multi-object spectroscopy. Both are hampered by the high stellar densities that we see in those stellar systems, so even with a very small slit, we cannot be sure to observe a single star, but will mostly see a blend of spectra from all the stars in the line of sight. This problem can be minimized by concentrating on the brightest stars, but then the sample of stars is strongly biased towards giants. When using an IFU for the observation, we also have the full spatial information of the field available for the analysis,

---

<sup>1</sup><http://ifs.wikidot.com/>

Instr	Type	Range [ $\text{\AA}$ ]	Resolution	Field of view	Pixel size
ARGUS	II	3 700 – 9 500	5 600 – 46 000	12" $\times$ 7" 6.6" $\times$ 4.2"	0.52" 0.30"
GMOS	I	4 000 – 11 000	630 – 4 300	5" $\times$ 7"	0.2"
Integral	II	3 700 – 8 000	$\leq 1.3 \text{\AA} - 22 \text{\AA}$	6.3" $\times$ 5.4" – 33.6" $\times$ 29.4"	0.45" – 2.7"
Kyoto 3DII	I	3 600 – 9 200	1200	3.6" $\times$ 2.8"	0.096"
OASIS	I	4 000 – 10 000	200 – 4 400	3.7" $\times$ 2.7" – 10.3" $\times$ 7.4"	0.09" – 0.26"
PMAS	II	3 500 – 9 000	1 000 – 25 000	8" $\times$ 8" 12" $\times$ 12" 16" $\times$ 16"	0.5" 0.75" 1.0"
SAURON	I	4 500 – 7 000	$\sim 1 500$	41" $\times$ 33" 11" $\times$ 9"	0.94" 0.27"
VIMOS	II	4 000 – 11 500	200 – 3 000	13" $\times$ 13" – 54" $\times$ 54"	0.33" – 0.67"
VIRUS-P	II	3 500 – 6 800	1.6 $\text{\AA}$ – 4.9 $\text{\AA}$	102" $\times$ 102"	4.3"
VIRUS-W	II	4 340 – 6 040 4 850 – 5 740	2 500 6 800	105" $\times$ 75" 105" $\times$ 75"	3.2" 3.2"
MUSE	III	4 650 – 9 300	2.6 $\text{\AA}$	60" $\times$ 60" 8" $\times$ 8"	0.2" 0.025"

**Table 1.1:** Selection of currently available IFUs for the optical domain in comparison to MUSE. The types are (I) lenslets, (II) fibres and (III) image-slicer. ARGUS, VIMOS and MUSE are operating at the VLT, while Integral, OASIS and SAURON are instruments of the William Herschel Telescope on La Palma. The GMOS instrument is available for the both Gemini telescopes (North on Hawaii & South in Chile) and Kyoto 3DII is attached to the Subaru telescope on Hawaii. The PMAS IFU is mounted on the 3.5m telescope on Calar Alto, Spain, and both VIRUS instruments are working at the 2.7 m Harlan J. Smith Telescope at the McDonald Observatory.

which for image-slicers like *MUSE* is even continuous, i. e. without gaps between the pixels. With this, we can use classical photometric techniques like PSF fitting for extracting thousands of single stellar spectra from the data cube.

In order to fully exploit the possibilities of an instrument like *MUSE*, a comprehensive library of stellar spectra is required for comparison with the observations. Since we are aiming for determining the abundances of single elements for the search for multiple populations, those need to be adjustable in the stellar library, so only synthetic spectra were considered. The decision was made to choose the most flexible option and so we calculated a new library of model atmospheres and synthetic spectra with *PHOENIX* (see Chapter 3).

Based on this new library of synthetic stellar spectra, methods for analysing *MUSE* spectra will be presented in Chapter 4. Due to the expected high number of spectra, this has to be done automatically, so a robust implementation is required. All the steps will be discussed that are required in order to derive radial velocities, stellar parameters and even single element abundances from the spectra. The methods have been tested

extensively and we even conducted a *dry run*, in which we tried to simulate and analyse a *MUSE* data cube as realistic as possible (see Chapter 5).

Since our goal is to do actual observations with *MUSE* as soon as the instrument is on sky, I will give recommendations for a *MUSE* proposal in Chapter 6. Finally, in Chapter 7, a summary of what has been done will be presented as well as an outlook on the work that still needs to be conducted in order to produce outstanding scientific results from real *MUSE* data.



## Chapter 2

# Globular Clusters

Globular clusters (*GCs* or *globulars*) are gravitationally bound collections of hundreds of thousands of old stars, which have a similar distribution of spectral types as has been found in elliptical galaxies or in the bulges of spiral galaxies. In the Milky Way, instead of being metal-rich like in the bulge, they are found to be metal-poor. Their name is derived from the Latin word *globulus*, which means *small sphere*. There are currently 157 GCs known in our galaxy (GGC, Galactic globular cluster, see Harris, 1996, his on-line updates<sup>1</sup> and Table A.1), which is significantly less than what has been estimated for our Galactic neighbour M31 (Andromeda Galaxy) with  $460 \pm 70$  clusters (Barmby & Huchra, 2001).

Among all the clusters that will be mentioned in this chapter,  $\omega$  Centauri is special case (see e. g. Gnedin et al., 2002). Not only does it have a Bayer designation<sup>2</sup>, which marks it a star, but as we will see, it also has a wide spread of metallicity that has always been explained by self-enrichment (Suntzeff & Kraft, 1996), i. e. it is able to retain its own stellar ejecta (Ikuta & Arimoto, 2000). Furthermore, unlike all other globular clusters, it has a retrograde galactic orbit and is almost coplanar with the Galactic disk. Therefore, it has often been suggested that  $\omega$  Centauri is the remaining nucleus of a stripped dwarf galaxy (see e. g. Majewski et al., 2000). Another curious case seems to be M54, a massive globular cluster lying in the nucleus of the Sagittarius dwarf galaxy, which shows some resemblance to  $\omega$  Centauri (see e. g. Layden & Sarajedini, 2000; Carretta et al., 2010b,a).

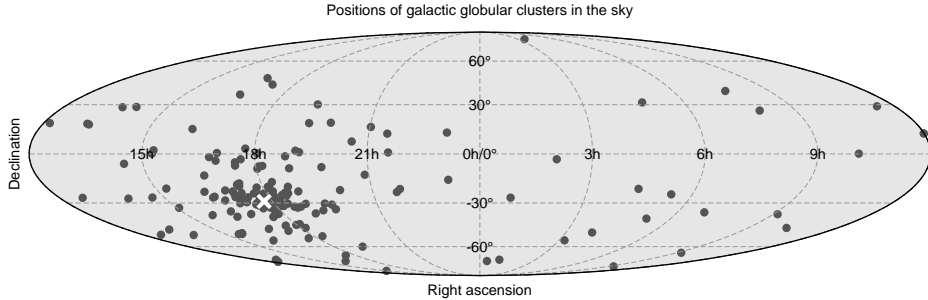


**Figure 2.1:** Positions of all known Galactic globular clusters with data taken from Harris (1996). The Galactic centre (Sgr A\*) is marked with a white cross.

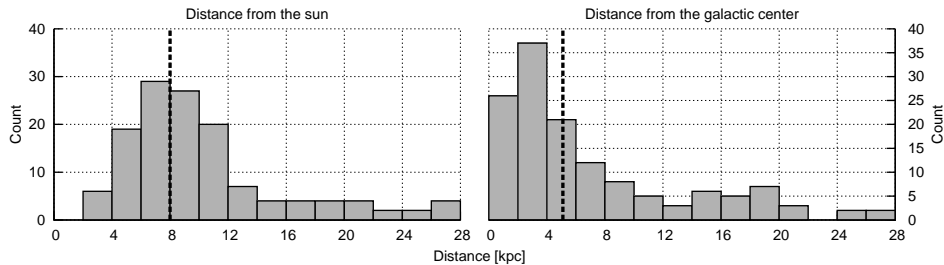


**Figure 2.2:** Distances of Galactic globular clusters from the sun are plotted on the left with the distance to the Galactic centre (8 kpc) marked with the dashed line (16 GGCs with  $d > 30$  kpc are missing in the plot). On the right, the distances from the Galactic centre are shown (with 13 GGCs with  $d > 30$  kpc missing). All the plotted clusters (which are 90% of the total number) are within 27.8 kpc, and still 50% of all GGCs are within 5.1 kpc (dashed line) around the Galactic centre. Plotted with data taken from Harris (1996).

## 2.1 Positions and shapes

Globular clusters orbit the core of their host galaxies as satellites, so in a plot of their on-sky positions (see Fig. 2.1), most Galactic clusters appear to accumulate around a single position (marked with a white cross), which denotes the location of the Galactic centre Sgr A\*. The distribution of the actual distances to the Galactic centre is plotted in Fig. 2.2, clearly showing that most of the Galactic globular clusters orbit the centre of the Milky Way in very close orbits. In fact, 50% of them are at a distance  $< 5.1$  kpc and 90% are within 28.1 kpc.

The sizes of GCs are usually measured using either the core radius  $r_c$  that measures the distance at which the apparent surface luminosity has dropped to half, or the half-light radius  $r_h$ , which contains half of the GCs total luminosity (or – as often used by

<sup>1</sup><http://www.physics.mcmaster.ca/~harris/mwgc.dat>

<sup>2</sup>In 1603, the German astronomer Johann Bayer introduced the first systematic naming of stars, using a lower-case Greek letter and the Latin name of the constellation. For most stars, their name roughly indicates an order in apparent brightness, e. g. in almost all constellations, the star designated by  $\alpha$  is the brightest.

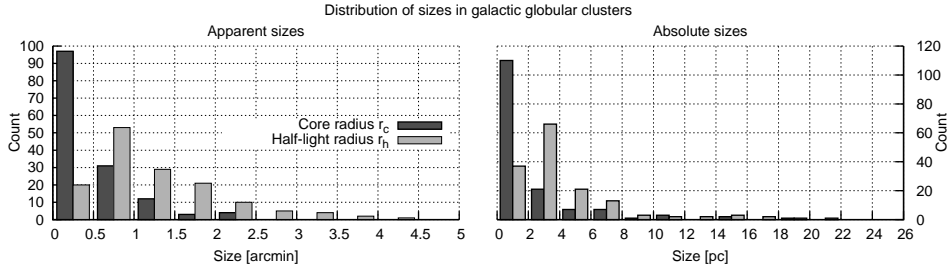


**Figure 2.3:** Plots of the distribution of radii in Galactic globular clusters with data taken from Harris (1996). On the left, apparent sizes on the sky are plotted, while absolute sizes are shown on the right.

theorists – half the mass, which is a more physical approach). As a third measurement for the size, the tidal radius  $r_t$  can be used, beyond which the dynamics are dominated by the external gravitational field of the galaxy. Figure 2.3 shows the distribution of core and half-light radii for Galactic globular clusters. Apparent sizes on sky are plotted as well as absolute sizes. Almost all GGCs have absolute half-light radii of  $r_h < 10$  pc, and coincidentally the mean of the apparent half-light radii is about 1 arcmin, with even the apparently largest cluster in the sky,  $\omega$  Centauri (NGC5139), having an absolute radius of only  $r_h = 9.3$  pc. On the other hand, there are very large GGCs with half-light radii of  $r_h = 25.4$  pc (Palomar 14) and  $r_h = 23.3$  pc (NGC2419).

Globular clusters are usually almost spherical, but tidal interactions can cause slight ellipticities. In the Milky Way, the ellipticity is usually quite small with an average of  $\epsilon = 1 - b/a \approx 0.08$  (Geyer et al., 1983; White & Shawl, 1987, and Table A.1). A similar value for  $\epsilon$  between 0.07 and 0.13 has been found for M31 (Lupton, 1989; Davoust & Prugniel, 1990; Staneva et al., 1996), whereas both in the SMC and the LMC the clusters seem to be more elliptical with  $\epsilon \approx 0.19$  in the former (Kontizas et al., 1990) and something between 0.11 and 0.22 in the latter (Geisler & Hodge, 1980; Geyer & Richtler, 1981; Frenk & Fall, 1982; Kontizas et al., 1989).

In Fig. 2.4, the distribution of stellar densities for a selection of globular clusters is plotted with data from the ACS dataset (Anderson et al., 2008), both for all stars in the sample and for only the stars above the main sequence turn-off (i. e. those that have evolved away from the MS), which has been estimated roughly by looking at the colour-magnitude diagram for each cluster. The coordinates for the centres of the clusters are taken from Goldsbury et al. (2010). Since they did not include M15, Simbad coordinates have been used for that one instead. We see an increase of the density towards the centres, which is quite significant for the case of M15, especially when looking at the more evolved stars only. The reason for this can be found in the core collapse of that cluster, which will be discussed later on.

The most common way for describing the density distribution of globular clusters is the empirical law found by King (1962), which is nowadays known as *King law* and is

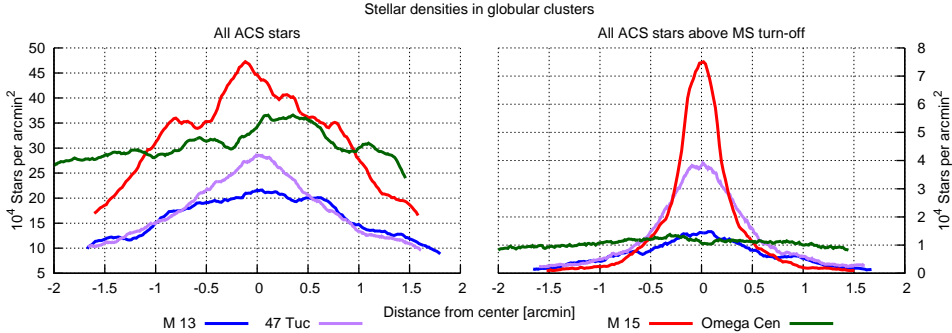


**Figure 2.4:** Distribution of stellar densities in a few selected globular clusters for all stars (left) and all stars that have already evolved beyond the main-sequence (right). Please note that not the total number of stars in  $1 \text{ arcmin}^2$  of the ACS data is plotted but just the stellar density as projected from  $20 \times 20 \text{ arcsec}^2$  sized fields.

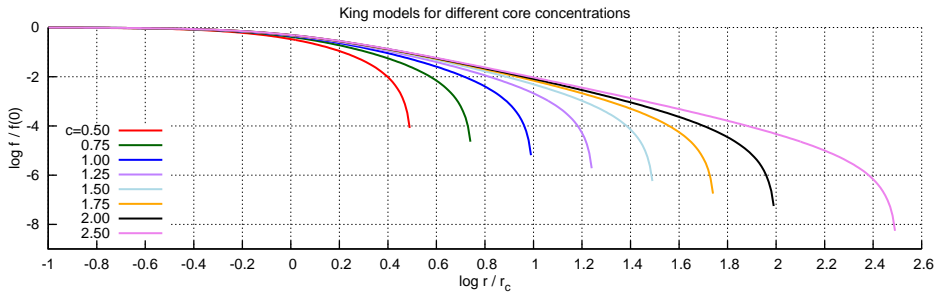


**Figure 2.5:** King models (King, 1962) for different core concentrations  $c = \log(r_t/r_c)$ , normalized to their value at  $r = 0$ , i. e.  $f(0)$ .

given by

$$f(r) = k \cdot \left[ \frac{1}{\sqrt{1 + (r/r_c)^2}} - \frac{1}{\sqrt{1 + (r_t/r_c)^2}} \right]^2, \quad (2.1)$$

with the free parameter  $k$ . He defined the ratio between  $r_t$  and  $r_c$  as the core concentration  $c$ , but we want to employ a more common definition using the logarithm of this ratio (see e. g. Harris, 1996), i. e.  $c = \log(r_t/r_c)$ . Thus, a large  $c$  indicates that the tidal radius  $r_t$  is large compared to the core radius  $r_c$ , which on the other hand means that the cluster has a small core with a high concentration of stars. Figure 2.5 shows the King models for a variety of different values for  $c$ . Those simple morphological models can then be used to create dynamical ones, which will be discussed later on.



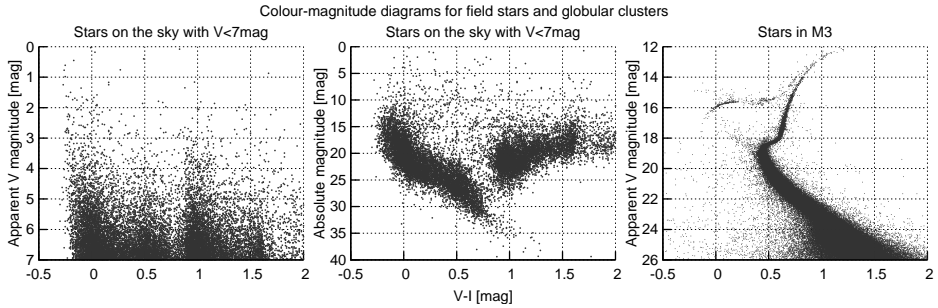


**Figure 2.6:** Comparison of colour-magnitude diagrams of field stars (left and middle, with Hipparcos data taken from Perryman & ESA (1997)) and stars in the globular cluster M3 (right, with HST ACS data taken from Anderson et al. (2008)).

## 2.2 Ages

Globular clusters have always been known to be very old due to their low metallicity and their CMDs (see below) being compatible with ages  $>10$  Gyrs only (see e.g. Sandage & Schwarzschild, 1952; Hoyle & Schwarzschild, 1955), but their absolute ages have been a big mystery for a very long time, since for a while they appeared to be older than the universe itself. The evolution of the supposed ages for both can be seen nicely in the biography of a single astronomer: Allen Sandage. In 1961 he estimated the age of M13 to be  $\sim 22$  Gyrs (Sandage, 1961). Unfortunately, he himself had already published an age of the universe of only  $\sim 13$  Gyrs three years earlier (Sandage, 1958), which is consistent with a Hubble constant of  $H_0 \approx 75$  km/s/Mpc. Ten years later he still kept the cluster age, but mentioned the possibility that  $H_0$  might be as small as 50 km/s/Mpc (Sandage, 1968), which, with an corresponding age of the Universe of  $t_0 = 1/H_0 \approx 20$  Gyrs, would better fit his estimated ages of globular clusters. Although he corrected the latter (including M13) to 10-13 Gyrs (Sandage, 1970), he stuck with  $H_0 \approx 50$  km/s/Mpc (Sandage, 1972) and opposed other astronomers who believed more in a value of  $H_0 \approx 100$  km/s/Mpc (see e.g. van den Bergh, 1970; de Vaucouleurs & Peters, 1981), which corresponds to an age of the universe of 10 Gyrs. Taking this higher number for  $H_0$  led to an 'age crisis' in the 1990s, but later observations of *WMAP* (Spergel et al., 2003) fixed the Hubble constant to  $H_0 = 72 \pm 5$  km/s/Mpc and therefore the age of the universe to  $t_0 = 13.7 \pm 0.2$  Gyrs. The accuracy has meanwhile been improved to  $H_0 = 71.0 \pm 2.5$  km/s/Mpc and  $t_0 = 13.75 \pm 0.13$  Gyrs respectively (Jarosik et al., 2011). Altogether, the determination of globular cluster ages, which we are going to discuss now, is of paramount importance for cosmology, since they give a lower limit on the age of the Universe.

Hertzsprung-Russell diagrams, which show the relationship between luminosities and temperatures of stars, are very important astronomical tools. For observers, the colour-magnitude diagrams (CMD) as a special case are often more useful, since a colour (like B-V or V-I) is much easier to measure than the temperature (or spectral type), and relative brightnesses easier than absolute fluxes respectively. When tak-

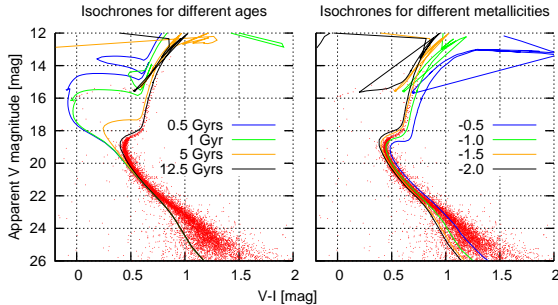


**Figure 2.7:** Subset of data points from the right plot in Fig. 2.6, over-plotted with some isochrones for different ages and metallicities from Marigo et al. (2008).

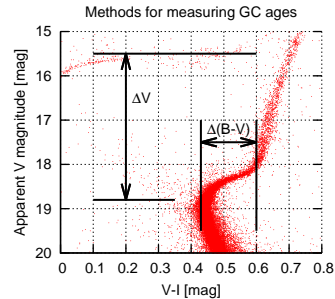


**Figure 2.8:** Illustration of vertical ( $\Delta V$ ) and horizontal ( $\Delta(B-V)$ ) methods for measuring GC ages.

ing all the stars with a V magnitude brighter than 7 mag from the Hipparcos catalogue (Perryman & ESA, 1997) and plotting their V magnitude versus their B-V colour, the result is a random scatter of points as shown in the left plot of Fig. 2.6. Of course, this is caused by the random distances of those stars from the sun, but we can easily calculate their absolute magnitudes using the parallaxes measured by Hipparcos. The resulting colour-magnitude diagram is shown in the central plot of Fig. 2.6, in which both the main-sequence (left) and the giants (right) are easily identifiable. The main reason why both still look rather scattered, can be found in the different ages of the stars.

In the right plot of Fig. 2.6, a colour-magnitude diagram from ACS@HST photometry (Anderson et al., 2008) for a globular cluster (M3) is shown, clearly presenting a well-defined main-sequence and a giant branch. Lower on the MS, we still see a significant scattering, but here it is mainly caused by the very low signal-to-noise ratio of those faint star measurements and the heavy crowding in globular clusters. We also see the *horizontal branch* (HB) on the upper left, which consists of Population II stars burning He in the core. Although theory and observations seem to agree that the HB morphology becomes redder with increasing metallicity, there are some examples of globular clusters with similar metallicities but different HB morphologies (for the distribution of metallicities in GGCs, see Fig. 2.10). Thus, something else must affect the evolution of the HB, which is why this phenomenon became known as the *second parameter problem*. Dotter et al. (2010) suggested that this second parameter is the age of the GC and that with the central density likely there is a third.

In the plot, a clear 'knee' is visible, which is the turn-off point from the main sequence to the giant branch: all the stars formerly higher up on the main-sequence have already started burning hydrogen in the shell and evolved to giants. Figure 2.7 shows a subset of the same data for M3 again, overplotted with theoretical isochrones by Marigo et al. (2008) for different ages and metallicities. We see significant changes in the shapes of the isochrones and especially in the positions of the main-sequence turn-off points (MSTO). The fact that the MSTO is so well-defined in the observational data tells us that the stars are all roughly of the same age, i. e. the duration of star formation in globular clusters was very short compared to their current ages. This also means

that presumably they all have formed from the same cloud of gas and dust and therefore their chemical composition should be very uniform. In fact, observations showed a variation in metallicity by no more than  $\sim 0.03$  dex for most GCs (Suntzeff, 1993). The mean metallicity in Galactic globular clusters is about  $-1.5$  dex – the overall distribution is plotted in Fig. 2.10. Later on we will see that GCs are not as simple objects as thought.

Several methods have been proposed for determining the absolute ages of globular clusters (see e. g. Stetson et al., 1996; Sarajedini et al., 1997; Meissner & Weiss, 2006). The preferred one for some time was *main sequence* fitting, for which the absolute magnitude of the MSTO was compared to theoretical values. The major problems of this method are the difficulties of measuring exact distances to the GCs and determining the reddening. Both can be avoided by using the  $\Delta V$  (or *vertical*) method (Gratton, 1985) instead that depends on the difference between the magnitudes of MSTO and HB at the colour of the MSTO, i. e.  $\Delta V = V_{\text{MSTO}} - V_{\text{HB}}$ . Alternatively, one can measure the colour difference between the MSTO and the base of the giant branch (the  $\Delta(B - V)$  or *horizontal* method, see Vandenberg et al., 1990). Both approaches for measuring GC ages are illustrated in Fig. 2.8. Together with new methods for determining the distances to GCs more accurately (like using the White Dwarf cooling sequence), new cluster ages compatible with the age of the universe were derived, e. g.  $12.7 \pm 0.7$  Gyrs for M4 (see e. g. Hansen et al., 2002), which finally solved the aforementioned ‘age crisis’. Absolute ages for 55 GGCs have been measured by Salaris & Weiss (2002).

All these methods for determining the absolute ages of GCs are limited by one or more uncertainties like distances, foreground reddenings, metallicities, bolometric corrections and our understanding of stellar evolution. Relative ages on the other hand are (almost) free of these effects. So instead of comparing the CMDs directly with theoretical isochrones, one can measure differences between GCs only in order to estimate relative ages, which works well for all methods discussed before. The highest accuracy of 2-7% for the relative ages of GCs so far has been presented by Marín-Franch et al. (2009) based on HST photometry of 64 GGCs. They shifted the MS of one GC both in magnitude and colour so that it matches the MS of another one. The relative age between both was then derived from the magnitude difference of the MSTO.

## 2.3 Time scales

Typical time scales for the evolution of globular clusters are the crossing time  $t_{\text{cross}}$ , the relaxation time  $t_{\text{relax}}$  and the evaporation time  $t_{\text{evap}}$ . With a characteristic cluster size  $R$  and a typical velocity  $v$  ( $\sim 10$  km/s), we get the crossing time  $t_{\text{cross}} \sim R/v$ , which is the time it takes a star to cross the whole cluster. The relaxation time is the typical time after which a star has had so many interactions with other stars that it is impossible to reconstruct its original velocity, i. e. it is the time after that all those interactions caused a change in velocity that is comparable with its original velocity. Therefore it depends on the number and strength of gravitational encounters and according to Binney &

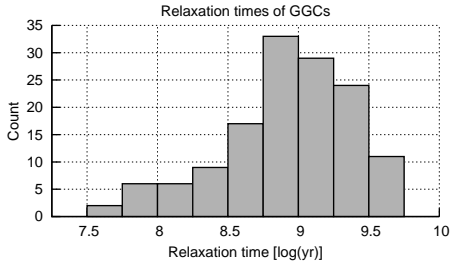


**Figure 2.9:** Relaxation times of Galactic globular clusters, plotted with data from Harris (1996).

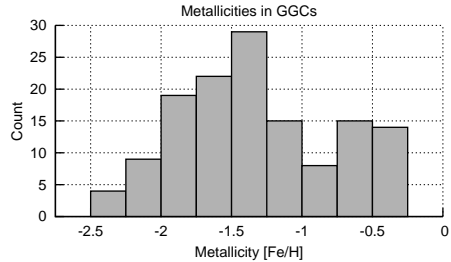


**Figure 2.10:** Distribution of metallicities in Galactic globular clusters, plotted with data from Harris (1996).

Tremaine (1987) it can be described as:

$$t_{\text{relax}} \approx \frac{0.1N}{\ln N} t_{\text{cross}}. \quad (2.2)$$

With a typical number of stars  $N$  of  $10^5 - 10^6$  and radii of  $R < 10$  pc, we get typical crossing times of  $t_{\text{cross}} < 10^6$  yr and therefore typical relaxation times of  $\sim 10^9$  years. Figure 2.9 shows the actual distribution of relaxation times for all Galactic globular clusters (see also Table A.1).

At last, the evaporation time  $t_{\text{evap}}$  is the time after which a cluster dissolves itself by ejecting members. According to Benacquista (2006) this can be estimated to:

$$t_{\text{evap}} = \frac{t_{\text{relax}}}{\gamma} = 136 \cdot t_{\text{relax}}, \quad (2.3)$$

where  $\gamma$  is the fraction of stars that are ejected every relaxation time. With a typical relaxation time this yields  $t_{\text{evap}} \sim 10^{10}$  yr.

We can conclude that the dynamical evolution happens on very different time scales with

$$t_{\text{cross}} \ll t_{\text{relax}} \ll t_{\text{evap}}. \quad (2.4)$$

which is quite different from what we see in other stellar systems. For galaxies with typically  $N \approx 10^{11}$  stars and an age of a couple of hundred  $t_{\text{cross}}$ , we get relaxation times larger than the age of the Universe, so (except for their cores) stellar encounters are negligible for their dynamical evolution. For open cluster with  $N \approx 100$  on the other hand, the crossing time is similar to the relaxation time and we see a quick evaporation of the system within a few hundred Myrs. Consequently, globular clusters are the only dynamically evolved large stellar systems with dynamical processes on time scales shorter than their age, which allows us to study topics like mass segregation, core collapse and stellar collisions and mergers in detail.

In all these systems, the dynamics on timescales  $\lesssim t_{\text{relax}}$  can be described as movement in a gravitational field created by a smooth mass distribution, rather than a collection of mass points. Thus, we are dealing with a *collisionless system*, which will help us modelling the dynamics of globular clusters, as will be discussed later.

## 2.4 Binaries and core collapse

In the middle of the 20th century, the ratio of main-sequence F and G stars in our solar neighbourhood in binary or multiple systems was assumed to be something like 70-80% (Heintz, 1969; Abt & Levy, 1976; Abt, 1983). By looking at solar-like F7-G9 stars in the solar neighbourhood within 22 pc, Duquennoy & Mayor (1991) were able to lower this number to 57%. It was (and still is) commonly believed in the astronomical community that this number is valid for all spectral types and therefore the ratio of multiple star systems in our galaxy is assumed to be about two-thirds<sup>3</sup>. This belief might have been encouraged by the realization that most stars are not born isolated, but in multiple-star systems (see e. g. Shu et al., 1987; Mathieu, 1994).

For O-type stars in young open cluster, Sana et al. (2008) found a binary fraction of 63%, and it even seems to be 82% for stars earlier than B1.5V (García & Mermilliod, 2001). This last number seems a bit high, but with a sample of only 37 stars it is poorly determined. Nevertheless, the binary fraction seems to be equal to or even higher than that of solar-like stars. Of course the total numbers of O-type stars is much less, so the impact on the overall binary fraction is negligible.

Recent studies of the initial mass function (IMF) have found that it peaks roughly between 0.1 and 0.5  $M_{\odot}$  for both field stars (Kroupa, 2002) and young clusters (Muench et al., 2002), which means that the majority of stars formed in the Galactic disk are M stars. For those, Fischer & Marcy (1992) found a binary fraction of  $42 \pm 9\%$ , and even a number as low as  $26 \pm 9\%$  has been suggested by Leinert et al. (1997). For both studies, only a few stars have been observed (100 and 34), but still, Lada (2006) claims that as many as two-thirds of all main-sequence stellar systems in the Galactic disk are single stars.

Although this number is still a lot smaller than the 70-80% that has been assumed to be the true binary fraction in the middle of the last century, it is still huge compared to the numbers we find in globular clusters: Cool & Bolton (2002) found a binary fraction of less than 5-7% in the dense central region of NGC6397 and a value of 10-20% has been found for sparse clusters like NGC288 by Bellazzini et al. (2002). For the outer regions of the latter cluster they even claim an upper limit of 10% with the most likely number of binaries to be zero. Some core-collapsed clusters like NGC6752 show a binary fraction between 15 and 38% in the core, which is probably  $<16\%$  beyond that (Rubenstein & Bailyn, 1997). So we see a huge difference between the binary fraction in field stars and open clusters and in globular clusters. This fact is quite important, because binary stars – even in there now observed small number – play a significant role in the evolution of globular clusters: not only do stars evolve differently in binary systems as the same stars in isolation, but binaries also provide the energy that prevents the clusters from a gravothermal collapse.

In a globular cluster, a lot of close encounters between stars happen, and when

---

<sup>3</sup>In line with other studies, in this thesis we define the binary fraction  $f$  to be equal to the ratio of the number of binary or multiple systems to the total number of objects in the sample. So  $f = 50\%$  implies that two-thirds of main-sequence stars in a given population are in binary systems.

they do, the members exchange both energy and momentum. Although energy can be exchanged in either direction, we see an effect called *equipartition*, which preferentially causes both stars to end up with the same amount of kinetic energy. If they are of different mass, the more massive one has to slow down while the lighter one speeds up. For the globular cluster 47 Tuc, observations using the HST (McLaughlin et al., 2006) show clear evidence that blue stragglers (see Section 2.5) move with lower velocity than average stars. As a result, the massive star sinks to a lower orbit closer to the centre and the lighter one rises to a higher one accordingly. So over a long period of time we see a concentration of massive stars near the core, which is a phenomenon called *mass segregation*.

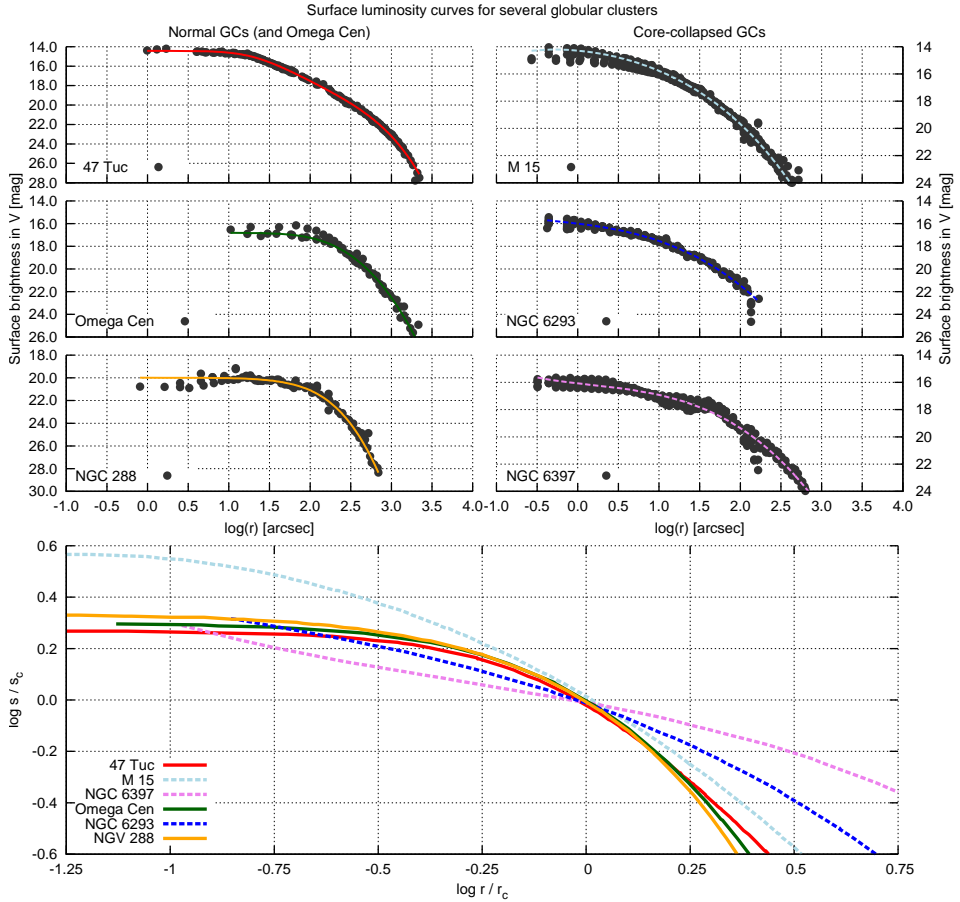
If one of the members of the encounter is a binary star, instead of migrating towards the centre it can either be destroyed in the process or release energy by contracting its orbit. In this so-called 'binary burning' phase, the cluster can retain its constant core density and velocity dispersion over many relaxation times. Only after the supply of binaries is exhausted can the migration of massive stars towards the centre continue (Fregeau et al., 2003; Goodman & Hut, 1989; Gao et al., 1991). According to Fregeau (2008), most globular clusters are not in the binary-burning phase yet, i. e. their cores can still contract unresisted, and only about 20% actually are.

Figure 2.11 shows the luminosity plotted as function of distance from the cluster centre for six globular clusters with over-plotted coloured lines, which are some best-fitting functions. In those plots, we do not see a clear difference between the three on the left and those on the right, but with known core radii  $r_c$ , we can plot the fits as logarithmic surface brightnesses in arbitrary units over  $\log(r/r_c)$  as shown in the lower plot. Obviously, for three of the clusters the luminosity continues to increase steadily all the way to the centre. Due to this observational anomaly, we call those clusters *core-collapsed*. For them, the mass segregation has advanced significantly and what we see as a cusp in the luminosity profile are the massive stars that have migrated inwards.

Now there seems to be a life for globular clusters after the core collapse (see e. g. Hut & Djorgovski, 1992). When due to the collapse, the density in the core reaches about  $10^7 M_\odot \text{pc}^{-3}$  with a few tens of stars, a couple of hard binaries<sup>4</sup> are formed (Cohn & Hut, 1984). When other stars interact with those binaries, they are likely to be ejected from the core, since their resulting velocity can be much larger than the escape velocity. Due to this, the binding energy of the core decreases and it starts expanding again. For GCs in this stage, we expect strong *gravothermal* oscillations in the central density with amplitudes up to  $10^6$  (Sugimoto & Bettwieser, 1983; Bettwieser & Sugimoto, 1984; Cohn et al., 1989). Nevertheless, after the first core collapse, stars outside the inner  $10^3 - 10^4$  AU are likely to continue expansion (Cohn & Hut, 1984).

---

<sup>4</sup>A *hard* binary is a binary system, for which the orbital binding energy is high enough, so that in an encounter with a third body the total energy is negative, which increases the binding energy even further and causes the third star to be ejected.



**Figure 2.11:** Plots of the surface luminosity curves for several non-core-collapsed and core-collapsed clusters and  $\omega$  Cen as a special case. Plotted with data from Trager et al. (1995) in black are measured luminosities with fitted function in colours. In the lower plot, the fits are plotted as logarithmic surface brightnesses in arbitrary units over  $\log(r/r_c)$  and matched in brightness at  $\log(r/r_c) = 0.0$ .

## 2.5 Blue stragglers

When looking at colour-magnitude diagrams of globular clusters, we sometimes see stars that are bluer and more luminous than the main-sequence turn-off points, which should not be there anymore but instead have evolved to giants already. They are known as *blue straggler stars (BSS)* and were first observed by Sandage (1953). Young as they are, they could not have formed together with the other stars in the GC, and even the observed multiple populations (see Section 2.7) are older than the BSS. Thus, other formation scenarios need to be found.

For a single BSS in 47 Tuc, Shara et al. (1997) were able to determine a mass of

$1.7 \pm 0.4 M_{\odot}$ , which would be twice that of the oldest hydrogen-burning cluster star. Furthermore, they found a high rotational velocity of  $v \sin i = 155 \pm 55$  km/s, indicating that the progenitor of the BSS might have been a binary system. In this scenario, the more massive component of the binary system evolves first and expands, until it fills its Roche lobe and mass starts flowing to its companion. After some time, the latter will appear as a massive main-sequence star, while the former will look more like a sub-giant (McCrea, 1964; Knigge et al., 2009).

Another explanation can be found in the merging of stars. However, especially in low-density GCs, the expected number of collisions between stars is too low to explain the observed number of BSS (Leonard, 1989). This problem can be solved by binary systems: as shown before, mass segregation will let them migrate towards the centres of their clusters, where the stellar density is much higher. Furthermore, for a binary-binary collision the cross-section is about 100 times larger than that for single-single collisions. Consequently, we can expect some BSS to form in the centre of GCs by merging of stars from former binary systems (*collisional merging*). On the other hand, stellar mergers can also occur in a binary system, in which its components spin down (*binary merging*) on time scales of about 50 Myrs (Mateo et al., 1990).

Both scenarios, accretion and merging, do not necessarily exclude each other. In fact, observations show evidence that both types can be found in GCs (Bailyn, 1992). For three different GCs (M3, 47Tuc, NGC6752), Mapelli et al. (2006) found the the density of BSS to be high in the centre, almost vanishing at intermediate radii (the so-called *zone of avoidance*) and increasing again for larger radii, which would be consistent with two different formation scenarios, i. e. mergers at the centre and accretion in the outskirts. However, for  $\omega$  Centauri they found no peak in the density of BSS whatsoever, and for other GCs the distribution also seems to be unimodal, e. g. in M75 (Contreras Ramos et al., 2012). Consequently, more observations will be required in order to determine the distribution and therefore the formation scenario of BSS.

## 2.6 Kinematics and black holes

Although in the end of the 18th century Pierre-Simon Laplace already suggested the existence of objects that are so heavy that not even light can escape their gravitational pull, and although Karl Schwarzschild already found a solution for Einstein's theory of general relativity characterizing black holes (which were only called that after a lecture by John Wheeler in 1967) in 1916, it took another almost sixty years before first observational evidence was found for their existence (Bolton, 1972; Webster & Murdin, 1972). After that, black holes were found to exist in two different flavours, the *stellar black holes* and the *super-massive (SMBH)* ones. The former are assumed to be created by the gravitational collapse of stars with  $\gtrsim 3 M_{\odot}$  when they reach the end of their lives. The largest stellar black hole that has been found so far has a mass of  $\approx 30 M_{\odot}$  (Silverman & Filippenko, 2008).

Super-massive black holes with masses  $> 10^5 M_{\odot}$  on the other hand are assumed



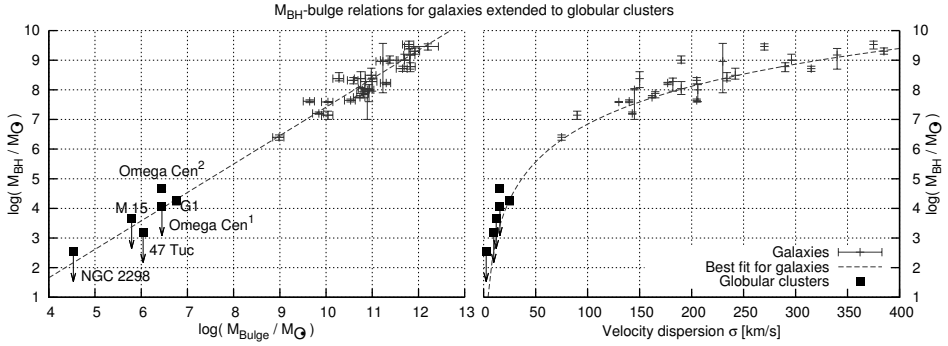


**Figure 2.12:**  $M_{BH}$ -bulge relations for galaxies (plusses with error bars), plotted with data taken from Marconi & Hunt (2003). On the left the relation between the mass of the bulges and those of the black holes are plotted with a best-fit (dashed) from the same publication using  $\log(M_{BH}/M_{\odot}) = 8.28 + 0.96 \cdot (\log(M_{bulge}/M_{\odot}) - 10.9)$ . On the right the mass of the black hole is plotted over the stellar velocity dispersion with a best-fit (dashed) from Gültekin et al. (2009) with  $\log(M_{BH}/M_{\odot}) = 8.12 + 4.24 \cdot \log(\sigma/200)$ . Data points for globular clusters (squares) have been added with data from van der Marel & Anderson (2010). The two points for  $\omega$  Cen indicate the conflicting results in the same publication (<sup>1</sup>) and in Noyola et al. (2010) (<sup>2</sup>).

to be located in the centre of every galaxy. For our Milky Way, the mass of the black hole has been determined by the movement of single stars (see e.g. a star with a 15.2-year orbit in Schödel et al., 2002) and multiple stars within one light-month (Eisenhauer et al., 2005) in its orbit to  $(3.6 \pm 0.3) \cdot 10^6 M_{\odot}$ . The position of the black hole is associated with the radio source Sagittarius A\*. In the Galactic neighbourhood, our very own black hole seems to be a smaller one as compared to the ones found in M31 with  $(1.1 - 2.3) \cdot 10^8 M_{\odot}$  (Bender et al., 2005) or in M87 with  $6.4 \pm 0.5 \cdot 10^9 M_{\odot}$  (Gebhardt & Thomas, 2009).

Black holes seem to play a fundamental role in the evolution of their host galaxies as the various relations between their masses and intrinsic properties of their surrounding bulge ( $M_{BH}$ -bulge relations) indicate. Figure 2.12 shows the relation of the mass of the black hole to both the mass (left) and the velocity dispersion (right) of the bulges in black. Furthermore we observe a strong correlation between AGN activity caused by accretion of the central black hole and star formation (Kauffmann et al., 2003).

Between these two extrema, we are missing black holes with  $30 M_{\odot} < M < 10^5 M_{\odot}$ . Under the assumption that globular clusters are something like *mini-bulges*, we could extrapolate the  $M_{BH}$ -bulge relations to lower masses and compare the results to actual observations of clusters. This has been done in Fig. 2.12 with observed data for some globular clusters marked in red. We see that for both their total mass and their velocity distribution the extrapolation yields black hole masses of  $10^3 - 10^4 M_{\odot}$ , which agrees well with the upper limits found in observations. We call this kind of black holes *intermediate mass black holes (IMBH)*, but evidence for their existence is still scarce.

Portegies Zwart & McMillan (2002) carried out N-body simulations of stars in globular clusters, which showed that near in time to the core-collapse, collisions in the centre of a globular cluster can result in the runaway growth of a super-massive object, which can end up with about 0.1% of the total cluster mass. Again, this result is

consistent with the scarce evidence from observations that exists at the moment. They concluded that all star clusters older than 5 Myrs with half-mass relaxation times of less than 100 Myrs are expected to contain an intermediate mass black hole.

For determining the mass (or even proving the existence) of an IMBH, one would usually measure the stellar velocities in the globular cluster. A strong indication for a black hole would be a rise of the velocity dispersion that cannot be explained by the increasing stellar mass density alone. Unfortunately only stars within the *sphere of influence* are affected directly by the black hole, for which according to Peebles (1972) has the radius  $r_i$ :

$$r_i = \frac{GM_{\text{BH}}}{\sigma^2}, \quad (2.5)$$

with the gravitational constant  $G$ , the mass  $M_{\text{BH}}$  of the black hole and the velocity dispersion  $\sigma$ . For the globular cluster 47 Tuc this would yield  $r_i \approx 6.73 \cdot 10^{-2}$  pc, which, in a distance of 4.5 kpc, gives an apparent radius of only  $\sim 3''$ .

Serendipitously, we can expect the velocity distribution around a black hole to be circular anisotropic (Gebhardt et al., 2003), so when looking directly into the centre of a cluster, one could even hope to see indications of rotational velocity around the central point. This, of course, would be complicated by the fact that there are still problems determining the exact dynamic centre of globular clusters (see discussions in Noyola et al., 2010; van der Marel & Anderson, 2010).

The first models for describing the dynamical processes in globular clusters were developed by King (1966). As we have seen before, for GCs the relaxation times are typically shorter than their ages, so they should be close to dynamical equilibrium with a Maxwellian velocity distribution function. Under the assumption that all stars have the same mass, he derived the distribution function

$$f(E) = A \cdot \begin{cases} e^{aE} - e^{-aE_0} & \text{if } E \leq E_0, \\ 0 & \text{if } E > E_0, \end{cases} \quad (2.6)$$

where  $A$  and  $a$  are positive constants. The specific energy  $E$  is given by  $E = v^2/2 + \Phi(r)$  with the mean-field gravitational potential  $\Phi(r)$ . The threshold  $E_0$  marks the energy above which the stars are considered unbound, i. e. the “edge” of the cluster, which correlates it with the tidal radius  $r_t$ . With what we have learned about the dynamics of globular clusters so far, it is easy to see that King models are not suited for describing the effects of mass segregation, binaries, core collapse and so forth. First attempts to improve this situation were made by Da Costa & Freeman (1976) for M3 using multi-mass models and equipartition of energy in the centre.

Today, the common way for describing the dynamics of a stellar system is a mass distribution function  $f(\vec{x}, \vec{v}, t)$  in phase space, which defines the total mass in  $d\vec{r}d\vec{v}$  as  $f(\vec{r}, \vec{v}, t)d\vec{r}d\vec{v}$ . With the constraint that the phase space volume should be conserved, we get the the collision-less Boltzmann equation:

$$\frac{\partial f}{\partial t} + \mathbf{v} \cdot \frac{\partial f}{\partial \mathbf{x}} - \frac{\partial \Phi}{\partial \mathbf{x}} \cdot \frac{\partial f}{\partial \mathbf{v}} = 0, \quad (2.7)$$

which, with some simplifications like the assumption of spherical symmetry (i. e.  $\Phi = \Phi(r)$ ), can be transformed into Jean's equation (see e. g. Binney & Tremaine, 2008). The mass density can be derived from the observed brightness profile in order to find the gravitational potential  $\Phi = \Phi_{\text{stars}}(r) - GM_{\text{BH}}/r$ , which best fits the observed velocities. Another approach is to use *Schwarzschild models*<sup>5</sup>, which are a combination of N-body models and analytic techniques (see e. g. Binney & Tremaine, 2008).

In order to prove the existence of an intermediate-mass black hole in the center of a globular cluster, we need to find solutions with  $M_{\text{BH}} > 0$ , which are significantly better than those with  $M_{\text{BH}} = 0$ . Unfortunately, there are effects that can mimic the evidence for the existence of a black hole. In order to model the mass density in a GC, we need to make assumptions about the radial dependency of the mass-to-light ratio  $M/L$ , and a wrong prediction at this point will yield an incorrect gravitational potential. Problems can also arise from the simplifications made for the model, e. g. the radial symmetry. Another source of error can be a radial velocity anisotropy, which can also be wrongly interpreted as evidence for a black hole (Binney & Mamon, 1982).

## 2.7 Multiple populations

As mentioned before (see Section 2.2), there are strong indications that globular clusters are very simple structures in which all stars have the same age and chemical composition. Of course, this simplistic picture was and still is very unlikely, since instantaneous star formation and complete chemical homogeneity of the preceding molecular cloud are not to be expected. Therefore, it was only a question of time before multiple populations (read this as “multiple generations of stars”) would be found. This summary is not supposed to be complete due to the complexity of the topic; a very comprehensive overview is given by Gratton et al. (2012).

One of the most impressive pieces of evidence for the existence of multiple stellar population (MPs) is the split main-sequence in  $\omega$  Cen, which has been found by Anderson (1997, 2002) and confirmed by Bedin et al. (2004a,b). Figure 2.13 shows colour-magnitude diagrams of the same cluster in different filters as observed with ACS@HST by Bellini et al. (2010). In the left and middle plot multiple turn-off points and red giant branches are easily recognizable. On the right, the main-sequence is shown, overplotted with density profiles at different magnitudes, where at least one split in the main-sequence is visible (see also Fig. 2 in Bellini et al., 2010). This gives visual proof that globular clusters are not as simple as thought and consist of several distinct generations of stars.

Although this discovery has only been made quite recently, first indications of multiple populations had already been found in the 1980s by Hesser & Bell (1980), who discovered differences in star-to-star nitrogen abundance of factors of about 5 in main-sequence stars of 47 Tuc. They concluded that this is impossible to achieve with a single generation of stars, since there is no mechanism able to mix N to the surface of

<sup>5</sup>Named after Martin Schwarzschild, the elder son of Karl Schwarzschild.

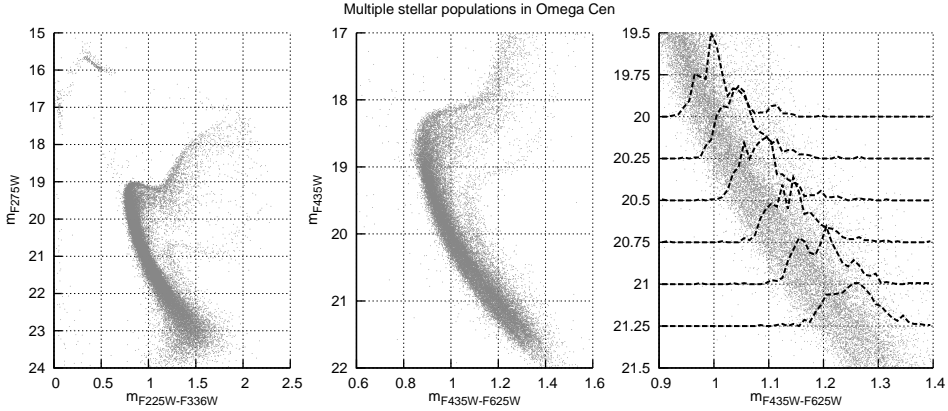


**Figure 2.13:** Colour-magnitude diagrams of  $\omega$  Cen in different filters, plotted with data taken with ACS@HST by Bellini et al. (2010). The right plot shows a zoomed-in view of the middle one with overlaid density profiles.

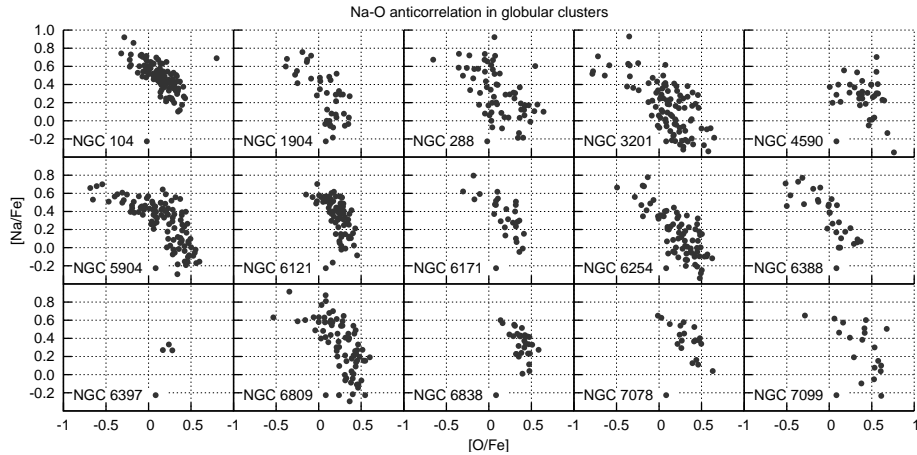


**Figure 2.14:** Na-O anti-correlation in globular clusters, plotted with data from Carretta et al. (2009b).

MS stars, so it had to be primordial. Later, similar work was done by Briley et al. (1996), who discovered a correlation between Na and CN in 47 Tuc, and by Gratton et al. (2001), who found clear indications for O-Na and Mg-Al anti-correlations in main-sequence turn-off stars and early subgiants in NGC6397 and NGC6752. Again, a mechanism was missing for creating this phenomenon, since temperatures of about 70 MK are required in order to produce Na and destroy Mg (Arnould et al., 1999), which could never be reached by MS stars. Similar variations have been found in all types of stars in globular clusters (see e. g. Gratton et al., 2004, and references therein). As an example, Fig. 2.14 shows the Na-O anti-correlation for 15 Galactic globular clusters with data from Carretta et al. (2009b).

Cluster	$\Delta[\text{Fe}/\text{H}]$	References
$\omega$ Cen	1.5	e. g. Norris & Da Costa (1995); Lee et al. (1999)
M54	0.2	Sarajedini & Layden (1995); Bellazzini et al. (2008)
Terzan 5	0.3	Ferraro et al. (2009)
NGC1851	0.08	Yong & Grundahl (2008)
NGC2419	0.2	Cohen et al. (2011)

**Table 2.1:** Observed spread in metallicity for several massive globular clusters.

We now believe that globular clusters have been formed over several generations, with a fraction of first generation stars (the so-called *polluters*) polluting the material from which the second generation was created (see e. g. Gratton et al., 2001, 2004; Ramírez & Cohen, 2002), which therefore now shows the peculiar chemical composition we can observe today, especially of light elements involved in proton-capture processes (C, N, O, F, Na, Mg, Al, Si; see e. g. Carretta et al., 2009a,b, and references therein). Possible candidates for the polluters are massive RGB stars with H-burning products in their convective envelopes (Ventura et al., 2001; D’Antona et al., 2002; Denissenkov & Herwig, 2003), fast-rotating massive stars that eject processed material (Prantzos & Charbonnel, 2006; Decressin et al., 2007) or massive binaries (de Mink et al., 2009).

Historically, multiple populations have first been found in massive globular clusters ( $\omega$  Cen, M54, NGC2808, NGC6388, 47 Tuc) and only later in smaller ones. However, until now, *all* surveyed globular clusters have been found to show the Na-O anticorrelation (except maybe Terzan 7 and Pal 12, see Sbordone et al., 2005; Cohen, 2004) and therefore *all* of them must be composed of multiple populations.

Especially the mass of the clusters seems to have a significant impact on their evolution. Carretta et al. (2010c) found that the amount of polluted material increases with total mass. Furthermore, until now a spread in iron abundance  $[\text{Fe}/\text{H}]$  has been found in the most massive clusters only, see Table 2.1 for details.

For  $\omega$  Cen, Bedin et al. (2004b) suggested a significantly different He abundance in the two populations that they have found. With Norris (2004) those two populations became three and he claimed a He abundance of  $Y \sim 0.38$  for the third population (as compared to  $Y \sim 0.23$  for the first). Piotto et al. (2005) used combined spectra to show that the blue main-sequence is about 0.3 dex more metal-rich than the red one and used a helium enrichment of  $\Delta Y \sim 0.14$  as an explanation. The same has been found for the more *normal* cluster NGC2808, for which Piotto et al. (2007) found three different main-sequences of same age and metallicity but different He abundances. A split MS has also been found in NGC6752 (Milone et al., 2010), 47 Tuc (Anderson et al., 2009) and NGC6397 (Milone et al., 2012a). According to di Criscienzo et al. (2010a,b), this can be explained by a light spread in He abundance for the latter two.

With all those new observations, we understand the evolution of globular clusters a lot better than we had before. They formed in a single burst of star formation, but some of the newborn stars started polluting their surrounding with heavier elements very quickly. From the ejected material originated a second generation of stars, for which

we now see the complex chemical composition. This whole process had to happen in a very short amount of time as indicated by the colour-magnitude diagrams of globular clusters.

One could now argue that globular cluster might have been born with multiple populations, but then we would see evidence for them in open clusters as well. The 1.3 Gyr old open cluster Trumpler 20 has been a prime candidate for this, since it shows a split MS, but Platais et al. (2012) showed that this can be explained by differential reddening entirely and that Trumpler 20 contains a single population of stars only. Thus, multiple populations have to form later during the evolution of the clusters. Predictions on the existence and form of multiple populations have been made by Bekki (2011), Conroy & Spergel (2011) and Vesperini et al. (2010).

## 2.8 Science goals with *MUSE*

With ESO's upcoming new instrument *MUSE* for the *VLT*, we think that we will be able to contribute to the research on globular clusters in several ways. Previous work has always been limited to a small number of bright stars, for which the spectra could be taken easily using a long-slit spectrograph or fibre-fed multi-object-spectroscopy. With the methods discussed in this thesis, we expect to get about 5 000 or more stellar spectra *per exposure*, with some of them from stars well below the main-sequence turn-off point, even in or at least near the centres of dense clusters. With about ten pointings per cluster this will yield a number of spectra, which is by orders of magnitudes larger than anything that has been done before.

At the moment we aim for three science goals, for which the current state of research has been discussed above.

**Binaries** : We are going to visit each observed field in the GCs multiple times. Therefore, we will be able to detect changes in radial velocities caused by binary stars.

**Intermediate-mass black holes** : Measuring the radial velocities will also be important for determining the velocity dispersion in the GCs, which will allow us to look for intermediate-mass black hole in their centres. Taking the results from multiple visits into account will increase the accuracy to the required level.

**Multiple populations** : For the spectra with a high signal-to-noise, we will be able to determine detailed atmospheric parameters and even the abundances of single elements, which might help us to find evidence for the existence of multiple populations.

In Chapter 4, methods will be discussed for the analysis of spectra, which will allow us to work on these science goals and Chapter 5 will show that the achieved accuracy will be good enough in order to produce significant scientific results, resulting in recommendations for actual observations of GCs with *MUSE* in Chapter 6.

## Chapter 3

# A new library of PHOENIX stellar atmospheres and synthetic spectra

For the analysis of *MUSE* spectra, we require a comprehensive library of stellar spectra in order to accurately determine atmospheric parameters (see Chapter 4). The use of *empirical* libraries guarantees real physical spectra, which are free of uncertainties due to limitations from atomic and molecular physics, e. g. line positions, oscillator strengths or line broadening. However, the spectra are limited both in spectral resolution and in wavelength coverage, and possible extensions of an existing library require some significant preparation and observing time. Furthermore, the chemical composition of the observed stars is not known exactly, resulting in possible systematic errors for abundance determinations. The spectra also cover only a small parameter space – especially the number of dimensions is usually restricted to effective temperature, surface gravity and metallicity. Examples for empirical libraries covering the optical wavelength range are the Indo-U.S. Library of Coudé Feed Stellar Spectra (also known as *cflib*, see Valdes et al., 2004), *MILES* (Sánchez-Blázquez et al., 2006), *STELIB* (Sánchez-Blázquez et al., 2006) and *ELODIE* (Prugniel & Soubiran, 2004). Note that all those libraries contain only low to medium resolution spectra.

*Synthetic* spectra on the other hand are limited by the completeness of the spectral line lists as well as by the knowledge of line broadening parameters and assumptions for the numerical solution (plane-parallel versus spherical geometry, local thermodynamic equilibrium *LTE* versus statistical equilibrium *NLTE*). Nevertheless, there are a lot of advantages of using synthetic libraries: the range of stellar parameters, element abundances, and both the wavelength range and the spectral resolution are known exactly and can be adjusted as needed. Presumably the best known set of model atmospheres currently available has been created by Kurucz (1979). Based on those, a lot of spectral libraries have been published, e. g. Rodríguez-Merino et al. (2005) in the

UV and Murphy & Meiksin (2004) and Munari et al. (2005) in the full optical domain. Another stellar atmosphere code called *TLUSTY* was created by Hubeny (1988), providing e. g. a grid of NLTE atmospheres for O stars (Lanz & Hubeny, 2003). Gustafsson et al. (2008) published a grid of spectra based on *MARCS*, which uses spherical symmetry for its models.

We are in fact using empirical libraries like *cflib* and *MILES* (see Chapter 5), but for some applications we require the flexibility of a synthetic library, e. g. to examine variations in the spectra when changing the abundances of single elements (see Section 4.11), which would be impossible to achieve with empirical spectra. Instead of extending an existing synthetic library, we opted for creating a new one using the latest state-of-the-art version of the stellar atmospheres code *PHOENIX* (Hauschildt & Baron, 1999). Previous publications using this code were e. g. Hauschildt et al. (1999a) and Hauschildt et al. (1999b). The latest grid of spectra (Brott & Hauschildt, 2005) was created for use with the *GAIA* mission (Lindegren et al., 2008). In the following, we will refer to spectra created with that version of *PHOENIX* as *AMES-cond-v2.6*. The code also has been used for the analysis of dust formation in ultra-cool atmospheres (Witte et al., 2011).

We used the current version 16 of *PHOENIX*, which has a new equation of state as well as an up-to-date atomic and molecular line list. This allowed us to produce spectra that match observations of cool stars significantly better than other synthetic libraries. The use of spherical geometry guarantees a consistent model grid from the main sequence up to giants. We adjusted the wavelength range and resolution to meet the requirements for science cases using other existing and upcoming instruments.

Parts of this Chapter have been submitted to the refereed journal *Astronomy & Astrophysics* (Husser et al., submitted).

## 3.1 The library

### 3.1.1 Dimensions and resolution

Since the library is still work in progress, only its present state is presented, which already covers most stellar populations that are not part of starburst regions (see Table 3.1). The grid is complete in its first three dimensions ( $T_{\text{eff}}$ ,  $\log(g)$  and  $[Fe/H]$ ). So far, a variation in the alpha element abundance has only been calculated as needed for the analysis of globular clusters, i. e. spectra with  $[\alpha/Fe] \neq 0$  in the range of  $-0.3 \leq [\alpha/Fe] \leq +0.8$  are available for  $T_{\text{eff}} \geq 3500\text{ K}$  and  $-2 \leq [Fe/H] \leq 0$  only.

The standard spectroscopic abundance notation is used in this thesis, which defines the ratio of two elements  $A$  and  $B$  in a star relative to their ratio in the sun:

$$[A/B] \equiv \log[n(A)/n(B)] - \log[n(A)/n(B)]_{\odot}, \quad (3.1)$$

with the number density  $n$ . We assume that  $[X/H] = [Fe/H]$  for most elements and thus,  $[Fe/H]$  denotes the overall metallicity. The abundances of the  $\alpha$  elements (O, Ne,



	Range		Step size
$T_{\text{eff}}$ [K]	2 300	- 7 000	100
	7 000	- 8 000	200
$\log(g)$	0.0	- +6.0	0.5
$[Fe/H]$	-4.0	- -2.0	1.0
	-2.0	- +1.0	0.5
$[\alpha/Fe]$	-0.3	- +0.8	0.1

**Table 3.1:** Parameter space of the grid. Alpha element abundances  $[\alpha/Fe] \neq 0$  are only available for  $T_{\text{eff}} \geq 3500\text{K}$  and  $-2 \leq [Fe/H] \leq 0$ .

Range [ $\text{\AA}$ ]		Sampling	
500	- 3 000	$\Delta\lambda$	$= 0.1\text{\AA}$
3 000	- 25 000	$R$	$\approx 500\,000$
25 000	- 55 000	$R$	$\approx 100\,000$

**Table 3.2:** Sampling of the spectra in the PHOENIX grid.

Mg, Si, S, Ar, Ca and Ti) are defined as

$$[\alpha/H] = [Fe/H] + [\alpha/Fe]. \quad (3.2)$$

A few spectra are missing in the grid, where *PHOENIX* was unable to compute the structure of the atmosphere due to various reasons. In case those 'holes' are surrounded by successfully calculated models, we provide interpolated spectra (see Section 3.3.2).

Although the new library was originally designed to be used for the analysis of *MUSE* spectra, we decided to increase both the wavelength range and the spectral resolution significantly in order to create some legacy value to be used by other projects. Both the wavelength limit in the IR and the spectral resolution were chosen to match CRIRES (Kaeufl et al., 2004) spectra. For the blue end of the spectra, we even go well below the range of X-Shooter (Vernet et al., 2011), which starts at 3 000  $\text{\AA}$ .

The grid now covers the whole wavelength range from 500  $\text{\AA}$  up to 5.5  $\mu\text{m}$  with a sampling as given in Table 3.2. Please note this really are sampling rates, i. e. the direct output of *PHOENIX*. The spectra have never been resampled or convolved with any kernel.

### 3.1.2 Calculation of model atmospheres and synthetic spectra

Synthesizing a spectrum with *PHOENIX* is a three-step process. First, the model atmosphere is being calculated, which we never started from scratch. Instead, we had a set of 766 atmospheres from a previous unpublished *PHOENIX* grid (P. Hauschildt, priv. comm.) available. From those, the grid was extended step by step, always using an existing neighbouring model as starting point. *PHOENIX* iterates a model atmosphere, until its criteria for convergence are reached. In order to limit the run time, we stopped after each 80 iterations and restarted *PHOENIX* if necessary. Parameter adjustments for many of the models had to be done individually in order to obtain fully converged model atmospheres.

The next step was to change *PHOENIX* to a mode that activates the use of special line profiles, which we used, e. g., for the Ca lines. In this mode, no convergence is

checked, so we carried out five more iterations by default in order to stratify the atmosphere again properly. Finally, from these intermediate models the spectra can be synthesized, which are always sampled on the same wavelength grid that has been specified according to Table 3.2. The whole process will be discussed in detail in Section 3.2.

Having access to the model atmospheres as well as the spectra allows us to quickly expand the grid in any given direction. For a subset of models we even set *PHOENIX* to output the full angular dependent radiation field, which can be used for calculating limb darkening coefficients (see Section 3.4).

Even in its current state (beginning of May 2012) with only  $\sim 45\,000$  synthetic spectra and corresponding model atmospheres, it took about  $2.6 \cdot 10^9$  CPU seconds or  $\sim 84$  CPU years for the new *PHOENIX* library to be calculated. It was computed on the *Ne-halem Cluster* of the GWDG<sup>1</sup> in about one year, parallelized on 20-50 nodes with 8 CPUs each.

### 3.1.3 Input parameters for *PHOENIX*

*PHOENIX* requires a set of input parameters, of which some will be discussed in detail below. Other important settings determining the numerical procedure are:

- Spherical symmetric mode with 64 layers is used for all models.
- The reference wavelength (in Å) defining the mean optical depth grid, which should be set to a wavelength with sufficient flux, is fixed to  $\lambda_\tau = 12000\text{Å}$  for  $T_{\text{eff}} < 5000\text{K}$  and  $\lambda_\tau = 5000\text{Å}$  for hotter stars.
- The outer pressure on the model atmosphere is set to  $10^{-6}\text{dyn cm}^{-2}$ .
- Condensation is included in the equation of state but ignored in the opacity ('Cond' setup, see Allard et al. (2001)).
- We do not handle dust settling at all in our model atmospheres, which might be unrealistic for the coolest stars in the grid.
- All model atmospheres have been calculated under the assumption of local thermodynamic equilibrium (LTE).
- All models with  $T_{\text{eff}} \leq 5000\text{K}$  include the full sample of molecules.
- All models with  $T_{\text{eff}} \geq 5000\text{K}$  are calculated with special line profiles for some species.

The last two items caused some major problems, which we are currently in the process of solving (see Section 5.10).

<sup>1</sup>Gesellschaft für wissenschaftliche Datenverarbeitung mbH Göttingen, <http://www.gwdg.de/index.php?id=2156>.

$\log(g)$	> 4	> 3	> 2	> 1.6	> 0.9	> 0	$\leq 0$
c	1	1.2	1.4	2	3	4	5

**Table 3.3:** Coefficients for calculating the mass in Eq. 3.6.

### 3.1.3.1 Mass

While plane-parallel geometry is a valid assumption for model atmospheres of main-sequence star, this is no longer true for giants. For those, *PHOENIX* offers a mode for spherical symmetry, which we used for all models in order to guarantee a homogeneous grid. Using that mode, a model is described by its effective temperature  $T_{\text{eff}}$ , surface gravity  $\log(g)$  and mass  $M_{\star}$ , from which both the radius and the luminosity can be derived. In order to get numerical stable and realistic atmospheres, we are using a varying mass throughout the grid and do not fix it to specific values (like in e. g. Hauschildt et al. (1999b) and Gustafsson et al. (2008)).

For main sequence stars we use the mass-luminosity relation, which can be approximated for solar type stars (Voigt, 1991) as:

$$L_{\star}/L_{\odot} = (M_{\star}/M_{\odot})^3. \quad (3.3)$$

Furthermore, we can calculate the luminosity from the effective temperature and radius. For the sun, the radius can be substituted by the surface gravity and mass, which yields:

$$L_{\star}/L_{\odot} = (T_{\text{eff},\star}/T_{\text{eff},\odot})^4 (R_{\star}/R_{\odot})^2 = (T_{\text{eff},\star}/T_{\text{eff},\odot})^4 M_{\star}/M_{\odot}. \quad (3.4)$$

By combining those two equations we get:

$$(T_{\text{eff},\star}/T_{\text{eff},\odot})^4 = (M_{\star}/M_{\odot})^2. \quad (3.5)$$

For lower surface gravities we let the values tend towards those of giants and super giants. Therefore, in the grid the mass is given by:

$$M_{\star} = c \cdot M_{\odot} \cdot (T_{\text{eff}}/5770 \text{ K})^2, \quad (3.6)$$

with values for the coefficient  $c$  given in Table 3.3. Fig. 3.1 shows the distribution of masses over the grid. For solar-like stars, we match  $M_{\star} = 1M_{\odot}$  almost exactly and the masses increase for hotter and larger stars as expected.

### 3.1.3.2 Convection

In *PHOENIX*, convection in the stellar atmosphere is described by the mixing length theory of turbulent transport, which goes back to Prandtl (1925) and, in the stellar context, to Vitense (1953) and Böhm-Vitense (1958). It is characterized by the *mixing length parameter*  $\alpha$ , which describes the ratio between the characteristic length that a volume of gas can rise in a stellar atmosphere before mixing with its surrounding and the pressure scale height ( $\alpha = l/H_p$ ), i. e. it is a value for the efficiency of the convective

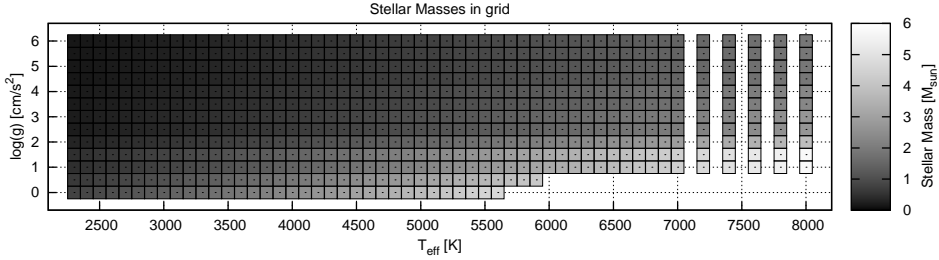


**Figure 3.1:** Distribution of stellar masses for different effective temperatures  $T_{\text{eff}}$  and surface gravities  $\log(g)$ , colour-coded in units of solar mass from  $0 M_{\odot}$  (black) to  $6 M_{\odot}$  (white).

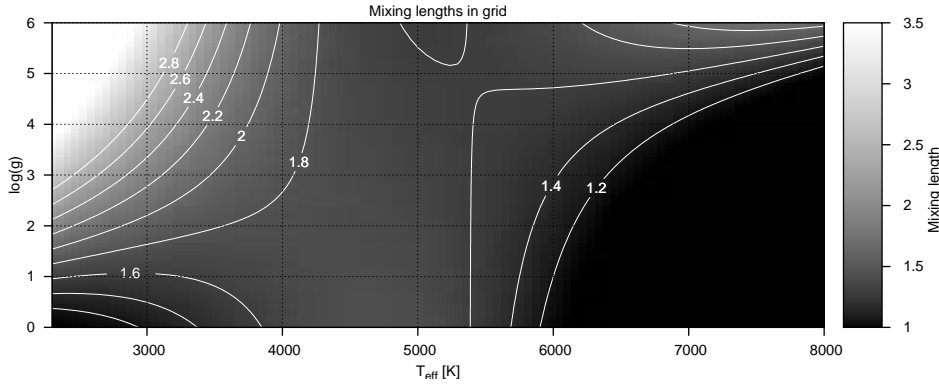


**Figure 3.2:** Distribution of the mixing length parameter  $\alpha$  in the PHOENIX grid.

energy transport – a large  $\alpha$  indicates an efficient energy transport, while it is inefficient for a small  $\alpha$ . In the latter case, the gas volume is allowed to rise to greater heights under the buoyant force, thus reaching higher velocities and carrying more heat before it is assumed to be dissipated.

For our spectra, we describe the mixing length parameter  $\alpha$  as discussed in Ludwig et al. (1999), where it has been calibrated using 3D RHD models. Since the authors emphasize that it might be incorrect to extrapolate the mixing length outside the ranges given in the paper ( $4300 \text{ K} \leq T_{\text{eff}} \leq 7100 \text{ K}$  and  $2.54 \leq \log(g) \leq 4.74$ ), we restrict the result to an interval  $\alpha \in [1, 3.5]$ . The distribution of mixing lengths in the grid is shown in Fig. 3.2. The majority of the models have an  $\alpha$  roughly between 1.5 and 2.5, while we had to cut off at  $\alpha = 3.5$  for models with  $T_{\text{eff}} \lesssim 3000 \text{ K}$ ,  $\log(g) \gtrsim 3$  and at  $\alpha = 1$  for those with  $T_{\text{eff}} \gtrsim 6000 \text{ K}$ ,  $\log(g) \lesssim 5$ .

### 3.1.3.3 Micro-turbulence

For our spectral library, we use the term *micro-turbulence* in a sense that large scale (macro) turbulent motion triggers small scale (micro) turbulent motion below the

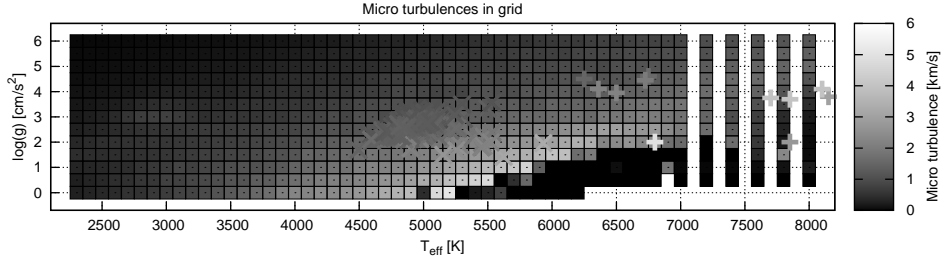


**Figure 3.3:** Distribution of micro-turbulences for that part of the PHOENIX grid with solar element abundances for different effective temperatures  $T_{\text{eff}}$  and surface gravities  $\log(g)$ . Colour-coded is the micro-turbulence from 0 km/s (black) to 6 km/s (white). We had to disable the convection for the giants with  $T_{\text{eff}} \gtrsim 5500$  K and therefore no micro-turbulence was applied to these spectra. In and around this area, we observe numerical instabilities causing single models to show differing results. Over-plotted are observational data points taken from Landstreet et al. (2009) (+) and Takeda et al. (2008) (x).

length scale of the mean free path of the photons. Macro-turbulent motion changes the shape of spectral lines but not their equivalent widths, therefore it can be applied on the final spectrum by means of a convolution. The micro-turbulence on the other hand affects the strengths of the lines (Gray, 2005), since it directly influences the line opacities, so it has to be included in the line forming process and can not be applied afterwards. In this model, both motions are strongly correlated and we use

$$v_{\text{micro}} = 0.5 \cdot \langle v_{\text{conv}} \rangle \quad (3.7)$$

to determine the amount of the micro-turbulence. This empirical approximation follows from 3D RHD investigations of cool M-stars (Wende et al., 2009), but also gives reasonable values for hotter stars (see Fig. 3.3). The mean value of the macro-turbulence,  $\langle v_{\text{conv}} \rangle$ , is taken from the PHOENIX atmospheres prior to spectral synthesis: the convective velocities from optical depths  $\log \tau = 1$  and lower are averaged in a way that only layers with non-zero values are included and then divided by a factor of two, i. e. micro-turbulence is assumed to be half of the mean convective velocity in the photosphere.

Since micro-turbulence mainly affects the strength and shape of the lines and not the structure of the atmosphere, it is only included in the computation of the high resolution synthetic spectra and not in the underlying model atmospheres. We did not attempt to further converge the atmospheres with the micro-turbulences derived from the previous iterations, which would have cost additional computational resources without noticeably changing the structure. Despite of the lack of a self-consistent description derived from first principles, this empirical description removes micro-turbulence as a free parameter.

Fig. 3.3 shows the distribution of micro-turbulences for spectra with solar element abundances. For cool stars our micro-turbulences are a lot smaller than the 2 km/s frequently assumed in model atmospheres and agree well with results from Wende et al. (2009). Over-plotted are observational data points taken from Landstreet et al. (2009)

and Takeda et al. (2008). The agreement with our values for stars on the upper main-sequence and the red giant branch is gratifying.

For effective temperatures above 6 500 K however, convective turbulence predicted by our models decreases steadily and cannot reproduce the significant broadening velocities observed by Landstreet et al. (2009) in F and A stars, but we note that their study does not display a unique relation of photospheric line broadening and atmospheric parameters, and includes a number of peculiar stars – e. g. all main sequence stars with  $\nu_{\text{micro}} \geq 3 \text{ km/s}$  in their sample are Am stars (yellow/very light plus symbols in Fig. 3.3). They also conclude that the line shapes of those stars cannot be understood in a simple micro-turbulence concept. These findings are essentially confirmed by RHD simulations (Freytag et al., 2012, and references therein), which however sample the hottest stars with convectively unstable atmospheres only very sparsely.

For giant stars of  $T_{\text{eff}} \sim 6500 \text{ K}$  we encountered strong numerical instabilities in the *PHOENIX* convection module due to the diminishing extension of the convectively unstable layer and had to disable it completely. For consistency with the rest of our grid we have chosen to publish these spectra with zero  $\nu_{\text{micro}}$ ; the user be advised that they cannot replace more detailed modelling using the micro-turbulence as a free parameter for those stars.

#### 3.1.3.4 Equation of state

The ACES (Astrophysical Chemical Equilibrium Solver, see Barman, in prep.) equation of state (EOS) that is used starting with *PHOENIX* version 16 is a state-of-the-art treatment of the chemical equilibrium in a stellar atmosphere. It uses the method of Smith & Missen (1982) with new experimental and theoretical thermodynamical data for 839 species (84 elements, 289 ions, 249 molecules, 217 condensates).

In each layer, the chemical equilibrium for all used atomic and molecular species is computed in dependence of the pressure, temperature and density. After computing the atmospheric structure with the equations of radiation and hydrodynamics, a new chemical equilibrium is calculated in a second step. This iterative process continues until convergence.

#### 3.1.3.5 Element abundances

The element abundances are scaled solar abundances taken from Asplund et al. (2009), where they are given for both the solar photosphere and meteorites. With the exception of Li, which is destroyed in the solar interior, and volatile elements that are depleted in meteorites, both sets of abundances therein agree within the errors; apart from the cases mentioned above, the measurements with respective smaller uncertainties (see Table 3.4) have been selected to best reproduce the proto-solar elemental composition (Lodders, 2003).

Elem.	Abund.		Elem.	Abund.		Elem.	Abund.				
1	H	12.00	31	Ga	3.04	63	Eu	0.52			
2	He	10.93	32	Ge	3.65	64	Gd	1.07			
3	Li	3.26	m	33	As	2.30	m	65	Tb	0.30	
4	Be	1.38	m	34	Se	3.34	m	66	Dy	1.10	
5	B	2.79	m	35	Br	2.54	m	67	Ho	0.48	
6	C	8.43		36	Kr	3.25		68	Er	0.92	
7	N	7.83		37	Rb	2.36	m	69	Tm	0.10	
8	O	8.69		38	Sr	2.87		70	Yb	0.92	m
9	F	4.56		39	Y	2.21		71	Lu	0.10	
10	Ne	7.93		40	Zr	2.58		72	Hf	0.85	
11	Na	6.24		41	Nb	1.46		73	Ta	-0.12	m
12	Mg	7.60		42	Mo	1.88		74	W	0.65	m
13	Al	6.45		44	Ru	1.75		75	Re	0.26	m
14	Si	7.51		45	Rh	1.06	m	76	Os	1.40	
15	P	5.41		46	Pd	1.65	m	77	Ir	1.38	
16	S	7.12		47	Ag	1.20	m	78	Pt	1.62	m
17	Cl	5.50		48	Cd	1.71	m	79	Au	0.80	m
18	Ar	6.40		49	In	0.76	m	80	Hg	1.17	m
19	K	5.08	m	50	Sn	2.04		81	Tl	0.77	m
20	Ca	6.34		51	Sb	1.01	m	82	Pb	2.04	m
21	Sc	3.15		52	Te	2.18	m	83	Bi	0.65	m
22	Ti	4.95		53	I	1.55	m	90	Th	0.06	m
23	V	3.93		54	Xe	2.24		92	U	-0.54	m
24	Cr	5.64		55	Cs	1.08	m				
25	Mn	5.43		56	Ba	2.18					
26	Fe	7.50		57	La	1.10					
27	Co	4.99		58	Ce	1.58					
28	Ni	6.22		59	Pr	0.72					
29	Cu	4.19		60	Nd	1.42					
30	Zn	4.56		62	Sm	0.96					

**Table 3.4:** Element abundances used in the PHOENIX grid, taken from Asplund et al. (2009). All the abundances in the table marked with an m are from meteorites, while the others are photospheric.

### 3.1.4 Comparison with previous *PHOENIX* models

Compared to previous *PHOENIX* models, a lot of changes were made like a new EOS, a new list of element abundances and new parametrizations for the mixing length and the micro turbulence. Consequentially, we observed some significant differences between spectra from previous *PHOENIX* grids and from this one.

As an example, Fig. 3.4 shows a comparison between model spectra from our new *PHOENIX* grid and from a previous one using *AMES-cond-v2.6* in the region around the TiO  $\epsilon$ -band for a typical M6 main-sequence star with  $T_{\text{eff}} = 2900\text{K}$  and  $\log g = 5.0$ . The TiO bands are known as robust temperature indicators, because they only weakly depend on gravity but are very sensitive to temperature (Mohanty et al., 2004; Reiners, 2005). In the new grid, we now see TiO  $\epsilon$ -bands that are significantly deeper than those

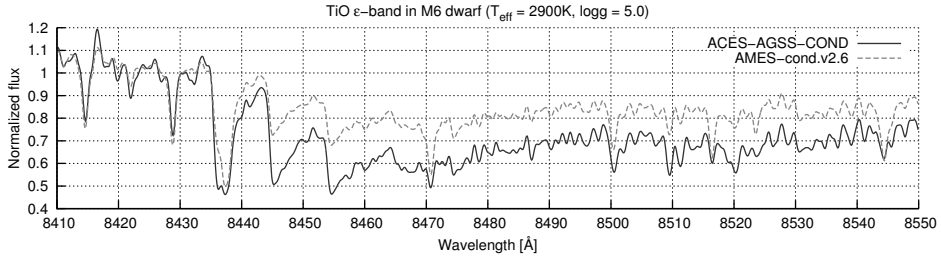


**Figure 3.4:** New PHOENIX spectrum (solid line) compared to one created using AMES-cond-v2.6 (dashed line). Both models are calculated for a typical M6 main sequence star ( $T_{\text{eff}} = 2900 \text{ K}$ ,  $\log g = 5.0$ ) and convolved to a spectral resolution of  $R = 10000$ . The new spectrum produces significantly deeper TiO bands than earlier PHOENIX models.

in older *PHOENIX* versions for identical atmospheric parameters. In this example, according to Ansgar Reiners (priv. comm.), the difference in temperature derived from the two models would be about 200 K.

### 3.1.5 Vacuum wavelengths

All the high-resolution spectra are provided in vacuum wavelengths  $\lambda_{\text{vac}}$ . If air wavelengths  $\lambda_{\text{air}}$  are required, e. g. IDL's vactoair method is available, which carries out the conversion using the following equation taken from Ciddor (1996), where it is applied for  $\lambda > 2000 \text{ \AA}$  only:

$$\lambda_{\text{air}} = \frac{\lambda_{\text{vac}}}{f}, \quad (3.8)$$

with

$$f = 1.0 + \frac{0.05792105}{238.0185 - \sigma_2} + \frac{0.00167917}{57.362 - \sigma_2}, \quad \sigma_2 = \left( \frac{10^4}{\lambda_{\text{vac}}} \right)^2. \quad (3.9)$$

## 3.2 The *PHOENIX* pipeline

The new library of model atmospheres and synthetic spectra has been calculated using the stellar atmosphere code *PHOENIX*. Each model requires an input file containing a list of comma-separated control parameters. While it is possible to create such file for each new model manually, this becomes quite cumbersome for tens of thousands of model atmospheres and spectra. Thus, we developed a set of tools, which help us organizing this bulk of data and running *PHOENIX* with the correct parameters for each model. Together they form the *PHOENIX* pipeline called *pyphoenix*. For some of its command line tools, the syntax and a short description will be given in Appendix B.

The basis for the pipeline is a template for the configuration file of *PHOENIX* (the so-called *namelist*), which contains variables of the form  $\{\$VAR\}$  that can be set au-



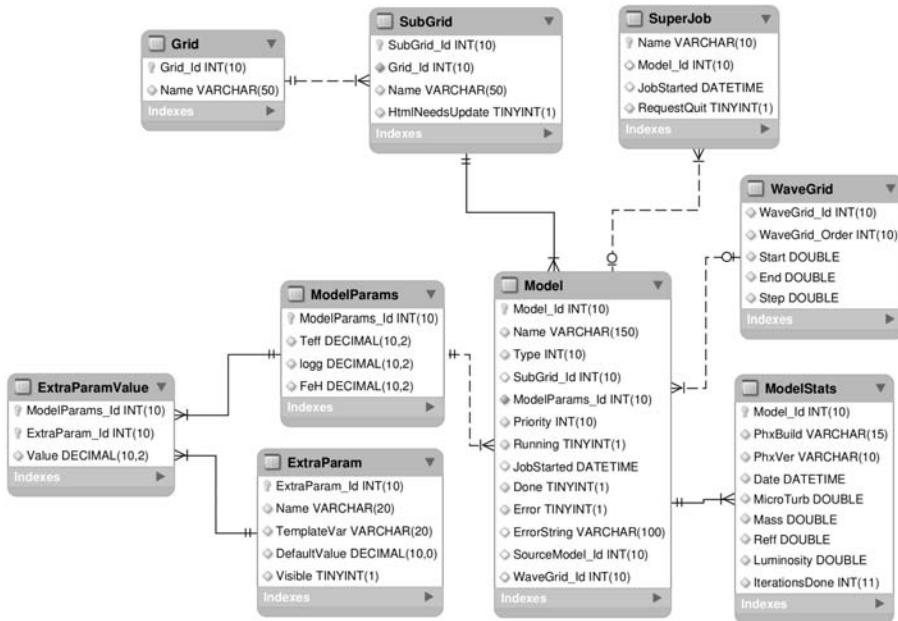


**Figure 3.5:** The MySQL database schema used for storing information about the models for the PHOENIX pipeline.

tomatically before starting *PHOENIX*. For example, the definitions for the model and iteration parameters look like this:

```
c='model parameter:',
  teff = ${TEFF}, logg = ${LOGG},
  zscale = ${MODEL_Z}, yscale = ${MODEL_Y}, alpha_scale = ${MODEL_ALPHA},
  m_sun=${M_SUN}, tau_conv_min=${TAUCONVMIN}, mixlng=${MIXLNG},

c='iteration parameter:',
  job = ${JOB}, iter = ${ITER}, ngrrad = ${NGRRAD},
```

As storage back end for the data a MySQL database is used, from which the data for each model can be obtained easily.

### 3.2.1 The MySQL database

The schema for the database that we are using for the pipeline is shown in Fig. 3.5. The central element is the *Model* table, which stores basic information about all the models. Each one has a unique identification number (*Model\_Id*) and a *Name*, which is primarily used for creating filenames for *PHOENIX* by adding an extension, e. g. the

atmospheres are stored in files called  $\langle Name \rangle.20$  and the spectra in  $\langle Name \rangle.7.gz$ . For a discussion of the naming scheme, see Section 3.2.5.

Each model has a *Type*, which describes the kind of calculation to be done by *PHOENIX*. At the moment, five different types are supported:

- 0 - LTE models, which are the basis for all spectra with  $T_{\text{eff}} \leq 5000$  K and for all NLTE models. The prefix for the names of those models is *lte*.
- 1 - NLTE models, used for *real* NLTE models with  $T_{\text{eff}} \geq 8000$  K and for calculating special NLTE line profiles for models with  $5000 \text{ K} < T_{\text{eff}} < 8000 \text{ K}$ . For the former, the prefix for the model names is *nlte*, while for the latter it is *ilte* (*improved LTE*) in order to avoid using the same name as the corresponding LTE model.
- 2 - The final spectrum with a prefix *lte* or *nlte* (depending on the mode of calculation) and the suffix *-HiRes*.
- 3 - Limb darkening, for which the output contains the full angular dependent radiation field that can be used to calculate limb darkening curves. The names of the models have the suffix *-LimbDarkening*.
- 4 - Line ID, for getting identifications for every wavelength bin with the suffix *-LineID*.

Using this scheme, in order to synthesize the spectrum of a solar-like star, we first need a LTE model (type 0), which serves as input for a spectrum (type 2). For hotter stars with  $T_{\text{eff}} > 5000$  K we need another intermediate model of type 1. We can easily define dependencies between the models, e. g. a spectrum cannot be calculated before its model atmosphere has successfully converged. Dependencies are indicated by the *SourceModel\_Id* field, which links to the *Model\_Id* of another model. In this field, a model can also link to itself in order to continue the calculation of an atmosphere that has not yet converged. Thus, each part (atmosphere, spectrum, ...) is treated separately and we can adjust its parameters individually, but calculating them in the correct order is taken care of automatically by following dependencies.

The physical input parameters are stored in another table called *ModelParams*, which links to the *Model* table via *ModelParams\_Id* and stores the effective temperature  $T_{\text{eff}}$ , the surface gravity  $\log(g)$  and the metallicity  $[Fe/H]$  for each model. This separate table design was chosen so that multiple models (e. g. an atmosphere and its spectrum) can share the same input parameters. Additional parameters can be put in the *ExtraParamValue* table, which links to an entry in both *ModelParams* and *ExtraParam*. The latter describes, how an extra parameter should be used, e. g. we use an additional parameter with the *Name* 'Alpha', which is represented by the variable `$MODEL_ALPHA` in the template for the *PHOENIX* input file. It has a *DefaultValue* of 0.0 and its value is included in the name of the model (*Visible*=1). For a model to use an additional parameter, there must be an entry in the *ExtraParamValue* table with the value and links to both a *Model* and an *ExtraParam*.

For all the different types, a wavelength grid needs to be defined, which can be done by setting a *WaveGrid\_Id*, which links to the *WaveGrid* table. For each ID it stores a list of *Start*, *End* and *Step* values to describe the wavelength grid.

Each model belongs to a *Grid*, which is subdivided into multiple *SubGrids*. A subgrid in this context is a batch of models with the same metallicity and equal extra parameters: the subgrid *Z-0.0* contains all spectra with solar metallicity, while the subgrid *Z-1.0.Alpha=+0.3* includes all models with  $[Fe/H] = -1.0$  and  $[\alpha/Fe] = +0.3$ . Except for the metallicity, parameters with their default values never show up in the name, e. g. there is no model having *Alpha=0.0* as part of its name. Be aware that actually not *Z* is given but  $[Fe/H]=\log(Z/Z_{\odot})$ .

A *Priority* can be assigned to a model in order to prioritize it against other models. If a model is currently being calculated (*Running=1*), the start time of the calculation is stored in *JobStarted*. After a run of PHOENIX, a model can either be finished (*Done=1*) or have failed with an error (*Error=1* with a description of the error in *ErrorString*).

After each call to PHOENIX, the *ModelStats* entry for the model is updated. It stores information about the used PHOENIX version (*PhxVer*) and the time of its compilation (*PhxBuild*), as well as date and time of when the calculation finished (*Date*). Furthermore, the used micro turbulence (*MicroTurb*), the *Mass*, the effective radius (*Reff*) and the total *Luminosity* are stored. For NLTE atmospheres, which may need more iterations than can be done in one PHOENIX run, the number of iterations that have already been calculated (*IterationsDone*) is also saved in the database. Finally, the *SuperJob* table is responsible for keeping track of jobs running in the batch system of the computing cluster as described in the next section.

### 3.2.2 The job manager

Although there is a batch system called Load Sharing Facility (LSF)<sup>2</sup> running on the *Nehalem Cluster* of the GWDG, an additional system is used to start PHOENIX and check its results. The maximum execution time for a job in the cluster is 48 hours, while the waiting time in the queue can be several days. Since a run of PHOENIX can take from a couple of minutes to several hours, a more efficient system is required to start new jobs.

In order to exploit the available time as well as possible, the jobs placed in the LSF queue call PHOENIX multiple times consecutively – therefore we call these jobs *superjobs* (*pyphoenix\_superjob.py*). Their only function is to pull an unfinished model from the database, call another script with this model, wait until that has finished and start from the beginning, unless a given amount of time (usually 40 hours) has passed, which causes them to quit automatically. The called script (*pyphoenix\_job.py*) finally prepares all the input files for PHOENIX, runs it and stores the results. This way, we can calculate dozens of model atmospheres and spectra one after another without having to put them into the LSF queue individually and having to wait for the job to start

<sup>2</sup><http://www.gwdg.de/index.php?id=1334>

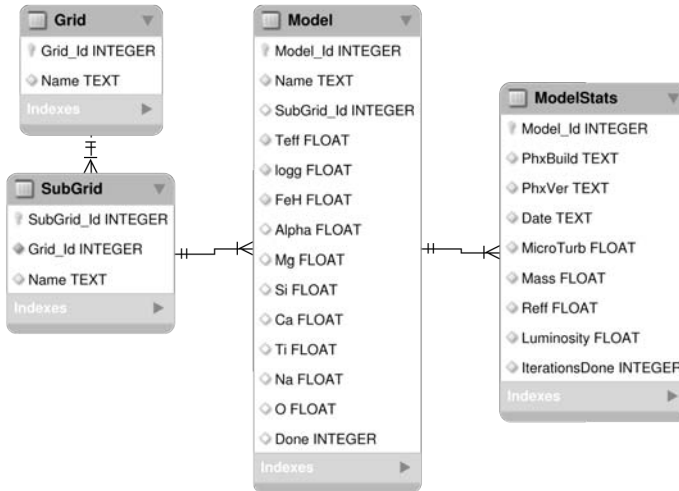


Figure 3.6: The *sqlite* database schema used for storing information about the models.

running again.

Usually, the number of *superjobs* in the queue is about 20-50. After one of them has finished, we need to add a new one to the queue, which is done by a *cron* job, which calls a script (*pyphoenix\_manager.py*) every five minutes. This script checks the number of jobs currently in the queue and starts new ones if necessary. For each *superjob*, we store a unique *Name* in the database as well as the *Model\_Id* of the model currently processed and the date and time of the beginning of its execution (*JobStarted*). Using an additional flag (*RequestQuit*), we can ask a *superjobs* to quit after it has finished computing the current model.

### 3.2.3 Exporting the database

Although a *MySQL* database is ideal for organizing the creation of the grid, due to its client/server architecture it is less suitable for distributing and using the spectra. For this, a file-based database system like *sqlite* is much more convenient, since it can just be copied to other computers together with the spectra. The script *pyphoenix\_export\_db\_to\_sqlite.py*, which takes the filename as single parameter, constructs a new *sqlite* database with tables as shown in Fig. 3.6 and fills it with all the models from the original *MySQL* database. Obviously, not all the data are copied but only what is required to work with the spectra. The script is usually invoked via *phxbackupdb.sh*, which also creates a backup of the whole *MySQL* database (using *mysqldump*).

### 3.2.4 Other command-line tools

A couple of command-line tools allow the creation and modification of models in the database. The most important ones are:

- **phxadd** adds a new model to a grid (see Section B.1).
- **phxch** applies given changes to an existing model (see Section B.3).
- **phxaddextra** adds a new extra parameter to the database (see Section B.2).
- **phxstatus** lists running jobs or detailed information about a single model (see Section B.4).
- **phxcheckauto** tries to resolve problems with the models by analyzing the error message and the log file and either acting automatically or making suggestions about what to do.

### 3.2.5 Files created by *PHOENIX* and the pipeline

The names for all models in the database are derived from the following naming scheme:

`<grid>/<subgrid>/<n>lte<Teff><log(g)><subgrid>.<grid>`

where `<grid>` is the name of the grid. As for the spectra discussed in this Chapter, this will always be `PHOENIX-ACES-AGSS-COND-2011`. The `<subgrid>` describes all the parameters in addition to  $T_{\text{eff}}$  and  $\log(g)$  as discussed in Section 3.2.1.

The name of the models always start with either `lte`, `ilte` or `nlte`, according to their type. The effective temperature `<Teff>` is given by five digits with leading zeros, if necessary. The surface gravity `<log(g)>` is denoted by its negative with two digits after the decimal point. In the filename itself the Z describing the metallicity is dropped, since the metallicity is explicitly given for all files. Two examples for the naming scheme would be:

- \* `PHOENIX-ACES-AGSS-COND-2011/Z-1.0.Alpha=+0.30/  
lte08000-2.00-1.0.Alpha=+0.30.PHOENIX-ACES-AGSS-COND-2011`
- \* `PHOENIX-ACES-AGSS-COND-2011/Z-0.0/  
lte06800-4.50-0.0.PHOENIX-ACES-AGSS-COND-2011`

*PHOENIX* writes a couple of files, of which we only keep the model atmosphere, the spectrum and an output file. In addition, the pipeline creates several log files and we also store the namelist of the *PHOENIX* run. Altogether this sums up to seven files for each model. The names of the files are derived from the name of the corresponding model, i. e. `<model>.<ext>`:

- `<model>.dqs`: The *namelist* with some surrounding *kshell* script that starts *PHOENIX*.
- `<model>.output` & `<model>.error`: *stdout* and *stderr* of the *PHOENIX* run.
- `<model>.log`: A log file created by the pipeline that contains a list of everything that has been done with the model.
- `<model>.out.gz`: The *PHOENIX* output file.
- `<model>.20`: The model atmosphere as calculated by *PHOENIX*.
- `<model>.7.gz`: The spectrum as synthesized by *PHOENIX*.

### 3.3 Processing the *PHOENIX* spectra

While the spectra created by *PHOENIX* are perfectly fine for some applications, for the analysis of *MUSE* spectra (see Chapter 4) some more work is required: FITS files are more convenient than the format of the files created by *PHOENIX* and spectra that for some reason could be computed need to be interpolated. Furthermore, they need to be convolved to the required spectral resolution and second derivatives need to be calculated, which are necessary for the interpolation method. Finally, the database files storing information about the spectra in a grid need to be optimized.

At the end of this section, listing 3.1 shows a full script that combines all the tools discussed below in order to prepare the spectra for the analysis of *MUSE* data. The syntax and a short description of the tools, which are part of our *spexxy* package for fitting spectra, used in this section will be presented in Appendix C.

#### 3.3.1 Converting to FITS files

The high-resolution spectra created by *PHOENIX* are written to files as ASCII tables with one line per wavelength point. In addition to the columns containing the wavelengths and the fluxes, there are others with supplementary data that usually is not required for working with the spectra. A typical *PHOENIX* output spectrum in our new library has a decompressed size of about 230 MB. Effectively, all the data except for the wavelengths and fluxes can be discarded and a conversion to a binary format also saves a lot of disc space and processing time.

For converting the *PHOENIX* spectra into the more convenient FITS format, we provide the tool *spexxyConvertPhxGrid* (see Section C.2). The files always contain one single primary extension, which holds the flux of the spectrum in units of  $[\text{erg/s/cm}^2/\text{cm}]$  on the stellar surface in form of a one-dimensional image. The files for the high-resolution spectra include a FITS keyword *WAVE* that stores a reference to the file containing the wavelength grid, which is saved in the same format as the spectra, but containing wavelength points instead of a flux array.

Keyword	Unit	Description
<b>Default keywords</b>		
CRPIX1	[px]	Reference pixel for wavelength grid
CRVAL1	[Å]	Wavelength at reference pixel
CDELTA1	[Å]	Increment for the wavelength grid
CTYPE1		Type of wavelength grid
NAXIS1		Number of data points in the spectrum.
<b>Basic atmospheric parameters</b>		
PHXTEFF	[K]	Effective temperature
PHXLOGG	[cm/s <sup>2</sup> ]	Surface gravity
PHXM_H	[dex]	Metallicity [ <i>Fe/H</i> ]
PHXALPHA	[dex]	Alpha element abundance
<b>Additional atmospheric parameters</b>		
PHXDUST	[T/F]	Dust in atmosphere, always <i>F</i> for this grid
PHXXI_L	[km/s]	Micro-turbulent velocity for LTE lines
PHXXI_M	[km/s]	Micro-turbulent velocity for molecular lines
PHXXI_N	[km/s]	Micro-turbulent velocity for NLTE lines
PHXMASS	[kg]	Stellar mass
PHXREFF	[cm]	Effective stellar radius
PHXLUM	[W]	Stellar luminosity
PHXMXLEN		Mixing length
<b><i>PHOENIX</i></b>		
PHXBUILD		Build date of Phoenix
PHXVER		Phoenix version
DATE	[local]	Finishing date of model calculation
PHXEOS		Equation of state
PHXCONV	[T/F]	Convection enabled in model
<b>Interpolation</b>		
INTERPOL	[T/F]	Spectrum was interpolated

**Table 3.5:** *Keywords in the FITS headers of the files containing the spectra.*

For the medium-resolution spectra that will be discussed later on, the wavelength grid is provided by a set of four FITS keywords. *CRVAL1* defines the wavelength at pixel *CRPIX1*, which is always 1 for our spectra. The step size is given by *CDELTA1* and the number of points by *NAXIS1*. The type of the wavelength grid is defined by the *CTYPE1* keyword — *WAVE* and *WAVE-LOG* for vacuum wavelengths on a linear and a logarithmic scale and *AWAV* and *AWAV-LOG* for air wavelengths respectively. With this information the whole wavelength grid can be calculated easily.

A list of all FITS keywords that are saved with the spectrum is given in Table 3.5. As mentioned before, there are models within the grid, for which we manually disabled the convection. For those we added another keyword *PHXCONV* with the value *F*. The files containing interpolated spectra (see next section) only include the date of their creation and the *basic atmospheric parameters*. Furthermore, for those spectra we added

the keyword *INTERPOL* with the value  $T$ .

For the high-resolution spectra, there is an additional FITS extension in the file containing a binary table that lists all the element abundances that have been used in the model.

### 3.3.2 Interpolating missing spectra

As discussed before, unfortunately there are single models that *PHOENIX* was not able to compute for various reasons. We fill these 'holes' in the grid by interpolating from the surrounding spectra, if possible. Before this can happen, we need to make sure that all the models in the database are actually present on disc and vice versa, which can be done using *spexyCheckGrid* (see Section C.1).

In order to interpolate missing spectra, we need to compile a list of models that actually failed to compute. This can be done using the *spexyExtractGrid* script, which will be discussed in detail in the next section. It extracts a subset of models from a given database file and one of its options is to take only those that have been flagged with an error. This new database file can then be used as input for *spexyFillGridHoles* (see Section C.5), which tries to interpolate missing spectra. For the interpolation, we use the same routines as will be discussed in Section 4.4.2, but for simplicity, the interpolation is only done along the  $T_{\text{eff}}$  axis.

An easy way for testing this method is to remove a single spectrum from the grid, interpolate it and compare the result with the original spectrum. In Fig. 3.7, this has been done for three different spectra, which are plotted each in a different wavelength range. The original spectrum is plotted on top in black, while the differences to it from its two neighbours (blue and green) and from the interpolated spectrum (red) are shown below. Obviously, there are discrepancies between the original spectra and the interpolated ones, but they are still small and are always within the bounds of their neighbours.

### 3.3.3 Extracting subgrids

The tools used for the analysis of observed spectra (see Chapter 4) retrieve the parameters and ranges of a grid from *sqlite* databases that contain a list of all available spectra (see Section 3.2.3). When fitting an observed spectrum against a grid with two dimensions (e. g.  $T_{\text{eff}}$  and  $\log(g)$ ), only those two will be determined. Since the original database file contains all spectra that have been calculated, we need a way to extract subsets of a given grid.

The script *spexyExtractGrid* extracts given dimensions from an existing grid (i. e. database file) and writes them into a new file (see Section C.4). Usually, a set of seven subgrids is extracted:

- **grid.db:** All the spectra that have successfully been calculated.



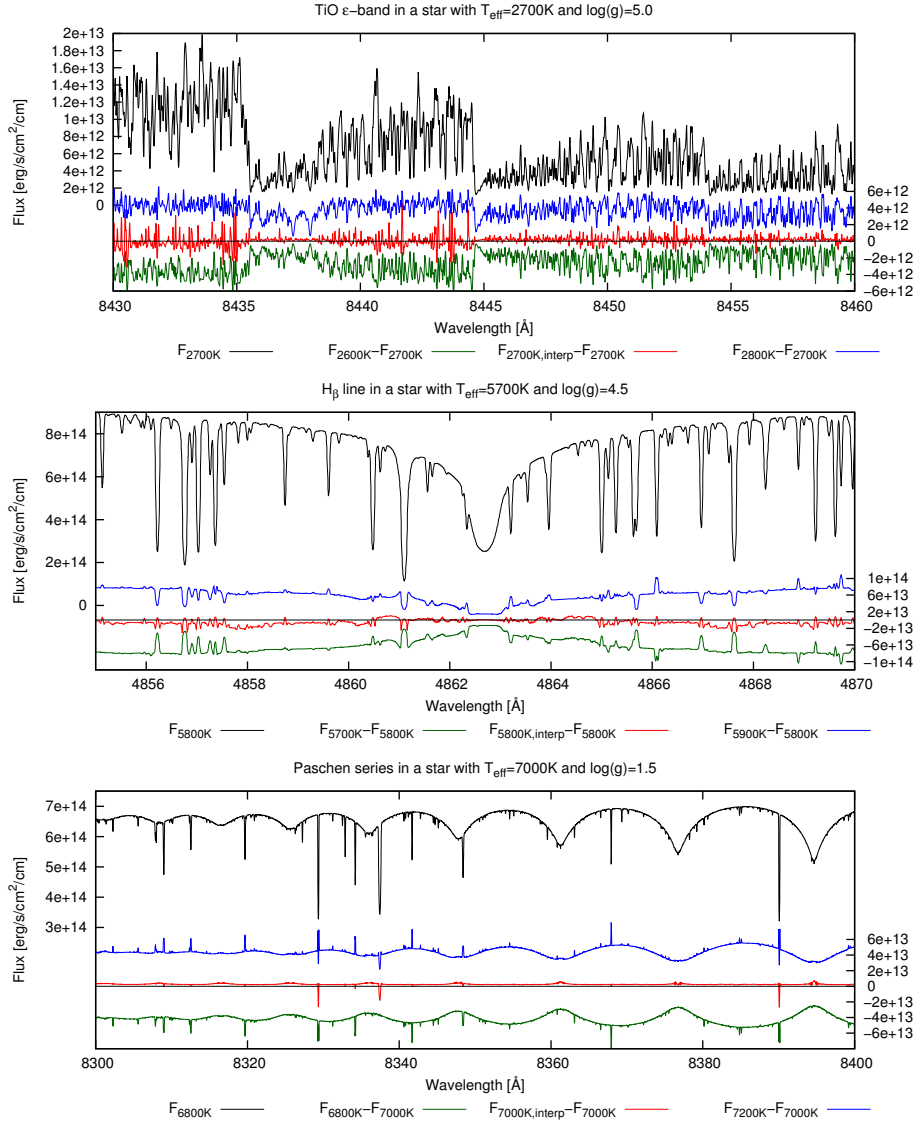


**Figure 3.7:** Quality of interpolation for three spectra: TiO  $\epsilon$ -band in an M dwarf with  $T_{\text{eff}} = 2700\text{K}$ ,  $\log(g) = 5.0$  (top), H $\beta$  in a solar-like star with  $T_{\text{eff}} = 5800\text{K}$ ,  $\log(g) = 4.5$  (middle) and parts of the Paschen series in a F giant with  $T_{\text{eff}} = 7000\text{K}$ ,  $\log(g) = 1.5$  (bottom). Plotted are the spectra themselves (black) and the differences to their two neighbours in  $T_{\text{eff}}$  (blue and green) and to the interpolated spectra with the same parameters (red).

- **failed.db**: All the spectra that could not be calculated for some reason, e. g. for which the model atmosphere did not converge. The need for this has been discussed above in Section 3.3.2.
- **gridParams.db**: The default grid covering all spectra in the four dimensions  $T_{\text{eff}}$ ,  $\log(g)$ ,  $[Fe/H]$  and  $[\alpha/Fe]$ , which will later be used for fitting observed spectra (see Chapter 4).
- **gridMg.db, gridSi.db, gridCa.db, gridTi.db**: All spectra with  $[Fe/H] = -1.5$  and  $[X/Fe] = \pm 0.3$  for the four alpha elements  $X \in [Mg, Si, Ca, Ti]$ . These grids will be used for determining the abundances of those elements (see Section 4.11).

The resulting files are simple *sqlite* databases again, which can be accessed from every tool that needs to acquire information about the spectra in the grid.

### 3.3.4 Convolution and resampling the spectra

Before comparing the spectra to observations, they need to be convolved to the same spectral resolution. The tool *spexyConvolveGrid* (see Section C.3) can do this in three different ways:

- Convolve with a Gaussian kernel in the wavelength domain.
- Convolve with a Gaussian kernel in the logarithmic domain.
- Convolve with a Gauss-Hermite kernel varying with wavelength in the logarithmic domain.

Although the first two seem to be straightforward, they are not for the spectra created by *PHOENIX* due to their non-constant sampling. Since we do not want to resample the high resolution spectra to a constant wavelength grid before further processing, common approaches like e. g. multiplication of spectrum and convolution kernel in Fourier space are not possible. Serendipitously, using an analytic function like a Gaussian (or Gauss-Hermite) allows us to evaluate the kernel for arbitrary values. Therefore, we can easily shift the kernel over the spectrum in order to calculate the convolution. Unfortunately, with  $n \approx 1.5 \cdot 10^6$  data points in the *PHOENIX* spectra, this is a time-consuming task with  $\mathcal{O}(n^2)$ . This time can be reduced significantly by combining the convolution with the resampling of the spectra. We can also limit the range of pixels that are affected by a kernel centered on a given point, e. g. to 5 FWHM, which speeds up the calculation to  $\mathcal{O}(m)$ , where  $m$  is the number of points in the resampled spectrum. Due to the varying sampling in the *PHOENIX* spectra, during the convolution the contribution of each data point needs to be scaled by the step size.

The convolution with a Gauss-Hermite varying with wavelength is also done by shifting the kernel over the spectrum, only now the FWHM of the Gaussian is changing for each new point. This allows us to simulate a varying spectral resolution over the

```

1 #!/ bin/bash
3 # create HiRes grid from PHOENIX files
spexxyConvertPhxGrid -i /path/to/phxmodels/ -o HiResFITS/
5
# copy database to HiRes
7 cp /path/to/phxmodels/Models/phoenixdb/phoenixdb.db HiResFITS/
9
# check grid
spexxyCheckGrid -d -g HiResFITS
11
# extract preliminary grids
13 cd HiResFITS
spexxyExtractGrid -d Teff logg FeH Alpha Mg -o grid.db
15 spexxyExtractGrid -d Teff logg FeH Alpha Mg -s 0 -o failed.db
cd ..
17
# interpolate holes
19 spexxyFillGridHoles -g HiResFITS
21
# check grid again
spexxyCheckGrid -g HiResFITS
23
# extract final grids
25 cd HiResFITS
spexxyExtractGrid -d Teff logg FeH Alpha Mg -o grid.db
27 spexxyExtractGrid -d Teff logg FeH Alpha Mg -s 0 -o failed.db
spexxyExtractGrid -d Teff logg FeH Alpha -v Mg=0 Si=0 Ca=0 Ti=0 -o gridParams.db
29 spexxyExtractGrid -d Teff logg Mg -v FeH=-1.5 Alpha=0 -o gridMg.db -p ../gridMasks
spexxyExtractGrid -d Teff logg Si -v FeH=-1.5 Alpha=0 -o gridSi.db -p ../gridMasks
31 spexxyExtractGrid -d Teff logg Ca -v FeH=-1.5 Alpha=0 -o gridCa.db -p ../gridMasks
spexxyExtractGrid -d Teff logg Ti -v FeH=-1.5 Alpha=0 -o gridTi.db -p ../gridMasks
33 cd ..
35
# convolve grids
spexxyConvolveGrid -o A1FITS -w 3000 10000 0.1 -f 1.0 -n
37 spexxyConvolveGrid -o MuseFITS -w 4550 9400 0.32 -f 2.4 -n -a -i A1FITS
39
# copy results
cp HiResFITS/*.db A1FITS/
41 cp HiResFITS/*.db MuseFITS/
43
# derivatives
spexxyGridDerivs -g MuseFITS/grid

```

**Listing 3.1:** *BASH script for creating lower resolution grids from the HiRes spectra.*

wavelength range. In Section 4.7, we will discuss a method for measuring the resolution – or, more accurately, the varying line spread function (LSF).

When convolving with a LSF, we can do that in a way that at every wavelength point, we have a constant offset (in km/s) to a fixed resolution (in Å), which can produce spectra that, convolved with a kernel in the logarithmic domain, have a resolution constant

in wavelength. For instance, the *MUSE* spectra will have a fixed spectral resolution of  $2.6\text{\AA}$ , but in Section 4.6 we will see, that we might want to convolve it again in the logarithmic domain, so we need model spectra with a slightly higher resolution.

At this point, the sampling of the spectra is usually chosen to be about a factor of ten higher than that of the observed spectra. This allows us to accurately shift the spectrum to a given radial velocity or even convolve it again later in the process.

### 3.3.5 Calculating 2nd derivatives

In Section 4.4.2, a spline interpolator will be discussed, which requires pre-calculated second-derivatives for the first dimension of the grid, i.e. the effective temperature  $T_{\text{eff}}$ . This can be done using the tool *spexxyGridDerivs* (see Section C.10), which uses methods that will be explained in detail in Section 4.4.2.

### 3.3.6 Final script

A simple yet complete script for creating all the necessary files for the analysis of *MUSE* spectra would now look like listing 3.1.

## 3.4 Limb Darkening

Especially in the exoplanet community, the need for an accurate description of the limb darkening of stars has increased significantly: for transiting planets the effect of an incorrect assumption in this aspect has similar effects as a wrong planet size and for gravitational micro-lensing observations it also changes the shape of the event. Missions like *Kepler* (Borucki et al., 2010) have increased the accuracy of measurements to a degree, where limb darkening definitely has to be considered.

For the analytic description of limb darkening, the most common laws are:

$$\frac{I(\mu)}{I(1)} = 1 - u(1 - \mu) \quad (\text{linear}), \quad (3.10)$$

$$\frac{I(\mu)}{I(1)} = 1 - a(1 - \mu) - b(1 - \mu)^2 \quad (\text{quadratic}), \quad (3.11)$$

$$\frac{I(\mu)}{I(1)} = 1 - c(1 - \mu) - d(1 - \sqrt{\mu}) \quad (\text{squareroot}), \quad (3.12)$$

$$\frac{I(\mu)}{I(1)} = 1 - e(1 - \mu) - f\mu \ln(\mu) \quad (\text{logarithmic}), \quad (3.13)$$

where  $I(1)$  is the intensity at the centre of the disc and  $a$ ,  $b$ ,  $c$ ,  $d$ ,  $e$  and  $f$  are the limb darkening coefficients. The distance to the centre is denoted by  $\mu$ , which is defined as  $\mu = \cos(\alpha)$ , where  $\alpha$  is the angle between the line of sight and the direction of the

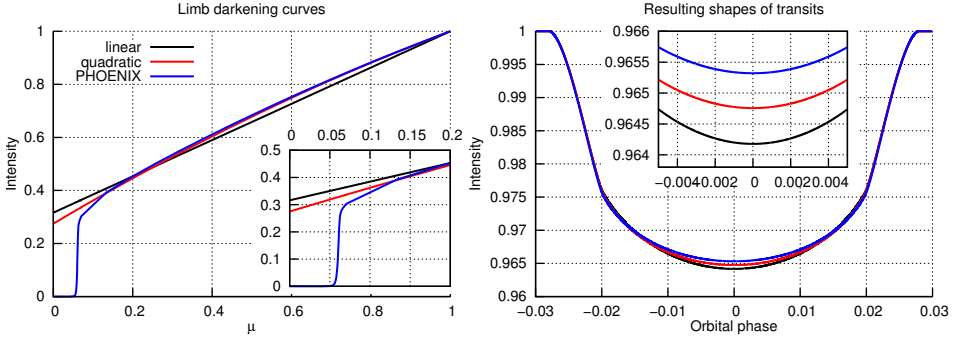


**Figure 3.8:** On the left, the limb darkening curve derived from a PHOENIX model with  $T_{\text{eff}}=5800\text{ K}$  and  $\log(g)=4.5$  is plotted in blue together with those from the linear (black) and quadratic (red) laws with coefficients from Claret (2000). On the right, those curves have been used by Holger M. Müller to simulate the shape of the light curve of a transiting planet in front of a host star with the given limb darkening.

emergent intensity, i. e.  $\mu = 1$  at the centre of the disc and  $\mu = 0$  at its edge. Another non-linear limb darkening law has been suggested by Claret (2000):

$$\frac{I(\mu)}{I(1)} = 1 - a_1(1 - \mu^{1/2}) - a_2(1 - \mu) - a_3(1 - \mu^{3/2}) - a_4(1 - \mu^2), \quad (3.14)$$

with the four coefficients  $a_1$  to  $a_4$ .

With *PHOENIX*, we have the possibility to output the full angular dependent radiation field, i. e. full spectra for different values of  $\mu$ . For the left plot in Fig. 3.8, each of those spectra for a star with  $T_{\text{eff}}=5800\text{ K}$  and  $\log(g)=4.5$  have been convolved with the response curve of a Johnson-V filter and integrated. The resulting curve has been scaled to fulfill  $I(1) = 1$  (blue line). Overplotted are the corresponding limb darkenings following the linear (black) and quadratic (red) laws with coefficients from Claret (2000). Most obviously, the curve derived from the *PHOENIX* model drops to zero before the edge of the disc, which is caused by the spherical symmetric mode that has been used for its calculation: the radius of the stars is chosen, so that it contains all flux in all wavelengths. Thus, for working with this data, we need to define a new edge.

One possible way suggested by Holger M. Müller (priv. comm.) is to pick the wavelength, in which the star is largest, find the  $\mu_e$  for which the intensity in this wavelength drops to  $1/e$  and rescale the curve so that  $\mu_e$  defines the new edge of the disc. He used this to simulate the shape of the light curve of a transiting planet in front of a host star with the given limb darkening as shown in the right plot of Fig. 3.8. The depths of the transits for the linear and the quadratic limb darkening laws already differ by  $\sim 0.5\%$ , and when using the limb darkening from the *PHOENIX* model it is more shallow by another  $\sim 0.5\%$ . This discrepancy is well measurable.

We have calculated the full angular dependent radiation fields for all models in our new library with solar element abundances. Our plan is to extend this data set and make it available for use in the astronomical community.

	Range		Step size
$T_{\text{eff}}$ [K]	3 500	– 9 750	250
$\log(g)$	0.0	– +5.0	0.5
$[Fe/H]$	-4.0	– 0.0	0.5
$[\alpha/Fe]$	-0.8	– +1.2	0.1

**Table 3.6:** Parameter space of the Synspec grid.

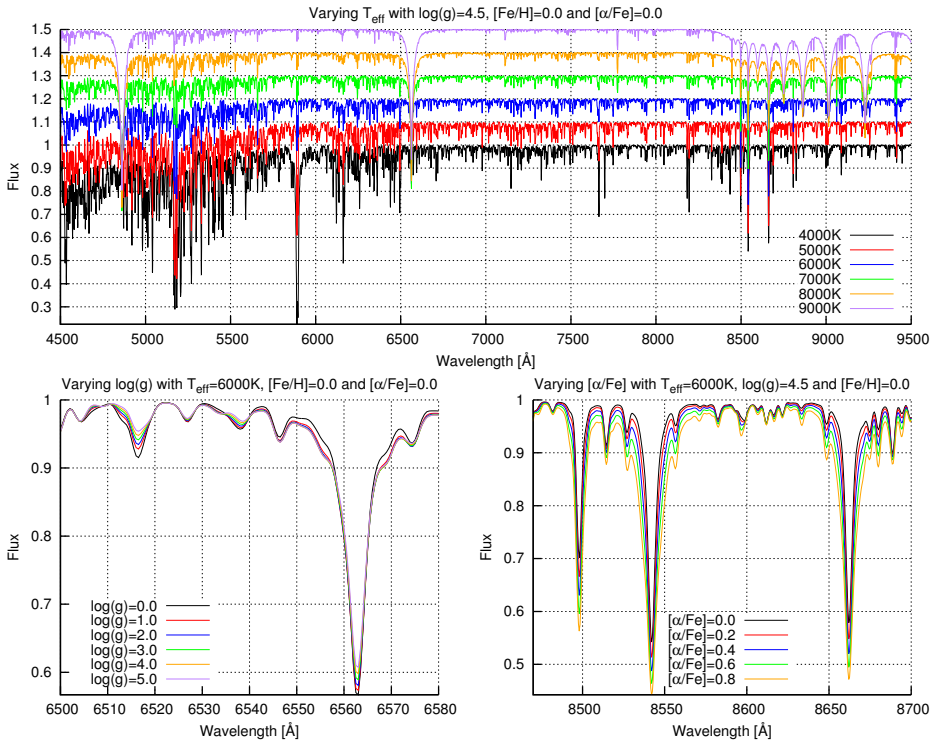


**Figure 3.9:** Some example Synspec spectra with  $\log(g)=4.5$ ,  $[Fe/H]=0$  and  $[\alpha/Fe]=0$  for various effective temperatures (top). The two plots at the bottom show variations in the spectra when changing the surface gravity (left,  $H_{\alpha}$  line) and alpha element abundance (right, CaII triplet).

### 3.5 Synspec

Before the new *PHOENIX* library was available, we used a set of spectra based on ATLAS9 model atmospheres (Castelli & Kurucz, 2004) that were synthesized using Synspec (Hubeny & Lanz, 2011). For the atomic line list, the one provided with Synspec, which is an extract of the Kurucz (CD-ROM 23) linelist GFALL, has been used. Furthermore, we used special profiles for the Hydrogen lines.

---

The parameter space for the grid is given in Table 3.6. The spectra were synthesized in the wavelength range from 3 500 Å to 9 500 Å with a step size of 0.01 Å. The stellar continuum was not included in the spectra. We are not using those spectra for development or testing anymore, but they will be used for illustration purposes in Chapter 4. Figure 3.9 shows some examples of these Synspec spectra.





## Chapter 4

# Analyzing *MUSE* data

In Chapter 2, we discussed the current state of research on globular clusters and where we want to contribute to it. Since *MUSE* is quite a unique instrument, we did not have any prior experience on how to analyze the data, so a main part of the work for this thesis consisted of evaluating existing methods and adapting them for our needs in order to achieve the best results possible. In this Chapter, a collection of methods will be discussed that proved useful.

### 4.1 Extraction of spectra from a *MUSE* cube

The reason why previous surveys of globular clusters obtained only a limited amount of spectra is that traditionally used techniques like multi-object spectroscopy are restricted to brighter and isolated stars in the field. Within the *MUSE* consortium (in person of Sebastian Kamann) a method has been developed to use integral field spectroscopy to overcome this limitation. For that, the additional spatial information in the data is used in order to extract spectra for the stars above the confusion limit using PSF fitting techniques, which we call “crowded field spectroscopy”. This deblending technique works so well that we obtain clean stellar spectra for a significantly higher number of stars than hitherto possible.

From the *MUSE* data reduction pipeline we will get a single exposure in form of a data cube with 300 by 300 spatial pixels and  $\sim 3\,600$  wavelength layers, i. e. in fact we get  $\sim 3\,600$  images of the same field, each at another wavelength. They are all exposed simultaneously, and therefore we do not have to bother about changing weather and seeing conditions between the images.

The details of the extraction are not the topic of this thesis (see Sebastian Kamann's PhD thesis for details), but a short introduction should be given. In the left two images of Fig. 4.1, a HST image of the *MUSE* field of view is shown and in one of them the positions of all stars catalogued by the *ACS Survey for Galactic Globular Clusters* (Anderson

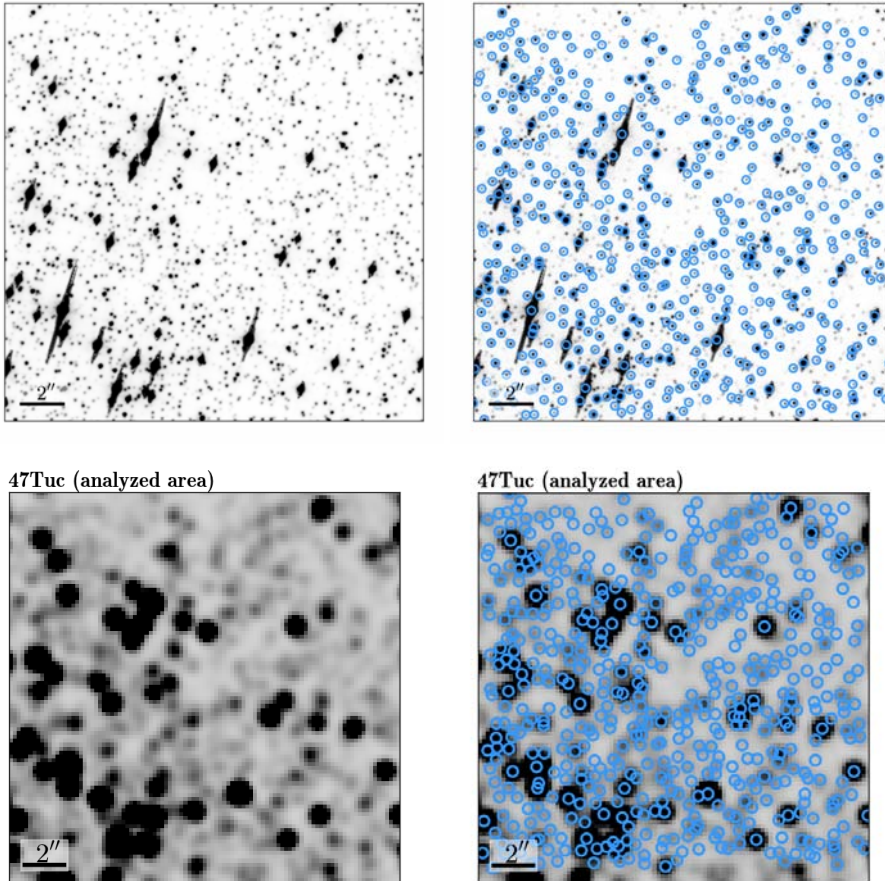
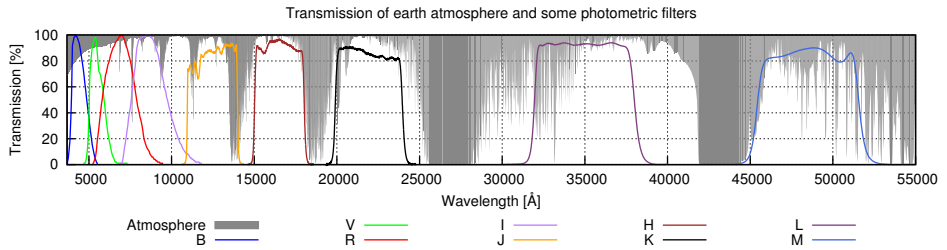


**Figure 4.1:** Sequence of images illustrating the process of extracting spectra from a *MUSE* data cube. Left two: For a given field, on a *HST* image all stars are marked with positions from Anderson et al. (2008). Right two: using the same positions with the wavelength integrated *MUSE* exposure allows us to identify all the stars, which are then extracted using PSF fitting techniques. Images by S. Kamann.

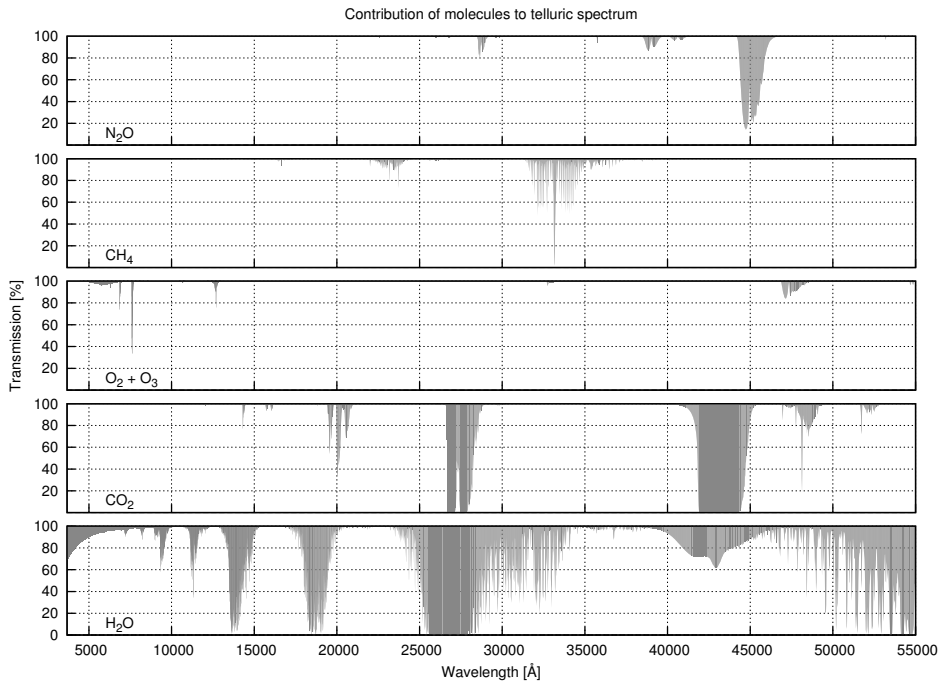
et al., 2008) are marked. Using those positions, we can also identify stars in the wavelength integrated *MUSE* exposure (see two right images). With the known positions a PSF fitting method similar to DAOPHOT (Stetson, 1987) can now extract the flux of each star in every image in order to obtain complete spectra.

## 4.2 Telluric line correction

When doing spectroscopy from the ground, the light has to travel through the Earth's atmosphere and the absorption lines of atmospheric molecules are superimposed on



(a) Transmission of the earth's atmosphere and some photometric filters. The telluric spectrum has been convolved to a resolution of  $R = \lambda/\Delta\lambda \approx 3000$ . Molecules included in the spectrum are:  $H_2O$ ,  $CO_2$ ,  $CH_4$ ,  $O_3$ ,  $N_2O$ ,  $CO$ ,  $O_2$ ,  $NO$ ,  $SO_2$ ,  $NO_2$ ,  $NH_3$ ,  $HNO_3$  and  $OCS$ .



(b) Contributions of different molecules to the telluric spectrum.

**Figure 4.2:** The telluric spectrum in the wavelength range 3 700 - 55 000Å as simulated for the site of the VLT on December 6, 2011, synthesized by Kathrin Ulbrich using an IDL program by Natascha Rudolf based on LBLRTM as used by Seifahrt et al. (2010).

the science spectrum. The main contributors are both rotational and vibrational (*rovibrational*) transitions of water vapour ( $H_2O$ ), carbon dioxide ( $CO_2$ ) and ozone ( $O_3$ ), but we also see features from nitrous oxide ( $N_2O$ ) and methane ( $CH_4$ ). From the Latin word *tellus* for *Earth*, we also call the lines created by those molecules *telluric*.

In Fig. 4.2(a) the telluric spectrum is plotted in the optical and NIR domain from

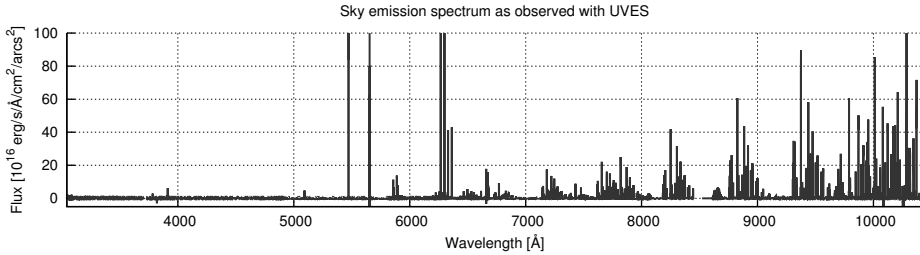


Figure 4.3: .

Night-sky emission spectrum from UVES observations by Hanuschik (2003).

3 700 to 55 000Å, over-plotted with the transmission curves of some standard photometric filters. We see that the centres and widths of the NIR filters (I, J, H, K, L, M) have been chosen carefully in order to avoid the regions with strong telluric features. The absorption we see at the blue end of the plotted spectrum is caused by Rayleigh Scattering, which makes the Earth's atmosphere opaque for wavelengths  $\lambda \lesssim 2000\text{Å}$ . Figure 4.2(b) shows how the different molecules contribute to the telluric spectrum.

Since the Earth's atmosphere is in local thermodynamic equilibrium below about 60 km, Kirchhoff's law applies and therefore we see the transitions of the molecules discussed above both as absorption lines superimposed on bright sources like stars and as emission lines in sky spectra. In Fig. 4.3 a night-sky emission spectrum is plotted that has been observed with UVES. Detailed studies have been done by Osterbrock et al. (1996, 1997) for the optical and NIR range from 3 865 Å to 10 600 Å, and have been extended by Rousselot et al. (2000) up to 22 500 Å.

The strengths of the telluric features depend sensitively on the current state of the atmosphere, i. e. its temperature, pressure and humidity. Although the major constituents of the atmosphere ( $O_2$ ,  $N_2$ ,  $Ar$ ) are quite constant at a given place (Adelman et al., 1996), this is not true for ozone and water vapour, which can vary significantly over time scales as short as hours and with an amplitude of  $\sim 0.1$  mag/airmass (Hayes & Latham, 1975).

It is fairly easy to remove the telluric emission features from a science spectrum, since for most observations we will have a good template in form of a sky spectrum simultaneously taken with the science observation. In not-so-crowded fields this will happen automatically for most types of observations. For our planned observations of globular clusters unfortunately there will be no patches of empty sky in the images and therefore we will need additional observations close in time and airmass to the science target.

The method usually used for removing the telluric absorption lines on the other hand requires a spectrum of a so-called *telluric standard star*, which also has to be taken close in time and airmass to the science target. A perfect telluric standard would be an ideal black body, which shows no intrinsic absorption or emission features at all. In that case the science spectrum can be divided by the continuum-corrected spec-

trum of the telluric standard in order to remove the telluric features. Therefore preferred candidates are early-type stars (spectral types mid B to late A), which show no absorption features besides those of hydrogen – in the optical and NIR this is mainly the Balmer and the Paschen series. The technique commonly used is to interpolate over the H lines, which of course eliminates all telluric features in those regions. Furthermore, A-type stars can rotate quite fast with velocities of more than 300 km/s (see e. g. Abt & Morrell, 1995), which broadens the intrinsic spectral lines significantly. Therefore interpolating over the lines gets difficult especially at the limit of the various hydrogen series.

To avoid this problem, Maiolino et al. (1996) developed a method for using nearby early G-type or late F-type main-sequence stars as telluric standards. They made use of the fact that those stars are close in type to the sun and therefore used a high-resolution spectrum of the sun obtained by Livingston & Wallace (1991). The correction spectrum was then created as the ratio of the solar spectrum to that of the observed telluric standard. This ratio, multiplied to the spectrum of the science target, should then remove all telluric features. Practical problems (see Vacca et al., 2003) arise from the fact that the number of observable F/G-type stars is lower than that of A stars, and that F/G-type stars show a lot of weak metal lines, which cause the quality of the method to depend strongly on how good the spectrum of the telluric standard matches that one of the sun.

Vacca et al. (2003) introduced a similar method using Vega as a template for the observation of telluric standards of spectral type A0 V. It benefits from the absence of spectral lines in most parts of an A-type star and tries to correct the remaining hydrogen features using a high-resolution model of Vega's intrinsic spectrum.

Another approach for removing telluric features is to use a synthetic spectrum instead of an observed one. While Lallement et al. (1993) only simulated a few  $H_2O$  lines around the sodium doublet at 589.5 nm, Seifahrt et al. (2010) introduced a method for calculating synthetic telluric spectra in an arbitrary wavelength range (using FASCODE/LBLRTM, see Clough et al., 1981, 1992), which models the transmission spectrum of the Earth's atmosphere above Cerro Paranal in Chile. The plots of telluric absorption lines in this section are all synthesized using their data.

Although until now we only discussed methods for removing the telluric features from a science spectrum, there are cases, where we want to keep them and even use them for our benefit. Griffin (1973) already suggested to use the absorption lines caused by the Earth's atmosphere in order to increase the accuracy of the wavelength calibration of an observed spectrum and therefore allowing to get more precise radial velocities with an accuracy of the order of 10 m/s. Nowadays Figueira et al. (2010b) claim to achieve an accuracy of 5-10 m/s with CRIRES or even down to 1-2 m/s with HARPS (Figueira et al., 2010a), if the atmospheric phenomena are corrected for using a simple atmospheric model.

If the line density of the Earth's atmosphere is not high enough, one can try to put an *absorption cell* in the light beam of the telescope, which superimposes the spectral lines of its containing gas onto the observed spectrum. This has been done e. g. with io-

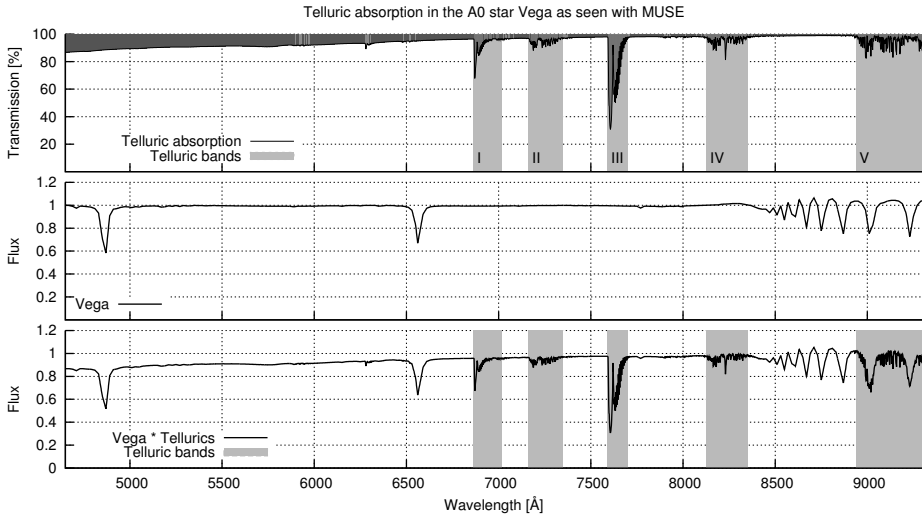


**Figure 4.4:** Telluric absorption in an A0-type star. The pure telluric spectrum is plotted on top and a clean spectrum of the A0-type star Vega in the middle (taken from Kurucz, 1979), both convolved to MUSE resolution and resampled accordingly. The lower plot shows the telluric lines superimposed on the Vega spectrum. In yellow those regions are marked that we are currently considering for the correction.

	$\lambda_{start}$ [Å]	$\lambda_{end}$ [Å]
I (B band)	6864	7020
II	7162	7350
III (A band)	7591	7703
IV	8128	8352
V	8938	9300

**Table 4.1:** Telluric regions that are currently considered in the correction.

dine (Marcy & Butler, 1992; Butler et al., 1996), hydrogen fluoride (Campbell & Walker, 1979) and ammonia (Bean et al., 2010). The advantage of using lines from either an absorption cell or the atmosphere over the classical way with a calibration lamp is primarily that the light takes the identical path through the telescope. Furthermore they are superimposed on the science spectrum during observation, so there is no need for extra calibration runs. A comprehensive list of advantages is given e. g. in Griffin (1973).

The aforementioned accuracies of  $\lesssim 10$  m/s for radial velocities are, of course, beyond the realms of possibility for *MUSE*, with its resolution of  $R \approx 3\,000$ ; we only require the removal of the telluric features from the observed science spectrum. Currently, we are using a method using A-type stars similar to the one described above, but this choice may change as the first real data from *MUSE* is processed.

Figure 4.4 shows the spectrum of the A0-type star Vega superimposed with the telluric lines shown before in Fig. 4.2(a). Currently we only remove the features marked

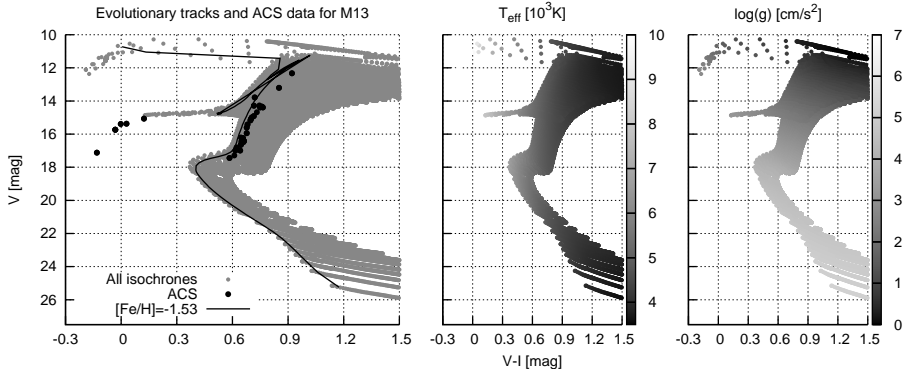


**Figure 4.5:** On the left hand side a single isochrone for an age of 12.7 Gyrs and  $[Fe/H] = -1.53$  is plotted as a black line with underlying grey points representing the data for all available metallicities for that age (Marigo et al., 2008). Plotted with black points are the ACS colours and magnitudes (Anderson et al., 2008) for the targets of a recent PMAS observation by Sebastian Kamann. In the other two plots, the effective temperatures (middle) and surface gravities (right) for all the data points from the isochrones are shown.

in yellow and listed in Table 4.1. The regions III and I with the strongest absorption are also known as Fraunhofer A and B bands and are both caused by molecular oxygen.

Since there are no further telluric features adjacent to the regions marked in Fig. 4.4 at both the red and the blue end, we can easily apply a local normalization by fitting a line through each region, which in total make up the telluric spectrum (with a value of one outside the regions) used for correcting the science spectra. Unfortunately this is not the case for region V, which therefore cannot be treated correctly. The tool we use for removing telluric features is *spexxyTellurics* (see Section C.15).

### 4.3 Parameter estimation using isochrones

In Chapter 2, we already discussed colour-magnitude diagrams (CMD) of globular clusters. Instead of using them for the determination of e. g. overall age and metallicity of GCs, we can utilize them for estimating stellar parameters by fitting observed colours and magnitudes to an isochrone in order to obtain the corresponding effective temperature, surface gravity and metallicity.

Figure 4.5 shows some ACS magnitudes (Anderson et al., 2008) for a recent PMAS observation by Sebastian Kamann in red. Underlying in green is a theoretical isochrone by Marigo et al. (2008) for a metallicity of  $[Fe/H] = -1.53$ . In black, the data for all available metallicities is plotted. Besides magnitudes in several filters, the isochrones provide effective temperatures, surface gravities and metallicities for every data point. The values for  $T_{\text{eff}}$  and  $\log(g)$  are plotted in the second and third plot of Fig. 4.5. Thus, we can now use this information to estimate stellar parameters for all the observed stars, i. e. all the red 'X's in the left plot.

Before using the measured magnitudes of a star for any analysis, we need to correct them for extinction and distance. The former can be represented by a value of  $E_{B-V}$  (see Section 4.9.2) obtained by using a full-sky dust map (e. g. Schlegel et al., 1998). For globular clusters, which are fairly constrained in size, we can simply use the extinction value given by Harris (1996). In case other colours than  $B$  and  $V$  are requested, they can be recalculated using *PHOENIX* spectra. The magnitudes in the isochrone (Marigo et al., 2008) are corrected for the distance of the cluster. They can be imported to *spexxy* using *spexxyImportIsochroneCMD* (see Section C.11), which takes care of both corrections.

The simple approach we are currently using finds the nearest neighbour in the isochrone for a given pair of magnitude and colour, from which the stellar parameters are taken. We estimate the accuracy by doing the same for other magnitudes and colours that are varied according to their observational errors. The fitting can be done using *spexxyIsoFit* (see Section C.13). For some spectra (low S/N, small wavelength range, etc), it might be better to use the value for  $\log(g)$  from the isochrone fit without trying to determine it spectroscopically. Kirby et al. (2009) used this method for fixing the surface gravity photometrically and they claim to have achieved an accuracy of  $\pm 0.06$  dex.

## 4.4 Interpolator for the grid of spectra

When trying to fit an observed spectrum against a grid of synthetic ones, the easiest way is to correlate it with every single spectrum in the grid and find the one that matches best. This might work well when the goal is just to categorize the observations roughly, but it is not suited to determine detailed parameters (e. g. the temperature) of a star unless the grid is refined to the required accuracy. Actually computing additional spectra using *PHOENIX* would require a significant amount of time.

A more practicable approach is to create a grid of model spectra with a fixed step size in all dimensions and then just interpolate spectra for every set of parameters that does not exist in the grid. For simple cases, a linear interpolation might be enough, but some applications require a more sophisticated approach like spline interpolation.

Serendipitously, there is one aspect of stellar spectra that makes interpolating between them more convenient than when handling other kind of data: all wavelengths points can be considered to be effectively independent, i. e. all interpolations can be performed using the flux at a single wavelength and its neighbours are not of interest. Of course this is not entirely true for convolved and resampled (and therefore also for observed) spectra, but in most cases, this effect is negligible.

### 4.4.1 Linear interpolation

For a tabulated function  $y_i = y(x_i)$ ,  $i = 0 \dots n$  we can always define a polynomial  $P$  of degree  $n$ , which goes through all of its points, i. e.  $P(x_i) = y_i$  for all  $i$ . In the standard



basis  $\{x^k \mid 0 \leq k \leq n\}$ , this would yield an equation

$$P(x_i) = \sum_{k=0}^n p_k x_i^k \quad (4.1)$$

with coefficients  $p_k$ . Therefore we have to solve a system of  $n + 1$  linear equations with

$$\begin{pmatrix} 1 & x_0 & \cdots & x_0^n \\ \vdots & \vdots & \ddots & \vdots \\ 1 & x_n & \cdots & x_n^n \end{pmatrix} \begin{pmatrix} p_0 \\ \vdots \\ p_n \end{pmatrix} = \begin{pmatrix} y_0 \\ \vdots \\ y_n \end{pmatrix}, \quad (4.2)$$

which is quite expensive to calculate, e. g. with Gaussian elimination it is  $\mathcal{O}(n^3)$ , where of course  $n$  is not the number of points in the spectra, but the number of values for each axis of the grid, e. g.  $n = 53$  for the  $T_{\text{eff}}$  axis for the current state of the *PHOENIX* grid.

The method described above becomes a lot easier if we decide to interpolate piecewise in the interval between  $x_j$  and  $x_{j+1}$ ; for two points we only need a polynomial of degree one, i. e. a line. Therefore the interpolation the value  $y$  at point  $x$  simplifies to

$$y = Ay_i + By_{j+1}, \quad (4.3)$$

with the coefficients

$$A = \frac{x_{j+1} - x}{x_{j+1} - x_j} \quad \text{and} \quad (4.4)$$

$$B = 1 - A = \frac{x - x_j}{x_{j+1} - x_j}. \quad (4.5)$$

In Fig. 4.6, a tabulated function  $f_i(x)$  is plotted (black circles), with values interpolated using a polynomial of 6th degree (black line). It also shows the results of a linear interpolation in blue, in which the major problem of this method for our application can easily be seen in the second plot: discontinuities in the first derivatives, and therefore singularities in the second derivatives as shown on the right.

The linear interpolation scheme can easily be extended to two dimensions using *bilinear* interpolation. With a  $N \times M$ -sized grid of evenly spaced tabulated function values, which consists of points  $(x_{1,j}, x_{2,k})$ ,  $j = 0 \dots N - 1$ ,  $k = 0 \dots M - 1$ , an intermediate point  $x = (x_1, x_2)$  is always surrounded by four grid points as shown in Fig. 4.7. Now the interpolation can be described as two linear interpolations in  $e_1$ . The results are used again for an interpolation in  $e_2$ . Those three interpolations can be combined into one by

$$y = (1 - t)(1 - u)y_0 + t(1 - u)y_1 + tu y_2 + (1 - t)u y_3, \quad (4.6)$$

with the coefficients

$$t = \frac{x_1 - x_{1,l}}{x_{1,u} - x_{1,l}}, \quad u = \frac{x_2 - x_{2,l}}{x_{2,u} - x_{2,l}}. \quad (4.7)$$

By extending this scheme, interpolation in higher dimensions is easily done. The number of grid points  $n$  needed for the interpolation grows with the  $d$ th power of two, where  $d$  is the number of dimensions, i. e.  $n = 2^d$ .

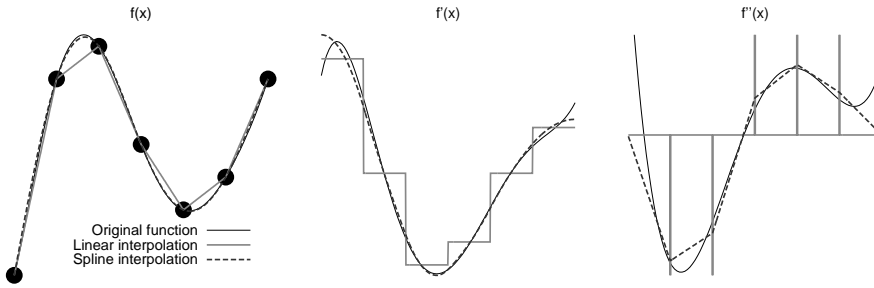


**Figure 4.6:** Plotted on the left is a tabulated function  $f_i(x)$  (black circles) with values interpolated using a polynomial of 6th degree (black line), linearly piecewise (grey line) and using a spline (dashed black line). In the second plot the first derivatives for all three are shown, while on the right the second derivatives are plotted.

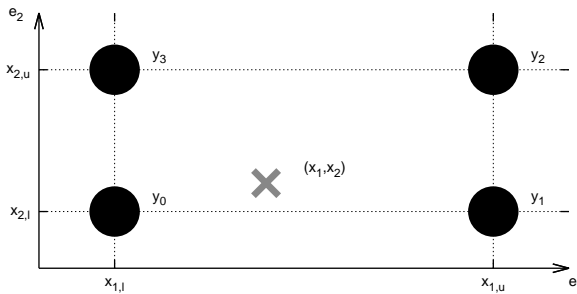


**Figure 4.7:** Labelling of points for the bilinear interpolation.

### 4.4.2 Spline interpolation

In Section 4.10, a non-linear minimization algorithm will be used to fit the stellar parameters of observed spectra. For that we need a Jacobi matrix, i. e. first derivatives, at every point within the parameter space. Thus, the spectra we interpolate from the grid must be differentiable and therefore have continuous first derivatives, which makes the linear interpolation described above a poor choice. A better alternative is a cubic spline interpolation in one dimension (see Press et al., 2007):

$$y = Ay_j + By_{j+1} + Cy_j'' + Dy_{j+1}'', \tag{4.8}$$

with coefficients  $A$  and  $B$  as defined in Eq. 4.4 and  $C$  and  $D$  as:

$$C = \frac{1}{6}(A^3 - A)(x_{j+1} - x_j)^2 \quad \text{and} \tag{4.9}$$

$$D = \frac{1}{6}(B^3 - B)(x_{j+1} - x_j)^2. \tag{4.10}$$

For the interpolation of value  $y$  at position  $x$ , we need both the value and the second derivative of its next lower (at  $x_j$ ) and next higher (at  $x_{j+1}$ ) neighbour. We can now

differentiate Eq. 4.8 with respect to  $x$  and find for the first and second derivatives:

$$\frac{dx}{dy} = \frac{y_{j+1} - y_j}{x_{j+1} - x_j} - \frac{3A^2 - 1}{6}(x_{j+1} - x_j)y_j'' + \frac{3B^2 - 1}{6}(x_{j+1} - x_j)y_{j+1}'', \quad (4.11)$$

$$\frac{d^2y}{dx^2} = Ay_j'' + By_{j+1}''. \quad (4.12)$$

By comparing Eq. 4.12 with Eq. 4.3 we see that the second derivatives are just linear interpolations. Due to this, they are inevitably continuous at the boundaries between to consecutive intervals.

Now we also want the first derivative to be continuous. For this we evaluate Eq. 4.11 at  $x = x_j$  for both the intervals  $(x_{j-1}, x_j)$  (I) and  $(x_j, x_{j+1})$  (II):

$$I \quad \left. \frac{dx}{dy} \right|_{x=x_j}^{(x_{j-1}, x_j)} = \frac{y_j - y_{j-1}}{x_j - x_{j-1}} + \frac{3A_1^2 - 1}{6}(x_j - x_{j-1})y_{j-1}'' + \frac{3B_1^2 - 1}{6}(x_j - x_{j-1})y_j'', \quad (4.13)$$

$$II \quad \left. \frac{dx}{dy} \right|_{x=x_j}^{(x_j, x_{j+1})} = \frac{y_{j+1} - y_j}{x_{j+1} - x_j} - \frac{3A_2^2 - 1}{6}(x_{j+1} - x_j)y_j'' + \frac{3B_2^2 - 1}{6}(x_{j+1} - x_j)y_{j+1}''. \quad (4.14)$$

With  $A_1 = \frac{x_j - x_{j-1}}{x_j - x_{j-1}} = 0, B_1 = 1 - A = 1$  and  $A_2 = 1, B_2 = 0$  accordingly, this simplifies to:

$$I \quad \left. \frac{dx}{dy} \right|_{x=x_j}^{(x_{j-1}, x_j)} = \frac{y_j - y_{j-1}}{x_j - x_{j-1}} + \frac{x_j - x_{j-1}}{6}y_{j-1}'' + \frac{x_j - x_{j-1}}{3}y_j'', \quad (4.15)$$

$$II \quad \left. \frac{dx}{dy} \right|_{x=x_j}^{(x_j, x_{j+1})} = \frac{y_{j+1} - y_j}{x_{j+1} - x_j} - \frac{x_{j+1} - x_j}{3}y_j'' - \frac{x_{j+1} - x_j}{6}y_{j+1}''. \quad (4.16)$$

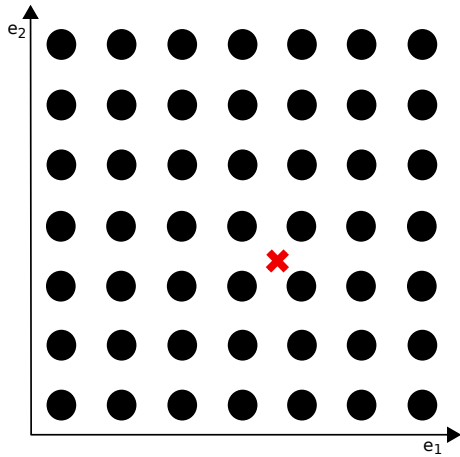
We can now force continuity by equalizing the respective right sides of equations (I) and (II). The result is

$$\frac{x_j - x_{j-1}}{6}y_{j-1}'' + \frac{x_{j+1} - x_{j-1}}{3}y_j'' + \frac{x_{j+1} - x_j}{6}y_{j+1}'' = \frac{y_{j+1} - y_j}{x_{j+1} - x_j} - \frac{y_j - y_{j-1}}{x_j - x_{j-1}}, \quad (4.17)$$

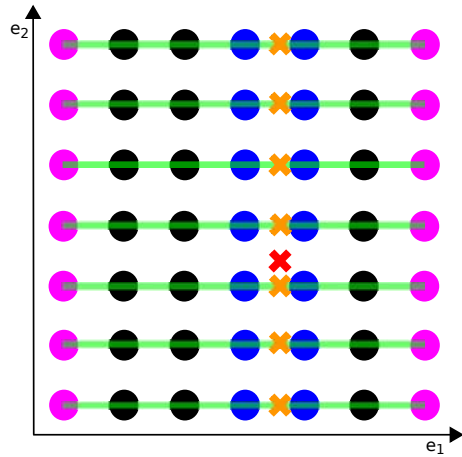
which yields  $n - 1$  equations for the  $n + 1$  unknowns  $y_i'', i = 0, \dots, n$ . Therefore in order to get a solution, we need two more equations, which can be obtained from the boundary conditions, which in our case can simply be set as  $y_0'' = 0$  and  $y_n'' = 0$ .

One reason why we favour this spline interpolation over the polynomial interpolation discussed before is the fact that the set of equations we just obtained is not only linear but also *tridiagonal*, i. e. each  $y_i$  only depends on its nearest neighbours at  $i \pm 1$ . This allows us to use a *tridiagonal algorithm* in order to solve the equations in  $\mathcal{O}(n)$ .

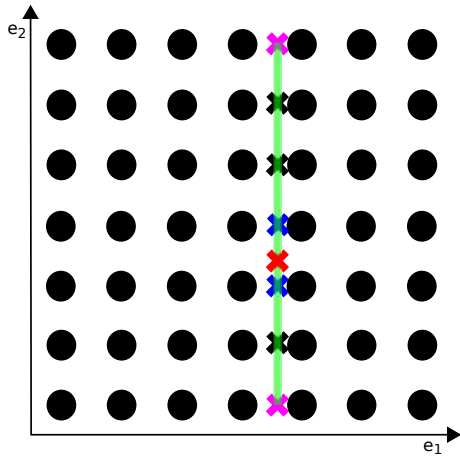
Just as for linear interpolation, this method can be extended to multiple dimensions, for which Fig. 4.8 shows an illustration. In Fig. 4.8(a) a two dimensional grid of spectra is shown with a cross marking a spectrum that we want to interpolate. First, we need to calculate the second derivatives in the first dimension  $e_1$ . For the first dimensions, all grid values are already known, so we can pre-calculate its second derivatives.



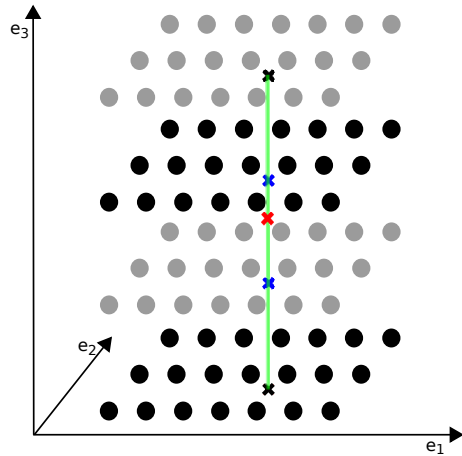
(a) A two dimensional grid of spectra (black circles) with another spectrum that we want to interpolate (red cross).



(b) Calculation of second derivatives in  $e_1$  (green line) with border values (violet) set to zero. Then interpolation in  $e_1$  from nearest neighbours (blue) for each value in  $e_2$ , resulting in a new set of spectra (orange).



(c) Calculation of second derivatives in  $e_2$  (green line) for previously interpolated spectra with border values (violet) set to zero. Then interpolation in  $e_2$  to get final interpolated spectrum (red).



(d) Extension into more dimensions by just repeating steps (a) to (c) recursively.

**Figure 4.8:** Illustration of the process of spline-interpolating spectra within a  $N$ -dimensional grid.

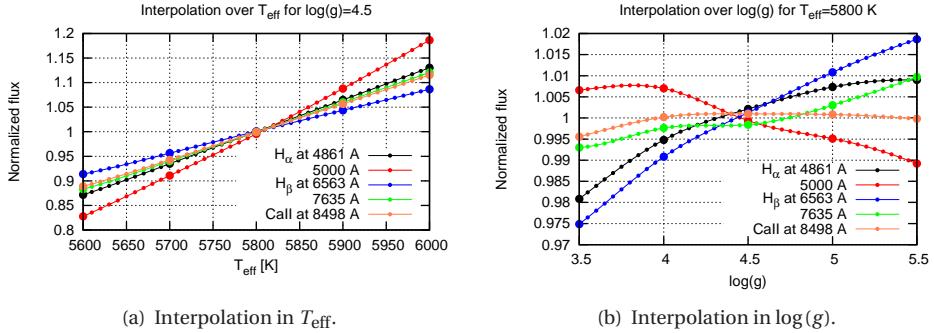


**Figure 4.9:** Quality of interpolation in  $T_{\text{eff}}$  and  $\log(g)$  for a sun-like star. Plotted are the normalized fluxes for three different absorption lines and two continuum points. Large circles indicate values from the grid while small ones are interpolated values.

The tool that can be used for this was described in Section 3.3.5. Although we double our need in disk space by doing this, we save a lot of computational time, since we do not have to recalculate the same derivatives again for every new interpolation. For the spectral grid presented in this thesis, the first dimension is the effective temperature  $T_{\text{eff}}$ . Once the second derivatives have been calculated, we can interpolate new spectra for each value of  $e_2$  using Eq. 4.8 (see orange crosses in Fig. 4.8(b)). For those we can then calculate second derivatives in the second dimension  $e_2$  and interpolate the requested spectrum as before (see Fig. 4.8(c)).

Using this approach, it is straightforward to extend the interpolation to more than two dimensions (see Fig. 4.8(d)). In principle, the last step has to be repeated for every new dimension  $e_i$  recursively, i. e. calculate the second derivatives for all the values in  $e_i$  and then interpolate the new spectrum. We provide a stand-alone tool called *spexxyInterpolate* (see Section C.12), which interpolates one or more spectra from a given grid.

In the end, what is important is the quality of the interpolated spectra. Figure 3.7 in Section 3.3.2 already showed that we can reproduce spectra of sufficient quality by interpolating from neighbours. An easy sanity check is to make sure that interpolated values always lie between those two from which they have been calculated – or at least not too far outside this range. This already eliminates errors due to wavy behaviour often seen with splines. So far, we have never observed such artefacts.

Almost more important than a completely accurate interpolation of the spectra is making sure that the change of the flux at a given wavelength is differentiable in every dimension in order to be able to build a Jacobian matrix. After all, this is why we use a spline interpolator instead of a simple linear one. Figure 4.9 shows the change in flux for five different wavelengths, when stepping through the grid both in  $T_{\text{eff}}$  (left) and in  $\log(g)$  (right); three are the centres of absorption lines ( $H_{\alpha}$ ,  $H_{\beta}$  and one of the lines in the IR CaII triplet) and two do not show any lines at all (i. e. are continuum).

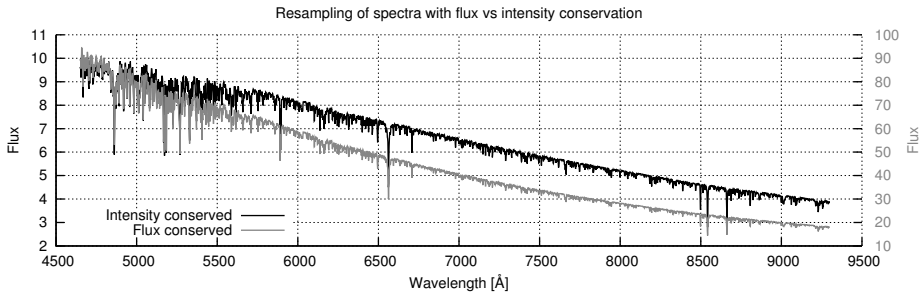


**Figure 4.10:** Result of resampling (black, left ordinate) and rebinning (red, right ordinate) a spectrum from a constant sampling in the logarithmic domain to a constant sampling in the wavelength domain.

In the plot, the large circles indicate values from spectra on the grid (i. e. no interpolation), while small circles mark interpolated fluxes. As one can see, the changes are very smooth as expected and do not show any artefacts from over-steered splines. For a better overview, the plotted flux curves have been normalized to a mean of one.

The computational time of the interpolation can easily be decreased by not taking all spectra into account when calculating the second derivatives but only the  $N$  nearest neighbours. This would presumably speed up the interpolation especially for grids with a large number of dimensions, since the computation time grows exponentially with that number. For example, at the moment it takes about ten times longer to interpolate a spectrum with given effective temperature  $T_{\text{eff}}$ , surface gravity  $\log(g)$  and metallicity  $[Fe/H]$  for an alpha-element abundance of  $[\alpha/Fe] \neq 0$  than it does for  $[\alpha/Fe] = 0$ .

## 4.5 Rebinning spectra

Quite commonly, the terms *rebinning* and *resampling* are assumed to be referring to one and the same process, while in fact they are not, when taking the words literally: in the context of spectra, *resampling* means to sample them at different wavelength points, which is usually done by some kind of interpolation between existing points. *Rebinning* on the other hand changes the size of the bins (for astronomical spectra usually the pixels on the CCD) that are used for the integration of the observed signal. In a real observation, by increasing the size of any given pixel on the CCD, we automatically increase the measured signal, although the position of the pixel, i. e. its wavelength, stays the same. When summing up the flux values of a rebinned spectrum, the resulting total flux is the same as in the original spectrum, which is not true for a resampled spectrum that we would have to integrate properly in order to get the same result. Due to this, resampling conserves the intensity, while rebinning conserves the flux.

In case both the input and the output sampling are constant, the difference be-

tween resampling and rebinning is just a multiplicative factor, e. g. rebinning a spectrum to a new grid that is ten times coarser can be done by summing up all the ten pixels from the spectrum that fall in one new bin, so the intensity in the rebinned spectrum is ten times higher. Of special interest is the situation, when we resample a spectrum from or to an irregular wavelength grid, which is the case, e. g., for a spectrum in the wavelength domain that is rebinned to a constant sampling in the logarithmic domain or vice versa. Here, the conversion factor changes with wavelength. Figure 4.10 shows a spectrum in the logarithmic domain that has been both resampled and rebinned to a constant sampling in wavelength. The differences in both the intensity and the shape of the continuum are obvious.

With *MUSE*, the spectra will have a constant sampling either in  $\lambda$  or in  $\log(\lambda)$ , so this conversion factor will always be a smooth function over wavelength, which is no problem for the continuum fit that will be described in Section 4.9.7. Thus, for all the fitting methods described in this Chapter, it does not matter, whether we rebin or resample the spectra. For reasons of consistency, we still rebin all the spectra instead of just resampling them, since the extra computation time is negligible. This allows us to process all kinds of spectra, even those with an irregular sampling.

While resampling is usually done by interpolating between existing points, we still need to define a method for rebinning. Ideally, integrating the original spectrum over the new bins would do it, but unfortunately it only works properly when rebinning to a step size much larger than in the original spectrum.

Assuming a spectrum with flux values  $f_i, i = 0 \dots N - 1$  at the  $N$  wavelength points  $\lambda_i, i = 0 \dots N - 1$ , for equally sampled  $\lambda_i$  with a step size of  $\Delta\lambda$  the  $N + 1$  borders of the bins are given by

$$b_i = \{\lambda_0 - \Delta\lambda/2, \lambda_0 + \Delta\lambda/2, \lambda_1 + \Delta\lambda/2, \dots, \lambda_{N-1} + \Delta\lambda/2\}, \quad i = 0 \dots N, \quad (4.18)$$

which can be adapted for non-constant samplings by adjusting the borders accordingly. Integrating the spectrum over  $b_i$  yields:

$$I = \left\{ 0, f_0, f_0 + f_1, \dots, \sum_{i=0}^{N-1} f_i \right\}. \quad (4.19)$$

Now we can interpolate this integrated flux  $I_i$  at the borders  $b'_j, j = 0 \dots M$  of the new bins, with  $M$  being the number of points in the rebinned spectrum and  $b'_j$  calculated accordingly. This yields an integrated flux  $I'_j$  of the final bins. By differentiating  $I'_j$ , we get the flux values  $f'_j$  of the rebinned spectrum:

$$f'_j = \{I'_1 - I'_0, I'_2 - I'_1, \dots, I'_M - I'_{M-1}\}. \quad (4.20)$$

It is easy to show that this method is valid for output step sizes that are a integer multiples of the original ones, since in those cases, the points in each bin are just summed up.

## 4.6 Radial velocities and line broadening

Simulating the effect of radial velocities on synthetic spectra can be done in multiple ways. Assuming a stationary observer, which in our case would be placed in the barycentre of our Solar System, the wavelength  $\lambda$  of a star moving with the velocity  $v_{\text{rad}}$  along our line of sight is changed according to Doppler's law by

$$\lambda' = \lambda \left( 1 + \frac{v_{\text{rad}}}{c} \right). \quad (4.21)$$

When measuring wavelengths on a logarithmic scale, the multiplicative factor becomes a constant offset independent of  $\log \lambda$ :

$$\log \lambda' = \log \lambda + \log \left( 1 + \frac{v_{\text{rad}}}{c} \right). \quad (4.22)$$

In extragalactic astronomy, the term *line-of-sight velocity distribution* (*LOSVD*) is commonly used for describing the observed velocity dispersion in galaxies. The broadening of absorption lines seen in the spectra of galaxies is caused by the combination of intrinsic velocity dispersion and the integration along the line-of-sight (see e. g. Bender, 1990). Those distributions are found to be sometimes highly non-Gaussian (see e. g. Halliday et al., 2001), which can be explained e. g. as kinematically decoupled cores (Jedrzejewski & Schechter, 1988) or central discs (van den Bosch et al., 1998).

We can now adopt this terminology for the analysis of stellar spectra, where we also often observe an intrinsic line broadening, in this case explainable by stellar rotation or by the spectrum being a blend of several stars. The easiest way to add an additional line broadening to a spectrum is to convolve it with a suitable kernel. Conveniently, we can simultaneously add the constant offset in wavelength from Eq. 4.22 by just moving the centre of the kernel away from the origin. The convolution can be written as

$$G(x) = [B * M](x), \quad (4.23)$$

where  $*$  denotes a convolution,  $B(x) = \mathcal{L}(cx)$  is the broadening function with the *LOSVD*  $\mathcal{L}(v)$ , the speed of light  $c$  and a model spectrum  $M$  that is used for the comparison with the observation  $G(x)$ .

Currently, we mostly use a Gaussian for the *LOSVD*, but an extension to a Gauss-Hermite series (van der Marel & Franx, 1993; Gerhard, 1993) for better matching non-Gaussian line broadenings is possible. While for absorption lines the intrinsic broadening is roughly Gaussian (e. g. thermal motion), this formalism is required when including the response function of the instrument (the *line spread function LSF*), which can be highly non-Gaussian. See Section 3.3.4 for how this method is used for that purpose. Following Cappellari & Emsellem (2004), a Gauss-Hermite expansion can then be described as:

$$\mathcal{L}(v) = \frac{e^{-0.5y^2}}{\sigma\sqrt{2\pi}} \left[ 1 + \sum_{m=3}^M h_m H_m(y) \right], \quad (4.24)$$

with the Hermite polynomials  $H_m$ ,  $y = (v - V)/\sigma$  and  $M$  free parameters ( $V, \sigma, h_3, \dots, h_M$ ), where  $V$  defines a shift on the wavelength axis (i. e. a radial velocity)



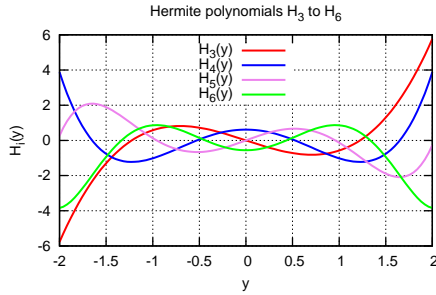


**Figure 4.11:** Plot of the Hermite polynomials  $H_3$  to  $H_6$  in the range -2 to 2.

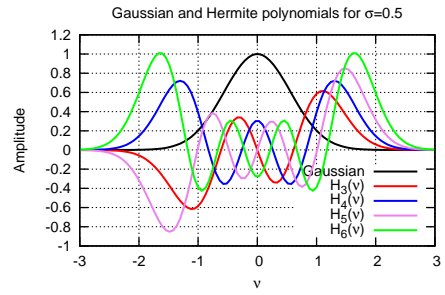


**Figure 4.12:** Plot of the summands of Eq. 4.24 with  $\sigma = 0.5$  and  $h_m = 0.5, 3 \leq m \leq 6$ .

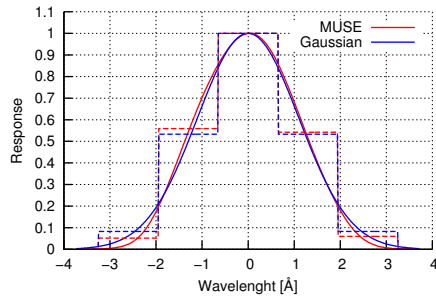


**Figure 4.13:** MUSE LSF at  $5000 \text{ \AA}$  and a Gaussian with  $2.6 \text{ \AA}$  FWHM at high resolution (lines) and integrated to the sampling of MUSE (dashed).

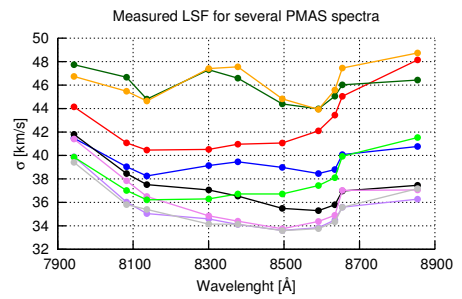


**Figure 4.14:** Line broadenings of Gaussian LSF for several PMAS spectra as measured by S. Kamann.

in units of wavelengths. We use the definition of the Hermite polynomials as given in van der Marel & Franx (1993) and which are e. g. listed in Cappellari et al. (2002):

$$H_3(y) = \frac{2y^3 - 3y}{\sqrt{3}}, \quad (4.25)$$

$$H_4(y) = \frac{4y^4 - 12y^2 + 3}{\sqrt{24}}, \quad (4.26)$$

$$H_5(y) = \frac{4y^5 - 20y^3 + 15y}{\sqrt{60}}, \quad (4.27)$$

$$H_6(y) = \frac{8y^6 - 60y^4 + 90y^2 - 15}{\sqrt{720}}. \quad (4.28)$$

Figure 4.11 shows a plot of the Hermite polynomials  $H_3$  to  $H_6$ . Multiplying them with a Gaussian as in Eq. 4.24 lets them fade out at the edges and scaling their abscissa stretches them according to the width of the Gaussian. The result is plotted in Fig. 4.12 with  $\sigma = 0.5$  and  $h_m = 0.5$  for all coefficients.

Cappellari & Emsellem (2004) describe how to use Gauss-Hermite polynomials for

fitting the LOSVD in pixel space by using a non-linear least-squares optimizer, which is penalized for non-Gaussian solutions, i. e. by the integrated square deviation of the line profile  $\mathcal{L}(v)$  from its best fitting Gaussian. Therefore the optimizer always prefers pure Gaussian profiles over those containing Hermite polynomials. The tool *spexxyFitLosvd* (see Section C.8) adopts this method for fitting the LOSVD

## 4.7 Line spread function

In astronomical imaging, *point spread functions (PSF)* are a well known term for describing the *blurring* of images. The simplest case is that of a star, since most of them are so far away that they can practically be assumed as point sources and thus, they should appear as ideal points in pictures, which can be described by delta functions. This is not the case, since the light from the star has to pass through the Earth's atmosphere and through the optical system of the telescope, which causes a broadening and lets stars appear as bright blobs with increasing brightness towards the centre. Since stars are point sources, the image of the star describes the PSF (which is also called *impulse response* or *response function*) of any given optical system. For extended sources, what we observe is a *blurred* image.

The same is true for spectroscopy and the emission and absorption lines in astronomical spectra. In this context, we speak of the *line spread function (LSF)*, which describes the broadening of spectral lines that happens between their creation in the stellar atmosphere and their detection on a CCD. Speaking of a spectrum with a resolution of  $R = 10000$  refers to a LSF with usually Gaussian shape with a FWHM of  $v = c/R \approx 30 \text{ km/s}$  in the logarithmic domain. A LSF like this can easily be handled by the LOSVD fit as described in Section 4.6.

More complicated are the cases where the LSF either is not constant with wavelength, or where its shape is not Gaussian. For instance, *MUSE* spectra have a LSF varying with wavelength (with roughly constant FWHM in the wavelength domain) and a shape, which can be described as the convolution of a box function (the projection of the slit on the detector) and a Gaussian-Hermite (the instrumental LSF). Within the consortium, we have a tool available, which convolves a given spectrum to *MUSE* resolution. All the tests presented in this thesis have been done using a Gaussian LSF constant with wavelength (in the wavelength domain), which is a good approximation (see Fig. 4.13). For real observations we will have to convolve the whole *PHOENIX* grid with the actual LSF.

For most other instruments, a Gaussian shape can be assumed, for which the width  $\sigma$  varies with wavelength. In case we have a sky spectrum available, we can measure the shape of the emission lines at different wavelength in order to determine the LSF (assuming  $\sigma_{\text{instrument}} \gg \sigma_{\text{intrinsic}}$ ), which has been done by S. Kamann for his PMAS spectra (see Fig. 4.14) that will be presented in Section 5.13. If we do not have a sky spectrum but a good approximation for the atmospheric parameters of a given spectrum, we can measure the difference between the line broadening of the spectrum and

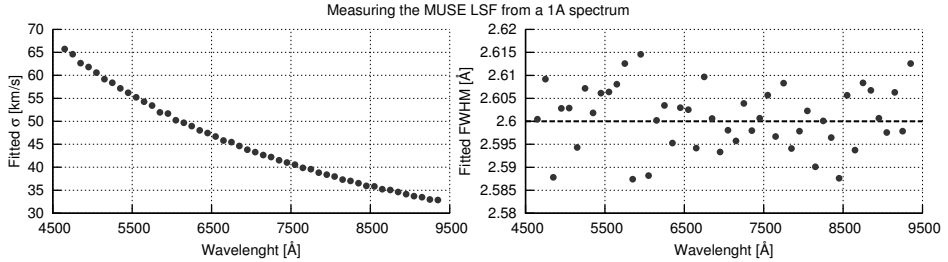


**Figure 4.15:** Fitting the (Gaussian) MUSE LSF with a model spectrum with 1 Å FWHM with the results plotted on the left. On the right, they have been transformed to the FWHM of the Gaussian in the wavelength domain and match the 2.6 Å of MUSE perfectly.

a matching model spectrum. With known LSF of the latter, we can calculate the absolute LSF of the observed spectrum easily. We determine the LSF by slicing the spectrum into bins, which are usually 100 Å wide, and running the same fit as described in Section 4.6 for each bin. This yields radial velocities and line broadenings for several wavelength ranges. While the former should ideally be constant, the change in the latter describes the LSF. For applying a LSF to a spectrum, we slice it into the same bins as before (just a little larger to create overlap) and convolve each one with a Gaussian with a width of  $\sigma$  as determined before. The final spectrum is created by blending the convolved spectra into one.

The tool provided for the determination of the LSF for a given spectrum is *spexxyLSF* (see Section C.14). Figure 4.15 shows an example for the LSF of a *MUSE* spectra that has been recovered by comparing the spectrum with a higher resolution one and fitting the line broadening.

## 4.8 Multiple components

The same formalism used for fitting the LOSVD in a spectrum can be extended to be used for multiple stellar components in the observed spectrum. Instead of having one model  $M$  in Eq. 4.23, we would have a set of  $K$  models  $M_i$ ,  $m = 1 \dots K$ . Then we could rewrite the equation to:

$$G(x) = \sum_{k=1}^K \omega_k [B * M_k](x), \quad (4.29)$$

which convolves all models with the same kernel  $B$  and add them together linearly using weighting factors  $\omega_k$ .

While this might work for a spectrum of two blended stars, which show almost identical radial velocities, this definitely becomes a problem when trying to fit physical binary systems. With their orbit around their common centre of mass, they will show different velocities – unless our line of sight is perpendicular to the plane of movement. For that case it would be better to have a different convolution kernel for each model.

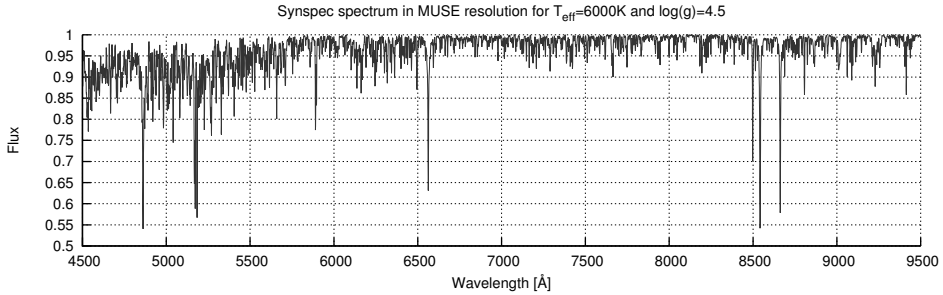


**Figure 4.16:** A spectrum for a sun-like star with  $T_{\text{eff}} = 5800\text{K}$ ,  $\log(g) = 4.5$  synthesized with *Synspec*.

Therefore our equation becomes:

$$G(x) = \sum_{k=1}^K \omega_k [B_k * M_k](x). \quad (4.30)$$

This increases the number of free parameters in the fit for every new component added. Two components can be fitted to a spectrum using *spexxyFitBinary* (see Section C.6).

## 4.9 Spectral continuum

There are multiple processes that can affect the overall shape of a spectrum beyond the form of the intrinsic stellar continuum and unresolved absorption and emission lines. The most important are *extinction* or *interstellar reddening* and problems with the reduction of the data (namely the flux calibration). Both can introduce a wavelength dependent error in the flux of the spectrum. In an actual observation, most of the time we cannot distinguish, whether the flux level at a given wavelength is caused by the intrinsic continuum or any of the other effects listed above. Therefore we combine all of them under the keyword *continuum*.

In Fig. 4.16 a spectrum is plotted with a continuum level of one for all wavelengths as created with *Synspec* (see Section 3.5). A spectrum like this is very convenient for further analyses, since we can concentrate on the spectral lines and do not have to bother with continuum emission. The second plot of Fig. 4.19 on the other hand shows the same spectrum synthesized with *PHOENIX*, which corresponds to what we can expect from an actual observation, i. e. we have a real intrinsic stellar continuum that we need to take care of.

In the following subsections, we will discuss what the different continuum contributions are, what they look like, and how they can be removed from an observed spectrum. Since the result is almost always a division by the continuum flux, this process is also called *normalization*. The list of methods that will be given is neither complete nor of the best ones possible, but just an overview.

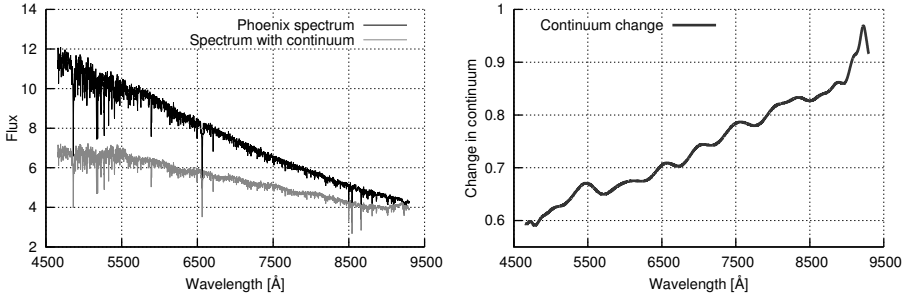


**Figure 4.17:** On the left hand side a PHOENIX spectrum ( $T_{\text{eff}} = 6000\text{K}$ ,  $\log(g) = 4.5$ ) is plotted in black together with the same spectrum in red, for which the continuum has been altered following the function on the right. The flux is given in arbitrary units.

As an example, a PHOENIX spectrum for a star with  $T_{\text{eff}} = 6000\text{K}$  and  $\log(g) = 4.5$  with solar element abundances is used. To complicate matters a little more, the spectrum contains additional noise with a signal to noise ratio of 100 as well as a change of the continuum level as might be caused, e. g., by strong reddening (see Fig. 4.17).

### 4.9.1 Stellar continuum

We often describe stars as black body radiators, which in fact they are not, or at least not exactly. The intensity of the radiation emitted by a black body is given by Planck's law:

$$B_{\lambda}(T) = \frac{2hc^2}{\lambda^5} \frac{1}{e^{hc/k_B\lambda T} - 1}, \quad (4.31)$$

with Planck's constant  $h$ , the Boltzmann constant  $k_B$  and the speed of light  $c$ . According to Wien's displacement law, this function peaks at:

$$\lambda_{\text{max}} = \frac{b}{T}, \quad (4.32)$$

with the constant  $b \approx 2.898 \cdot 10^{-3} \text{ m K}$ .

Integrating  $B_{\lambda}(T)$  over all wavelengths yields the total intensity  $B(T)$ . The total flux, i. e. the emission of a black body into the half space, can be derived from this by  $F = \pi B(T)$ . By executing the integration of  $B_{\lambda}(T)$ , we get the Stefan-Boltzmann law:

$$F = \pi B(T) = \sigma T^4, \quad (4.33)$$

with the Stefan-Boltzmann constant  $\sigma = \frac{2\pi^5 k^4}{15c^2 h^3}$ . The flux of a star at its surface is described by the integral of all fluxes  $F_{\lambda}$  at wavelengths  $\lambda$ :

$$F = \int_0^{\infty} F_{\lambda} d\lambda, \quad (4.34)$$

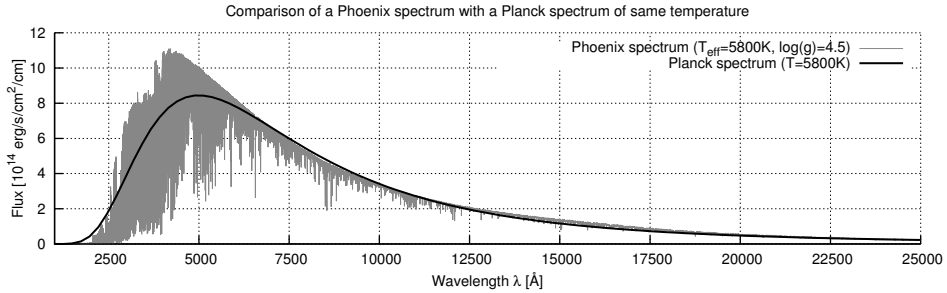


**Figure 4.18:** Comparison of a PHOENIX spectrum (black) with a Planck spectrum of same temperature (red).

	Calculated from	Flux [ $10^{10}$ erg/s/cm $^2$ ]
I	Integration of <i>PHOENIX</i> spectrum	6.326
II	Stefan-Boltzmann law	6.417
III	Using <i>PHOENIX</i> values for luminosity and radius	6.416

**Table 4.2:** Flux of a star calculated in different ways for a star with  $T_{\text{eff}} = 5800\text{K}$  and  $\log(g) = 4.5$ .

which, for the sun, is  $6.33 \cdot 10^7 \text{Wm}^{-2}$ .

The *effective* temperature  $T_{\text{eff}}$  is now the temperature of a black body that emits the same total radiation as the star, i. e. that  $T$  that fulfills the Stefan-Boltzmann law (Eq. 4.33). In case of our sun,  $T_{\text{eff}} \approx 5780\text{K}$ . Figure 4.18 shows the comparison of a *PHOENIX* spectrum with a Planck spectrum of the same temperature. As one sees, they do not match, particularly at  $\lambda < 7000 \text{Å}$ .

Just to show how well this works, Table 4.2 lists the flux of a star with  $T_{\text{eff}} = 5800\text{K}$  and  $\log(g) = 4.5$  calculated in three different ways: (I) numerical integration of the corresponding spectrum from our new *PHOENIX* grid, (II) calculated from the Stefan-Boltzmann law and (III) using the total luminosity  $L$  and the effective radius  $r$  (both given by *PHOENIX* after computation of that model has finished), which allow the calculation of the total flux as  $F = L/4\pi r^2$ . The slight discrepancy in (I) is caused by the fact that the spectra do not cover all flux in the stars due to a limited wavelength range.

Back to Planck's law, we can also define a *radiance* temperature  $T_{\lambda}$  at every wavelength point  $\lambda$ . We can assume that at least the temperature of those layers in the star, which emit the radiation observed at a given wavelength  $\lambda$ , is about  $T_{\lambda}$ . Therefore the radiance temperature changes with wavelength and we cannot just remove the continuum by calculating that one of a black body with the same temperature.

Figure 4.19 shows some spectra with the resolution and wavelength range of *MUSE*. As one can see, at least for the hotter stars (middle and bottom) and larger wavelengths it is fairly easy to determine the continuum, since the line density is quite low. On the other hand at the blue end this can already become a difficult task, and it is almost impossible for cooler stars (bottom), for which there are so many absorption lines that we almost cannot see any continuum at all.

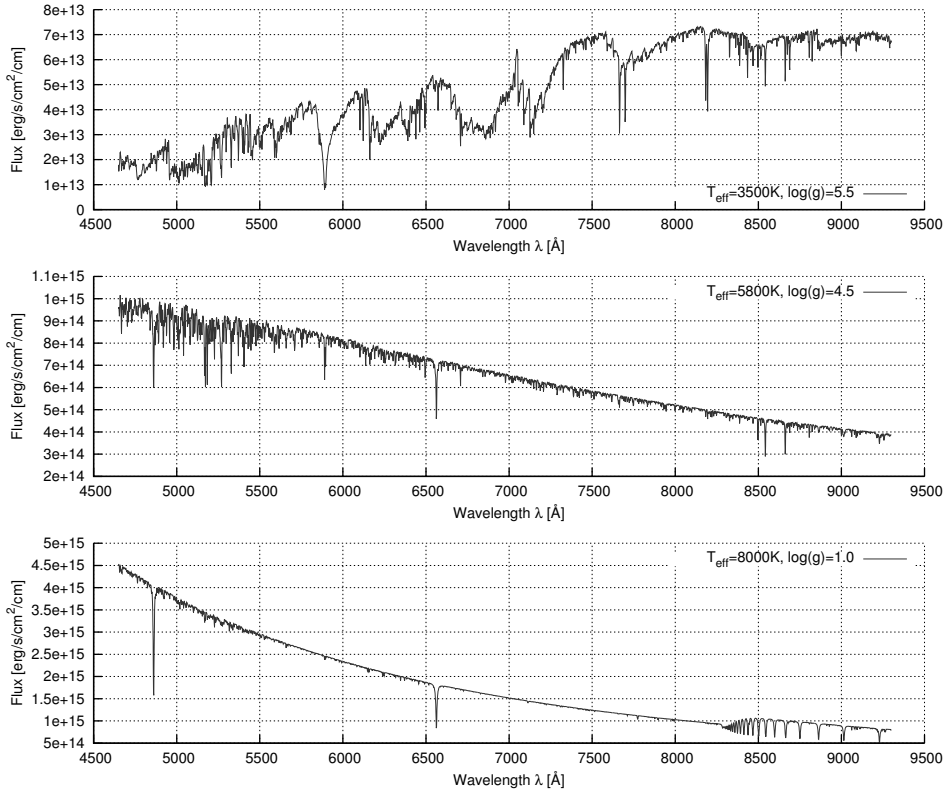


**Figure 4.19:** Spectra at MUSE resolution for three different stars with  $T_{\text{eff}} = 3500\text{K}$  and  $\log(g) = 5.5$  (top),  $T_{\text{eff}} = 5800\text{K}$  and  $\log(g) = 4.5$  (middle) and  $T_{\text{eff}} = 8000\text{K}$  and  $\log(g) = 1.0$  (bottom).

## 4.9.2 Extinction

Assuming we had a really fast spaceship and could do observations of our sun from a distance of a few kpc, we would quickly notice that the sun looks fainter than we would expect from the distance we travelled. This effect is called *extinction* and is caused by dust filling the space between the stars. In the solar neighbourhood, the rate of extinction in the V band seems to be about  $1.2\text{mag/kpc}$  (Vergely et al., 1998). In our spaceship, the sun will also look more reddish than from our usual point of view on Earth. This is why we also call this effect *interstellar reddening*, which is caused by a stronger attenuation at lower wavelengths, i. e. more blue than red light is absorbed and scattered by the dust. A similar effect can be seen at sunrise or sunset, when the atmosphere in direction of the sun is filled with dust and we can enjoy a red sky.

Traditionally, the strength of the extinction from the UV to the NIR is described as  $E_{B-V} = A_B - A_V$ , which is the difference of total extinctions in the B and V filter bands. In our own galaxy,  $R_V \equiv A_V / E_{B-V} = 3.13 \pm 0.10$  (Schultz & Wiemer, 1975) is roughly a

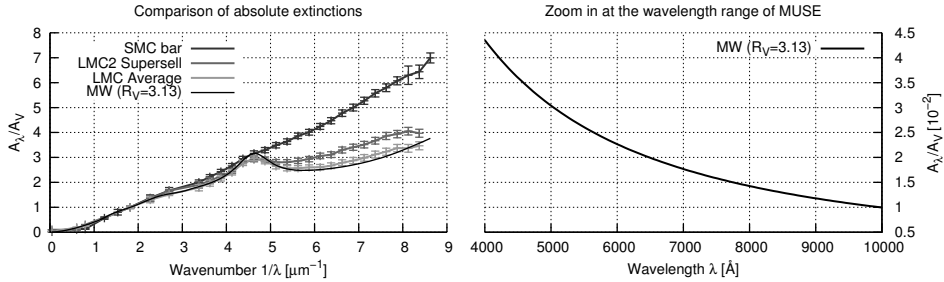


**Figure 4.20:** Comparison of extinction laws for SMC and LMC with data taken from Gordon et al. (2003) on the left. Over-plotted is the “average” Milky Way curve for  $R_V = 3.13$  with coefficients  $a(x)$  and  $b(x)$  taken from Cardelli et al. (1989). On the right, the Milky Way curve is plotted again in the wavelength range of MUSE.

constant for most lines of sight, but can vary strongly for some others, e. g. the galactic centre.

For spectroscopic observations, the absolute extinction  $A_\lambda/A_V$ , which compares the total extinction at a given wavelength  $\lambda$  to that in the V band, is of more interest. Following Cardelli et al. (1988), this can be modelled at optical wavelengths as

$$A_\lambda/A_V = a(x) + b(x)/R_V, \quad (4.35)$$

with  $x \equiv \lambda^{-1}$  and two wavelength dependent coefficients  $a(x)$  and  $b(x)$ . Pei (1992) adapted a standard graphite-silicate model and was able to match the observed extinction curves by only adjusting the graphite-to-silicate ratio. As a result, he found the Galactic extinction curve to be described well by an equal amount of graphite and silicate grains, whereas the one for the SMC requires silicate grains only and the LMC represents an intermediate situation.

Figure 4.20 shows the extinction curves for the LMC, the SMC and our Milky Way. One can easily see the differences between them and a strong increase in extinction towards lower wavelengths (or higher wavenumbers). The prominent “bump” at  $2175 \text{\AA}$  ( $\sim 4.60 \mu\text{m}^{-1}$ ), which was first observed by Stecher (1965), is still not fully understood: Bradley et al. (2005) made organic carbon and amorphous silicates, which are present in the interstellar medium, responsible for the increased extinction at that wavelength.

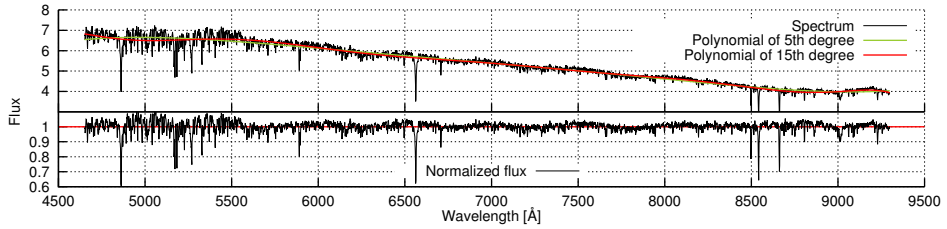
### 4.9.3 Normalizing with a polynomial

The continuum flux  $C$  of a spectrum can be approximated as a polynomial of degree  $k$ :

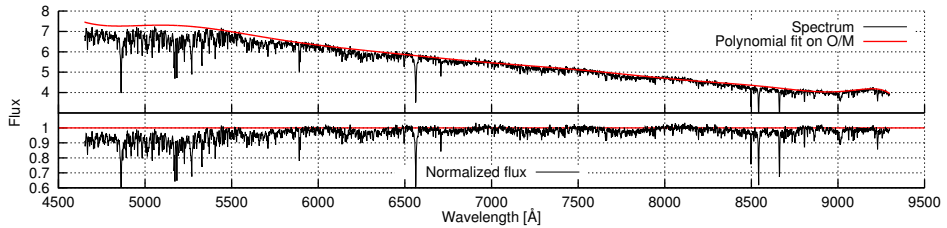
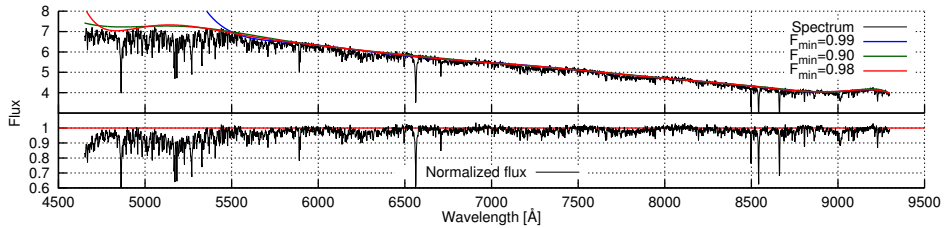
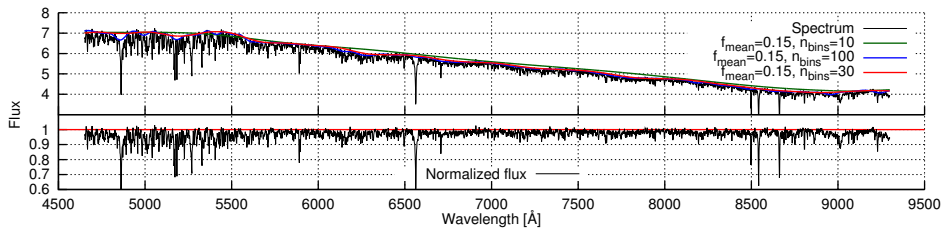
$$C(x) = \sum_{i=0}^k p_k P_k(x), \quad (4.36)$$

with coefficients  $p_k$  and  $P_k$  usually set to  $P_k(x) = x^k$ . We can now fit the continuum by finding those  $p_k$  for a given  $k$ , for which the resulting polynomial  $C$  fits the observed





(a) Using a polynomial. Two best-fit continua of different degree are shown.

(b) Using a template spectrum. Plotted is the same data as in Fig. 4.22, but for the whole range of *MUSE*.(c) Using a template and only taking into account those points that are assumed to be continuum, i.e. with  $F_{tpl} > F_{min}$ . The estimated continua for three different values of  $F_{min}$  are plotted.(d) Using the maximum values in bins. Plotted are the continua for  $n_{bins} = 10, 30, 100$  and  $f_{mean} = 0.15$ .

**Figure 4.21:** Comparison of different methods for normalizing a spectrum. For each method, the original spectrum is plotted together with one or more results for the continuum. Below, the normalized spectra are shown, which have been created using the red continuum from above.

spectrum best, e.g. using a linear least-squares fit. The degree  $k$  of the polynomial must be chosen according to the expected shape of the continuum. For example, if we just assume an extinction to be present in the data, a small  $k$  is sufficient, while for

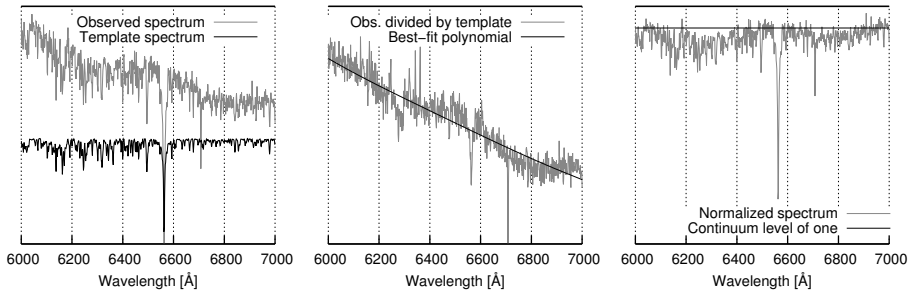


**Figure 4.22:** Observed spectrum with matching template (left), residuals with best-fit polynomial (middle) and final normalized spectrum (right).

incorrect flux calibrations with discontinuities in the observed spectra a large  $k$  might be necessary.

Fig. 4.21(a) shows how this method works. Our sample spectrum is shown in black together with two polynomials of degree 5 (green) and 15 (red) that best match the spectrum. For the latter one, the spectrum divided by the polynomial is plotted again in the lower part of the plot. With a reddening curve as smooth as the one we are using, as expected a higher value for  $k$  does not affect the result significantly.

On the other hand, the line density and the width of single lines in the observed spectrum have a massive effect on the quality of the polynomial fit. In the region between  $7000\text{ \AA}$  and  $8000\text{ \AA}$  there are only a few faint absorption lines and the determination of the continuum works pretty well. But the more lines we have and the deeper they are, the continuum estimation gets worse, since we are taking into account the whole spectrum and not continuum regions only. Therefore, we can conclude that this method works very well for hotter stars with fewer lines and in regions with a low line density. For cooler stars or high line densities, as we see them especially in the blue, the results are quite useless.

#### 4.9.4 Using a template spectrum

As we have just seen, the major problem when finding the continuum are absorption (and, if present, emission) lines. One way to include only continuum regions of the spectrum in the fit is the use of a template spectrum without continuum flux, e. g the Synspec spectra we presented in Section 3.5. If the template has similar stellar parameters as the observation, we can divide our spectrum with the template and fit a polynomial to the result for determining the continuum.

Figure 4.22 shows an observed spectrum together with a matching template on the left hand side. In the middle, the residuals (i. e. the spectrum divided by the template) are plotted together with the best-fitting polynomial. As one can see, we can even use this method with a template that does not exactly match the observation, since the

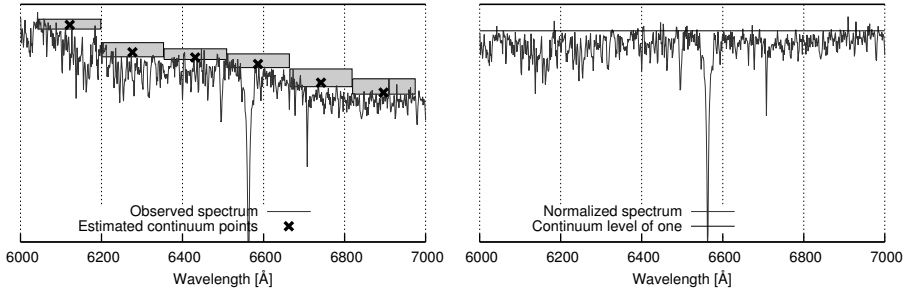


**Figure 4.23:** Observed spectrum with the regions containing the 15% largest values in each bin (boxes) and estimated continuum points (left) and normalized spectrum (right).

polynomial fit smooths out misfits. Finally, on the right hand side the resulting normalized spectrum is shown. In Fig. 4.21(b) the normalization for a whole *MUSE* spectrum is plotted. Compared to the result of the previously discussed method (see Fig. 4.21(a)), the continuum does not depend on the line density anymore and we do not see the typical over-steering of the continuum near deep absorption lines as before.

Of course, this method only works if we have a matching template spectrum without continuum flux. Although we do not need a perfect template, differences in the result are expectable when using different templates. And most often we need to normalize a spectrum before we can determine the stellar parameters, which in turn we need in order to pick a good template spectrum. This problem can be reduced a little by ignoring spectral lines when fitting the polynomial, which is easy to do with a template that roughly matches the observed spectrum. The stellar parameters for the template can be taken e. g. from photometry. Now the normalization works exactly as described above, but for the polynomial fit on the residuals we take into account only those points, for which the flux  $F_{tpl}$  in the template is larger than a given threshold  $F_{min}$ .

Figure. 4.21(c) shows the result for three different values of  $F_{min}$ . The smaller  $F_{min}$  the more we approach the result of the original method, but with a too large  $F_{min}$  we can create errors in the continuum as e. g. plotted in blue for  $F_{min} = 0.99$ . Since in the template we do not have any points with a flux even close to one in that region, the polynomial is not constrained and we obtain a useless continuum. Thus, the choice of  $F_{min}$  is always a compromise and one has to select it carefully for every spectrum.

Another way of circumventing the problem of picking a suitable template is to move the normalization into the analysis. The determination of stellar parameters is mostly done as some kind of cross-correlation with a given grid of spectra, so whenever we compare our observation with another model, we could normalize it again.

### 4.9.5 Maximum values in bins of spectrum

Unfortunately we do not always have a matching template spectrum at hand, so for those cases we need to find a way to determine continuum regions without using a template. One possible way for achieving this is illustrated in Fig. 4.23. First we split the spectrum into  $n_{bins}$  equally sized wavelength bins and calculate the mean of the  $M$  largest values in each bin, where  $M$  is defined as a given fraction  $f_{mean}$  of the total number  $N$  of points in each bin ( $M = f_{mean} \cdot N$ ). In practice this means sorting the points in each bin by value and then calculating the mean of the first  $M$  points. In Fig. 4.23, the regions containing those  $M$  points in every bin are marked in red, whereas the mean values are marked as blue crosses. As previously discussed for the other methods, we can now fit a polynomial to those points and divide the spectrum by the result.

Instead of fitting a polynomial to the points, at least for this method and the one using templates we can also use splines (see Section 4.4.2), which allow us get rid of one of the free parameters in the fit: the degree of the polynomial. Figure. 4.21(d) shows how the method just described performs when using splines instead of a polynomial. With this, there are only two free parameters left, i. e. the number of bins  $n_{bins}$  and the fraction of points  $f_{mean}$  to use for calculating the mean.

The fraction  $f_{mean}$  is mostly just a scaling factor, i. e. the smaller  $f_{mean}$ , the more flux we get in the estimated continuum. While for noise-free spectra this parameter is not very important, in case of existing noise it becomes quite critical, since a low value would then usually only take noisy values into account. A higher value on the other hand will smooth out the noise a little bit. Significantly more relevant is the number of bins  $n_{bins}$ : the more bins we have, the better we can follow the contour of a spectrum, but with too many points we push the continuum into broad absorption lines. This effect can be seen in the blue curve of Fig. 4.21(d), where we used  $n_{bins} = 100$ , which in the case of a *MUSE* spectrum produces bins that are only  $46.5 \text{ \AA}$  wide. Since for example the  $H\beta$  line at  $4861 \text{ \AA}$  is broader, the normalized spectrum will show a line depths that is smaller than in the original spectrum. A too small number for  $n_{bins}$  on the other hand will produce a continuum with too much flux, since in this case the estimated continuum points mostly depend on the slope of the spectrum. This effect can be seen well in the left plot of Fig. 4.23, where the red rectangles, marking the regions in which the mean is calculated, only include a few points at their blue and none at their red end due to the slope of the spectrum in this range.

### 4.9.6 Applying correction to both the model and the observation

The best way of counteracting the problems described above is to normalize both the observed and the model spectrum, since then both will be affected the same way. In Fig. 4.24 this has been done for our sample spectrum and the original one before applying the changes. As one can see, the residuals between the normalized observation and the normalized model are usually about 1%, therefore it is mainly caused by the noise we applied to our test spectrum with a signal-to-noise ratio of 100.

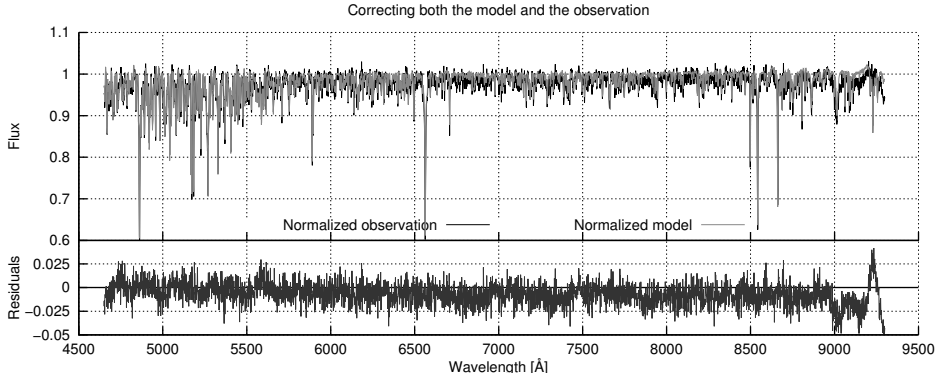


**Figure 4.24:** Observation (black) and model (red), both normalized in the same way, are shown at the top with the residuals plotted below, which are mostly caused by the noise in the observation ( $S/N=100$ ) and not by the normalization method.

### 4.9.7 Fitting continuum difference only

Although the methods described above for normalizing a spectrum to a continuum flux of one works for most spectra, it is not always a good idea to do so. For example for cooler stars with  $T_{\text{eff}} \lesssim 4000\text{K}$  we do not see a real continuum and correcting it could mean destroying important information, e. g. the depth of molecular absorption bands. Furthermore, in most cases we do not need a continuum corrected spectrum, but only the *continuum difference* between the observation and the model in form of a multiplicative polynomial. With that we can still use all the information from the absorption lines and forget about the general shape of the spectra. The free parameters for the continuum fit that have been found working with one spectrum, should correctly fit the continuum of all other spectra of a single observation, since the continuum difference should be about the same. Therefore we do not have to adjust those parameters for every new spectrum.

Before we start with this, it is important to consider the choice of polynomials used for the fit. As described in Section 4.9.3, a polynomial can be fitted to data using a linear least-squares fit, i. e. in principle we always try to find those coefficients  $p_k$  for a linear combination of polynomials  $P_k(x)$ , which best fits the data.

The previously used polynomials  $P_k(x) = x^k$  are not the best choice for creating a linear combination, since they are not orthogonal. In order to get a better set of polynomials  $P_k$ , we start with the definition for orthogonality and define  $P_k$  in the interval  $[-1, 1]$ . Therefore they have to fulfill the following equation:

$$\int_{-1}^1 P_n(x)P_m(x)dx = 0 \quad \forall m, n \in \mathbb{N}_0 \quad \text{with} \quad m \neq n. \quad (4.37)$$

Using the Gram-Schmidt process for orthonormalizing vectors and the boundary condition  $P_k(1) = 1$  we get the *Legendre* polynomials, which are the solutions for Legen-

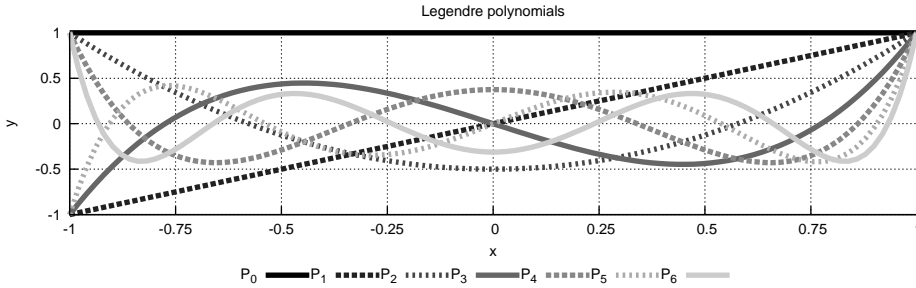


Figure 4.25: Legendre polynomials  $P_0$  to  $P_6$ .

dre's differential equation. They can also be expressed using Rodrigues' formula:

$$P_k(x) = \frac{1}{2^k k!} \frac{d^k}{dx^k} \left[ (x^2 - 1)^k \right]. \quad (4.38)$$

In Fig. 4.25 the first seven Legendre polynomials are plotted, which are defined as:

$$P_0(x) = 1, \quad (4.39)$$

$$P_1(x) = x, \quad (4.40)$$

$$P_2(x) = 1/2 \cdot (3x^2 - 1), \quad (4.41)$$

$$P_3(x) = 1/2 \cdot (5x^3 - 3x), \quad (4.42)$$

$$P_4(x) = 1/8 \cdot (35x^4 - 30x^2 + 3), \quad (4.43)$$

$$P_5(x) = 1/8 \cdot (63x^5 - 70x^3 + 15x), \quad (4.44)$$

$$P_6(x) = 1/16 \cdot (231x^6 - 315x^4 + 105x^2 - 5). \quad (4.45)$$

Since the Legendre polynomials as we just defined them are only defined in the range  $[-1, 1]$ , we need to apply a linear coordinate transform, i. e. we have to stretch it to the wavelength range  $[\lambda_{start}, \lambda_{end}]$  of the spectrum we are working on:

$$P_{\lambda,k}(\lambda) = P_k \left( \frac{\lambda - 0.5 \cdot (\lambda_{start} + \lambda_{end})}{0.5 \cdot (\lambda_{end} - \lambda_{start})} \right). \quad (4.46)$$

With this new set of polynomials, we can apply the same method described above when using a template, which however can now be an arbitrary model spectrum that does not necessarily need to be continuum-free as the Synspec spectra used before. Since we are only fitting continuum differences now, we cannot do the correction independently from further analyses, but need to combine both. This will be discussed in detail in Section 4.10.

What we want to find is a transformation from our model spectrum  $m$  to the observed spectrum  $s$ , i. e. a matrix  $A$  that fulfills  $Am = s$ . The matrix consists of weighted Legendre polynomials up to the the desired degree  $d$ , which are sampled accordingly

to the two spectra on wavelength points  $\lambda_i, i = 1 \dots n$ , where  $n$  is the number of points in the spectra:

$$A = \begin{pmatrix} p_0 P_{\lambda,0}(\lambda_1) & p_0 P_{\lambda,0}(\lambda_2) & \cdots & p_0 P_{\lambda,0}(\lambda_n) \\ p_1 P_{\lambda,1}(\lambda_1) & p_1 P_{\lambda,1}(\lambda_2) & \cdots & p_1 P_{\lambda,1}(\lambda_n) \\ \vdots & \vdots & \ddots & \vdots \\ p_d P_{\lambda,d}(\lambda_1) & p_d P_{\lambda,d}(\lambda_2) & \cdots & p_d P_{\lambda,d}(\lambda_n) \end{pmatrix} \quad (4.47)$$

$$(4.48)$$

$$= \begin{pmatrix} P_{\lambda,0}(\lambda_1) & P_{\lambda,0}(\lambda_2) & \cdots & P_{\lambda,0}(\lambda_n) \\ P_{\lambda,1}(\lambda_1) & P_{\lambda,1}(\lambda_2) & \cdots & P_{\lambda,1}(\lambda_n) \\ \vdots & \vdots & \ddots & \vdots \\ P_{\lambda,d}(\lambda_1) & P_{\lambda,d}(\lambda_2) & \cdots & P_{\lambda,d}(\lambda_n) \end{pmatrix} \cdot \begin{pmatrix} p_0 \\ p_1 \\ \vdots \\ p_d \end{pmatrix}. \quad (4.49)$$

Therefore we can write  $Am = s$  as:

$$\underbrace{\begin{pmatrix} P_{\lambda,0}(\lambda_1) & P_{\lambda,0}(\lambda_2) & \cdots & P_{\lambda,0}(\lambda_n) \\ P_{\lambda,1}(\lambda_1) & P_{\lambda,1}(\lambda_2) & \cdots & P_{\lambda,1}(\lambda_n) \\ \vdots & \vdots & \ddots & \vdots \\ P_{\lambda,d}(\lambda_1) & P_{\lambda,d}(\lambda_2) & \cdots & P_{\lambda,d}(\lambda_n) \end{pmatrix}}_B \cdot \underbrace{\begin{pmatrix} m(\lambda_1) \\ m(\lambda_2) \\ \vdots \\ m(\lambda_n) \end{pmatrix}}_p \cdot \underbrace{\begin{pmatrix} p_0 \\ p_1 \\ \vdots \\ p_d \end{pmatrix}}_p = \underbrace{\begin{pmatrix} s(\lambda_1) \\ s(\lambda_2) \\ \vdots \\ s(\lambda_n) \end{pmatrix}}_s, \quad (4.50)$$

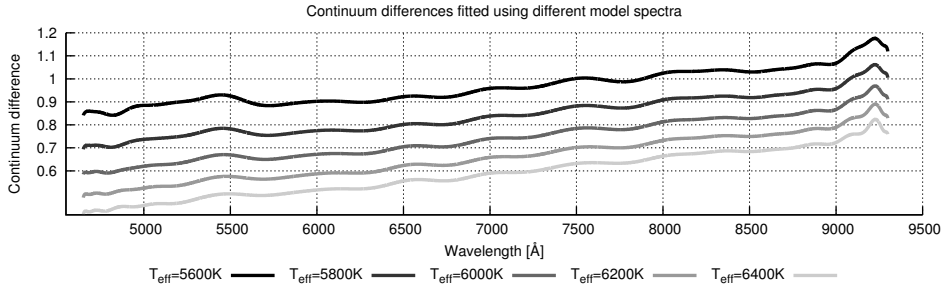
which gives us a set of linear equations  $Bp = s$  with coefficients  $p = (p_0, \dots, p_d)$ . For solving this, functions are available in all major programming languages, e. g. by using external libraries like GSL for C++.

In Fig. 4.26(a) the continuum differences are calculated between our sample spectrum (see Fig. 4.17) and five different model spectra with  $T_{\text{eff}} \in [5600\text{K}, 5800\text{K}, 6000\text{K}, 6200\text{K}, 6400\text{K}]$ ,  $\log(g) = 4.5$  and solar element abundances. Legendre polynomials up to a degree of forty were used for the fit. Most prominent in the plot are the offsets between the continuum differences caused by the different continuum fluxes in the model spectra, but we also see minor changes between them.

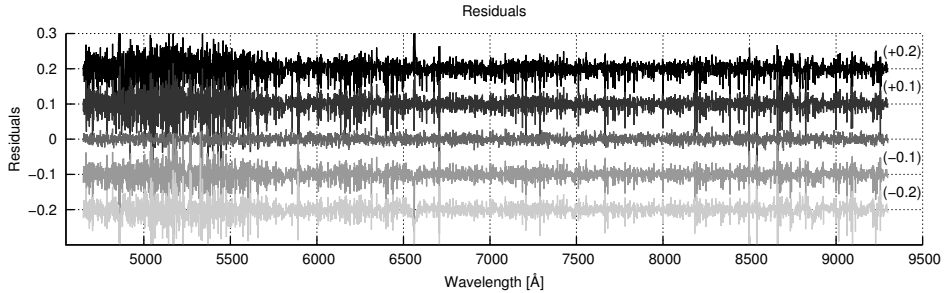
Now we can multiply the continuum differences with the corresponding model spectrum and have a look at the residuals of the results with our sample spectrum (see Fig. 4.26(b)). Using the model with  $T_{\text{eff}} = 6000\text{K}$  we see a perfect fit, since the parameters of that one match those of our sample spectrum exactly. The remaining residuals are caused only by the noise that we added. The further we move away from this temperature, the stronger the residuals become. Thus, applying a continuum difference never results in a completely wrong model spectrum that looks like the observed one.

## 4.10 Fitting stellar parameters

All the parts discussed in this Chapter can now be assembled in order to implement a fitting routine for stellar parameters. Since finding a good method was an iterative



(a) Estimated continuum differences for our sample spectrum with five different model spectra.



(b) Residuals of our sample spectrum and five different model spectra that have been multiplied with the corresponding continuum difference from Fig. 4.26(a). The residuals are plotted with offsets, which are given in the legend.

**Figure 4.26:** Estimating the continuum difference (i. e. the multiplicative polynomial that transforms one continuum into another) using model spectra with incorrect stellar parameters.

progress, several of them had to be evaluated before the decision was made about which one to use. In the following, two different approaches will be presented, but only the second one has been used for all the tests that will be discussed in Chapter 5.

### 4.10.1 Method 1

The first method was introduced by Kirby et al. (2009). Before they started the analysis of their medium-resolution spectra ( $R \approx 6\,500$ ) covering the wavelength range between  $6\,400$  and  $9\,000$  Å, they had to normalize them using a template with a flat continuum, similar to the method discussed in Section 4.9.4. Then they determined the radial velocities by cross-correlating the observed spectra with a synthetic spectrum with  $T_{\text{eff}}=4\,500$  K,  $\log(g)=1.5$ ,  $[Fe/H]=-1.5$  and  $[\alpha/Fe]=+0.2$  in the spectral region around the Ca II triplet ( $8\,450 \text{ Å} < \lambda < 8\,700 \text{ Å}$ ).

They estimated the atmospheric parameters ( $T_{\text{eff}}$ ,  $\log(g)$  and  $[Fe/H]$ ) photometrically (see Section 4.3) and the result for the surface gravity was kept, while the values for effective temperature and metallicity were refined spectroscopically. For doing this,



they determined the regions in the spectra sensitive to a change in Fe abundance (and for some  $\alpha$  elements, see Section 4.11). A Levenberg-Marquardt optimization against a grid of synthetic spectra was done to determine  $T_{\text{eff}}$  and  $[Fe/H]$  from those regions only. Then the fit was repeated for  $[\alpha/Fe]$  as free parameter in regions susceptible to changes in  $\alpha$  abundance, while fixing  $T_{\text{eff}}$ ,  $\log(g)$  and  $[Fe/H]$ . Finally, the observed spectra were normalized again and the metallicity alone was determined again with the new value for  $[\alpha/Fe]$ , in order to compensate for changes in opacity caused by a changed  $\alpha$  element abundance. They also fitted the abundances of single  $\alpha$  element abundance (Mg, Si, Ca and Ti), which we adopted for our needs (see Section 4.11).

Although this method seems to work fairly well, the need e. g. for normalizing the spectra is something we would like to avoid, following the discussion in Section 4.9. Furthermore, we could introduce systematic errors by cross-correlating with a non-matching model for the determination of the radial velocity. Fixing (or even just loosely constraining) the surface gravity to a value obtained by photometry is an interesting option that we have used for some of the tests in Chapter 5. Fitting  $\log(g)$  using spectroscopy only can be tricky, if the spectral resolution is not known exactly, as will be discussed in Section 5.4.

## 4.10.2 Method 2

The method that we have decided to use has been presented by Koleva et al. (2009). All atmospheric parameters and the LOSVD are determined simultaneously using a weighted non-linear least squares minimization<sup>1</sup> against our new library of synthetic *PHOENIX* spectra (see Chapter 3). Therefore, the fit is done with usually six free parameters:  $T_{\text{eff}}$ ,  $\log(g)$ ,  $[Fe/H]$ ,  $[\alpha/Fe]$ ,  $v_{\text{rad}}$  and line broadening  $\sigma$  (which is often fixed, leaving five free parameters).

In each iteration of the Levenberg-Marquardt optimization, a model spectrum with the given atmospheric parameters is interpolated from the grid of *PHOENIX* spectra (see Section 4.4.2). If a line spread function is defined, the model is convolved accordingly (see Section 4.7), before the LOSVD is being applied to it (see Section 4.6). At this point, the higher sampling of the model is no longer required and therefore it is rebinned to the wavelength grid of the observed spectrum (see Section 4.5). If the fit contains multiple components (Section 4.8), they are now weighted against each other and combined – a single model only gets scaled so that its mean flux is equal to that of the observed spectrum. Finally, the continuum difference between model and observation is determined and applied (see Section 4.9.7), before the resulting model spectrum is returned to the Levenberg-Marquardt algorithm.

A flow chart illustrating the the whole fitting process is shown in Fig. 4.27 as we use it and as it is implemented as a tool called *spexxyFitParams* (see Section C.9).

<sup>1</sup>Currently we are using the Levenberg-Marquardt implementation from the ALGLIB (<http://www.alglib.net/>) by Sergey Bochkanov and Vladimir Bystritsky, which is free-to-use for academic purposes. Unfortunately, in its current version (3.5.0, but we use 3.4.0), it does not output a covariance matrix for a finished optimization, so we can not give errors for the results. Until now, we did not have time to implement that feature by ourselves.

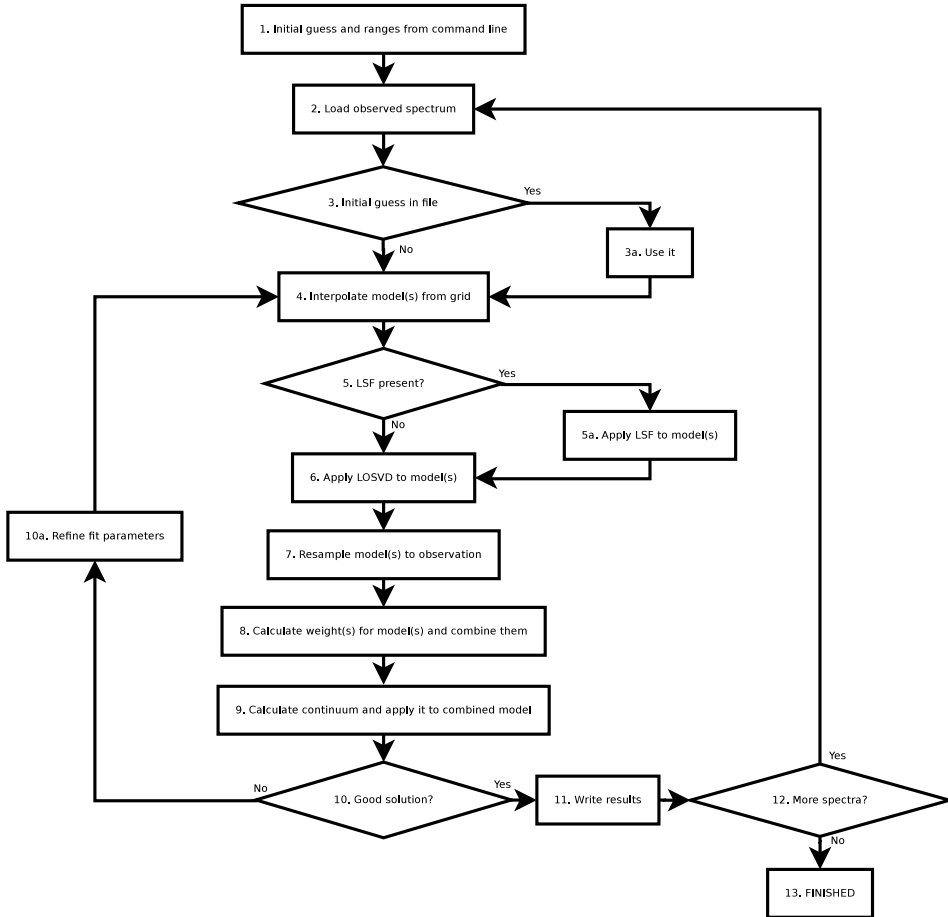
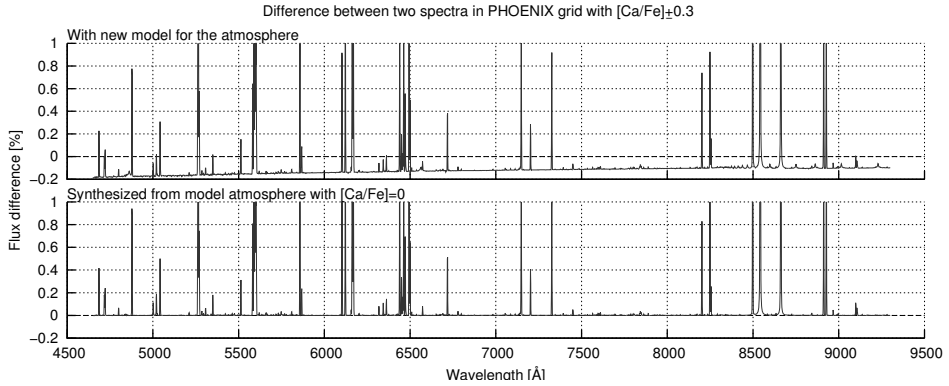


Figure 4.27: Flow chart illustrating the complete fitting process.

## 4.11 Fitting single alpha element abundances

As demonstrated by Kirby et al. (2008, 2009), accurate abundances for several alpha elements (Mg, Si, Ca, Ti) can be measured from medium-resolution spectra ( $R \sim 6500$ ). In order to find the best synthetic spectra for matching the observations, they took only those spectral regions that are most sensitive to changes in the abundances of the single elements into account for the fit. The mask for Mg was created by comparing two synthetic spectra with  $T_{\text{eff}} = 4000 \text{ K}$ ,  $\log(g) = 1.5$ ,  $[Fe/H] = -1.5$  and  $[Mg/Fe] = \pm 0.3$  and including only those wavelengths, at which both differ by more than 0.5%. This was repeated for spectra with effective temperatures of 5000 K, 6000 K, 7000 K and 8000 K, including all new regions in the determination of the abundance that show large enough variations. The same procedure was used for creating the masks for Si, Ca



**Figure 4.28:** Difference between two PHOENIX spectra with  $T_{\text{eff}} = 6000 \text{ K}$ ,  $\log(g) = 2.0$ ,  $[Fe/H] = -1.5$  and  $[Ca/Fe] = \pm 0.3$ . Plotted for spectra, for which a new model atmosphere has been calculated (top), and for spectra that are synthesized from existing models with  $[Ca/Fe]=0$  (bottom). Both plots have been cut off at  $\pm 1\%$ .

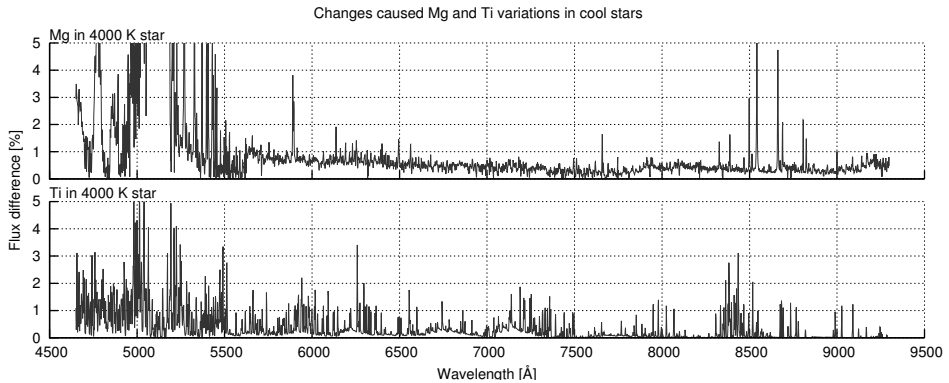


**Figure 4.29:** Same plots as in Fig. 4.28, but for variations of Mg and Ti in 4000 K stars.

and Ti. Kirby et al. (2009) claimed that for the spectral resolution of their spectra the regions for the four alpha elements did not overlap. Thus, they were able to simply use the variation of  $[\alpha/Fe]$  in their grid of synthetic spectra together with those masks for fitting the abundances of Mg, Si, Ca and Ti.

When trying to use this method with our *PHOENIX* spectra in *MUSE* resolution, we encounter a couple of problems. First, for all spectra we calculated new model atmospheres. Thus, by changing even the abundance of a single element, we changed the total opacity of the atmosphere. In the upper plot of Fig. 4.28 this is shown for the example of Ca: by increasing the abundance of that element, all the Ca lines became deeper, i. e. we get less flux from those regions. But that flux has to come out somewhere, so what we see is a change in continuum flux, and therefore two spectra with  $[Ca/Fe] \pm 0.3$  do not only differ in the regions dominated by Ca lines, but over the

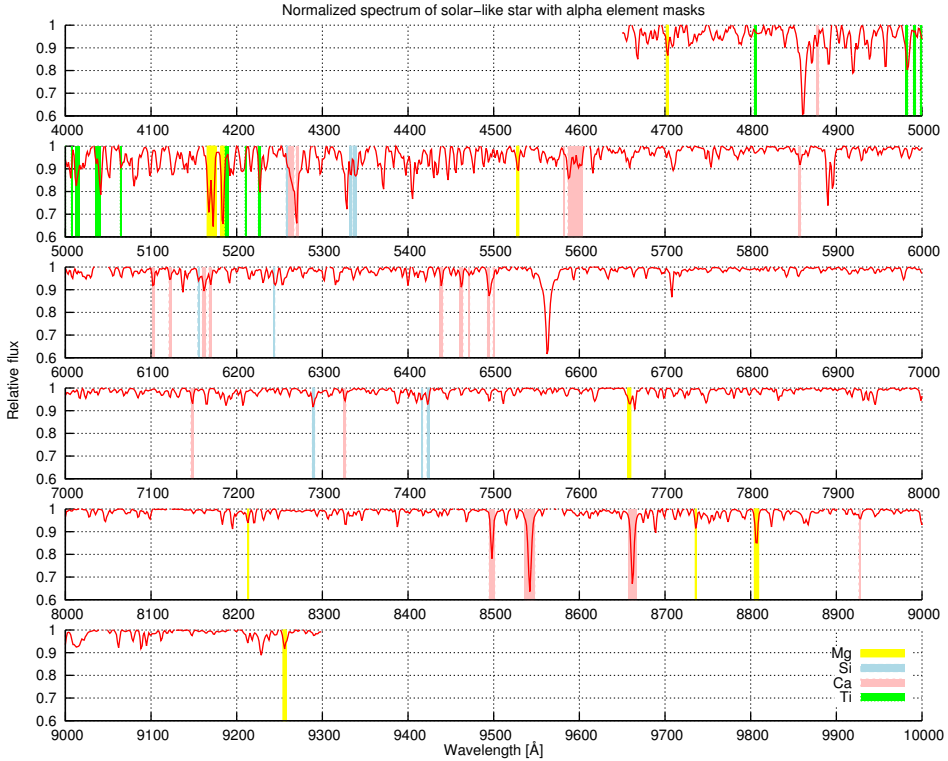


**Figure 4.30:** Normalized spectrum of a star with  $T_{\text{eff}}=6000\text{ K}$ ,  $\log(g)=5.0$  and  $[\text{Fe}/\text{H}]$  with alpha element masks.

whole wavelength range. We solved this problem, by synthesizing the required spectra again *without* calculating a new atmosphere (see lower plot of Fig. 4.28). Unfortunately, *PHOENIX* cannot synthesize a spectrum without any recalculations of the atmospheric models. Thus, the results are not perfect, but acceptable for most spectra.

Another problem when fitting cool stars seems to be caused by line density in the MOOG spectra used by Kirby et al. (2009), which is significantly smaller than in our *PHOENIX* spectra. Figure 4.29 shows the difference spectra for both  $[\text{Mg}/\text{Fe}]\pm 0.3$  and  $[\text{Ti}/\text{Fe}]\pm 0.3$  for a 4000 K star. Obviously, especially at the blue end of the spectra, the variation in those two elements cause a significant difference in flux. Thus, the fit regions for the alpha elements on spectra of cool stars will overlap massively, making it impossible to fit them independently. Therefore we suggest that the method in this form is applicable for stars with  $T_{\text{eff}}\gtrsim 5000\text{ K}$  only.

Even for hotter stars, with the spectral resolution of *MUSE*, we observe an overlap of the fitting regions. Therefore, instead of using the method discussed above for determining the fitting regions, we decided to create the masks from matching templates only, i. e. for creating the Ca mask for a star with  $T_{\text{eff}}=6000\text{ K}$  and  $\log(g)=5.0$ , we use

synthetic spectra with those parameters and  $[Fe/H] = -1.5$ ,  $[Ca/Fe] = \pm 0.3$  only. By doing this, we can avoid overlapping regions completely for most stars. However, this reduces the number of pixels used in the fitting process significantly: for the spectrum mentioned above with 3577 pixels, only 28 are used for the abundance determination of Mg, and 14 for Si, 69 for Ca and 23 for Si respectively (see Fig. 4.30). In Section 5.8 we will see that this seems to be enough.

For the actual fit we used the same methods as described before for determining the stellar parameters. *spexyFitElements* (see Section C.7) loads all the results from a previous run of *spexyFitParams* and automatically creates the masks. In the fit, the stellar parameters and the LOSVD are kept fixed, while the alpha element abundance is fitted as well as the continuum. The latter is necessary in order to compensate variations of the continuum flux for different alpha element abundances. This is done for all masks in order to determine the abundances for the single elements.



# Chapter 5

## Results

In this Chapter, results from tests conducted using the spectra from our new *PHOENIX* library (see Chapter 3) will be presented as well as those from our first *dry run*, which was intended to simulate real *MUSE* data as realistically as possible. Unfortunately, we encountered some problems with the *PHOENIX* spectra, so the analysis of Miles and PMAS spectra, which will be discussed afterwards, has been done using other stellar spectral libraries.

### 5.1 Quality of fits varying with temperature

Since our method for fitting stellar parameters is based on absorption lines, it is a valid assumption that the quality of the fit depends strongly on the number of lines in the observed spectrum and therefore on the effective temperature of the star – in atmospheres of hotter stars less absorption lines are present than in cooler stars.

For testing this, we simulated spectra with a varying effective temperature  $T_{\text{eff}}$ , a surface gravity of  $\log(g)=4.5$  and solar element abundances. The spectra were convolved to *MUSE* resolution and noise ( $S/N=100$ ) was added. For every  $T_{\text{eff}}$ , ten spectra were created and fitted and the means and standard deviations of the results were calculated for each parameter. While the number is quite low for significant statistics, at least it is enough to identify the general trend.

As a result, we found the differences between the calculated mean values and the input parameters to be insignificantly small ( $\Delta T_{\text{eff}} \lesssim 4\text{ K}$ ,  $\Delta \log(g) \lesssim 0.01$ ,  $\Delta [Fe/H] \lesssim 0.005$  and  $\Delta v_{\text{rad}} \lesssim 0.2\text{ km/s}$ ) over all temperatures. In Fig. 5.1, the standard deviations are plotted for the four parameters  $T_{\text{eff}}$ ,  $\log(g)$ ,  $[Fe/H]$  and  $v_{\text{rad}}$ . As expected, they increase with temperature, but are still within the accuracy limits we are aiming for. Thus, we can conclude that the quality of the fits does not depend on the temperature of the star and therefore on the number of lines in the spectrum, at least in the tested range.

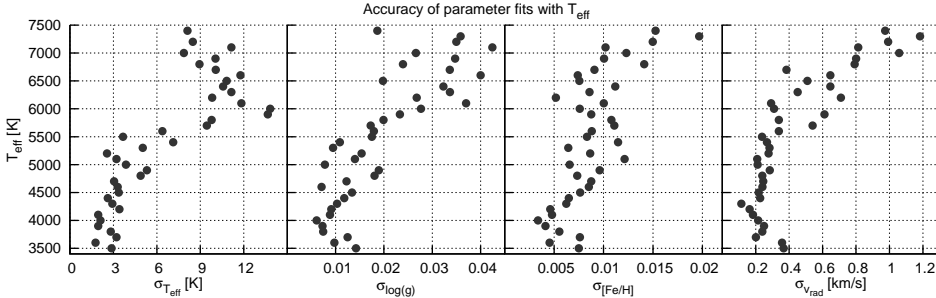


**Figure 5.1:** Accuracy of parameter fits for different temperatures. Plotted are the standard deviations of  $T_{\text{eff}}$ ,  $\log(g)$ ,  $[Fe/H]$  and  $v_{\text{rad}}$  for multiple fits of spectra with varying effective temperature.

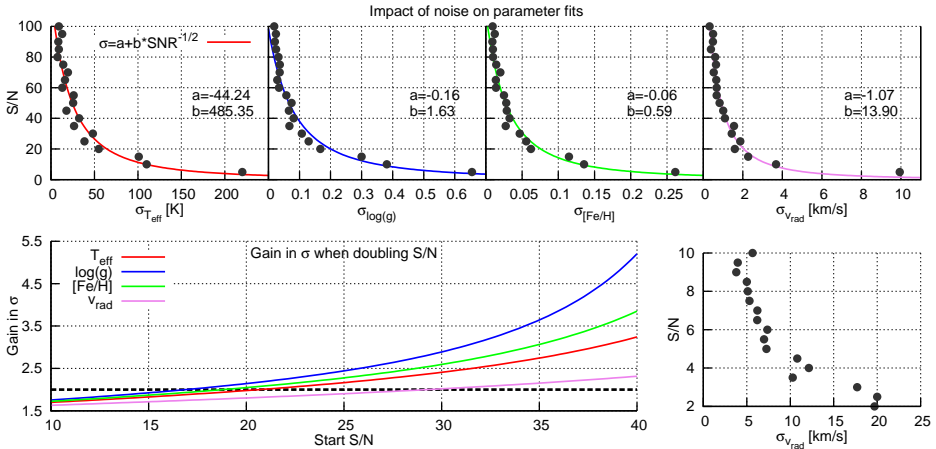


**Figure 5.2:** On top, the impact of noise on the accuracy of the four fitted parameters  $T_{\text{eff}}$ ,  $\log(g)$ ,  $[Fe/H]$  and  $v_{\text{rad}}$  is shown. The over-plotted coloured curves are fits of a function  $\sigma = a + b/\sqrt{S/N}$  to the data. On the lower right, some more values for  $v_{\text{rad}}$  are plotted for lower values of  $S/N$ . On the lower left, it is illustrated how the accuracies in all parameters change, when doubling the  $S/N$  ratio, e.g. by increasing the exposure by a factor of four.

## 5.2 Impact of noise on fitting parameters

Noise is an intrinsic but unwanted ingredient of astronomical imaging. During the photographic age it was mainly caused by cosmic rays and the granularity of the photographic film. For the CCDs used today, there is thermal noise, caused by electrons generated by heat (due to this, scientific CCDs are always cooled to low temperatures), readout noise, introduced during the conversion from an analogue to a digital signal during readout of the CCD, and the intrinsic Poisson noise of any photon counting device. There are ways of correcting for large-scale variations caused by thermal and readout noise using so-called DARK and BIAS frames, but due to the random behaviour of noise this method cannot remove small-scale fluctuations entirely.



The strength of noise is usually measured by the *signal-to-noise ratio*  $S/N$ . This means, if we observe a signal, which is intrinsically constant with a value of  $A$ , and we see fluctuations in the signal with a standard deviation of  $\sigma$ , the signal to noise ratio is  $A/\sigma$ . Typical values for  $S/N$  are about 50, which means that on a normalized spectrum we would see a superimposed random variation with a standard deviation of  $\sigma = 1/50$ .

In Fig. 5.2, the impact of noise on the accuracy of the parameter fits is shown. At each  $S/N$  level between 5 and 100, twenty spectra were simulated and fitted. While the mean value of the results is close to the input parameters (i. e. we see no systematic errors introduced by noise), we do see a strong variation in the standard deviation as shown in the upper plots for the four fitted parameters  $T_{\text{eff}}$ ,  $\log(g)$ ,  $[Fe/H]$  and  $v_{\text{rad}}$ . Since the radial velocity is the only value for which we want to get a good estimate with a single *MUSE* exposure, on the lower right some more standard deviations are shown for lower signal-to-noise ratios. For  $S/N < 5$  we start getting significant shifts in the mean values.

In astronomical imaging, we expect the signal-to-noise ratio to drop by a factor of  $\sqrt{2}$  when doubling the exposure time  $T$ , i. e. we see the  $S/N$  changing with exposure time as  $1/\sqrt{T}$ . Similarly, we fitted a function  $\sigma = a + b/\sqrt{S/N}$  to the results for each parameter with the resulting values for  $a$  and  $b$  printed in each plot. A value of  $a \neq 0$  as obtained for all parameters causes the gain in  $\sigma$  to depend on the initial  $S/N$ , which is illustrated in the lower plot of Fig. 5.2. For example, when starting at  $S/N=30$  we can double the signal-to-noise ratio by increasing the exposure time by a factor of 4 (since  $\sqrt{4} = 2$ , see above), which would improve the accuracy of the fitted value for  $v_{\text{rad}}$  by a factor of two or even a factor of three for  $\log(g)$  (see Fig. 5.2). Of course, this is also true for decreasing  $S/N$ , which degrades the accuracy faster than a strict inverse square-root law would suggest.

Altogether, the quality of the fitted parameters depends highly on the signal-to-noise ratio of the observed spectra, which means that every increase in  $S/N$  is precious. Thus, exposure times should be as long as possible without over-exposing too many pixels on the CCD and we need to optimize our observation strategy accordingly.

## 5.3 Line broadening

With our methods, we can not only measure a radial velocity shift in the spectra, but also a line broadening. This has been done for simulated *MUSE* spectra, which have been convolved with a Gaussian with  $\sigma = 50$  km/h. The left plot of Fig. 5.3 shows the results for several signal-to-noise ratios. At least for  $S/N > 20$ , we can fit  $\sigma$  well, but even for very low noise levels, we see an offset in the determined line broadening, which is caused by the slight under-sampling of *MUSE* spectra. In the right plot, the influence of the sampling on the quality of the results is shown: the better we sample the spectra, the closer we get to the actual line broadening of 50 km/h.

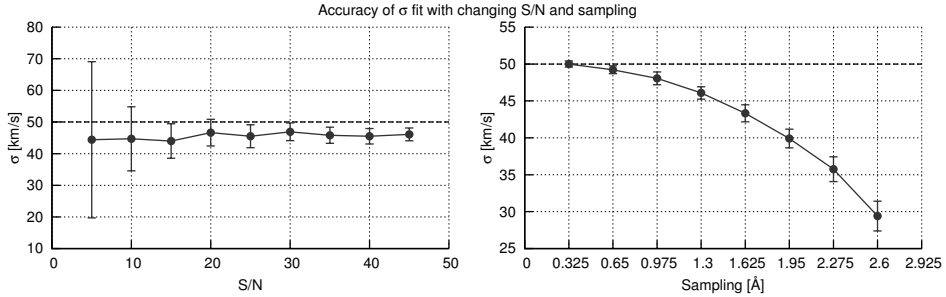


**Figure 5.3:** Accuracy of line broadening fits shown on simulated MUSE spectra. On the left, they have been sampled to the actual  $1.3\text{Å}$  of MUSE and the accuracy of the fits for the line broadening  $\sigma$  is plotted for increasing signal-to-noise ratios. On the right, no noise was added, but we varied the sampling rate.

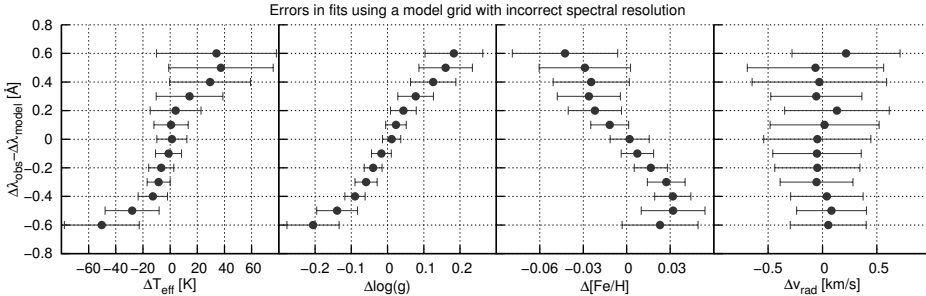


**Figure 5.4:** Impact of incorrect spectral resolution of model spectra when fitting an observed spectrum. Plotted are the deviations of the fits from the input parameters  $T_{\text{eff}}$ ,  $\log(g)$ ,  $[\text{Fe}/\text{H}]$  and  $v_{\text{rad}}$  for several differences in resolution between observation and models ( $\Delta\lambda_{\text{obs}} - \Delta\lambda_{\text{model}}$ ).

## 5.4 Resolution of model spectra

As discussed in Section 4.10.2, when fitting an observed spectrum, we can either have the line broadening  $\sigma$  as a free parameter and let the fit routine find the best value for it, or we assume that we know the spectral resolution of the observed spectrum exactly and fix  $\sigma$  to this value, which may be zero in case the model spectra are convolved to the exact resolution of the observation. The latter case sometimes is preferable, since it is usually faster (i. e. less parameters to fit).

It is important to know, whether we introduce systematic errors, if the spectral resolution of the models does not match the resolution of the observed spectrum. For testing this, we used a spectrum of a solar-like star ( $T_{\text{eff}}=5778\text{K}$ ,  $\log(g)=4.44$ ), convolved it to a given resolution in the range of  $\Delta\lambda = 2.0\dots3.2\text{Å}$  and added some noise ( $S/N=100$ ). Then we tried to fit it using a *PHOENIX* grid, in which the spectra are convolved to  $2.6\text{Å}$ .

The results are shown in Fig. 5.4, where the quality of the fits for the four parameters  $T_{\text{eff}}$ ,  $\log(g)$ ,  $[\text{Fe}/\text{H}]$  and  $v_{\text{rad}}$  is plotted. As we can see, systematic errors do occur

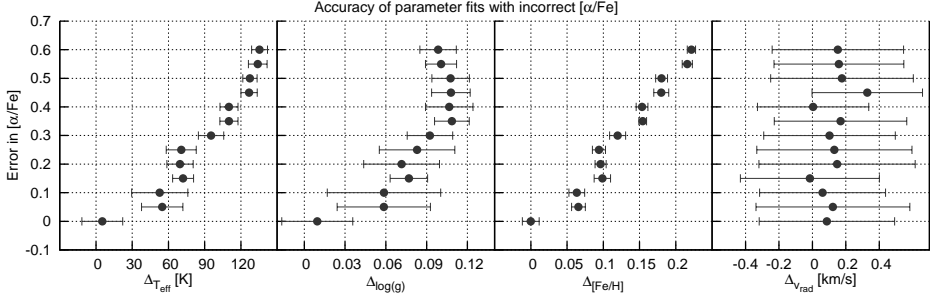


Figure 5.5: Fitting stellar parameters with an alpha element abundance fixed to zero.

for  $T_{\text{eff}}$  and  $[Fe/H]$ , when using incorrect spectral resolutions, but they are quite small – the effect on  $\log(g)$  is quite significant, which can be explained by the fact that both resolution and surface gravity affect the width of the lines. For the radial velocities, we do not see a systematic error at all, which was expected, since the positions of the absorption lines do not change when convolving a spectrum.

After all, when trying to fit an observed spectrum with a fixed resolution, we need to know it exactly. Leaving the line broadening  $\sigma$  as a free parameter in the fit can solve this problem – unless the spectral resolution changes with wavelength. In that case, we need to estimate the LSF precisely (see Section 4.7) and apply it to the model spectra, before comparing them with the observed spectrum.

## 5.5 Neglecting the alpha element abundance

In all previous tests, we neglected the alpha element abundance and fixed it to zero, which was no problem, since the spectra had  $[\alpha/Fe]=0$ . In real observations, especially of globular clusters, this will not be the case. Nevertheless, there is at least one good reason to continue the accustomed practice even for those spectra: speed. Including the alpha element abundance as free parameter in the fits not only adds another dimensions to the minimization routine, but also makes the interpolation of spectra from the grid more time-consuming.

In Fig. 5.5 spectra with a varying alpha element abundance were fitted while fixing the model spectra at  $[\alpha/Fe]=0$ . The radial velocities of course are not affected at all and the rise of  $[Fe/H]$  was expected, since the minimization tries to compensate for the underestimated alpha element abundance with an increase of the overall metallicity. However, we also see an increasing systematic error for both  $T_{\text{eff}}$  and  $\log(g)$ , which cannot be explained that easily. Presumably, the underestimation of the alpha element abundance mildly flattens some of the deeper absorption lines like those of the Ca II triplet, which overall looks like an increase of surface gravity. And with the systematic error in  $\log(g)$ , we also get an error in  $T_{\text{eff}}$ .

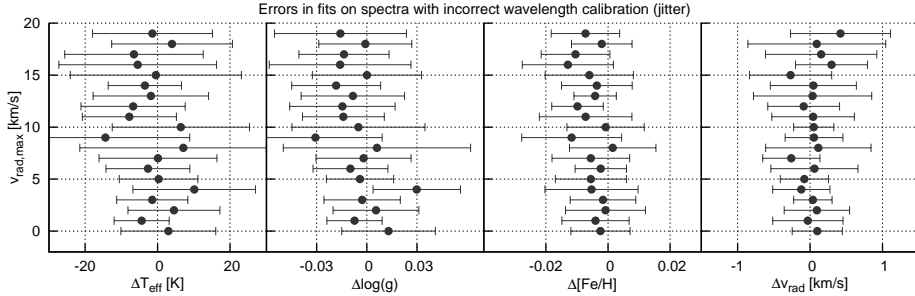


Figure 5.6: Accuracy of parameter fits with a random jitter in wavelengths caused by an incorrect calibration.

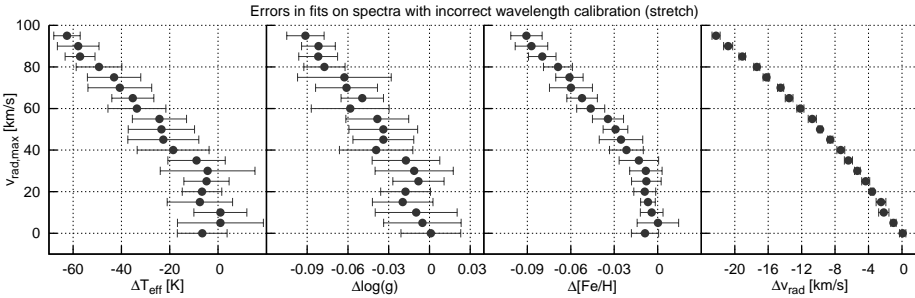


Figure 5.7: Accuracy of parameter fits with a stretched wavelength grid.

## 5.6 Problems with the calibration

Some problems that we might face during the analysis of *MUSE* spectra have nothing to do with the observed target at all, but are introduced artificially. Even before the spectra are extracted from the cube, the data taken on the CCDs of the detector has to undergo several steps, particularly the wavelength and the flux calibration.

### 5.6.1 Wavelength calibration

For *MUSE*, wavelength calibration will be done using a calibration lamp. The positions of the emission lines can only be measured to a given accuracy, so evidently a *jitter* is imposed on the wavelengths with an amplitude  $A$  usually well below the spectral resolution of the spectrograph, which for *MUSE* means that we expect an accuracy of  $A \ll 168$  km/s in the blue and  $A \ll 84$  km/s in the red. Assuming that we can determine a radial velocity accurate to 0.1 px, Fig. 5.6 shows the effect on this jitter for velocities  $< 20$  km/s. For this test, a solar spectrum was created and a random offset in the range  $[-v_{\text{rad,max}}, v_{\text{rad,max}}]$  was added to the wavelength of each point. Finally, the spectrum was resampled to a fixed step size again. The plots show the resulting means and standard deviations for  $T_{\text{eff}}$ ,  $\log(g)$ ,  $[Fe/H]$  and  $v_{\text{rad}}$ . Obviously, a random jitter in

the wavelength calibration has no effect at all on the results.

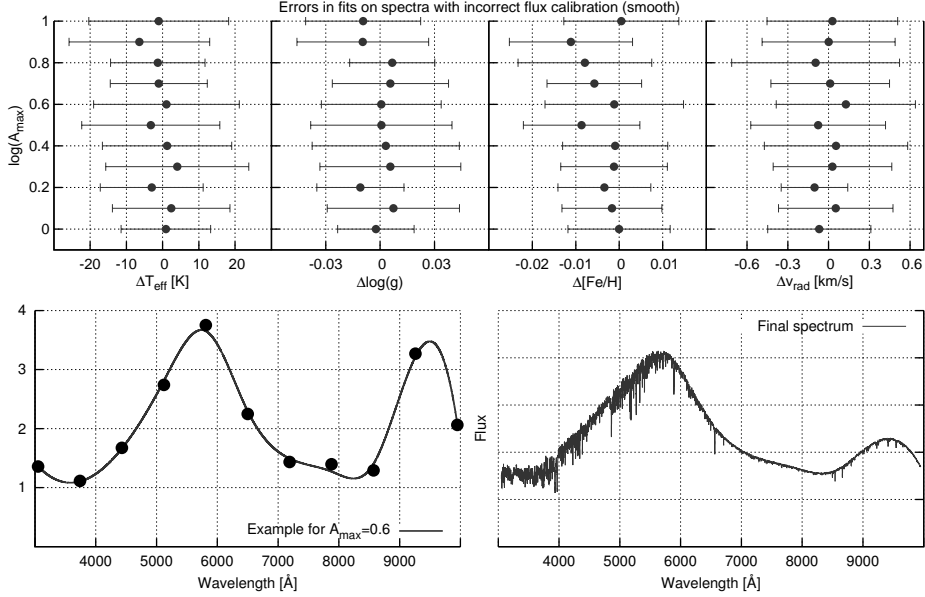
Depending on the arc lamp used for the calibration, there can also be broad regions in the spectrum without emission lines. The interpolation in those ranges can produce a jitter as discussed above, but also a stretch, where an initial error is increasing up to a certain point. We simulated a rather extreme case, for which we fix the central wavelength to its real value and stretch the spectrum in both directions, i. e. increase the step size by a constant offset until we reach a maximum error  $\nu_{\text{rad,max}}$  at the edges.

Figure 5.7 shows the effects of this stretch for velocities up to  $\nu_{\text{rad,max}} = 100$  km/s, which are roughly 2 px at the blue end of a *MUSE* spectrum and 1 px at the red end. We see that the radial velocity is affected immediately and shifts towards lower values, which is caused by the higher number of spectral lines in the blue, i. e. the fit for radial velocity is more sensitive in the blue than in the red. For  $\nu_{\text{rad,max}} \gtrsim 30$  km/s, we also see a drift in the fitted values for the other parameters, which we would like to avoid. Therefore we need the wavelength calibration to produce an accuracy of better than  $\sim 30$  km/s for each wavelength point. Serendipitously, in real observations a problem like this can be identified easily by comparing radial velocities at the blue end of the spectra with those at the red end.

### 5.6.2 Flux calibration

The flux calibration is usually done by observing a *standard star*, for which the spectrum is well known. This can be compared to a calibrated spectrum of the same star, which yields a correction curve that can be applied to all further observed spectra for calibrating their fluxes. The problems that can occur are usually large-scale and smooth, so we simulated an error in flux calibration by putting eleven equally spaced points in a spectrum with a value of  $A < 10^{A_{\text{max}}}$  each. A spline was used for a smooth interpolation and a stellar spectrum was multiplied with the result in order to produce an incorrect flux calibration (see lower two plots in Fig. 5.8). By varying the maximum amplitude  $A_{\text{max}}$ , we simulated several strengths of the error. As shown in the upper plot of Fig. 5.8, this has no effect whatsoever on the results, if the order of Legendre polynomials used for fitting the continuum is high enough.

To test a more extreme case, we added a non-continuous step to the spectrum and varied its size. In the lower plot of Fig. 5.9 an example is shown together with the results in the upper plot. Obviously, a step in the spectrum has a significant effect on the results, which even by increasing the order of Legendre polynomials used for fitting the continuum can only be eliminated up to a certain point. Since an error like this would affect all spectra from an observation, it would be easier to remove the step manually before starting the analysis.



**Figure 5.8:** Systematic errors produced by an incorrect flux calibration. The maximum value of the change in flux is given by  $A_{\max}$  as  $10^{A_{\max}}$ . Below an example is shown for  $A_{\max} = 0.6$ , i. e. a maximum change of  $\sim 4$ . On the left the method for creating a random change in flux is shown as described in the text. On the right the sample spectrum multiplied with this change is plotted.

## 5.7 Binaries

Binary stars can appear in observed spectra in two ways. If the components are almost of the same spectral type and equally bright, the absorption lines in the spectrum appear broadened with a strength depending on the velocity difference  $\Delta v$  between both stars. For high velocities or high-resolution spectra, we even see a split in the lines. With the resolution of *MUSE*, in order to see such split in the  $H_{\alpha}$  line, we would need a  $\Delta v$  larger than the spectral resolution, i. e.

$$\Delta v > c \left( \frac{\lambda_{H_{\alpha}} + 2.6 \text{ \AA}}{\lambda_{H_{\alpha}}} - 1 \right) \approx 118 \text{ km/s.} \quad (5.1)$$

In Fig. 5.10, the line broadening in a system consisting of two solar-like stars is shown for several values of  $\Delta v$ , most of them with lower velocities that are more realistic for binaries and one, for which the split is clearly visible. The spectrum of a single star is plotted in red with a shift of  $0.5 \cdot \Delta v$  and marked with error bars with a length according to a S/N of 50. As we see, for  $\Delta v < 50$  km/s, it would clearly be impossible to fit such a line broadening with a signal-to-noise ratio of even as high as 50.

If we know that a given spectrum is a blend of two stellar spectra (e. g. from HST photometry), we can use this knowledge to our advantage and increase the quality of

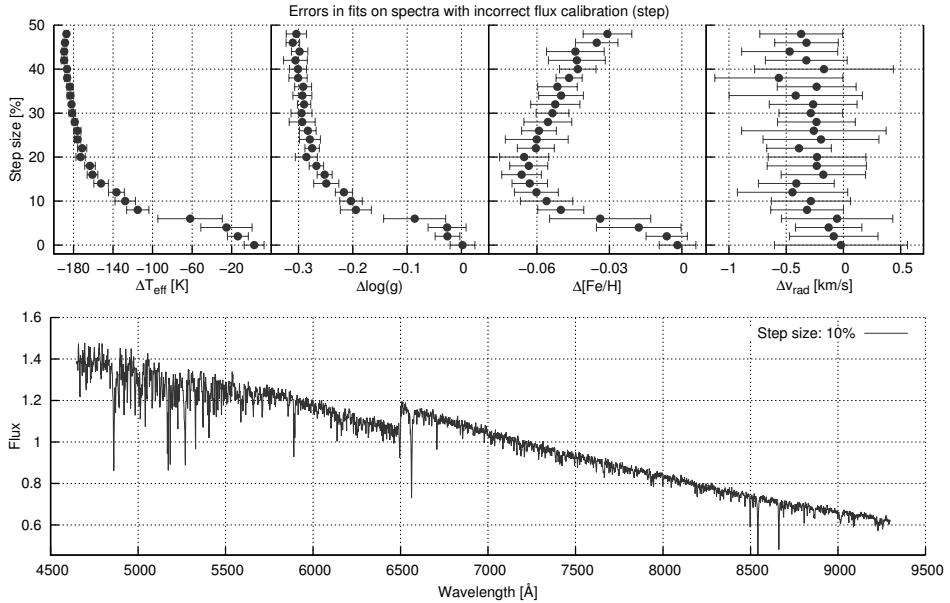


**Figure 5.9:** Systematic errors produced by a discontinuity in the spectrum for several step sizes are shown in the upper plot. An example of a spectrum with a step size of 10% is shown below.

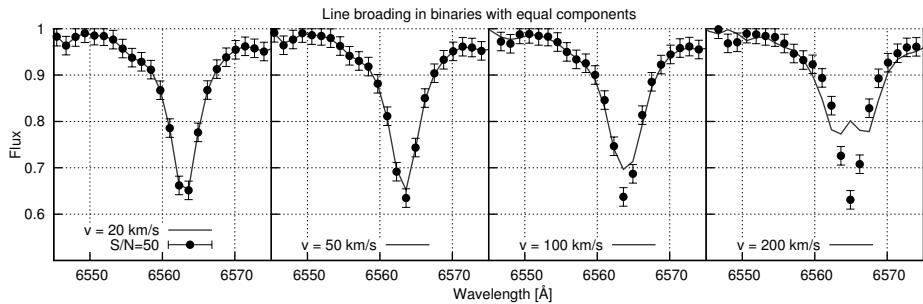


**Figure 5.10:** Line broadening in binaries with equal components for different separation velocities in black. The spectrum of a single star is plotted in red with error bars according to a S/N of 50. Both stars have  $T_{\text{eff}}=5800$  K,  $\log(g)=4.5$  and solar element abundances.

the fit by using two components instead of one. The two plots in Fig. 5.11 each show blends of two stellar spectra (black dots) with parameters given in Table 5.1, together with the best-fitting spectra when using one component only (red) and two components (blue). In the left example, the first star was scaled by a factor of 10, so it is clearly dominating the spectrum and a fit with one component already gives reasonable results (see Table 5.1), but even in this case, the results of the two-component fit are better. The results become even better, when both stars have about the same brightness as shown in the second example (right plot in Fig. 5.11). In order to get good results, we

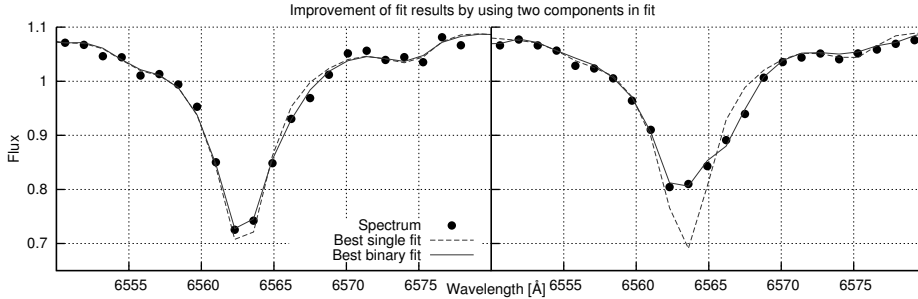


**Figure 5.11:** Two examples of how the quality of the fit results can be improved by fitting two components instead of one. Both plotted spectra (black dots, shown is the  $H_{\alpha}$  line) consist of two stellar spectra with parameters given in Table 5.1. For the left example the first spectra is scaled by a factor of 10, while for the right example it is 1.3. A low noise with  $S/N=100$  was added. In both plots the red line shows the best-fitting spectrum using a single component, while the blue one was fitted with two components.

	Star 1				Star 2			
	$T_{\text{eff}}[\text{K}]$	$\log(g)$	$[Fe/H]$	$v_{\text{rad}}[\text{km/s}]$	$T_{\text{eff}}[\text{K}]$	$\log(g)$	$[Fe/H]$	$v_{\text{rad}}[\text{km/s}]$
Input	5 800	4.5	0.0	0.0	5 400	4.0	0.0	150
(I) Single	5 757	4.38	-0.06	2.69				
(I) Binary	5 810	4.53	0.04	-1.70	5 453	3.86	-0.37	133.65
(II) Single	5 693	4.18	-0.26	28.46				
(II) Binary	5 807	4.49	-0.02	-0.14	5 396	3.98	0.03	149.88

**Table 5.1:** Fit results for spectra in Fig. 5.11.

really need to fit two components instead of one.

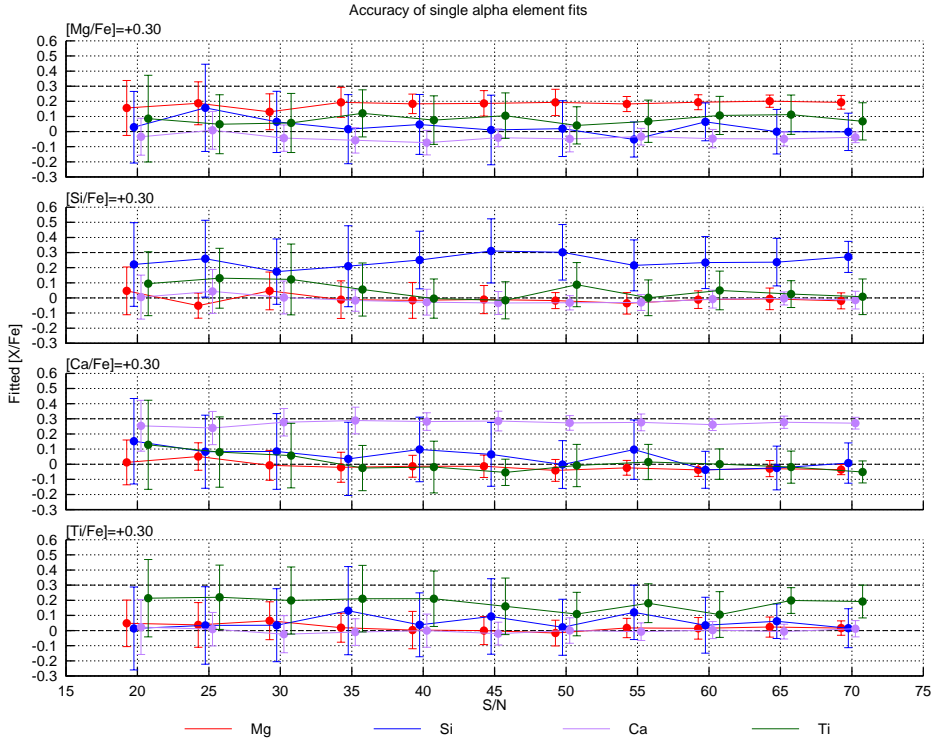
## 5.8 Single alpha element abundances

As discussed in Section 4.11, our new *PHOENIX* library includes spectra with  $[X/Fe] \pm 0.3$  for the alpha elements  $X \in [\text{Mg}, \text{Si}, \text{Ca}, \text{Ti}]$ , synthesized from fully converged model atmospheres. They have a metallicity fixed to  $[Fe/H] = -1.5$  and the sampling in effective temperature ( $\Delta T_{\text{eff}} = 200 \text{ K}$ ) and surface gravity ( $\Delta \log(g) = 1.0$ ) is coarser than in the published library.

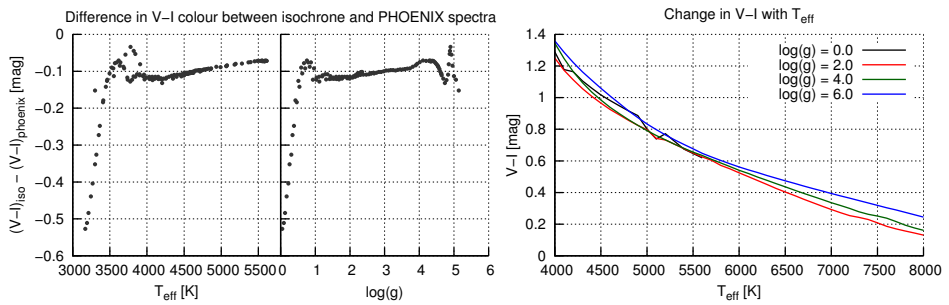
For testing the fit of single alpha elements, we selected spectra for a solar-like star with  $T_{\text{eff}} = 5800 \text{ K}$ ,  $\log(g) = 4.0$  and  $[X/Fe] = +0.3$  for all four elements. Since determining the abundances of single alpha elements always is a two-step process using our methods, we first had to fit the stellar parameters as in all the tests discussed above. Since most of the alpha elements (except for one) were not enhanced, we fixed  $[a/Fe] = 0$ . After a successful determination of the parameters, the second fit was started. Not using perfectly matching stellar parameters as initial guess is more realistic, since in real observations we will also have to determine those values first.

Figure 5.12 shows the mean and standard deviation of the fits for various signal-to-





**Figure 5.12:** Results of single alpha element fits for four different spectra with  $T_{\text{eff}}=5800\text{ K}$ ,  $\log(g)=4.0$  and  $[Fe/H]=-1.5$ . For each, one of the four elements Mg, Si, Ca and Ti has been enhanced by +0.3, while the others are kept unchanged.



**Figure 5.13:** Difference between  $V-I$  colours in the isochrone and in PHOENIX spectra on the left. The change in  $V-I$  colour with  $T_{\text{eff}}$  is plotted on the right as calculated from PHOENIX spectra.

noise ratios. We can see that Mg, Ca and Ti are mostly fitted nicely, with the exception of the Mg and Ti enhanced spectra, for which we seem to have significant systematic errors for both Mg and Ti – curiously we do not observe an error in Mg for the Ti en-

hanced spectrum, so it is presumably caused by stronger variations of the overall spectrum with high Mg enrichment. The error bars for the Si fits are larger than those of the other three elements, but with a large enough sample, an enrichment of 0.3 dex as in this tests should still be detectable.

## 5.9 Isochrone fit

We received a set of 179 spectra of stars in M5 from Evan Kirby (priv. comm.), which have been observed with DEIMOS (Faber et al., 2003), a multi-object spectrograph at the Nasmyth focus of the Keck II telescope. In addition to the processed spectra, he sent us BVRIJHK magnitudes and results from isochrone fits for the effective temperature  $T_{\text{eff}}$ , the surface gravity  $\log(g)$  and the metallicity  $[Fe/H]$ . Kirby et al. (2009) claimed that they were able to determine the surface gravity photometrically with an accuracy of  $\pm 0.06$  dex with their methods and their fitted spectra seem to confirm that. Thus, we tried to reproduce those results using our isochrone fitting method.

We used an isochrone by Marigo et al. (2008) for an age of 12.7 Gyrs, which seems to work fine for most GCs. The distance of 7.5 kpc and the extinction of  $E_{B-V} = 0.03$  (which is small enough to ignore) was taken from Harris (1996). In the list of surface gravities provided by E. Kirby, there are a couple of values that obviously indicate a failed fit, so we ignored those stars. For the rest, we found an almost perfect agreement to his values with  $\Delta \log(g) = -0.016 \pm 0.032$ . Therefore, fixing the surface gravity photometrically – at least for problematic spectra – seems to be a reasonable idea.

When testing the accuracy of the isochrone fits for the effective temperature, we noticed that the colour indices from our *PHOENIX* spectra always ended up too blue. So we took a single isochrone and recalculated the  $V - I$  colours using *PHOENIX* spectra. The results are shown in the left two plots of Fig. 5.13, showing an offset of  $\sim 0.1$  mag. The larger differences for cooler stars are probably caused by the model atmospheres used by Marigo et al. (2008) for calculating the colours. Since *PHOENIX* has made vast improvements in modelling cool stars over the past years, the *PHOENIX* colours are presumably more reliable than those derived from other model atmospheres. For higher temperatures, the difference in colour seems to be fairly constant, so we could just correct for this. The right plot in Fig. 5.13 shows, how the  $V - I$  colour varies with temperature. For our offset of  $\sim 0.1$  mag this would correspond to an error in  $T_{\text{eff}}$  of  $\sim 250$ -500 K.

## 5.10 Problems with the *PHOENIX* spectra

In order to further investigate the problem, we calculated a *PHOENIX* spectrum with solar parameters ( $T_{\text{eff}} = 5778$  K,  $\log(g) = 4.44$ ) and derived several colours, which we compared to those obtained from a solar spectrum from CALSPEC, which is a set of composite stellar spectra used for HST calibrations (see e. g. Turnshek et al., 1990; Colina &

Source	$U - B$ [mag]	$B - V$ [mag]	$V - R$ [mag]	$R - I$ [mag]	$V - I$ [mag]
CALSPEC	0.083	0.645	0.446	0.325	0.771
<i>PHOENIX</i> (old)	0.058	0.581	0.440	0.330	0.771
<i>PHOENIX</i> (new)	0.068	0.630	0.440	0.326	0.766
Ground	0.173 $\pm 0.064$	0.642 $\pm 0.016$	0.354 $\pm 0.010$	0.332 $\pm 0.008$	0.688 $\pm 0.014$

**Table 5.2:** Measured colours from *PHOENIX* spectra with solar parameters and from a solar spectrum from CALSPEC. For comparison, colours as measured from the ground by Holmberg et al. (2006) are listed as well, which of course are affected by the absorption of the Earth's atmosphere.

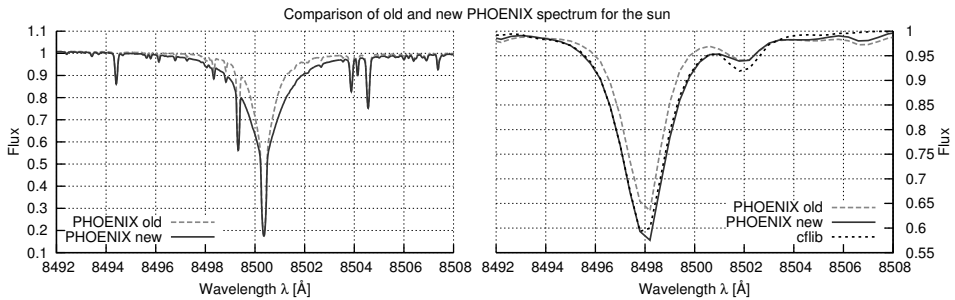


**Figure 5.14:** Comparison of old and new *PHOENIX* spectra in one of the lines of the CaII triplet. On the left, the high resolution spectra. On the right, they are convolved to 1 Å FWHM, shifted to air wavelengths and compared to an interpolated solar spectrum from the *cflib* library.

Bohlin, 1997). The results are listed in Table 5.2 with the entry called '*PHOENIX* (old)' being the one measured from the *PHOENIX* spectrum. Obviously, especially the value for  $B - V$  is too low.

Serendipitously, we quickly identified the major problem: we assumed that for higher temperatures we could neglect the effect of molecules, so we did not use them for models with  $T_{\text{eff}} > 5500$  K. This limit, of course, was set much too low, resulting in a sun without molecular absorption lines and, e. g., a missing G band. Therefore, we recalculated the solar model with molecules, resulting in better matching colours, see '*PHOENIX* (new)' in the table.

Another problem that we encountered with our *PHOENIX* spectra was that we could not reproduce the shape of some broad absorption lines, e. g. the lines of the near infrared Ca II triplet. The right plot in Fig. 5.14 shows a *PHOENIX* spectrum in red and an interpolated spectrum from the *cflib* library (Valdes et al., 2004). Obviously, the strength of our line is significantly too small. *PHOENIX* offers the possibility to use special line profiles for given species, which we used to improve our spectra. We calculated a new *PHOENIX* spectrum, which is plotted in green in Fig. 5.14. On the left, it is compared with the old spectrum, showing a significantly broader absorption line. In the plot on the right, we now match the *cflib* spectrum almost perfectly.

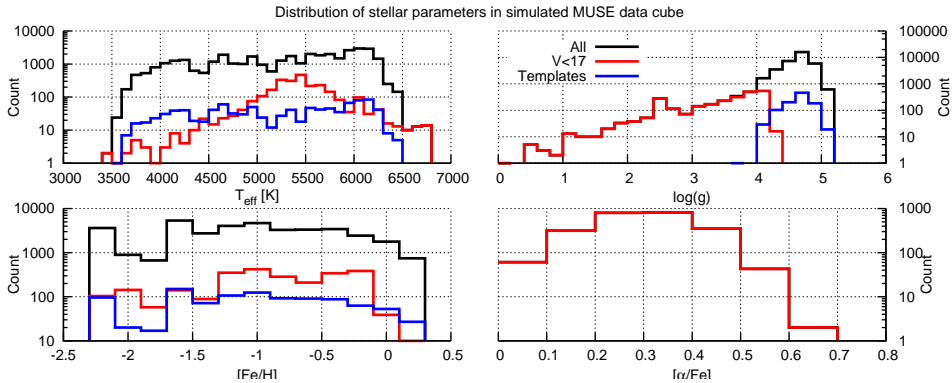


**Figure 5.15:** Distribution of stellar parameters for all  $\sim 37\,000$  stars (black) in the simulated data cube. All stars with  $V < 17$  mag ( $\sim 2\,500$ , plotted in red) have been handled separately and only they have an alpha element abundance  $[\alpha/\text{Fe}] > 0$ . For the rest, 1 000 stars (blue) have been chosen, from which all the others are derived by multiplication with a factor that scales them to the given magnitude.

Some of the special line profiles have already been used for the spectra from our *PHOENIX* library with  $T_{\text{eff}} > 5\,000$  K. As we will see in Section 5.12, all fits of spectra with  $T_{\text{eff}} \approx 5\,000$  K and  $T_{\text{eff}} \approx 5\,500$  K show some significant systematic error. Most presumably this is caused by discontinuities caused by activating molecules and special profiles in the model atmospheres. Thus, we are going to recalculate all spectra for  $T_{\text{eff}} > 4\,000$  K with molecules and special line profiles. This will take some time and therefore all results presented in this Chapter are produced using the old *PHOENIX* spectra.

## 5.11 MUSE dry run

Within the *MUSE* consortium the decision was made to conduct *dry runs*, which are supposed to simulate real observations as well as possible, for every science case. For the globular clusters, we have finished our first dry run, which still lacks some realism, but was a good way for testing our methods for extracting the spectra from the data cube (done by Sebastian Kamann in Potsdam) and analyzing them. For all the numbers presented in this section, especially the standard deviations in the plots, please keep in mind that we are dealing with only small numbers of spectra, so even a single bad fitting result can have a significant effect. Therefore, they are not supposed to be exact statistical results, but only rough estimates of what we can expect of future *MUSE* observations of globular clusters.

### 5.11.1 The simulated *MUSE* cube

For creating the simulated *MUSE* cube, we took all the stars from the central  $1 \text{ arcmin}^2$  of the data collected for 47 Tuc by the *ACS Globular Cluster Survey* (Anderson et al.,

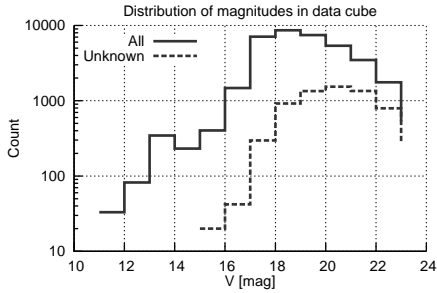


**Figure 5.16:** *Distribution of magnitudes in data cube with those stars not in the ACS catalogue plotted with a dashed line.*

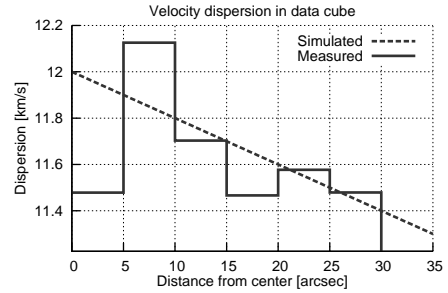


**Figure 5.17:** *Velocity dispersion in data cube.*

2008). We used the ACS magnitudes in an isochrone fit (see Section 4.3) for a rough determination of the stellar parameters  $T_{\text{eff}}$  and  $\log(g)$  for all 30 394 stars in the field (see Fig. 5.15). For the metallicity, we chose a more unrealistic uniform distribution, which allowed us to test the quality of the fits with varying  $[Fe/H]$  better as when using a tightly constrained value for all stars.

The radial velocities were assumed to have a dispersion of 12 km/s at the centre, decreasing with 1 km/s per 50 arcsec towards the edge (plotted in Fig. 5.17 as a black line). The red line in the plot is an attempt to reconstruct the velocity dispersion again from the input velocities by calculating standard deviations of the radial velocities for stars within concentric rings around the centre. As a consequence, the central bin up to 5 arcsec gives a bad result due to the small size of the region.

The final data cube was created using positions from the ACS survey. We assumed to have no AO available and a DIMM seeing of 0.8 arcsec, which is a little worse than the median seeing on Cerro Paranal with 0.66 arcsec (Sarazin, 1998). In addition to the stars from the ACS data, we added  $\sim 6\,500$  more objects to the data cube at random positions in order to simulate an incomplete catalogue, which can easily happen next to very bright stars. The distribution of magnitudes in the data cube is plotted in Fig. 5.16: in black for all stars and in red for those stars that are not in the ACS catalogue. As one can see, they account for a significant number of stars below the turn-off at 17 mag, but there are also some giants, which we will have to deal with in the analysis. An image with the integrated white light of all 36 973 in the data cube is shown in Fig. 5.18.

Since the spectra were synthesized in Göttingen while the data cube was created in Potsdam and Lyon, we had to transfer all the required data. We tried to reduce its amount as much as possible while keeping the simulation realistic. For this, we took all the stars brighter than 17 mag (2573 in total) and interpolated the spectra for them using the stellar parameters obtained by the isochrone fit. We then also added a non-zero alpha element abundance with  $[\alpha/Fe]=0.3\pm 0.2$  for those spectra only. From the stars fainter than 17 mag, we chose 1 000 for which we created the spectra. All the other spectra were derived from this sample by applying a multiplicative factor, which scales

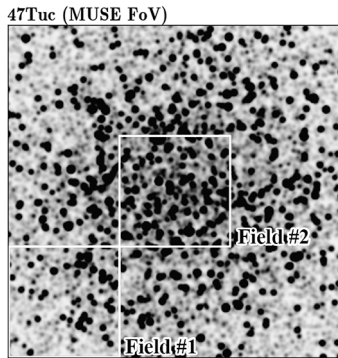


**Figure 5.18:** Integrated white light image of the simulated MUSE data cube based on observations of 47 Tuc with the two analyzed sub-fields marked in red.

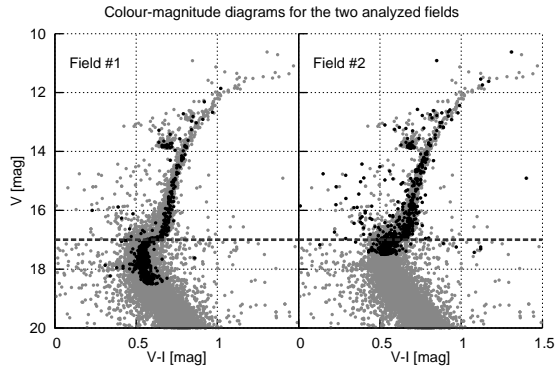


**Figure 5.19:** Colour-magnitude diagram of 47 Tuc plotted with data from Anderson et al. (2008) in grey. Points in black mark those spectra that we were able to extract from field 1 (left) and 2 (right). The dashed line marks the position of the main-sequence turn-off at  $V \approx 17$  mag.

them to the observed ACS magnitudes. By doing this, we were able to reduce the number of spectra required from  $\sim 37\,000$  to  $\sim 3\,500$ .

### 5.11.2 Extraction of spectra

In order to get results in a reasonable time, we did not analyze the whole cube, but only two sub-fields, which are marked in red in Fig. 5.18. Sebastian Kamann was able to extract 897 spectra from the first field at the edge and 904 from the second field in the centre of the cluster. For both, the colour-magnitude diagrams are plotted in Fig. 5.19 in red over the CMD for the whole cluster. With the sub-fields being about  $1/9$  the size of the total field, we therefore can expect to extract  $\sim 8\,000$  spectra from an entire MUSE data cube. The dashed blue line in Fig. 5.19 marks the position of the main-sequence turn-off at  $V \approx 17$  mag. Having fit results for both fields will allow us to compare the performance of our methods in dense regions (centre) and in more sparsely populated areas.

### 5.11.3 Noise

In order to get an idea of the quality of each extracted spectrum  $S$ , we compared it with its input spectrum  $O$  by calculating the residuals  $R$  in the normalized spectrum, i. e.  $R \equiv (S - O)/O$ . In the left plot of Fig. 5.20, the residuals for four different spectra are plotted, including one with high noise (purple), low noise (orange), more noisy in the blue (blue) and more noisy in the red (red). The last two cases are usually caused by the throughput of the instrument, which is smallest at the edges of the spectrum. Furthermore, most spectra in the cube have less flux in the red and therefore the noise

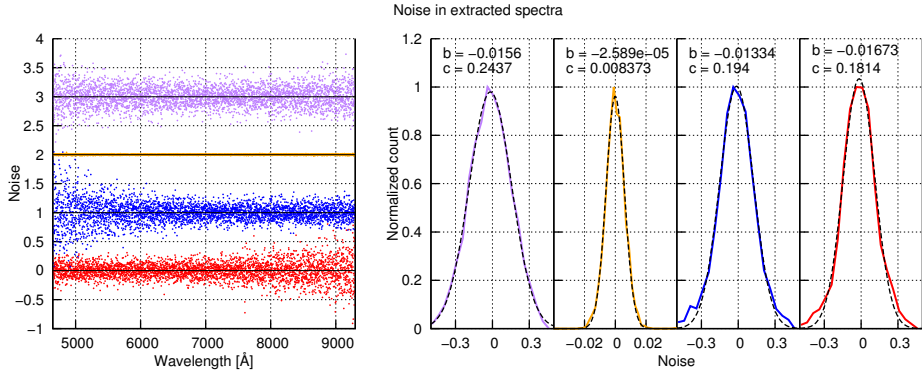


**Figure 5.20:** Analysis of the noise on the spectra produced by the extraction process. Residuals of four spectra are plotted on the left with their distribution shown in the right four plots.

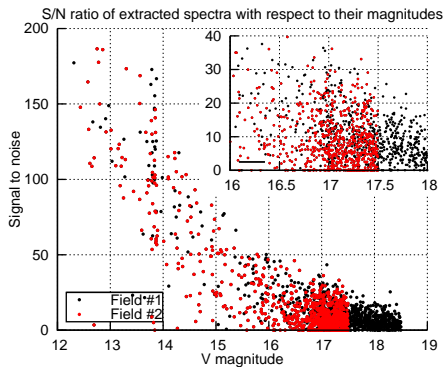


**Figure 5.21:** S/N ratio of extracted spectra over their magnitude for field 1 (black) and 2 (red).

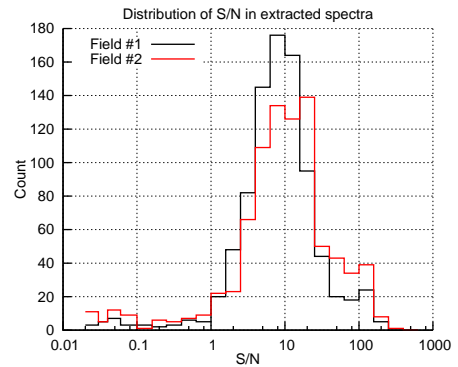


**Figure 5.22:** Distribution of S/N ratios of extracted spectra for field 1 (black) and 2 (red).

level increases there.

The four plots on the right in Fig. 5.20 show the distributions of the noise for each spectrum (in same colours), together with one dashed black line for each, which is a best-fitting Gaussian with  $ae^{-b/c^2}$ . The values for the coefficients  $b$  and  $c$  are given in the plot, and for all of them  $b \ll c$ , i. e. there is no significant offset of the distributions from zero. Furthermore, the Gaussians seem to fit the data very well and therefore we can assume that the noise in the spectrum is normally distributed. This allows us to calculate signal-to-noise ratios easily for all spectra, which now are just the inverse of the standard deviations of the residuals discussed above. In Fig. 5.21, the resulting S/N ratios are plotted over the V magnitude of the input spectra for both fields. The distribution of S/N ratios for all stars is shown in Fig. 5.22. In field 1, we got 370 (41%) spectra with a S/N ratio larger than 10 and 616 (68%) with  $S/N \geq 5$ . For the second field, the numbers are 440 (49%) and 638 (71%) respectively. In a whole MUSE field with

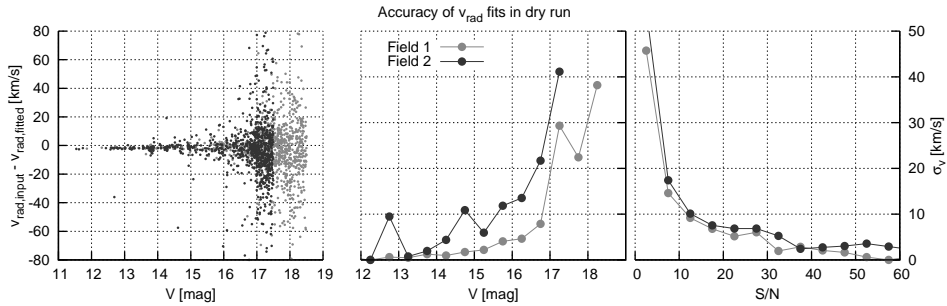


**Figure 5.23:** Accuracy of radial velocity fits in the dry run for both fields 1 (grey) and 2 (black). On the left, the differences between input velocities and best fits are plotted over the magnitude of the star, whereas in the central plot the standard deviations of 0.5 mag sized bins are shown. The plot on the right shows the same data but plotted over S/N instead of magnitude.

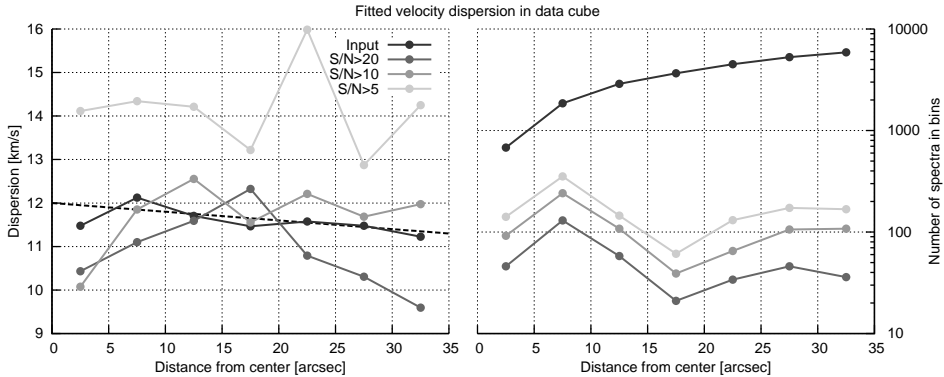


**Figure 5.24:** Reconstruction of the velocity dispersion for three different values for the S/N cut-off on the left with the analytical dispersion that had been applied to the spectra plotted as dashed black line. The number of spectra used for calculating the dispersion in each bin is plotted on the right.

~8 000 extracted spectra, we can therefore expect to get ~3 500 spectra with a signal-to-noise ratio larger than 10 and ~5 500 with  $S/N \geq 5$ . As we will see later, the limit for obtaining accurate stellar parameters is  $S/N \approx 50$ , which has been reached by ~6% of the stars in field 1 and ~11% in field 2. In an entire *MUSE* field, we therefore expect to get between about 500 and 900 spectra with a sufficiently high signal-to-noise ratio for determining stellar parameters from a single exposure.

### 5.11.4 Radial velocities

With the method discussed in Section 4.10.2, we can fit the stellar parameters and the radial velocities for all spectra. The left plot of Fig. 5.23 shows the difference between the input velocity and the fitted one over the magnitude of the star for both sub-fields. The central plot was created with the same data as the left one, but shown here are the



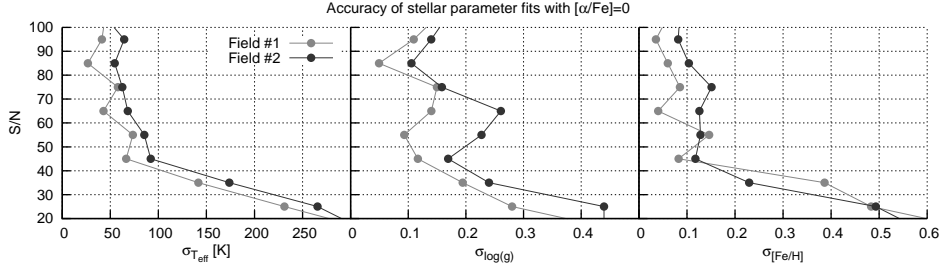


**Figure 5.25:** Accuracy of stellar parameter fits for both fields 1 (grey) and 2 (black) with effective temperatures  $T_{\text{eff}}$  on the left, surface gravities  $\log(g)$  in the centre and metallicities  $[Fe/H]$  on the right.

standard deviations in bins of size 0.5 mag. On the right, again the same data are shown, but this time plotted over the signal-to-noise ratio as estimated above. Although the overall performance is worse than in previous theoretical tests (see Section 5.2), we also find significant shifts of the mean residuals for  $S/N < 5$  only. According to the right plot in Fig. 5.23, a signal-to-noise ratio of 5 will be enough to determine the radial velocity with an accuracy better than 20 km/s. For  $S/N > 10$ , we can even get down to  $v_{\text{rad}} \pm 10$  km/s – enough to find most binaries (see Section 6.5).

We can now try to reconstruct the velocity dispersion from the fitted radial velocities. Figure 5.24 shows the change of the velocity dispersion as a function of distance to the cluster centre for three different cut-off values for the signal-to-noise ratio. The reconstruction from the input velocities (see Fig. 5.17) has also been included in the plot for comparison. For best results, we usually would want to include radial velocities from high  $S/N$  spectra only, but in that case the numbers will be too low for good statistics, as can be seen at the red curve for spectra with  $S/N > 20$ . However, a low value for the cut-off will artificially increase the velocity dispersion due to uncertainties in the measured velocities (see green curve for spectra with  $S/N > 5$ ). A cut-off at  $S/N = 10$  (blue) seems to be a good choice for this data.

With real observations, we will have multiple visits at several pointings, which will increase the number of spectra that can be used for the reconstruction of the velocity dispersion dramatically. Not only will we have more spectra with a high  $S/N$ , but we can also co-add high-noise spectra from multiple visits in order to lower the noise level and increase the fit results – with 10 visits, we can increase the signal-to-noise ratio of the spectra by a factor of  $\sqrt{10} \approx 3$ . Therefore we should be able to detect indications for intermediate-mass black holes in the centres of globular clusters – if they exist.

### 5.11.5 Stellar parameters

For simplicity, we only fitted the stellar parameters  $T_{\text{eff}}$ ,  $\log(g)$  and  $[Fe/H]$ , while fixing  $[\alpha/Fe] = 0$ . A fit with all four parameters has only been done for all stars in field 1 with  $V < 17$  mag, i. e. all stars that do have a non-zero alpha element abundance (see next Section 5.11.6).

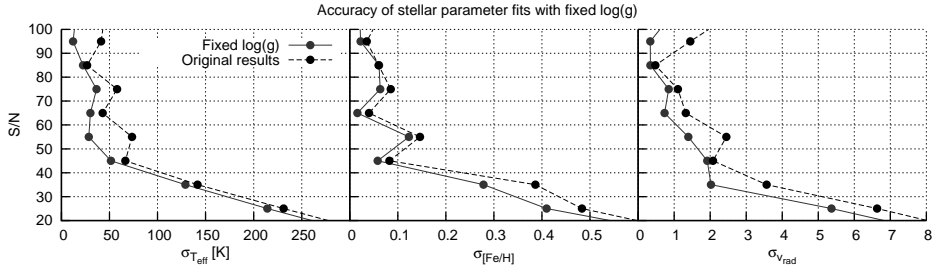


**Figure 5.26:** Fit of spectra from field 1 with surface gravities fixed to the values from the input spectra and  $[\alpha/Fe]$  fixed to 0 (for  $V > 17$  mag) or 0.3 (for  $V < 17$  mag). Results are plotted with solid lines and the old results from figs. 5.23 and 5.25 with dashed lines for comparison.

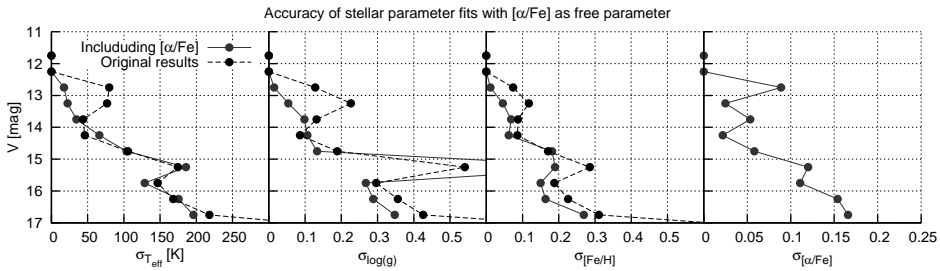


**Figure 5.27:** Results of the fits with the alpha element abundance  $[\alpha/Fe]$  as a free parameter with solid lines and the original results for comparison with dashed lines. The artefact at  $V \approx 15$  mag is due to the low numbers in the statistics.

In Fig. 5.25, the standard deviations of the differences between input and fitted parameters are plotted over the signal-to-noise ratios. Although not shown in the plots, we observed a systematic error in all three parameters: they were overestimated by  $\sim 50$  K ( $T_{\text{eff}}$ ), 0.1-0.2 dex ( $\log(g)$ ) and  $\sim 0.1$  dex ( $[Fe/H]$ ). Further systematic errors are present for signal-to-noise ratios smaller than 30. One major factor responsible for this can be found in the alpha element abundances of zero used in the fits, as was shown in Section 5.5.

As a consequence, if it is required to fix  $[\alpha/Fe]$  (e. g. to save computational time), it should be fixed to a good approximation, e. g. the mean alpha element abundance of the cluster. Another improvement could be to also fix or at least loosely constrain the surface gravity  $\log(g)$  to a value estimated by photometry, as it was suggested in Section 4.10.1. Both has been done for the fits shown in Fig. 5.26, where  $\log(g)$  has been fixed to the value from the input spectrum and  $[\alpha/Fe]$  to 0 (for  $V > 17$  mag) or 0.3 (for  $V < 17$  mag). Both the new (red) and the old (black) results are plotted and an improvement is clearly visible.

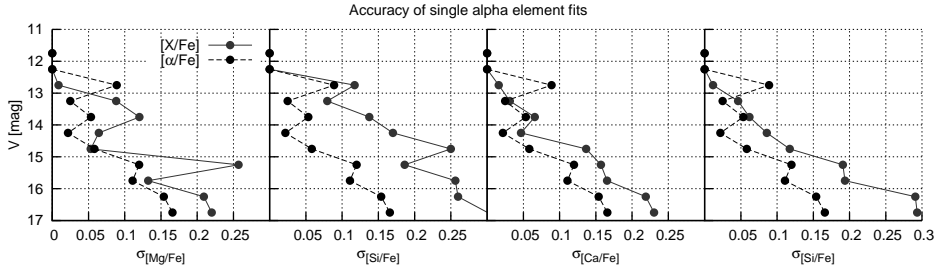


**Figure 5.28:** Results of the abundance fits for Mg, Si, Ca and Ti. For comparison, the alpha element abundances fitted in the the previous run have been added as dashed lines (see Fig. 5.27).

Source	H $\alpha$ [Å]	H $\beta$ [Å]	H $\gamma$ [Å]	H $\delta$ [Å]
NIST	6562.79	4861.35	4340.47	4101.73
0058	6562.77 (-0.02)	4801.29 (-0.06)	4349.38 (-0.09)	4101.74 (+0.01)
	6562.81 (+0.02)	4861.33 (-0.02)	4340.36 (-0.11)	4101.79 (-0.06)
0329	6562.40 (-0.39)	4861.22 (-0.13)	4340.48 (+0.01)	4101.97 (+0.24)
	6562.81 (+0.02)	4861.29 (-0.06)	4340.38 (-0.09)	4101.77 (+0.04)
0607	6563.04 (+0.25)	4861.24 (-0.11)	4340.39 (-0.08)	4101.64 (-0.09)
	6562.81 (+0.02)	4861.26 (-0.09)	4340.39 (-0.08)	4101.78 (+0.05)

**Table 5.3:** Measured wavelengths for lines of Balmer series in some spectra from the Miles library and in PHOENIX spectra with the same stellar parameters (second line for each star). Air wavelengths from the NIST database are given for comparison together with differences to those for each measured wavelength (in brackets).

### 5.11.6 Alpha element abundances

For all the spectra brighter that  $V=17$  mag, i. e. those that were created with  $[\alpha/Fe] \neq 0$ , we ran the parameter fits again with the alpha element abundance as a free parameter. Figure 5.27 shows the results of this test, this time plotted over magnitude, since the sample was also selected by magnitude. We see a slight improvement in the accuracies and the systematic errors observed before vanished completely (not plotted) – the accuracy in alpha element abundance is  $<0.2$  dex.

Using this results, we can try to determine the abundances of single alpha elements. This has been done in Fig. 5.28. Since we are still dealing with very small numbers, the outliers are not of interest. We see that at least for Mg and Ca we can achieve accuracies comparable to those in  $[\alpha/Fe]$  fits with  $<0.2$  dex. If we could repeat this with other elements, this would be good enough for the determination of the variations in light elements that was presented in Fig. 2.14.

## 5.12 Miles library

The *Medium-resolution Isaac Newton Telescope library of empirical spectra (MILES*, see Sánchez-Blázquez et al., 2006) is a library of 985 spectra spanning a large range in atmo-

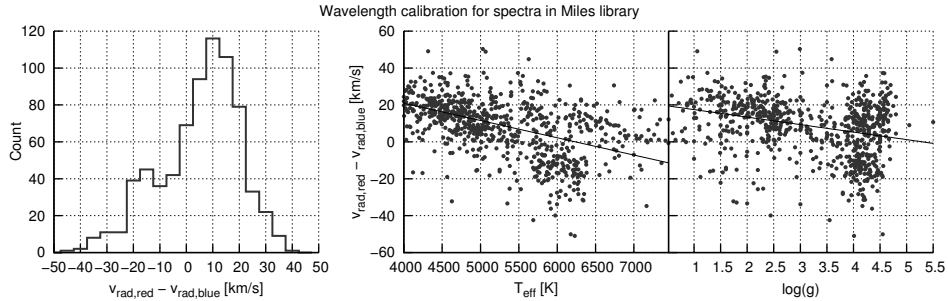


**Figure 5.29:** Measured radial velocities  $v_{\text{rad,blue}}$  at the blue end (3850 - 4150 Å) and  $v_{\text{rad,red}}$  at the red end (6400 - 6700 Å) of the spectra in the Miles library. Plotted on the left is a histogram for the difference  $v_{\text{rad,blue}} - v_{\text{rad,red}}$ : a compression of the wavelength grid is indicated by negative values, while a stretch produces positive values. In the right two plots, the trend of this stretch is shown as a function of  $T_{\text{eff}}$  and  $\log(g)$  together with linear regressions.

spheric parameters and covering a wavelength range from 3525 to 7500 Å at a spectral resolution of  $\sim 2.56$  Å (Prugniel et al., 2011). For all spectra, stellar parameters have been determined (Cenarro et al., 2007) and they have been shifted to the rest frame. We are using the latest version of the library (9.1, see Falcón-Barroso et al., 2011) for testing the methods described in this thesis.

### 5.12.1 Wavelength calibration

When starting to work with the Miles library, we discovered a problem with the wavelength calibration of the spectra. We measured the wavelengths of the lines of the Balmer series and compared them to the values given by the NIST database<sup>1</sup>. In order to avoid a bias due to an inaccurate measuring method, we repeated this for *PHOENIX* spectra with the same atmospheric parameters as the tested Miles spectra for comparison. The results are listed in Table 5.3. While some of the spectra are very well calibrated (e. g. 0058) with deviations in the line positions smaller than the accuracy of the measuring method, for some other we see a significant drift in some of the lines: the shift of 0.39 Å of the  $H_{\alpha}$  line measured in spectrum 0329 corresponds to a radial velocity of  $\sim 18$  km/s.

Those results indicate a stretch (or compression) in the wavelength grid of the spectra. In order to get a better understanding of the quantity of this effect, we extracted parts at the red and at the blue end of the Miles spectra and fitted the LOSVD for both. The differences  $\Delta v_{\text{rad}}$  in radial velocities are plotted in Fig.5.29. Obviously, for a major part of the spectra the difference between the wavelengths of absorption lines at their red and their blue end is  $\sim 10$  km/s larger than it should be. A second peak in the histogram indicates a compression by the same amount for some other spectra. Plotting the  $\Delta v_{\text{rad}}$  over  $T_{\text{eff}}$  and  $\log(g)$  shows that the latter are concentrated around 6000 K

<sup>1</sup><http://www.nist.gov/pml/data/asd.cfm>

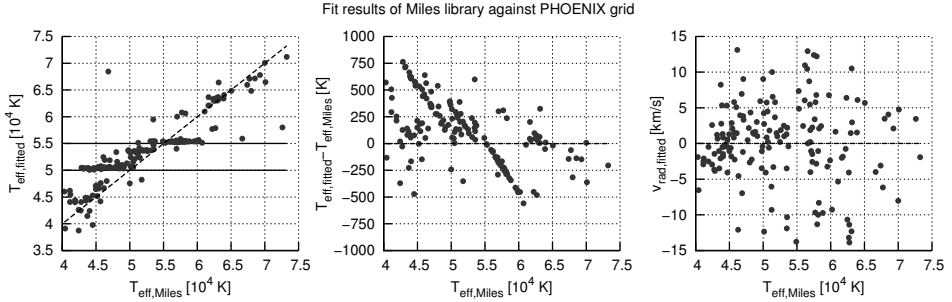


**Figure 5.30:** Fit of the spectra from the Miles library against our PHOENIX grid. The left two plots show the fit of  $T_{\text{eff}}$  and the solid lines indicate the temperatures of 5 000 K and 5 500 K (see text). In the right plot, the result for the radial velocities are shown, which are all zero in the Miles library.

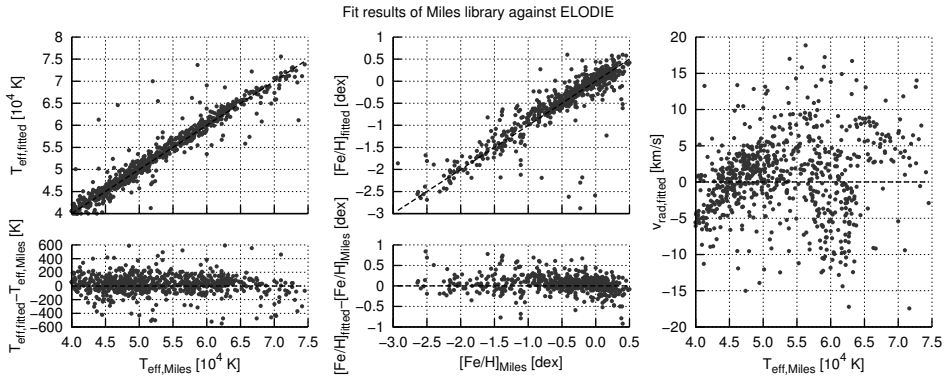


**Figure 5.31:** Fit of the spectra from the Miles library against ELODIE spectra. Plotted are the results for  $T_{\text{eff}}$  (left),  $[\text{Fe}/\text{H}]$  (centre) and  $v_{\text{rad}}$  (right).

with surface gravities  $\gtrsim 4$ . However, as we have seen in Section 5.6.1, for most of the spectra the error in the wavelength calibration should be small enough to be negligible.

### 5.12.2 Atmospheric parameters and radial velocities

For fitting the spectra from the Miles library, we fixed the surface gravities to the values given by Cenarro et al. (2007). This was necessary, since the spectral resolution is not constant for all spectra, but varies with wavelength around the mean value of  $2.56 \text{ \AA}$ . By constraining  $\log(g)$ , we can fit against model spectra convolved to  $2.56 \text{ \AA}$  without having to expect to large errors due to the incorrect spectral resolution (compare with Section 5.4).

The results for  $T_{\text{eff}}$  and  $v_{\text{rad}}$  are plotted in Fig. 5.30. The radial velocities are fitted very well with  $v_{\text{rad}} = 1.25 \pm 7.56 \text{ km/s}$ . Since the resolution of the Miles spectra is

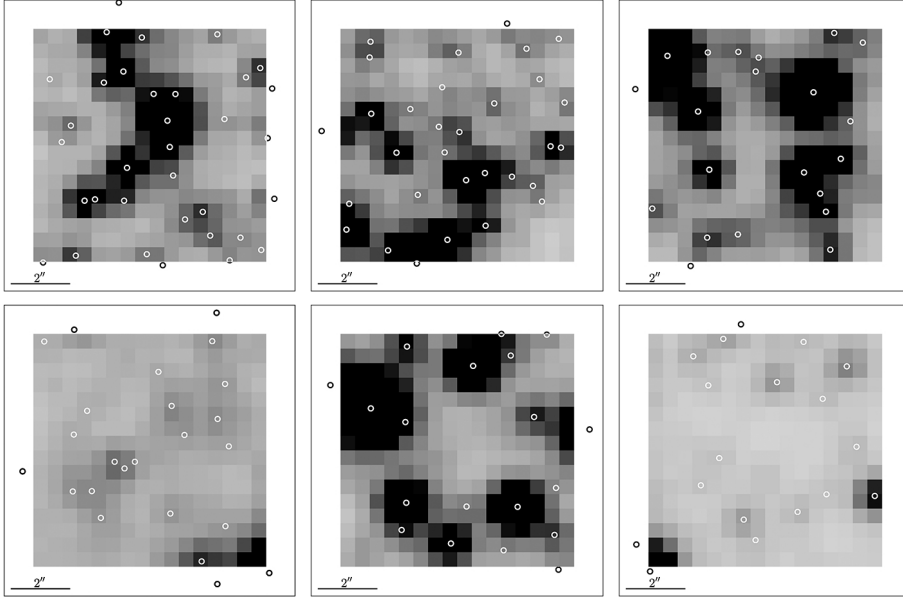


**Figure 5.32:** Fields in M13 observed with PMAS. Stars, for which spectra have been extracted are marked with circles. Plots have been done by S. Kamann.

comparable to that of *MUSE*, so are the achieved accuracies in  $v_{\text{rad}}$ . The effective temperatures on the other hand show larger variations and the fits seem to favour results around 5 000 K and 5 500 K (see solid lines). This shows one of the problems, we currently have with our new library *PHOENIX* spectra: those are the two temperatures, above which we start using special line profiles and disable molecules respectively – this seemingly produces a large discontinuity in the grid, which causes the fits to end up preferably at those temperatures (see Section 5.10).

In order to test our methods with the Miles spectra anyway, we ran the fits again using spectra from the ELODIE library (Prugniel et al., 2007) as models, which are included in the ULySS package (Koleva et al., 2009). Using those empirical spectra, the results get significantly better (see Fig. 5.31): the effective temperature has no *preferred* values anymore and the deviation from the values determined by Cenarro et al. (2007) is  $\Delta T_{\text{eff}} = 32.89 \pm 220.17$  K only, i. e. we see a small systematic error and the accuracy is worse than in previous tests with simulated data but still good. This could probably be improved by determining the LSF for each spectrum. For the metallicity, we get  $\Delta[\text{Fe}/\text{H}] = 0.05 \pm 0.21$ .

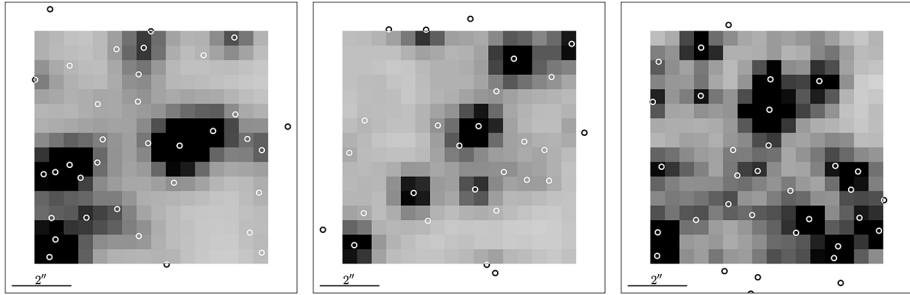


**Figure 5.33:** Fields in M92 observed with PMAS. Stars, for which spectra have been extracted are marked with circles. Plots have been done by S. Kamann.

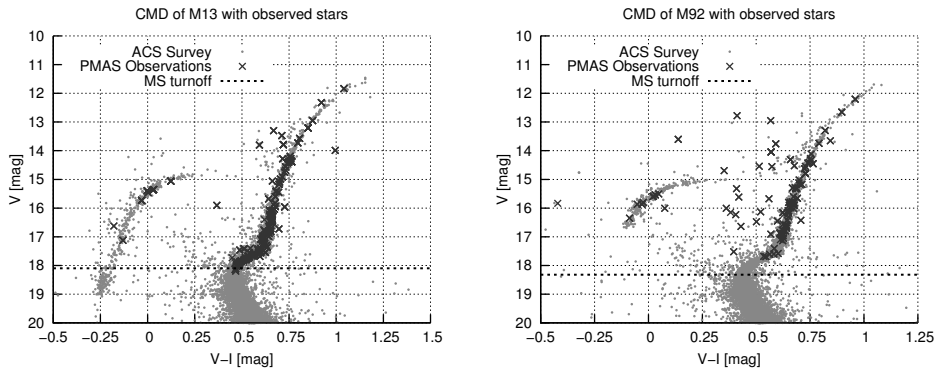


**Figure 5.34:** Colour-magnitude diagrams of the two globular clusters M13 and M92 in grey from Anderson et al. (2008). Over-plotted in black are those stars, for which spectra have been extracted from the PMAS cubes successfully.

## 5.13 PMAS data of M13 and M92

A couple of observations of M13 and M92 have been done by Sebastian Kamann from the AIP in Potsdam using the PMAS IFU at the 3.5 m telescope on Calar Alto<sup>2</sup>. Six fields in M13 and three in M92 have been observed multiple times during two visits to the observatory in 2011. The resulting data cubes have  $16 \times 16$  spatial pixels with  $0.5''/\text{px}$ , resulting in a field of view of  $8 \times 8 \text{ arcsec}^2$ . For each dataset, S. Kamann identified the stars using the star catalogue from Anderson et al. (2008) (see figs. 5.32 and 5.33) and extracted the spectra (522 for M13 and 223 for M92) in the wavelength range from  $7700 \text{ \AA}$  to  $8900 \text{ \AA}$  with a spectral resolution of  $\sim 8000$ , which he provided for testing our methods. In Fig. 5.34, the CMDs for both clusters are plotted, in which the observed stars are marked with red crosses. The MS turn-off points are indicated by blue dashed lines

<sup>2</sup>Centro Astronómico Hispano Alemán (CAHA) at Calar Alto, operated jointly by the Max-Planck Institut für Astronomie and the Instituto de Astrofísica de Andalucía (CSIC).

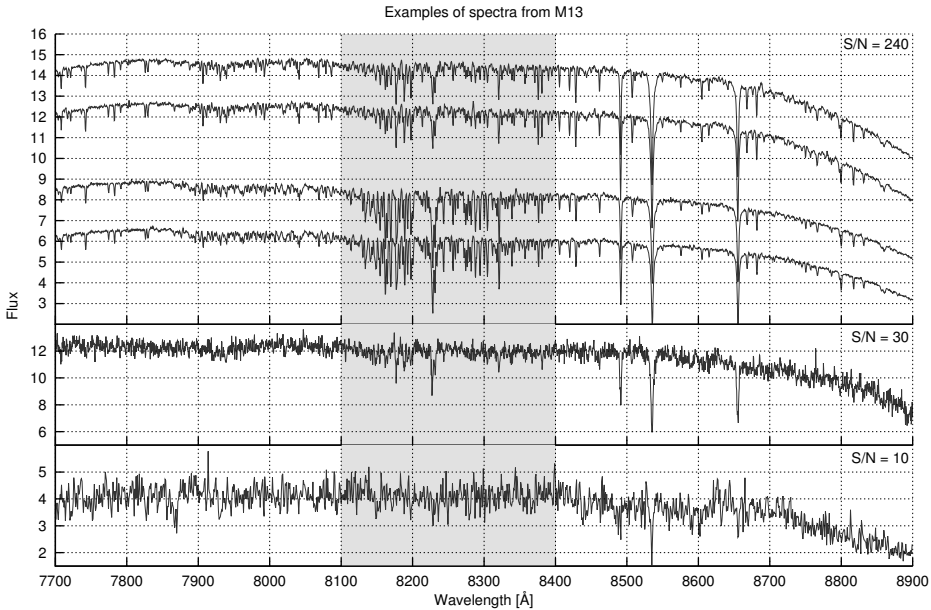


**Figure 5.35:** Some spectra from the M13 sample. In the upper plot, four spectra with a very high S/N from the same star are plotted. Below, examples with more typical signal-to-noise ratios are shown. The grey box shows the region that we discarded due to telluric absorption.

and obviously no MS stars are included in the sample.

During the analysis of the spectra, we discovered that in our library of *PHOENIX* spectra we had an issue with the shape of the lines of the Ca triplet, which we could not reproduce properly (see Section 5.10). Thus, another set of model spectra had to be used. The *ELODIE* library from the last section was also not available for this analysis, since it does not cover the wavelength range of the observations. Serendipitously, we obtained a preliminary interpolator for the *cfib* library (Valdes et al., 2004) from Philippe Prugniel (priv. comm.), which includes the required wavelength range at a resolution of  $\sim 1$  Å FWHM. We did not fit the LSF of the PMAS spectra, since the only visible features are the lines of the Ca triplet, which cover only a small range, but we allowed the line broadening parameter  $\sigma$  to vary in the fits.

Unfortunately, we did not have a good telluric standard available for the correction of the spectra. In fact, a standard star was observed, but with that we were not able to remove the tellurics properly. Therefore, we decided to mask the whole wavelength range from 8 100 to 8 400 Å, which does not show many features anyway, and excluded it from the fits. Figure 5.35 shows some examples of spectra that have been extracted from the M13 data cubes with the discarded regions marked in yellow. In the upper plot, four spectra from different visits of the same star with very high S/N are plotted. Below, two more typical spectra from the sample are shown.



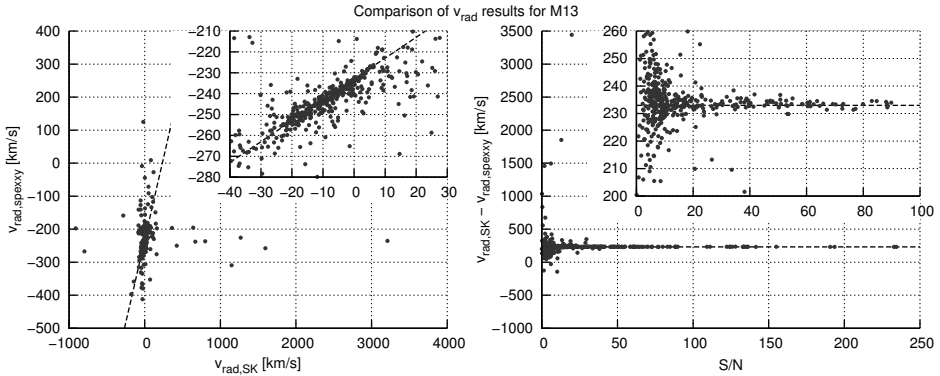


**Figure 5.36:** Comparison of the radial velocities fitted by S. Kamann ( $v_{\text{rad,SK}}$ ) and our results ( $v_{\text{rad,spexy}}$ ) for M13.

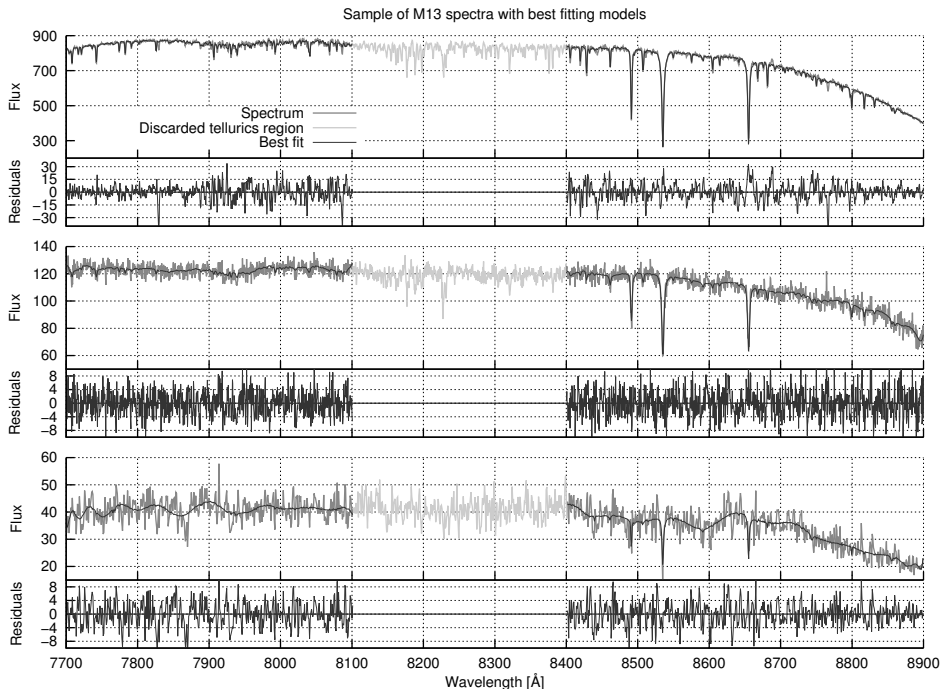


**Figure 5.37:** Some spectra from the M13 cube and their best fitting model spectra from the cflib library. The greyed out parts have been discarded from the analysis due to tellurics.

### 5.13.1 Radial velocities

Since S. Kamann has not published his own results yet, in this thesis only comparisons with his fitted radial velocities will be presented, which do not allow to draw conclu-

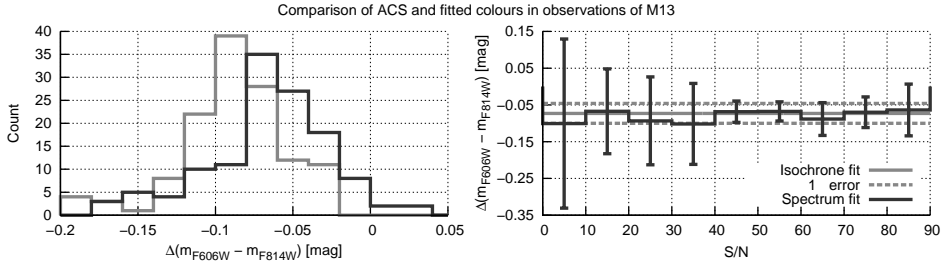


**Figure 5.38:** Colours determined from PHOENIX spectra with atmospheric parameter as given by the fits. On the left, the distribution of the difference between the colours from the spectroscopic fits and those given by the ACS data is plotted. On the right, the differences are plotted as a function of signal-to-noise of the spectra.

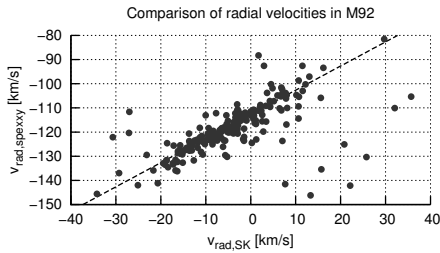


**Figure 5.39:** Comparison of the radial velocities fitted by S. Kamann ( $v_{\text{rad,SK}}$ ) and our results ( $v_{\text{rad,spexxy}}$ ) for M92.

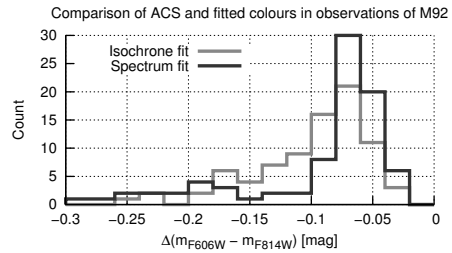


**Figure 5.40:** Same plot as the left one in Fig. 5.38, but for M92.

sions about the velocity dispersions in the two clusters. He determined  $v_{\text{rad}}$  by taking the brightest spectrum from each sample and cross-correlating it against all others. This way, no absolute velocities are obtained and he still requires a fixed zero-point, which we can provide using our methods.

Figure 5.36 shows the comparison of results for M13. On the left, our values for  $v_{\text{rad}}$  are plotted over those determined by S. Kamann, while on the right the same data is plotted as a function of signal-to-noise. A linear regression for all spectra with  $S/N > 20$  and excluding the obvious outliers (which are mainly HB stars) yields a zero-point of  $-233.5 \pm 1.9$  km/s, which is indicated by a dashed green line. For M92, the results are plotted in Fig. 5.39, resulting in an offset of  $-112.8 \pm 1.8$  km/s.

### 5.13.2 Effective temperatures and colours

Since we expected the wavelength range of the PMAS spectra to be much too small for a spectral analysis beyond radial velocities, we fitted the atmospheric parameters with an isochrone using ACS magnitudes. The only available information that we had about the stars beside the PMAS spectra were colours, so we interpolated PHOENIX spectra with the same parameters, calculated their colours and compared them with ACS data.

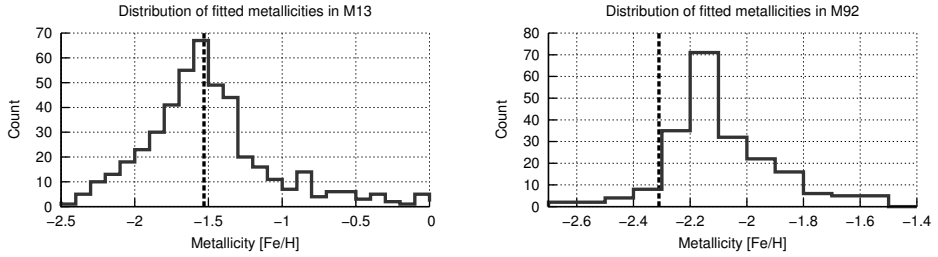


**Figure 5.41:** Distribution of the fitted metallicities for both M13 and M92. Plotted with dashed lines are the mean value given by Harris (1996), which is  $[Fe/H] = -1.53$  for the former and  $[Fe/H] = -2.31$  for the latter.

The red line in the left plot of Fig. 5.38 shows a histogram of the differences between both colours, and as expected (see Section 5.9), we see a shift of about 0.05–0.1 mag due to the problems with our *PHOENIX* spectra. Nevertheless, the central peak is rather concentrated with  $\sigma \approx 0.03$ , which indicates a good fit. The differences in colour for M92 are plotted in Fig. 5.40, showing similar results.

For the  $\nu_{\text{rad}}$  fits presented before, we let  $T_{\text{eff}}$  and  $[Fe/H]$  free to vary (while fixing  $\log(g)$  photometrically) in order to match the shape of the Ca lines as good as possible, which should increase the accuracy of the resulting radial velocities. This gave us a new set of effective temperatures and metallicities, for which we also calculated colours from *PHOENIX* spectra as discussed above. The results for M13 are plotted with a blue line in Fig. 5.38. As we see, the resulting colours are slightly more blue than those from the isochrone fit, but still they concentrate at one single value. In the right plot, the difference in colour is plotted as a function of signal-to-noise. At least for  $S/N \gtrsim 40$ , the error bars are smaller than 0.1 mag, which is equivalent to about 300–400 K in this region of the CMD (see Fig. 5.13). The results for the fits of M92 are again shown in Fig. 5.40.

Three spectra with different signal-to-noise ratios from the M13 data cubes are plotted in Fig. 5.37 in black. The regions that have been discarded due to telluric absorption are marked in yellow. Over-plotted are the best-fitting models from the *cflib* library in red. Plotted below each spectra are the residuals, showing that we were able to reproduce the shape of the spectra very well.

### 5.13.3 Metallicities

Assuming that all the observed stars are members of the two clusters, we can compare the fitted metallicities with the ones given by Harris (1996), which is  $[Fe/H] = -1.53$  for M13 and  $[Fe/H] = -2.31$  for M92. In Fig. 5.41, this has been done for both GCs. For M13, the mean metallicity matches the literature value very well, but for M92, a metal abundance was determined, which is slightly too large. This seems to be caused by the *cflib* library, which has been used for the fits. Obviously, it is not well defined for metallicities this low.

	#	Mean S/N	$T_{\text{eff}}$ [K]	$[Fe/H]$ [dex]	$v_{\text{rad}}$ [km/s]
1	4	212.25	4348.34 ±6.39	-1.49 ±0.03	-237.97 ±1.29
2	8	98.88	4600.96 ±27.25	-1.61 ±0.05	-233.55 ±1.06
3	4	108.50	4861.68 ±7.80	-1.77 ±0.11	-245.45 ±0.33
4	5	58.20	5199.53 ±54.26	-1.68 ±0.10	-253.39 ±1.93
5	4	90.25	5147.38 ±18.30	-1.89 ±0.11	-235.97 ±0.57
6	4	67.75	4974.76 ±56.78	-1.53 ±0.04	-239.40 ±0.79
7	3	116.00	4711.91 ±68.28	-1.32 ±0.01	-238.73 ±0.39
8	4	138.50	4477.71 ±13.05	-1.61 ±0.05	-228.90 ±1.44
9	4	105.75	4716.51 ±13.46	-1.53 ±0.08	-237.66 ±0.90
10	4	60.00	4931.55 ±37.14	-1.44 ±0.04	-251.22 ±0.57
11	3	72.67	4865.38 ±35.53	-1.82 ±0.01	-243.54 ±0.04
12	4	67.25	4992.14 ±28.57	-1.56 ±0.11	-250.60 ±0.63
13	3	50.00	5004.98 ±89.85	-1.63 ±0.06	-234.10 ±2.22

**Table 5.4:** Comparison of results from fits for spectra of the same star. The second column is the number of spectra taken for that star, which have their mean signal-to-noise ratios given in the third column. The following columns are means and standard deviations for  $T_{\text{eff}}$ ,  $[Fe/H]$  and  $v_{\text{rad}}$ .

### 5.13.4 Comparison of results for multiple visits

Since for most of the stars multiple spectra have been obtained, we can compare their results. We picked a sample of thirteen stars from M13 that have been observed at least three times and for which the spectra have a mean signal-to-noise ratio of 50 or more and a minimum S/N of at least 10.

Table 5.4 gives the number of spectra for each of those stars and their mean signal-to-noise together with means and standard deviations for the effective temperatures, the metallicities and the heliocentrically corrected radial velocities. Keeping in mind the small wavelength range of the PMAS spectra, the compliance of the results for  $T_{\text{eff}}$  and  $[Fe/H]$  is astonishing. Of course, this does not mean that we determined those parameters correctly, but similar values for different spectra are a strong indication that we actually did.

## Chapter 6

# A proposal for *MUSE* observations

Within the *MUSE* consortium a preliminary decision has been made that about 100 hours of GTO time will be used for the observations of globular clusters. In this chapter I want to use the results from all the conducted tests and from the dry run in order to define criteria for successful observations. Possible targets will be discussed as well as observation strategies best suited for reaching our scientific goals.

### 6.1 Selection of globular clusters

A sample of 1958 red giant stars in 19 galactic globular cluster has been observed by Carretta et al. (2009b) using the FLAMES/GIRAFFE and FLAMES/UVES spectrographs at the VLT in order to measure the abundances of Fe, Na, and O. With *MUSE* we expect to get further down in the CMD, even well below the MS turn-off. Thus, observing those cluster again with *MUSE*, would complement the existing data. For the giants we can compare our results with existing ones, which will help us analyzing all the fainter stars in our observations. The list of observed globular clusters is given in Table 6.1, including two more targets, for which estimates for the masses of potential intermediate-mass black holes in their centres are available (van der Marel & Anderson, 2010).

### 6.2 Exposure times

Using the data from Anderson et al. (2008), we can estimate the crowding limit and the background luminosity for several pointings in all globular clusters from our sample. We collected lists of all stars within a field of  $1 \text{ arcmin}^2$  around the centre and around two points in a distance of 30 and 60 arcsec. Since we expect to be able to extract  $\sim 5\,000$

Name		RA	Dec	$M_{\text{total}} [M_{\odot}]$	$\sigma_v$ [km/s]	$r_h$ [']	cc
NGC 104	47 Tuc	00:24:05.71	-72:04:52.7	$1.1 \cdot 10^6$ <sup>(2)</sup>	11.0	3.17	
NGC 288		00:52:45.24	-26:34:57.4	$1.11 \cdot 10^5$ <sup>(2)</sup>	2.9	2.23	
NGC 1904	M 79	05:24:10.59	-24:31:27.3	$3.57 \cdot 10^5$ <sup>(2)</sup>	5.3	0.65	
NGC 2298		06:48:59.41	-36:00:19.1	$3.4 \cdot 10^4$ <sup>(1)</sup>	1.52	0.98	
NGC 2808		09:12:03.10	-64:51:48.6	$1.32 \cdot 10^6$ <sup>(2)</sup>	13.4	0.80	
NGC 3201		10:17:36.82	-46:24:44.9	$1.95 \cdot 10^5$ <sup>(2)</sup>	5.0	3.10	
NGC 4590	M 68	12:39:27.98	-26:44:38.6	$3.06 \cdot 10^5$ <sup>(2)</sup>	2.5	1.51	
NGC 5139	$\omega$ Cen	13:26:47.28	-47:28:46.1	$2.8 \cdot 10^6$ <sup>(1)</sup>	16.8	5.00	
NGC 5904	M 5	15:18:33.22	+02:04:51.7	$8.34 \cdot 10^5$ <sup>(2)</sup>	5.5	1.77	
NGC 6121	M 4	16:23:35.22	-26:31:32.7	$2.25 \cdot 10^5$ <sup>(2)</sup>	4.0	4.33	
NGC 6171	M 107	16:32:31.86	-13:03:13.6	$2.04 \cdot 10^5$ <sup>(2)</sup>	4.1	1.73	
NGC 6218	M 12	16:47:14.18	-01:56:54.7	$4.93 \cdot 10^5$ <sup>(2)</sup>	4.5	1.77	
NGC 6254	M 10	16:57:09.05	-04:06:01.1	$2.25 \cdot 10^5$ <sup>(2)</sup>	6.6	1.95	
NGC 6388		17:36:17.23	-44:44:07.8	$1.50 \cdot 10^6$ <sup>(2)</sup>	18.9	0.52	
NGC 6397		17:40:42.09	-53:40:27.6	$1.59 \cdot 10^5$ <sup>(2)</sup>	4.5	2.90	c
NGC 6441		17:50:13.06	-37:03:05.2	$1.30 \cdot 10^6$ <sup>(2)</sup>	18.0	0.57	
NGC 6752		19:10:52.11	-59:59:04.4	$3.64 \cdot 10^5$ <sup>(2)</sup>	4.9	1.91	c
NGC 6809	M 55	19:39:59.71	-30:57:53.1	$2.41 \cdot 10^5$ <sup>(2)</sup>	4.0	2.83	
NGC 6838	M 71	19:53:46.49	+18:46:45.1	$3.67 \cdot 10^4$ <sup>(2)</sup>	2.3	1.67	
NGC 7078	M 15	21:29:58.33	+12:10:01.2	$6.2 \cdot 10^5$ <sup>(1)</sup>	13.5	1.00	c
NGC 7099	M 30	21:40:22.12	-23:10:47.5	$2.74 \cdot 10^5$ <sup>(2)</sup>	5.5	1.03	c

**Table 6.1:** List of globular clusters that have been observed by Carretta et al. (2009b), plus two more ( $\omega$  Cen and NGC2298), for which van der Marel & Anderson (2010) give estimates for the mass of a potential black hole. All centre coordinates are taken from Goldsbury et al. (2010) and all velocity dispersions  $\sigma_v$  and half-light radii  $r_h$  are from Harris (1996) – with the exception of NGC1904, for which the coordinates are from Simbad and  $\sigma_v$  has been estimated using Fig. 6.3. The total masses  $M_{\text{total}}$  of the clusters are either taken from van der Marel & Anderson (2010) <sup>(1)</sup> or Gnedin & Ostriker (1997) <sup>(2)</sup>. A 'c' in the last column marks the GC as core-collapsed. NGC1904 is the only object from the list for which no ACS observation from Anderson et al. (2008) is available.

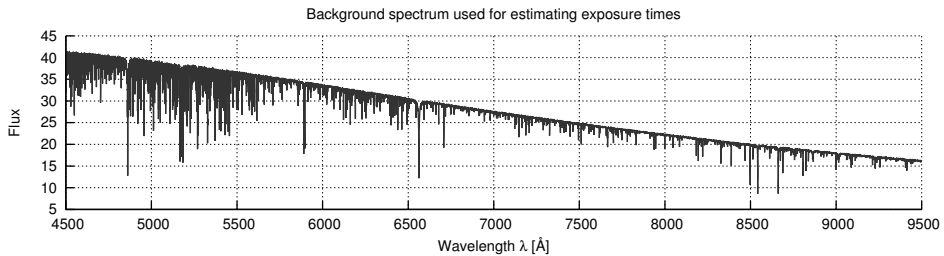


**Figure 6.1:** All spectra from the MUSE dry run co-added, except the brightest 5 000, used as background spectrum for estimating exposure times with MUSE.

spectra from every data cube, we assumed the magnitude of the 5 000th brightest star in the sample to correspond with the crowding limit  $m_{\text{crowd}}$ . The background luminosity  $m_{\text{back}}$  was then obtained by calculating the combined brightness of all stars in the field fainter than  $m_{\text{crowd}}$  and dividing it by the area of  $3600 \text{ arcsec}^2$ .

Name	$d_{\text{centre}} = 0 \text{ arcsec}$				$d_{\text{centre}} = 30 \text{ arcsec}$				$d_{\text{centre}} = 60 \text{ arcsec}$			
	$n_{\text{stars}}$	$m_{\text{crowd}}$ [Vmag]	$m_{\text{back}}$ [ $\frac{V_{\text{mag}}}{\text{asec}^2}$ ]	$t_{\text{exp}}$ [sec]	$n_{\text{stars}}$	$m_{\text{crowd}}$ [Vmag]	$m_{\text{back}}$ [ $\frac{V_{\text{mag}}}{\text{asec}^2}$ ]	$t_{\text{exp}}$ [sec]	$n_{\text{stars}}$	$m_{\text{crowd}}$ [Vmag]	$m_{\text{back}}$ [ $\frac{V_{\text{mag}}}{\text{asec}^2}$ ]	$t_{\text{exp}}$ [sec]
NGC 104	23383	17.65	17.09	44.1	19813	17.99	17.75	53.3	13980	19.19	19.67	137.1
NGC 288	3626	30.82	-	-	3248	30.52	-	-	2637	30.40	-	-
NGC 2298	6029	24.66	26.81	-	4453	32.02	-	-	2147	32.02	-	-
NGC 2808	41298	18.99	17.89	204.6	37346	19.35	18.53	249.6	30121	20.55	20.21	-
NGC 3201	3766	29.67	-	-	3522	29.51	-	-	3113	30.16	-	-
NGC 4590	11529	22.55	23.30	-	9822	23.44	24.24	-	6630	25.20	26.71	261.8
NGC 5139	31120	19.46	19.13	225.4	31414	19.52	19.22	236.6	29760	19.65	19.43	-
NGC 5904	17198	19.36	19.32	185.2	14839	19.85	20.16	276.0	11065	21.79	22.71	-
NGC 6121	1728	28.79	-	-	1535	29.43	-	-	1170	29.43	-	-
NGC 6171	3466	28.59	-	-	2994	29.37	-	-	2019	29.37	-	-
NGC 6218	4607	27.93	-	-	4185	27.87	-	-	3140	28.57	-	-
NGC 6254	9042	21.50	22.70	-	7890	22.55	23.88	-	5715	24.69	27.08	-
NGC 6388	52472	19.30	18.16	281.5	47325	19.97	18.89	524.5	35620	21.21	20.59	-
NGC 6397	2604	27.53	-	-	2122	26.89	-	-	1388	26.94	-	-
NGC 6441	59098	19.58	18.53	351.4	51856	20.39	19.27	-	38366	21.63	20.91	-
NGC 6752	9034	19.73	20.93	210.4	7290	21.38	22.99	-	4733	29.29	-	-
NGC 6809	5069	26.80	31.60	-	4695	30.38	-	-	4038	30.38	-	-
NGC 6838	1743	28.93	-	-	1636	30.39	-	-	1395	30.60	-	-
NGC 7078	39524	19.32	18.47	246.0	37138	19.82	19.25	354.3	28027	21.38	21.28	-
NGC 7099	14196	20.60	21.05	597.6	11555	21.69	22.54	-	7116	24.54	25.96	-

**Table 6.2:** Crowding limits, background luminosities and estimated exposure times for three different pointings for each of the GCs from our sample.

An exposure time calculator (ETC) for *MUSE* is already available<sup>1</sup> and so we could use the previously calculated magnitudes for estimating exposure times. Since the magnitudes in the ACS catalogue are given for the F606W filter of ACS, we created a *PHOENIX* spectrum of a star at the main-sequence turn-off (F5V, i. e.  $T_{\text{eff}}=6\,300\text{ K}$  and  $\log(g)=4.5$ ) and calculated the difference between the magnitude in F606W and Johnson V to  $m_{\text{F606W}} - m_{\text{V}} = 0.10\text{ mag}$ , which we added to both  $m_{\text{crowd}}$  and  $m_{\text{back}}$ . In order to obtain a good spectrum for the background, we used the data created for the *MUSE* dry run (see Section 5.11) and co-added all spectra except for the brightest 5 000 (see Fig. 6.1). The ETC was then used to calculate the exposure time  $t_{\text{exp}}$ , which is required to achieve a signal-to-noise ratio of 10 for a point source (a F5V star) at the crowding limit  $m_{\text{crowd}}$  in front of a background (the combined spectrum) with a surface brightness of  $m_{\text{back}}$ . This was done using a spatial binning of  $3 \times 3$ , since this is about the size of the PSF that is used for extracting the spectra from the cube.

All the results are presented in Table 6.2. For each pointing at every cluster it lists the number of stars  $n_{\text{stars}}$  in the ACS catalogue within  $1\text{ arcmin}^2$ . In case this is less than 5 000, the crowding limit equals to the faintest star in the sample and no background luminosity is given. Exposure times are listed for  $t_{\text{exp}} < 600\text{ sec}$  only. Globular clusters with less than 5 000 stars in a given pointing could also be observed, but we will have to discuss within the consortium whether we want to do this or not.

<sup>1</sup><http://www.eso.org/observing/etc/bin/gen/form?INS.MODE=swspectr&INS.NAME=muse>

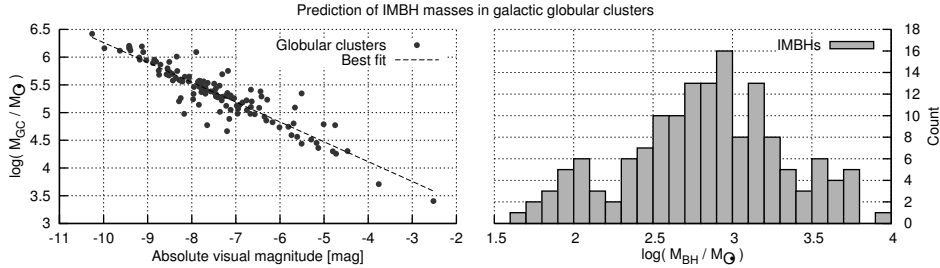


**Figure 6.2:** Correlation between absolute magnitude of GCs and their total mass on the left plotted with data from Harris (1996); Gnedin & Ostriker (1997). A linear best fit to the data is indicated with a dashed blue line. On the right, a distribution of estimated masses for the central IMBHs is plotted using the  $M_{BH}$ -bulge relation shown in Fig. 2.12.

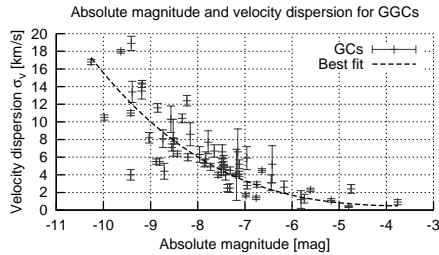


**Figure 6.3:** Plot of velocity dispersion over absolute magnitude for globular clusters and a best-fitting function, plotted with data taken from Harris (1996).

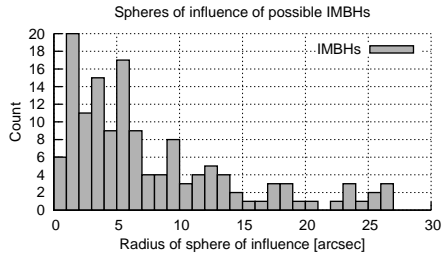


**Figure 6.4:** Distribution of estimated radii for the spheres of influence for galactic globular clusters. 15 GCs with estimated radii  $>30$  arcsec are missing in this plot.

### 6.3 Intermediate-mass black holes

The total mass  $M_{GC}$  of a globular cluster is directly correlated to its absolute visual magnitude  $M_V$ , as is shown in the left plot of Fig. 6.2 with total masses from Gnedin & Ostriker (1997). Therefore, for each GC with unknown mass, it can be estimated easily ( $M_{GC}(M_V) \approx 2.68 - 0.36M_V$ ). Furthermore, we can use those total masses for predicting the masses of possible central IMBHs using the  $M_{BH}$ -bulge relation from Fig. 2.12. The right plot in Fig. 6.2 shows the distribution of estimated BH masses for all galactic globular clusters. Unfortunately, Harris (1996) also does not present velocity dispersions for all GCs. Those that are given, are plotted in Fig. 6.3 together with a best-fitting function ( $\sigma_v(M_V) \approx -0.55 - 1.07M_V - 0.37M_V^2 - 0.04M_V^3$ ) that can be used for estimating the velocity dispersions  $\sigma_v$  for the other clusters.

Having estimates for the masses of possible black holes in the centre of each globular cluster and the corresponding velocity dispersions, we can calculate the radii of the spheres of influence ( $r_i$ ) according to Eq. 2.5 and project those radii to apparent sizes on the sky using the known distances to the GCs. The distribution of those apparent radii is plotted in Fig. 6.4, in which 15 GCs are missing with  $r_i > 15$  arcsec.



Name	$M_{\text{BH}}$ [ $M_{\odot}$ ]	$r_i$ [arcsec]	WFM $r_i$ [px]	NFM $r_i$ [px]	$n_{\text{stars}}$	$m_{\text{crowd}}$ [Vmag]	$m_{\text{back}}$ [ $\frac{V_{\text{mag}}}{\text{asec}^2}$ ]
NGC 104	< 1500 ( <sup>1</sup> )	< 2.44	12.2	97.6	18	16.63	15.75
NGC 288	4572	5.41	27.1	216.5	91	25.01	27.63
NGC 2298	< 340 ( <sup>1</sup> )	< 12.09	60.5	483.6	459	20.76	21.33
NGC 2808	4920	2.53	12.7	101.3	20	17.68	16.64
NGC 3201	784	5.68	28.4	227.2	101	24.75	27.26
NGC 4590	1210	16.66	83.3	666.4	871	21.00	21.62
NGC 5139	< 1200 ( <sup>1</sup> )	< 0.73	3.7	29.2	1	19.02	19.35
NGC 5904	3160	12.38	61.9	495.1	481	18.43	18.03
NGC 6121	900	22.68	113.4	907.2	1615	27.82	-
NGC 6171	819	6.75	33.8	270.1	143	22.20	24.37
NGC 6218	1910	17.44	87.2	697.6	955	22.71	24.70
NGC 6254	900	4.17	20.8	166.6	54	19.94	20.51
NGC 6388	5560	1.40	7.0	55.8	6	15.90	15.28
NGC 6397	645	12.28	61.4	491.3	473	21.33	24.01
NGC 6441	4850	1.14	5.7	45.8	4	17.26	15.97
NGC 6752	1430	13.19	66.0	527.7	546	17.72	17.77
NGC 6809	961	9.87	49.4	394.8	306	23.59	25.41
NGC 6838	158	6.62	33.1	264.7	137	27.14	-
NGC 7078	< 4400 ( <sup>1</sup> )	< 2.06	8.7	69.5	13	16.10	15.37
NGC 7099	1090	3.94	19.7	157.5	48	17.83	16.95

**Table 6.3:** Masses for intermediate-mass black holes, which are either upper limits from van der Marel & Anderson (2010)<sup>(1)</sup> or estimates using the  $M_{\text{BH}}$ -bulge relation. Sizes for the spheres of influence are given as apparent radii on sky and as number of spatial pixels in a *MUSE* data cube for both the Wide-Field Mode (WFM) and the Narrow-Field Mode (NFM). In the last three columns, the number of stars listed in the ACS catalogues within the sphere of influence is given together with the crowding limit and the background luminosity as discussed before.

Estimated masses for potential intermediate-mass black holes for all the globular clusters in our sample are listed in Table 6.3 together with corresponding radii for the spheres of influences, which are given as both the apparent size on sky and as number of spatial pixels in the *MUSE* data cube for both the Wide-Field Mode (WFM) and the Narrow-Field Mode (NFM). This should help identifying GCs for which we might even be able to search for IMBHs using the WFM, like NGC6121, NGC6218 or NGC4590 – for all three the estimated spheres of influences almost fill up the entire *MUSE* FOV. However, for other clusters like  $\omega$  Cen (NGC5139), it might be difficult to find an IMBH even with the NFM. In the last three columns, the number of stars in the catalogues provided by Anderson et al. (2008) are given, which are within the potential sphere of influence. We also provide a crowding limit that has been calculated under the assumption that we can extract  $\frac{5000 \cdot \pi r_i^2}{3600 \text{arcsec}^2}$  stars from a round area with radius  $r_i$ . The background luminosities have been determined accordingly.

## 6.4 Multiple populations

At the moment it is difficult to predict, how strong our contribution to the research on multiple populations with *MUSE* will be. We are able to measure metallicities quite accurately, so the GCs with a large split in  $[Fe/H]$  (see Table 2.1) might be interesting to observe, but with  $\omega$  Cen currently there is only one of them in our sample. The abundances of some light elements will be measurable with *MUSE*, so Carretta et al. (2009b) as the basis of our sample was well chosen, since they determined Fe, Na, and O abundances using high resolution spectroscopy. We will have to investigate further, which light elements we are able to measure accurately with *MUSE*.

## 6.5 Binaries

In a binary system with known mass of its components and their separation, we can easily calculate the orbital periods and velocities. This has been done in fig 6.5 for four different types of binaries. In the upper left plot, a binary system of two main-sequence components is shown, where one has solar mass with a lower mass companion. This kind of binary can be detected using photometry, because usually the components are so close that they cannot be resolved into two stars and therefore the binary appears as a single star, which is redder and brighter than the main-sequence. Milone et al. (2012b) used this method to detect binaries for mass ratios of  $q > 0.5$ , which has been marked with a dashed black line in the plot.

With *MUSE*, we want to detect the binaries spectroscopically. Binary systems composed of similar main-sequence stars ( $q \approx 1$ ) will only appear with broadened absorption lines, which is immeasurable with the low spectral resolution of *MUSE* (see Section 5.7). But for lower values of  $q$ , the binary system has one dominant component, which will show a periodic variation in radial velocity that is well detectable with *MUSE*. In the plot, some levels of equal maximum velocity are plotted with coloured lines, i. e. each system on a given line orbits with the given velocity. The black lines with the grey areas indicate equal levels of orbital periods, so each system on one of those lines needs the same amount of time for one orbit. Usually a binary system is considered as detected after observing three orbits. Thus, after three years of observations with an accuracy of  $\sim 10$  km/s in radial velocity, all binaries below the green and the top black line are detectable.

The system with a giant star (with  $1.5 M_{\odot}$ ) is in principal a variation of the MS-MS binary, where the mass ratio  $q$  is smaller. Nevertheless, this kind of systems is much more difficult to detect using photometry, because no shift to the well-defined MS can be measured. Not detectable using photometry, but within the range of *MUSE* are other systems with one dominant component, where the companion is for instance a white dwarf or a neutron star, which are shown in the lower two plots of fig 6.5. For those systems, we will always only see one of their components, showing a variation in radial velocity. Consequently, the search for binaries using *MUSE* does not compete

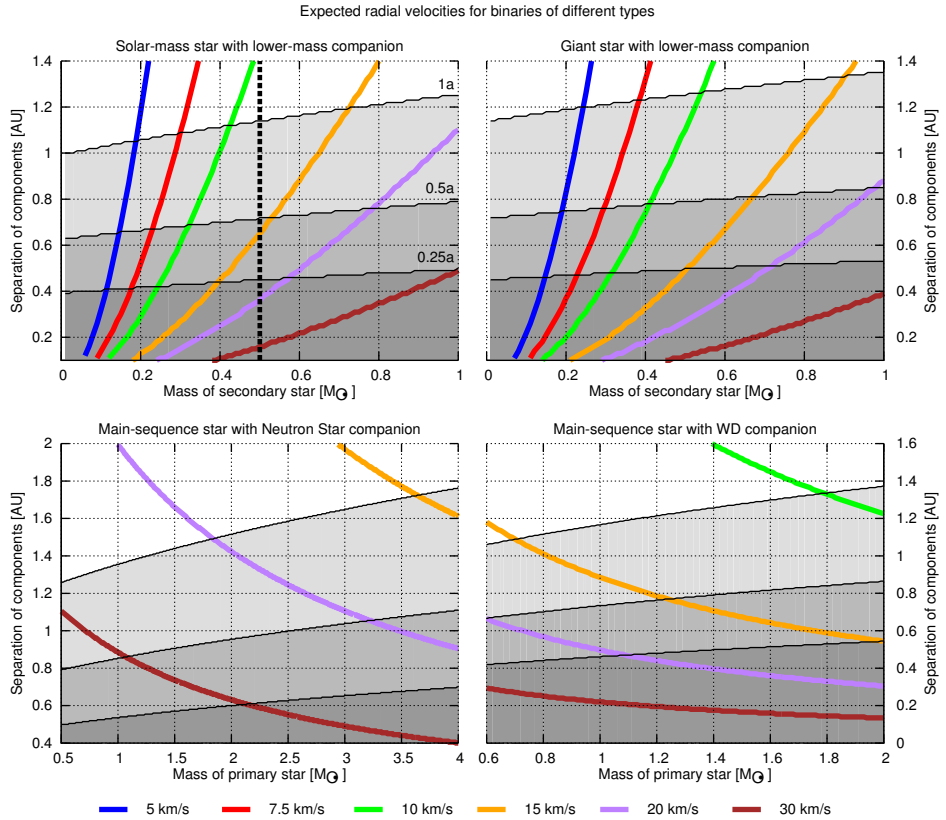


**Figure 6.5:** Expected radial velocities in binary systems for four different types of companions: solar-mass star with lower mass companion (upper left), main-sequence star with white dwarf (upper right), main-sequence star with neutron star (lower left) and giant star with lower mass companion (lower right). The black lines are orbital periods and for each plot they represent from top to bottom: 1a, 0.5a, 0.25a. The dashed black line in the upper left plot is the assumed detection limit for HST photometry, i. e. each binary right of this line is detectable by HST.

with HST observations, but is more complementary.

Of uppermost importance for the search for binaries is the observing strategy. In order to find binaries with both short and long orbital periods, ideally the observations need to be done on a logarithmic time scale or, which is usually easier to achieve, scattered randomly over the whole time of the program. Since the VLT is an Earth-bound observatory, this can only be done during those times when the targets are actually visible. The only circumpolar globular cluster from our sample is 47 Tuc (NGC104). For the other eighteen, annual visibility charts are plotted in Fig. 6.6. They are well distributed in RA, so each time of the year a few of them are observable.

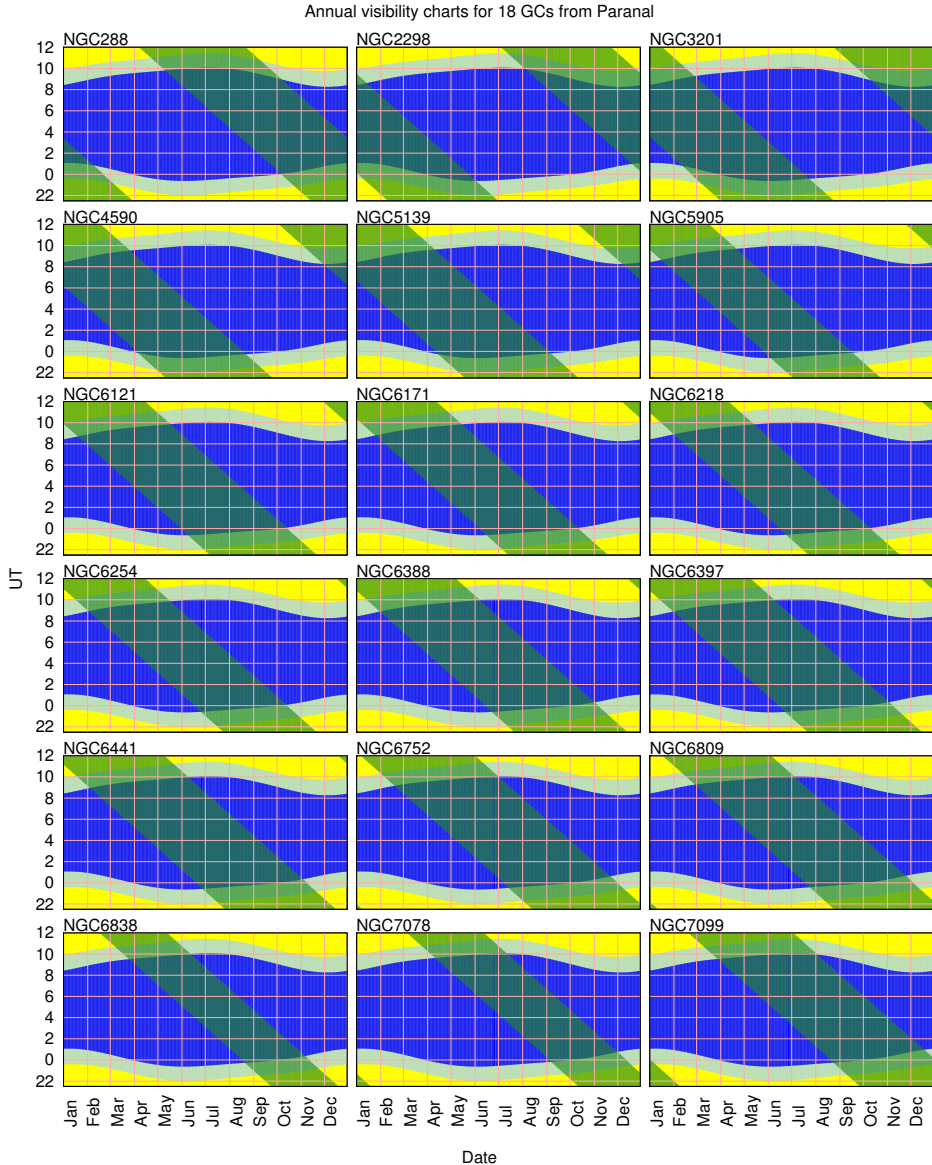


**Figure 6.6:** Annual visibility of the globular clusters from Paranal. Blue indicates night time and yellow day time with light blue marking the twilight in between. During times plotted in green the objects are at an altitude of 30 degrees or higher and observable. NGC104 (47 Tuc) is missing in this overview, because it is visible all year long.

No	RA	Dec	$d$ ["]	$n_{\text{stars}}$	$m_{\text{crowd}}$ [Vmag]	$m_{\text{back}}$ [ $\frac{V_{\text{mag}}}{\text{asec}^2}$ ]	$t_{\text{exp}}$ [sec]
1	00:24:01.376	-72:05:12.70	26.3	20417	17.94	17.65	51.8
2	00:24:01.376	-72:04:32.70	25.9	20573	17.93	17.64	52.0
3	00:24:10.043	-72:04:32.70	30.5	20668	17.91	17.62	51.0
4	00:24:10.043	-72:05:12.70	30.8	20243	17.93	17.66	51.6
5	00:24:05.710	-72:03:52.70	59.9	14446	19.20	19.64	141.1
6	00:24:14.377	-72:03:32.70	90.7	10884	20.81	21.77	711.1
7	00:24:05.710	-72:05:52.70	60.3	14841	19.20	19.64	141.3
8	00:23:57.042	-72:06:12.70	88.3	11379	20.80	21.68	710.1

**Table 6.4:** Coordinates, distances  $d$  to cluster centre, crowding limit, background luminosity and estimated exposure time for each pointing from Fig. 6.7

## 6.6 Example pointings for 47 Tuc

A HST image of 47 Tuc is shown in Fig. 6.7, covering the same area for which Anderson et al. (2008) provide their comprehensive star catalogue. Thus, in case we want to rely on this data, we cannot do observations outside the  $\sim 3.5 \times 3.5$  arcmin<sup>2</sup> presented in the picture. Eight possible pointings are added as coloured rectangles with a size of  $1 \times 1$  arcmin<sup>2</sup> each. They are placed in a way that they are all within the boundaries of the image and have an overlap with other pointings. Especially the centre  $20 \times 20$  arcsec<sup>2</sup> of the cluster are covered by four different pointings, giving us more spectra for each star in that area. A list of coordinates and distances to the cluster centre is given in Table 6.4. The two pointings at the edges are positioned  $\sim 90$  arcsec away from the centre, allowing us to obtain spectra as far out as  $\sim 130$  arcsec.

Also given in the table are the numbers of stars  $n_{\text{stars}}$  listed by Anderson et al. (2008) for each pointing. Due to its large size, even in the two outmost fields we will have more than 10 000 stars. Crowding limits  $m_{\text{crowd}}$  and background luminosities  $m_{\text{back}}$  have been estimated as discussed before as well as exposure times with *MUSE* that will allow us to obtain spectra of stars at the crowding limit with a signal-to-noise ratio of at least 10.

Summing up all exposure times yields a total of  $\sim 1\,900$  sec. Assuming a readout time and the duration for moving a little offset with the VLT of each 1 min, a single visit to all pointings of 47 Tuc can be done in about 48 min – or in one hour including the time for the acquisition at the beginning. Alternatively, we could do two consecutive visits in a little over 100 minutes. In that case, the overhead would only be slightly larger than 50%. Repeating this ten times over the duration of the program would produce twenty exposures per field in less than 20 hours, i. e. less than 20% of the available time.

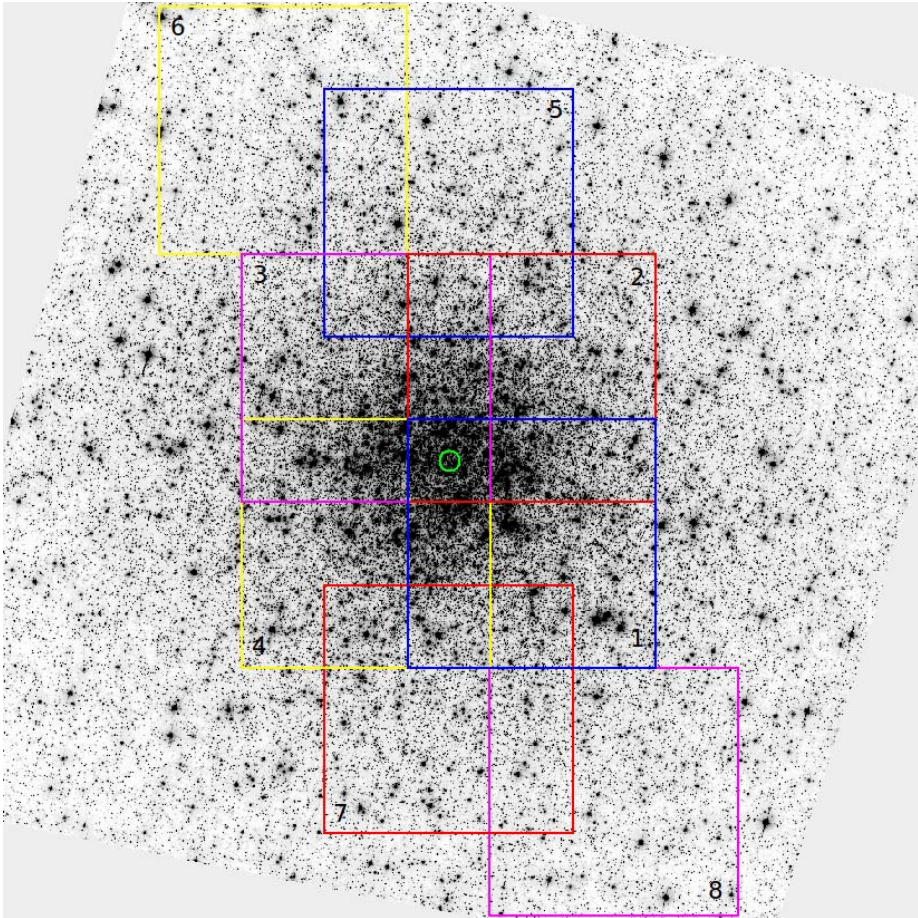


**Figure 6.7:** Example pointings for 47 Tuc. The image covers the same area on sky as the catalogue from the ACS survey. The sphere of influence of the potential intermediate-mass black hole in the centre is marked in green. Eight pointings are shown with coloured boxes. The image was taken as part of program 10775 of the HST by the PI Sarajedini.

## Chapter 7

# Conclusions and outlook

The primary intention of this work is to prepare observations of globular clusters with the upcoming new instrument *MUSE* at the VLT. I presented the current state of research on this topic (Chapter 2) and discussed methods that are required for analyzing data taken with *MUSE* (Chapter 4).

I showed that we will achieve an accuracy in the measurements of radial velocities that is high enough to detect binaries and to find evidence for a potential intermediate-mass black hole (Chapter 5). We can also determine atmospheric parameters and even single element abundances accurately. After conducting the *MUSE* dry run (see Section 5.11) I can estimate some numbers: we will presumably be able to determine the radial velocities of  $\sim 3\,500$  stars from a single *MUSE* exposure with an accuracy that is high enough to find a large number of binaries and set an upper limit for the masses of potential intermediate-mass black holes. For up to  $\sim 1\,000$  spectra, it will also be possible to estimate stellar parameters such as effective temperature  $T_{\text{eff}}$ , surface gravity  $\log(g)$ , metallicity  $[Fe/H]$  and even alpha element abundance  $[\alpha/Fe]$  with a good precision. Taking multiple images per pointing will enable us to co-add the extracted spectra in order to analyze even a larger quantity of stars. With about 10 pointings per globular cluster, we will therefore have precise stellar parameters for up to  $\sim 10\,000$  stars and will be able to search for binaries in a sample of even  $\sim 35\,000$  stars. Usually, we can expect to have a seeing on Paranal of better than the 0.8 arcsec that we assumed for the dry run and later we will even have the AO system. Thus, the expected numbers should be even higher than the ones just given.

Therefore, with *MUSE*, we will obtain an unprecedented number of stellar spectra from a couple of galactic globular clusters. While previous spectroscopic studies mostly observed giant star, we will be able to go all the way down to the main sequence. The suggested observation strategy (Chapter 6) will produce a couple of thousands of spectra for each cluster, obtained over multiple epochs. Until now, we have only briefly started to think about the ways in which this treasure of data can be exploited – the possibilities discussed in this thesis are only the tip of the iceberg. The sheer number of

spectra will allow us to collect statistics that before had only been possible using photometry – a field, in which the *ACS Survey of Galactic Globular Clusters* has started a whole new era with its precise magnitude measurements of thousands of stars in a major part of the Galactic GCs. For instance, although we will not achieve the accuracy in measuring single element abundances as has been reached by other groups using high-resolution spectroscopy, the large amount of available spectra will presumably allow us to approach a problem like that statistically.

Before this will happen, some more work has to be done in order to improve the methods used for the analysis. A part of this can only be done when the instrument actually is on sky, e. g. we need to examine the shape and stability of the LSF of *MUSE* precisely as well as the quality of the wavelength and flux calibration. For the tests presented in this thesis, the LSF was assumed to be a Gaussian with a FWHM of exactly 2.6 Å. This has to be changed as soon as we know about its true shape. Furthermore, all the methods have to be better prepared for use with real observations. Especially the removal of telluric lines appears to be a possible pitfall as has been demonstrated in the analysis of PMAS data (see Section 5.13). Either we need to observe telluric standard stars more frequently or model the absorption of the Earth's atmosphere in another way, e. g. like Seifahrt et al. (2010), who successfully modelled and removed telluric absorption from high-resolution CRIRES spectra. The removal can even be part of the fitting process, in which the telluric absorption is parameterized in some way – or we make use of the fact that exactly the same telluric lines are superimposed on thousands of stellar spectra.

Although our method for interpolating spectra (see Section 4.4.2) works fine, it may not be the best solution for this problem. For each interpolation, dozens of spectra need to be loaded from disc, which takes a long time. Thus, the program for fitting atmospheric parameters spends most of its time with this. A simple improvement would be to optimize the calculation of second derivatives: at the moment, they are calculated from all the spectra along a given dimension, e. g. for interpolating a spectrum with  $\log(g)=4.44$ , all 13 spectra with surface gravities between 0.0 and 6.0 need to be loaded – multiple times for each combination of  $T_{\text{eff}}$ ,  $[Fe/H]$  and  $[\alpha/Fe]$ . Restricting this to neighbouring values will speed up the process significantly. Another approach would be the one used by the ULYSS package (Koleva et al., 2009): for their interpolator they fit a polynomial over all available spectra for each wavelength point (see Eq. 3 in Prugniel et al., 2011). In order to interpolate a spectrum, they only need to evaluate these polynomials. We have already used this method for the analysis of Miles (Section 5.12) and PMAS (Section 5.13) spectra. We need to investigate further, whether this would be an advisable approach for use with our *PHOENIX* library.

This new *PHOENIX* library (Chapter 3) is a comprehensive set of synthetic spectra covering the parameter space required for analyzing spectra of stars in globular clusters, which took a considerable amount of time to compute (~84 CPU years) and maintain. A state-of-the-art stellar atmosphere code has been used and we increased both the spectral resolution and the wavelength range in order to make it usable for data obtained with other instruments like CRIRES and X-Shooter. Unfortunately, in the last couple of weeks we found some problems with the spectra (Section 5.10), but latest



tests produced spectra that matched observations a lot better and we are confident that soon we will be able to make an improved version of the library available for the public. Furthermore, we intend to extend the grid towards higher temperatures. We also want to continue the work on limb darkening (Section 3.4), which will hopefully be of use especially for the exoplanet community.

Altogether it seems that we will be able to contribute significantly to the research on globular clusters. *MUSE* is an amazing instrument, which, although primarily designed for high-*Z* studies, suits our needs very well. I am looking forward to its First Light.



# Bibliography

- ABT, H. A. (1983) Normal and abnormal binary frequencies. *ARA&A*, **21**, 343–372.
- ABT, H. A. & LEVY, S. G. (1976) Multiplicity among solar-type stars. *ApJS*, **30**, 273–306.
- ABT, H. A. & MORRELL, N. I. (1995) The Relation between Rotational Velocities and Spectral Peculiarities among A-Type Stars. *ApJS*, **99**, 135.
- ADELMAN, S. J., GULLIVER, A. F. & HOLMGREN, D. E. (1996) Telluric Lines. In *M.A.S.S., Model Atmospheres and Spectrum Synthesis*, edited by S. J. Adelman, F. Kupka, & W. W. Weiss, vol. 108 of *Astronomical Society of the Pacific Conference Series*.
- ALLARD, F., HAUSCHILD, P. H., ALEXANDER, D. R., TAMANAI, A. & SCHWEITZER, A. (2001) The Limiting Effects of Dust in Brown Dwarf Model Atmospheres. *ApJ*, **556**, 357–372.
- ALLINGTON-SMITH, J. R., CONTENT, R., HAYNES, R. & LEWIS, I. J. (1997) Integral field spectroscopy with the Gemini Multiobject Spectrographs. In *Society of Photo-Optical Instrumentation Engineers (SPIE) Conference Series*, edited by A. L. Ardeberg, vol. 2871 of *Society of Photo-Optical Instrumentation Engineers (SPIE) Conference Series*.
- ANDERSON, A. J. (1997) *Mass Segregation in Globular Clusters M92, 47 Tucanae, and Omega Centauri*. Ph.D. thesis, UNIVERSITY OF CALIFORNIA, BERKELEY.
- ANDERSON, J. (2002) Main-Sequence Observations with HST. In *Omega Centauri, A Unique Window into Astrophysics*, edited by F. van Leeuwen, J. D. Hughes, & G. Piotto, vol. 265 of *Astronomical Society of the Pacific Conference Series*.
- ANDERSON, J., PIOTTO, G., KING, I. R., BEDIN, L. R. & GUHATHAKURTA, P. (2009) Mixed Populations in Globular Clusters: Et Tu, 47 Tuc? *ApJ*, **697**, L58–L62.
- ANDERSON, J., SARAJEDINI, A., BEDIN, L. R., KING, I. R., PIOTTO, G., REID, I. N., SIEGEL, M., MAJEWSKI, S. R. ET AL. (2008) The Acs Survey of Globular Clusters. V. Generating a Comprehensive Star Catalog for each Cluster. *AJ*, **135**, 2055–2073.
- ARNOULD, M., GORIELY, S. & JORISSEN, A. (1999) Non-explosive hydrogen and helium burnings: abundance predictions from the NACRE reaction rate compilation. *A&A*, **347**, 572–582.

- ARRIBAS, S., CARTER, D., CAVALLER, L., DEL BURGO, C., EDWARDS, R., FUENTES, F. J., GARCIA, A. A., HERREROS, J. M. ET AL. (1998) INTEGRAL: a matrix optical fiber system for WYFFOS. In *Society of Photo-Optical Instrumentation Engineers (SPIE) Conference Series*, edited by S. D'Odorico, vol. 3355 of *Society of Photo-Optical Instrumentation Engineers (SPIE) Conference Series*.
- ASPLUND, M., GREVESSE, N., SAUVAL, A. J. & SCOTT, P. (2009) The Chemical Composition of the Sun. *ARA&A*, **47**, 481–522.
- BACON, R., ACCARDO, M., ADJALI, L., ANWAND, H., BAUER, S., BISWAS, I., BLAIZOT, J., BOUDON, D. ET AL. (2010) The MUSE second-generation VLT instrument. In *Society of Photo-Optical Instrumentation Engineers (SPIE) Conference Series*, vol. 7735 of *Society of Photo-Optical Instrumentation Engineers (SPIE) Conference Series*.
- BACON, R., ADAM, G., BARANNE, A., COURTES, G., DUBET, D., DUBOIS, J. P., EMSELLEM, E., FERRUIT, P. ET AL. (1995) 3D spectrography at high spatial resolution. I. Concept and realization of the integral field spectrograph TIGER. *A&AS*, **113**, 347.
- BACON, R., COPIN, Y., MONNET, G., MILLER, B. W., ALLINGTON-SMITH, J. R., BURBAU, M., CAROLLO, C. M., DAVIES, R. L. ET AL. (2001) The SAURON project - I. The panoramic integral-field spectrograph. *MNRAS*, **326**, 23–35.
- BAILYN, C. D. (1992) Are there two kinds of blue stragglers in globular clusters? *ApJ*, **392**, 519–521.
- BARDEN, S. C. & WADE, R. A. (1988) DensePak and spectral imaging with fiber optics. In *Fiber Optics in Astronomy*, edited by S. C. Barden, vol. 3 of *Astronomical Society of the Pacific Conference Series*.
- BARMAN, T. (in prep.) Astrophysical Chemical Equilibrium Solver, in preparation.
- BARMBY, P. & HUCHRA, J. P. (2001) M31 Globular Clusters in the Hubble Space Telescope Archive. I. Cluster Detection and Completeness. *AJ*, **122**, 2458–2468.
- BEAN, J. L., SEIFAHRT, A., HARTMAN, H., NILSSON, H., WIEDEMANN, G., REINERS, A., DREIZLER, S. & HENRY, T. J. (2010) The CRIRES Search for Planets Around the Lowest-mass Stars. I. High-precision Near-infrared Radial Velocities with an Ammonia Gas Cell. *ApJ*, **713**, 410–422.
- BEDIN, L. R., PIOTTO, G., ANDERSON, J., CASSISI, S., KING, I. R., MOMANY, Y. & CARRARO, G. (2004a)  $\omega$  Centauri: The Population Puzzle Goes Deeper. *ApJ*, **605**, L125–L128.
- BEDIN, L. R., PIOTTO, G., ANDERSON, J., KING, I. R., CASSISI, S. & MOMANY, Y. (2004b) The double main sequence of Omega Centauri. *Memorie della Societa Astronomica Italiana Supplementi*, **5**, 105.
- BEKKI, K. (2011) Secondary star formation within massive star clusters: origin of multiple stellar populations in globular clusters. *MNRAS*, **412**, 2241–2259.

- BELLAZZINI, M., FUSI PECCI, F., MESSINEO, M., MONACO, L. & ROOD, R. T. (2002) Deep Hubble Space Telescope WFPC2 Photometry of NGC 288. I. Binary Systems and Blue Stragglers. *AJ*, **123**, 1509–1527.
- BELLAZZINI, M., IBATA, R. A., CHAPMAN, S. C., MACKEY, A. D., MONACO, L., IRWIN, M. J., MARTIN, N. F., LEWIS, G. F. ET AL. (2008) The Nucleus of the Sagittarius Dwarf Galaxy and M54: a Window on the Process of Galaxy Nucleation. *AJ*, **136**, 1147–1170.
- BELLINI, A., BEDIN, L. R., PIOTTO, G., MILONE, A. P., MARINO, A. F. & VILLANOVA, S. (2010) New Hubble Space Telescope WFC3/UVIS Observations Augment the Stellar-population Complexity of  $\omega$  Centauri. *AJ*, **140**, 631–641.
- BENACQUISTA, M. J. (2006) Relativistic Binaries in Globular Clusters. *Living Reviews in Relativity*, **9**, 2.
- BENDER, R. (1990) Unraveling the kinematics of early-type galaxies - Presentation of a new method and its application to NGC4621. *A&A*, **229**, 441–451.
- BENDER, R., KORMENDY, J., BOWER, G., GREEN, R., THOMAS, J., DANKS, A. C., GULL, T., HUTCHINGS, J. B. ET AL. (2005) HST STIS Spectroscopy of the Triple Nucleus of M31: Two Nested Disks in Keplerian Rotation around a Supermassive Black Hole. *ApJ*, **631**, 280–300.
- BETTWIESER, E. & SUGIMOTO, D. (1984) Post-collapse evolution and gravothermal oscillation of globular clusters. *MNRAS*, **208**, 493–509.
- BINNEY, J. & MAMON, G. A. (1982) M/L and velocity anisotropy from observations of spherical galaxies, or must M87 have a massive black hole. *MNRAS*, **200**, 361–375.
- BINNEY, J. & TREMAINE, S. (1987) *Galactic Dynamics*. Princeton Series in Astrophysics, Princeton University Press, Princeton, NJ.
- BINNEY, J. & TREMAINE, S. (2008) *Galactic Dynamics*. Princeton Series in Astrophysics, Princeton University Press.
- BÖHM-VITENSE, E. (1958) Über die Wasserstoffkonvektionszone in Sternen verschiedener Effektivtemperaturen und Leuchtkräfte. Mit 5 Textabbildungen. *ZAp*, **46**, 108.
- BOLTON, C. T. (1972) Identification of Cygnus X-1 with HDE 226868. *Nature*, **235**, 271–273.
- BORUCKI, W. J., KOCH, D., BASRI, G., BATALHA, N., BROWN, T., CALDWELL, D., CALDWELL, J., CHRISTENSEN-DALSGAARD, J. ET AL. (2010) Kepler Planet-Detection Mission: Introduction and First Results. *Science*, **327**, 977–.
- BRADLEY, J., DAI, Z. R., ERNI, R., BROWNING, N., GRAHAM, G., WEBER, P., SMITH, J., HUTCHEON, I. ET AL. (2005) An Astronomical 2175 Å Feature in Interplanetary Dust Particles. *Science*, **307**, 244–247.

- BRILEY, M. M., SMITH, V. V., SUNTZEFF, N. B., LAMBERT, D. L., BELL, R. A. & HESSER, J. E. (1996) Sodium abundance variations in main-sequence stars of the globular cluster 47 Tucanae. *Nature*, **383**, 604–606.
- BROTT, I. & HAUSCHILDT, P. H. (2005) A PHOENIX Model Atmosphere Grid for Gaia. In *The Three-Dimensional Universe with Gaia*, edited by C. Turon, K. S. O’Flaherty & M. A. C. Perryman, vol. 576 of *ESA Special Publication*.
- BUTLER, R. P., MARCY, G. W., WILLIAMS, E., MCCARTHY, C., DOSANJH, P. & VOGT, S. S. (1996) Attaining Doppler Precision of 3 M s<sup>-1</sup>. *PASP*, **108**, 500.
- CAMPBELL, B. & WALKER, G. A. H. (1979) Precision radial velocities with an absorption cell. *PASP*, **91**, 540–545.
- CAPPELLARI, M. & EMSSELLEM, E. (2004) Parametric Recovery of Line-of-Sight Velocity Distributions from Absorption-Line Spectra of Galaxies via Penalized Likelihood. *PASP*, **116**, 138–147.
- CAPPELLARI, M., VEROLME, E. K., VAN DER MAREL, R. P., KLEIJN, G. A. V., ILLINGWORTH, G. D., FRANX, M., CAROLLO, C. M. & DE ZEEUW, P. T. (2002) The Counter-rotating Core and the Black Hole Mass of IC 1459. *ApJ*, **578**, 787–805.
- CARDELLI, J. A., CLAYTON, G. C. & MATHIS, J. S. (1988) The determination of ultraviolet extinction from the optical and near-infrared. *ApJ*, **329**, L33–L37.
- CARDELLI, J. A., CLAYTON, G. C. & MATHIS, J. S. (1989) The relationship between infrared, optical, and ultraviolet extinction. *ApJ*, **345**, 245–256.
- CARRETTA, E., BRAGAGLIA, A., GRATTON, R., D’ORAZI, V. & LUCATELLO, S. (2009a) Intrinsic iron spread and a new metallicity scale for globular clusters. *A&A*, **508**, 695–706.
- CARRETTA, E., BRAGAGLIA, A., GRATTON, R. G., LUCATELLO, S., BELLAZZINI, M., CATANZARO, G., LEONE, F., MOMANY, Y. ET AL. (2010a) Detailed abundances of a large sample of giant stars in M 54 and in the Sagittarius nucleus. *A&A*, **520**, A95.
- CARRETTA, E., BRAGAGLIA, A., GRATTON, R. G., LUCATELLO, S., BELLAZZINI, M., CATANZARO, G., LEONE, F., MOMANY, Y. ET AL. (2010b) M54 + Sagittarius =  $\omega$  Centauri. *ApJ*, **714**, L7–L11.
- CARRETTA, E., BRAGAGLIA, A., GRATTON, R. G., LUCATELLO, S., CATANZARO, G., LEONE, F., BELLAZZINI, M., CLAUDI, R. ET AL. (2009b) Na-O anticorrelation and HB. VII. The chemical composition of first and second-generation stars in 15 globular clusters from GIRAFFE spectra. *A&A*, **505**, 117–138.
- CARRETTA, E., BRAGAGLIA, A., GRATTON, R. G., RECIO-BLANCO, A., LUCATELLO, S., D’ORAZI, V. & CASSISI, S. (2010c) Properties of stellar generations in globular clusters and relations with global parameters. *A&A*, **516**, A55.

- CASTELLI, F. & KURUCZ, R. L. (2004) New Grids of ATLAS9 Model Atmospheres. *ArXiv Astrophysics e-prints*.
- CENARRO, A. J., PELETIER, R. F., SÁNCHEZ-BLÁZQUEZ, P., SELAM, S. O., TOLOBA, E., CARDIEL, N., FALCÓN-BARROSO, J., GORGAS, J. ET AL. (2007) Medium-resolution Isaac Newton Telescope library of empirical spectra - II. The stellar atmospheric parameters. *MNRAS*, **374**, 664–690.
- CIDDOR, P. E. (1996) Refractive index of air: new equations for the visible and near infrared. *Appl. Opt.*, **35**, 1566.
- CLARET, A. (2000) A new non-linear limb-darkening law for LTE stellar atmosphere models. Calculations for  $-5.0 \leq \log[M/H] \leq +1$ ,  $2000 \text{ K} \leq T_{\text{eff}} \leq 50000 \text{ K}$  at several surface gravities. *A&A*, **363**, 1081–1190.
- CLOUGH, S. A., IACONO, M. J. & MONCET, J.-L. (1992) Line-by-Line Calculations of Atmospheric Fluxes and Cooling Rates: Application to Water Vapor. *J. Geophys. Res.*, **97**, 15761–15785.
- CLOUGH, S. A., KNEIZYS, F. X., ROTHMAN, L. S. & GALLERY, W. O. (1981) Atmospheric spectral transmittance and radiance - FASCOD1B. In *Society of Photo-Optical Instrumentation Engineers (SPIE) Conference Series*, vol. 277 of *Society of Photo-Optical Instrumentation Engineers (SPIE) Conference Series*.
- COHEN, J. G. (2004) Palomar 12 as a Part of the Sagittarius Stream: The Evidence from Abundance Ratios. *AJ*, **127**, 1545–1554.
- COHEN, J. G., HUANG, W. & KIRBY, E. N. (2011) The Peculiar Chemical Inventory of NGC 2419: An Extreme Outer Halo "Globular Cluster". *ApJ*, **740**, 60.
- COHN, H. & HUT, P. (1984) Is there life after core collapse in globular clusters? *ApJ*, **277**, L45–L48.
- COHN, H., HUT, P. & WISE, M. (1989) Gravo-thermal oscillations after core collapse in globular cluster evolution. *ApJ*, **342**, 814–822.
- COLINA, L. & BOHLIN, R. (1997) Absolute Flux Distributions of Solar Analogs from the UV to the Near-IR. *AJ*, **113**, 1138–1144.
- CONROY, C. & SPERGEL, D. N. (2011) On the Formation of Multiple Stellar Populations in Globular Clusters. *ApJ*, **726**, 36.
- CONTENT, R. (1997) New design for integral field spectroscopy with 8-m telescopes. In *Society of Photo-Optical Instrumentation Engineers (SPIE) Conference Series*, edited by A. L. Ardeberg, vol. 2871 of *Society of Photo-Optical Instrumentation Engineers (SPIE) Conference Series*.
- CONTRERAS RAMOS, R., FERRARO, F. R., DALESSANDRO, E., LANZONI, B. & ROOD, R. T. (2012) The Unimodal Distribution of Blue Straggler Stars in M75 (NGC 6864). *ApJ*, **748**, 91.

- COOL, A. M. & BOLTON, A. S. (2002) Blue Stars and Binary Stars in NGC 6397: Case Study of a Collapsed-Core Globular Cluster. In *Stellar Collisions, Mergers and their Consequences*, edited by M. M. Shara, vol. 263 of *Astronomical Society of the Pacific Conference Series*.
- DA COSTA, G. S. & FREEMAN, K. C. (1976) The structure and mass function of the globular cluster M3. *ApJ*, **206**, 128–137.
- D'ANTONA, F., CALOI, V., MONTALBÁN, J., VENTURA, P. & GRATTON, R. (2002) Helium variation due to self-pollution among Globular Cluster stars. Consequences on the horizontal branch morphology. *A&A*, **395**, 69–75.
- DAVOUST, E. & PRUGNIEL, P. (1990) On the flattening of globular clusters. *A&A*, **230**, 67–72.
- DE MINK, S. E., POLS, O. R., LANGER, N. & IZZARD, R. G. (2009) Massive binaries as the source of abundance anomalies in globular clusters. *A&A*, **507**, L1–L4.
- DE VAUCOULEURS, G. & PETERS, W. L. (1981) Hubble ratio and solar motion from 200 spiral galaxies having distances derived from the luminosity index. *ApJ*, **248**, 395–407.
- DECRESSIN, T., MEYNET, G., CHARBONNEL, C., PRANTZOS, N. & EKSTRÖM, S. (2007) Fast rotating massive stars and the origin of the abundance patterns in galactic globular clusters. *A&A*, **464**, 1029–1044.
- DENISSEKOV, P. A. & HERWIG, F. (2003) The Abundance Evolution of Oxygen, Sodium, and Magnesium in Extremely Metal Poor Intermediate-Mass Stars: Implications for the Self-Pollution Scenario in Globular Clusters. *ApJ*, **590**, L99–L102.
- DI CRISCIENZO, M., D'ANTONA, F. & VENTURA, P. (2010a) A detailed study of the main sequence of the globular cluster NGC 6397: can we derive constraints on the existence of multiple populations? *A&A*, **511**, A70.
- DI CRISCIENZO, M., VENTURA, P., D'ANTONA, F., MILONE, A. & PIOTTO, G. (2010b) The helium spread in the globular cluster 47 Tuc. *MNRAS*, **408**, 999–1005.
- DOTTER, A., SARAJEDINI, A., ANDERSON, J., APARICIO, A., BEDIN, L. R., CHABOYER, B., MAJEWSKI, S., MARÍN-FRANCH, A. ET AL. (2010) The ACS Survey of Galactic Globular Clusters. IX. Horizontal Branch Morphology and the Second Parameter Phenomenon. *ApJ*, **708**, 698–716.
- DUQUENNOY, A. & MAYOR, M. (1991) Multiplicity among solar-type stars in the solar neighbourhood. II - Distribution of the orbital elements in an unbiased sample. *A&A*, **248**, 485–524.
- EISENHAEUER, F., ABUTER, R., BICKERT, K., BIANCAT-MARCHET, F., BONNET, H., BRYNNEL, J., CONZELMANN, R. D., DELABRE, B. ET AL. (2003) SINFONI - Integral field



- spectroscopy at 50 milli-arcsecond resolution with the ESO VLT. In *Society of Photo-Optical Instrumentation Engineers (SPIE) Conference Series*, edited by M. Iye & A. F. M. Moorwood, vol. 4841 of *Society of Photo-Optical Instrumentation Engineers (SPIE) Conference Series*.
- EISENHAUER, F., GENZEL, R., ALEXANDER, T., ABUTER, R., PAUMARD, T., OTT, T., GILBERT, A., GILLESSEN, S. ET AL. (2005) SINFONI in the Galactic Center: Young Stars and Infrared Flares in the Central Light-Month. *ApJ*, **628**, 246–259.
- FABER, S. M., PHILLIPS, A. C., KIBRICK, R. I., ALCOTT, B., ALLEN, S. L., BURROUS, J., CANTRALL, T., CLARKE, D. ET AL. (2003) The DEIMOS spectrograph for the Keck II Telescope: integration and testing. In *Society of Photo-Optical Instrumentation Engineers (SPIE) Conference Series*, edited by M. Iye & A. F. M. Moorwood, vol. 4841 of *Society of Photo-Optical Instrumentation Engineers (SPIE) Conference Series*.
- FALCÓN-BARROSO, J., SÁNCHEZ-BLÁZQUEZ, P., VAZDEKIS, A., RICCIARDELLI, E., CARDIEL, N., CENARRO, A. J., GORGAS, J. & PELETIER, R. F. (2011) An updated MILES stellar library and stellar population models. *A&A*, **532**, A95.
- FERRARO, F. R., DALESSANDRO, E., MUCCIARELLI, A., BECCARI, G., RICH, R. M., ORIGLIA, L., LANZONI, B., ROOD, R. T. ET AL. (2009) The cluster Terzan 5 as a remnant of a primordial building block of the Galactic bulge. *Nature*, **462**, 483–486.
- FIGUEIRA, P., PEPE, F., LOVIS, C. & MAYOR, M. (2010a) Evaluating the stability of atmospheric lines with HARPS. *A&A*, **515**, A106.
- FIGUEIRA, P., PEPE, F., MELO, C. H. F., SANTOS, N. C., LOVIS, C., MAYOR, M., QUELOZ, D., SMETTE, A. ET AL. (2010b) Radial velocities with CRIRES. Pushing precision down to 5–10 m/s. *A&A*, **511**, A55.
- FISCHER, D. A. & MARCY, G. W. (1992) Multiplicity among M dwarfs. *ApJ*, **396**, 178–194.
- FREGEAU, J. M. (2008) X-Ray Binaries and the Current Dynamical States of Galactic Globular Clusters. *ApJ*, **673**, L25–L28.
- FREGEAU, J. M., GÜRKAN, M. A., JOSHI, K. J. & RASIO, F. A. (2003) Monte Carlo Simulations of Globular Cluster Evolution. III. Primordial Binary Interactions. *ApJ*, **593**, 772–787.
- FRENK, C. S. & FALL, S. M. (1982) An ellipticity - age relation for globular clusters in the Large Magellanic Cloud. I - Measurements. *MNRAS*, **199**, 565–580.
- FREYTAG, B., STEFFEN, M., LUDWIG, H.-G., WEDEMAYER-BÖHM, S., SCHAFFENBERGER, W. & STEINER, O. (2012) Simulations of stellar convection with CO5BOLD. *Journal of Computational Physics*, **231**, 919–959.
- GAO, B., GOODMAN, J., COHN, H. & MURPHY, B. (1991) Fokker-Planck calculations of star clusters with primordial binaries. *ApJ*, **370**, 567–582.

- GARCÍA, B. & MERMILLIOD, J. C. (2001) High-mass binaries in the very young open cluster NGC 6231. Implication for cluster and star formation. *A&A*, **368**, 122–136.
- GEBHARDT, K., RICHSTONE, D., TREMAINE, S., LAUER, T. R., BENDER, R., BOWER, G., DRESSLER, A., FABER, S. M. ET AL. (2003) Axisymmetric Dynamical Models of the Central Regions of Galaxies. *ApJ*, **583**, 92–115.
- GEBHARDT, K. & THOMAS, J. (2009) The Black Hole Mass, Stellar Mass-to-Light Ratio, and Dark Halo in M87. *ApJ*, **700**, 1690–1701.
- GEISLER, D. & HODGE, P. (1980) Ellipticities of globular clusters of the Large Magellanic Cloud. *ApJ*, **242**, 66–73.
- GERHARD, O. E. (1993) Line-of-sight velocity profiles in spherical galaxies: breaking the degeneracy between anisotropy and mass. *MNRAS*, **265**, 213.
- GEYER, E. H., NELLES, B. & HOPP, U. (1983) Ellipticity variations within some globular clusters of the Galaxy and the Magellanic Clouds. *A&A*, **125**, 359–367.
- GEYER, E. H. & RICHTLER, T. (1981) On the Ellipticities of the Blue and Red Globular Clusters in the Large Magellanic Cloud. In *IAU Colloq. 68: Astrophysical Parameters for Globular Clusters*, edited by A. G. D. Philip & D. S. Hayes.
- GNEDIN, O. Y. & OSTRIKER, J. P. (1997) Destruction of the Galactic Globular Cluster System. *ApJ*, **474**, 223.
- GNEDIN, O. Y., ZHAO, H., PRINGLE, J. E., FALL, S. M., LIVIO, M. & MEYLAN, G. (2002) The Unique History of the Globular Cluster  $\omega$  Centauri. *ApJ*, **568**, L23–L26.
- GOLDSBURY, R., RICHER, H. B., ANDERSON, J., DOTTER, A., SARAJEDINI, A. & WOODLEY, K. (2010) The ACS Survey of Galactic Globular Clusters. X. New Determinations of Centers for 65 Clusters. *AJ*, **140**, 1830–1837.
- GOODMAN, J. & HUT, P. (1989) Primordial binaries and globular cluster evolution. *Nature*, **339**, 40–42.
- GORDON, K. D., CLAYTON, G. C., MISSELT, K. A., LANDOLT, A. U. & WOLFF, M. J. (2003) A Quantitative Comparison of the Small Magellanic Cloud, Large Magellanic Cloud, and Milky Way Ultraviolet to Near-Infrared Extinction Curves. *ApJ*, **594**, 279–293.
- GRATTON, R., SNEDEN, C. & CARRETTA, E. (2004) Abundance Variations Within Globular Clusters. *ARA&A*, **42**, 385–440.
- GRATTON, R. G. (1985) Deep photometry of globular clusters. V - Age derivations and their implications for galactic evolution. *A&A*, **147**, 169–177.
- GRATTON, R. G., BONIFACIO, P., BRAGAGLIA, A., CARRETTA, E., CASTELLANI, V., CENTURION, M., CHIEFFI, A., CLAUDI, R. ET AL. (2001) The O-Na and Mg-Al anticorrelations in turn-off and early subgiants in globular clusters. *A&A*, **369**, 87–98.

- GRATTON, R. G., CARRETTA, E. & BRAGAGLIA, A. (2012) Multiple populations in globular clusters. Lessons learned from the Milky Way globular clusters. *A&A Rev.*, **20**, 50.
- GRAY, D. (2005) *The observation and analysis of stellar photospheres*. Cambridge University Press.
- GRIFFIN, R. (1973) On the possibility of determining stellar radial velocities to  $0.01 \text{ km s}^{-1}$ . *MNRAS*, **162**, 243–253.
- GÜLTEKIN, K., RICHSTONE, D. O., GEBHARDT, K., LAUER, T. R., TREMAINE, S., ALLER, M. C., BENDER, R., DRESSLER, A. ET AL. (2009) The M- $\sigma$  and M-L Relations in Galactic Bulges, and Determinations of Their Intrinsic Scatter. *ApJ*, **698**, 198–221.
- GUSTAFSSON, B., EDVARDSSON, B., ERIKSSON, K., JØRGENSEN, U. G., NORDLUND, Å. & PLEZ, B. (2008) A grid of MARCS model atmospheres for late-type stars. I. Methods and general properties. *A&A*, **486**, 951–970.
- HALLIDAY, C., DAVIES, R. L., KUNTSCHNER, H., BIRKINSHAW, M., BENDER, R., SAGLIA, R. P. & BAGGLEY, G. (2001) Line-of-sight velocity distributions of low-luminosity elliptical galaxies. *MNRAS*, **326**, 473–489.
- HANSEN, B. M. S., BREWER, J., FAHLMAN, G. G., GIBSON, B. K., IBATA, R., LIMONGI, M., RICH, R. M., RICHER, H. B. ET AL. (2002) The White Dwarf Cooling Sequence of the Globular Cluster Messier 4. *ApJ*, **574**, L155–L158.
- HANUSCHIK, R. W. (2003) A flux-calibrated, high-resolution atlas of optical sky emission from UVES. *A&A*, **407**, 1157–1164.
- HARRIS, W. E. (1996) A Catalog of Parameters for Globular Clusters in the Milky Way. *AJ*, **112**, 1487.
- HAUSCHILDT, P. H., ALLARD, F. & BARON, E. (1999a) The NextGen Model Atmosphere Grid for  $3000 \leq T_{\text{eff}} \leq 10,000 \text{ K}$ . *ApJ*, **512**, 377–385.
- HAUSCHILDT, P. H., ALLARD, F., FERGUSON, J., BARON, E. & ALEXANDER, D. R. (1999b) The NEXTGEN Model Atmosphere Grid. II. Spherically Symmetric Model Atmospheres for Giant Stars with Effective Temperatures between 3000 and 6800 K. *ApJ*, **525**, 871–880.
- HAUSCHILDT, P. H. & BARON, E. (1999) Numerical solution of the expanding stellar atmosphere problem. *Journal of Computational and Applied Mathematics*, **109**, 41–63.
- HAYES, D. S. & LATHAM, D. W. (1975) A rediscussion of the atmospheric extinction and the absolute spectral-energy distribution of VEGA. *ApJ*, **197**, 593–601.
- HEINTZ, W. D. (1969) A Statistical Study of Binary Stars. *JRASC*, **63**, 275.
- HESSER, J. E. & BELL, R. A. (1980) CN variations among main-sequence 47 Tucanae stars. *ApJ*, **238**, L149–L153.

- HOLMBERG, J., FLYNN, C. & PORTINARI, L. (2006) The colours of the Sun. *MNRAS*, **367**, 449–453.
- HOYLE, F. & SCHWARZSCHILD, M. (1955) On the Evolution of Type II Stars. *ApJS*, **2**, 1.
- HUBENY, I. (1988) A computer program for calculating non-LTE model stellar atmospheres. *Computer Physics Communications*, **52**, 103–132.
- HUBENY, I. & LANZ, T. (2011) Synspec: General Spectrum Synthesis Program. In *Astrophysics Source Code Library, record ascl:1109.022*.
- HUSSER, T.-O., WENDE - VON BERG, S., DREIZLER, S., HOMEIER, D., REINERS, A., BARMAN, A. & HAUSCHILDT, P. H. (submitted) A new extensive library of PHOENIX stellar atmospheres and synthetic spectra. *A&A*.
- HUT, P. & DJORGOVSKI, S. (1992) Rates of collapse and evaporation of globular clusters. *Nature*, **359**, 806–808.
- IKUTA, C. & ARIMOTO, N. (2000) Self-enrichment in omega Centauri. *A&A*, **358**, 535–546.
- JAROSIK, N., BENNETT, C. L., DUNKLEY, J., GOLD, B., GREASON, M. R., HALPERN, M., HILL, R. S., HINSHAW, G. ET AL. (2011) Seven-year Wilkinson Microwave Anisotropy Probe (WMAP) Observations: Sky Maps, Systematic Errors, and Basic Results. *ApJS*, **192**, 14.
- JEDRZEJEWSKI, R. & SCHECHTER, P. L. (1988) Evidence for dynamical subsystems in elliptical galaxies. *ApJ*, **330**, L87–L91.
- KAEUFL, H.-U., BALLESTER, P., BIEREICHEL, P., DELABRE, B., DONALDSON, R., DORN, R., FEDRIGO, E., FINGER, G. ET AL. (2004) CRIRES: a high-resolution infrared spectrograph for ESO's VLT. In *Society of Photo-Optical Instrumentation Engineers (SPIE) Conference Series*, edited by A. F. M. Moorwood & M. Iye, vol. 5492 of *Society of Photo-Optical Instrumentation Engineers (SPIE) Conference Series*.
- KAUFFMANN, G., HECKMAN, T. M., TREMONTI, C., BRINCHMANN, J., CHARLOT, S., WHITE, S. D. M., RIDGWAY, S. E., BRINKMANN, J. ET AL. (2003) The host galaxies of active galactic nuclei. *MNRAS*, **346**, 1055–1077.
- KING, I. (1962) The structure of star clusters. I. an empirical density law. *AJ*, **67**, 471.
- KING, I. R. (1966) The structure of star clusters. III. Some simple dynamical models. *AJ*, **71**, 64.
- KIRBY, E. N., GUHATHAKURTA, P., BOLTE, M., SNEDEN, C. & GEHA, M. C. (2009) Multi-element Abundance Measurements from Medium-resolution Spectra. I. The Sculptor Dwarf Spheroidal Galaxy. *ApJ*, **705**, 328–346.
- KIRBY, E. N., GUHATHAKURTA, P. & SNEDEN, C. (2008) Metallicity and Alpha-Element Abundance Measurement in Red Giant Stars from Medium-Resolution Spectra. *ApJ*, **682**, 1217–1233.

- KNIGGE, C., LEIGH, N. & SILLS, A. (2009) A binary origin for 'blue stragglers' in globular clusters. *Nature*, **457**, 288–290.
- KOLEVA, M., PRUGNIEL, P., BOUCHARD, A. & WU, Y. (2009) ULySS: a full spectrum fitting package. *A&A*, **501**, 1269–1279.
- KONTIZAS, E., KONTIZAS, M., SEDMAK, G. & SMAREGLIA, R. (1989) Ellipticities at R(h) of LMC star clusters. *AJ*, **98**, 590–595.
- KONTIZAS, E., KONTIZAS, M., SEDMAK, G., SMAREGLIA, R. & DAPERGOLAS, A. (1990) The morphology of star clusters in the SMC. *AJ*, **100**, 425–430.
- KROUPA, P. (2002) The Initial Mass Function of Stars: Evidence for Uniformity in Variable Systems. *Science*, **295**, 82–91.
- KURUCZ, R. L. (1979) Model atmospheres for G, F, A, B, and O stars. *ApJS*, **40**, 1–340.
- LADA, C. J. (2006) Stellar Multiplicity and the Initial Mass Function: Most Stars Are Single. *ApJ*, **640**, L63–L66.
- LALLEMENT, R., BERTIN, P., CHASSEFIERE, E. & SCOTT, N. (1993) Correction of spectra for telluric absorption lines with the help of a molecular data bank and high resolution forward modelling: H,O lines around the sodium doublet at 589.5 NM. *A&A*, **271**, 734.
- LANDSTREET, J. D., KUPKA, F., FORD, H. A., OFFICER, T., SIGUT, T. A. A., SILAJ, J., STRASSER, S. & TOWNSHEND, A. (2009) Atmospheric velocity fields in tepid main sequence stars. *A&A*, **503**, 973–984.
- LANZ, T. & HUBENY, I. (2003) A Grid of Non-LTE Line-blanketed Model Atmospheres of O-Type Stars. *ApJS*, **146**, 417–441.
- LAURENT, F., ADJALI, L., ARNS, J., BACON, R., BOUDON, D., CAILLIER, P., DAGUISÉ, E., DELABRE, B. ET AL. (2010) MUSE integral field unit: test results on the first out of 24. In *Society of Photo-Optical Instrumentation Engineers (SPIE) Conference Series*, vol. 7739 of *Society of Photo-Optical Instrumentation Engineers (SPIE) Conference Series*.
- LAYDEN, A. C. & SARAJEDINI, A. (2000) Photometry of the Globular Cluster M54 and the Sagittarius Dwarf Galaxy: The Age-Metallicity Relation. *AJ*, **119**, 1760–1792.
- LE FÈVRE, O., SAISSE, M., MANCINI, D., BRAU-NOGUE, S., CAPUTI, O., CASTINEL, L., D'ODORICO, S., GARILLI, B. ET AL. (2003) Commissioning and performances of the VLT-VIMOS instrument. In *Society of Photo-Optical Instrumentation Engineers (SPIE) Conference Series*, edited by M. Iye & A. F. M. Moorwood, vol. 4841 of *Society of Photo-Optical Instrumentation Engineers (SPIE) Conference Series*.
- LEE, Y.-W., JOO, J.-M., SOHN, Y.-J., REY, S.-C., LEE, H.-C. & WALKER, A. R. (1999) Multiple stellar populations in the globular cluster  $\omega$  Centauri as tracers of a merger event. *Nature*, **402**, 55–57.

- LEINERT, C., HENRY, T., GLINDEMANN, A. & MCCARTHY, JR., D. W. (1997) A search for companions to nearby southern M dwarfs with near-infrared speckle interferometry. *A&A*, **325**, 159–166.
- LEONARD, P. J. T. (1989) Stellar collisions in globular clusters and the blue straggler problem. *AJ*, **98**, 217–226.
- LINDEGREN, L., BABUSIAUX, C., BAILER-JONES, C., BASTIAN, U., BROWN, A. G. A., CROPPER, M., HØG, E., JORDI, C. ET AL. (2008) The Gaia mission: science, organization and present status. In *IAU Symposium*, edited by W. J. Jin, I. Platais & M. A. C. Perryman, vol. 248 of *IAU Symposium*.
- LIVINGSTON, W. & WALLACE, L. (1991) *An atlas of the solar spectrum in the infrared from 1850 to 9000 cm<sup>-1</sup> (1.1 to 5.4 micrometer)*.
- LODDERS, K. (2003) Solar System Abundances and Condensation Temperatures of the Elements. *ApJ*, **591**, 1220–1247.
- LUDWIG, H.-G., FREYTAG, B. & STEFFEN, M. (1999) A calibration of the mixing-length for solar-type stars based on hydrodynamical simulations. I. Methodical aspects and results for solar metallicity. *A&A*, **346**, 111–124.
- LUPTON, R. H. (1989) The ellipticities of a sample of globular clusters in M31. *AJ*, **97**, 1350–1359.
- MAIOLINO, R., RIEKE, G. H. & RIEKE, M. J. (1996) Correction of the Atmospheric Transmission in Infrared Spectroscopy. *AJ*, **111**, 537.
- MAJEWSKI, S. R., PATTERSON, R. J., DINESCU, D. I., JOHNSON, W. Y., OSTHEIMER, J. C., KUNKEL, W. E. & PALMA, C. (2000)  $\omega$  Centauri : Nucleus of a milky way dwarf spheroidal ? In *Liege International Astrophysical Colloquia*, edited by A. Noels, P. Magain, D. Caro, E. Jehin, G. Parmentier, & A. A. Thoul , vol. 35 of *Liege International Astrophysical Colloquia*.
- MAPELLI, M., SIGURDSSON, S., FERRARO, F. R., COLPI, M., POSSENTI, A. & LANZONI, B. (2006) The radial distribution of blue straggler stars and the nature of their progenitors. *MNRAS*, **373**, 361–368.
- MARCONI, A. & HUNT, L. K. (2003) The Relation between Black Hole Mass, Bulge Mass, and Near-Infrared Luminosity. *ApJ*, **589**, L21–L24.
- MARCY, G. W. & BUTLER, R. P. (1992) Precision radial velocities with an iodine absorption cell. *PASP*, **104**, 270–277.
- MARIGO, P., GIRARDI, L., BRESSAN, A., GROENEWEGEN, M. A. T., SILVA, L. & GRANATO, G. L. (2008) Evolution of asymptotic giant branch stars. II. Optical to far-infrared isochrones with improved TP-AGB models. *A&A*, **482**, 883–905.

- MARÍN-FRANCH, A., APARICIO, A., PIOTTO, G., ROSENBERG, A., CHABOYER, B., SARAJEDINI, A., SIEGEL, M., ANDERSON, J. ET AL. (2009) The ACS Survey of Galactic Globular Clusters. VII. Relative Ages. *ApJ*, **694**, 1498–1516.
- MATEO, M., HARRIS, H. C., NEMEC, J. & OLSZEWSKI, E. W. (1990) Blue stragglers as remnants of stellar mergers - The discovery of short-period eclipsing binaries in the globular cluster NGC 5466. *AJ*, **100**, 469–484.
- MATHIEU, R. D. (1994) Pre-Main-Sequence Binary Stars. *ARA&A*, **32**, 465–530.
- MCCREA, W. H. (1964) Extended main-sequence of some stellar clusters. *MNRAS*, **128**, 147.
- MCLAUGHLIN, D. E., ANDERSON, J., MEYLAN, G., GEBHARDT, K., PRYOR, C., MINNITI, D. & PHINNEY, S. (2006) Hubble Space Telescope Proper Motions and Stellar Dynamics in the Core of the Globular Cluster 47 Tucanae. *ApJS*, **166**, 249–297.
- MEISSNER, F. & WEISS, A. (2006) Global fitting of globular cluster age indicators. *A&A*, **456**, 1085–1096.
- MILONE, A. P., MARINO, A. F., PIOTTO, G., BEDIN, L. R., ANDERSON, J., APARICIO, A., CASSISI, S. & RICH, R. M. (2012a) A Double Main Sequence in the Globular Cluster NGC 6397. *ApJ*, **745**, 27.
- MILONE, A. P., PIOTTO, G., BEDIN, L. R., APARICIO, A., ANDERSON, J., SARAJEDINI, A., MARINO, A. F., MORETTI, A. ET AL. (2012b) The ACS survey of Galactic globular clusters. XII. Photometric binaries along the main sequence. *A&A*, **540**, A16.
- MILONE, A. P., PIOTTO, G., KING, I. R., BEDIN, L. R., ANDERSON, J., MARINO, A. F., MOMANY, Y., MALAVOLTA, L. ET AL. (2010) Multiple Stellar Populations in the Galactic Globular Cluster NGC 6752. *ApJ*, **709**, 1183–1194.
- MOHANTY, S., BASRI, G., JAYAWARDHANA, R., ALLARD, F., HAUSCHILDT, P. & ARDILA, D. (2004) Measuring Fundamental Parameters of Substellar Objects. I. Surface Gravities. *ApJ*, **609**, 854–884.
- MUENCH, A. A., LADA, E. A., LADA, C. J. & ALVES, J. (2002) The Luminosity and Mass Function of the Trapezium Cluster: From B Stars to the Deuterium-burning Limit. *ApJ*, **573**, 366–393.
- MUNARI, U., SORDO, R., CASTELLI, F. & ZWITTER, T. (2005) An extensive library of 2500 10 500 Å synthetic spectra. *A&A*, **442**, 1127–1134.
- MURPHY, T. & MEIKSIN, A. (2004) A library of high-resolution Kurucz spectra in the range  $\lambda\lambda 3000\text{--}10\,000$ . *MNRAS*, **351**, 1430–1438.
- NORRIS, J. E. (2004) The Helium Abundances of  $\omega$  Centauri. *ApJ*, **612**, L25–L28.
- NORRIS, J. E. & DA COSTA, G. S. (1995) The Giant Branch of omega Centauri. IV. Abundance Patterns Based on Echelle Spectra of 40 Red Giants. *ApJ*, **447**, 680.

- NOYOLA, E., GEBHARDT, K., KISSLER-PATIG, M., LÜTZGENDORF, N., JALALI, B., DE ZEEUW, P. T. & BAUMGARDT, H. (2010) Very Large Telescope Kinematics for Omega Centauri: Further Support for a Central Black Hole. *ApJ*, **719**, L60–L64.
- OSTERBROCK, D. E., FULBRIGHT, J. P. & BIDA, T. A. (1997) Night-Sky High-Resolution Spectral Atlas of OH Emission Lines for Echelle Spectrograph Wavelength Calibration. II. *PASP*, **109**, 614–623.
- OSTERBROCK, D. E., FULBRIGHT, J. P., MARTEL, A. R., KEANE, M. J., TRAGER, S. C. & BASRI, G. (1996) Night-Sky High-Resolution Spectral Atlas of OH and O2 Emission Lines for Echelle Spectrograph Wavelength Calibration. *PASP*, **108**, 277.
- PASQUINI, L., AVILA, G., BLECHA, A., CACCIARI, C., CAYATTE, V., COLLESS, M., DAMIANI, F., DE PROPRIIS, R. ET AL. (2002) Installation and commissioning of FLAMES, the VLT Multifibre Facility. *The Messenger*, **110**, 1–9.
- PEEBLES, P. J. E. (1972) Star Distribution Near a Collapsed Object. *ApJ*, **178**, 371–376.
- PEI, Y. C. (1992) Interstellar dust from the Milky Way to the Magellanic Clouds. *ApJ*, **395**, 130–139.
- PERRYMAN, M. A. C. & ESA (eds.) (1997) *The HIPPARCOS and TYCHO catalogues. Astrometric and photometric star catalogues derived from the ESA HIPPARCOS Space Astrometry Mission*, vol. 1200 of *ESA Special Publication*.
- PIOTTO, G., BEDIN, L. R., ANDERSON, J., KING, I. R., CASSISI, S., MILONE, A. P., VILLANOVA, S., PIETRINFERNI, A. ET AL. (2007) A Triple Main Sequence in the Globular Cluster NGC 2808. *ApJ*, **661**, L53–L56.
- PIOTTO, G., VILLANOVA, S., BEDIN, L. R., GRATTON, R., CASSISI, S., MOMANY, Y., RECIO-BLANCO, A., LUCATELLO, S. ET AL. (2005) Metallicities on the Double Main Sequence of  $\omega$  Centauri Imply Large Helium Enhancement. *ApJ*, **621**, 777–784.
- PLATAIS, I., MELO, C., QUINN, S. N., CLEM, J. L., DE MINK, S. E., DOTTER, A., KOZHURINA-PLATAIS, V., LATHAM, D. W. ET AL. (2012) The effects of differential reddening and stellar rotation on the appearance of multiple populations in star clusters: the case of Trumpler 20. *ArXiv e-prints*.
- PORTEGIES ZWART, S. F. & MCMILLAN, S. L. W. (2002) The Runaway Growth of Intermediate-Mass Black Holes in Dense Star Clusters. *ApJ*, **576**, 899–907.
- PRANDTL, L. (1925) *Zeitschr. Angewandte Math. Mech.*, **5**, 136.
- PRANTZOS, N. & CHARBONNEL, C. (2006) On the self-enrichment scenario of galactic globular clusters: constraints on the IMF. *A&A*, **458**, 135–149.
- PRESS, W. H., TEUKOLSKY, S. A., VETTERLING, W. T. & FLANNERY, B. P. (2007) *Numerical Recipes 3rd Edition: The Art of Scientific Computing*. 3rd edn., Cambridge University Press, New York, NY, USA.



- PRUGNIEL, P. & SOUBIRAN, C. (2004) New release of the ELODIE library. *ArXiv Astrophysics e-prints*.
- PRUGNIEL, P., SOUBIRAN, C., KOLEVA, M. & LE BORGNE, D. (2007) New release of the ELODIE library: Version 3.1. *ArXiv Astrophysics e-prints*.
- PRUGNIEL, P., VAUGLIN, I. & KOLEVA, M. (2011) The atmospheric parameters and spectral interpolator for the MILES stars. *A&A*, **531**, A165.
- RAMÍREZ, S. V. & COHEN, J. G. (2002) Abundances in Stars from the Red Giant Branch Tip to Near the Main-Sequence Turnoff in M71. III. Abundance Ratios. *AJ*, **123**, 3277–3297.
- REINERS, A. (2005) Calibrating models of ultralow-mass stars. *Astronomische Nachrichten*, **326**, 930–933.
- RODRÍGUEZ-MERINO, L. H., CHAVEZ, M., BERTONE, E. & BUZZONI, A. (2005) UVBLUE: A New High-Resolution Theoretical Library of Ultraviolet Stellar Spectra. *ApJ*, **626**, 411–424.
- ROTH, M. M., KELZ, A., FECHNER, T., HAHN, T., BAUER, S.-M., BECKER, T., BÖHM, P., CHRISTENSEN, L. ET AL. (2005) PMAS: The Potsdam Multi-Aperture Spectrophotometer. I. Design, Manufacture, and Performance. *PASP*, **117**, 620–642.
- ROUSSELOT, P., LIDMAN, C., CUBY, J.-G., MOREELS, G. & MONNET, G. (2000) Night-sky spectral atlas of OH emission lines in the near-infrared. *A&A*, **354**, 1134–1150.
- RUBENSTEIN, E. P. & BAILYN, C. D. (1997) Hubble Space Telescope Observations of the Post-Core-Collapse Globular Cluster NGC 6752. II. A Large Main-Sequence Binary Population. *ApJ*, **474**, 701.
- SALARIS, M. & WEISS, A. (2002) Homogeneous age dating of 55 Galactic globular clusters. Clues to the Galaxy formation mechanisms. *A&A*, **388**, 492–503.
- SANA, H., GOSSET, E., NAZÉ, Y., RAUW, G. & LINDER, N. (2008) The massive star binary fraction in young open clusters - I. NGC 6231 revisited. *MNRAS*, **386**, 447–460.
- SÁNCHEZ-BLÁZQUEZ, P., PELETIER, R. F., JIMÉNEZ-VICENTE, J., CARDIEL, N., CENARRO, A. J., FALCÓN-BARROSO, J., GORGAS, J., SELAM, S. ET AL. (2006) Medium-resolution Isaac Newton Telescope library of empirical spectra. *MNRAS*, **371**, 703–718.
- SANDAGE, A. (1958) Current Problems in the Extragalactic Distance Scale. *ApJ*, **127**, 513.
- SANDAGE, A. (1968) A New Determination of the Hubble Constant from Globular Clusters in M87. *ApJ*, **152**, L149.
- SANDAGE, A. (1970) Main-sequence photometry, color-magnitude diagrams, and ages for the globular clusters M3, M13, M15, and M92. *ApJ*, **162**, 841.

- SANDAGE, A. (1972) The redshift-distance relation. II. The Hubble diagram and its scatter for first-ranked cluster galaxies: A formal value for  $q_0$ . *ApJ*, **178**, 1–24.
- SANDAGE, A. R. (1953) The color-magnitude diagram for the globular cluster M 3. *AJ*, **58**, 61–75.
- SANDAGE, A. R. (1961) The Ages of the Open Cluster NGC 188 and the Globular Clusters M3, M5, and M13 Compared with the Hubble Time. *AJ*, **66**, 53.
- SANDAGE, A. R. & SCHWARZSCHILD, M. (1952) Inhomogeneous Stellar Models. II. Models with Exhausted Cores in Gravitational Contraction. *ApJ*, **116**, 463.
- SARAJEDINI, A., CHABOYER, B. & DEMARQUE, P. (1997) The Relative Ages of Galactic Globular Clusters. *PASP*, **109**, 1321–1339.
- SARAJEDINI, A. & LAYDEN, A. C. (1995) A photometric study of the globular cluster M54 and the sagittarius dwarf galaxy: Evidence for three distinct populations. *AJ*, **109**, 1086–1094.
- SARAZIN, M. (1998) Astroclimate During Science Verification. *The Messenger*, **93**, 2–2.
- SBORDONE, L., BONIFACIO, P., MARCONI, G., BUONANNO, R. & ZAGGIA, S. (2005) Family ties: Abundances in Terzan 7, a Sgr dSph globular cluster. *A&A*, **437**, 905–910.
- SCHLEGEL, D. J., FINKBEINER, D. P. & DAVIS, M. (1998) Maps of Dust Infrared Emission for Use in Estimation of Reddening and Cosmic Microwave Background Radiation Foregrounds. *ApJ*, **500**, 525.
- SCHÖDEL, R., OTT, T., GENZEL, R., HOFMANN, R., LEHNERT, M., ECKART, A., MOUAWAD, N., ALEXANDER, T. ET AL. (2002) A star in a 15.2-year orbit around the supermassive black hole at the centre of the Milky Way. *Nature*, **419**, 694–696.
- SCHULTZ, G. V. & WIEMER, W. (1975) Interstellar reddening and IR-excess of O and B stars. *A&A*, **43**, 133–139.
- SEIFAHRT, A., KÄUFL, H. U., ZÄNGL, G., BEAN, J. L., RICHTER, M. J. & SIEBENMORGEN, R. (2010) Synthesising, using, and correcting for telluric features in high-resolution astronomical spectra. A near-infrared case study using CRIFRES. *A&A*, **524**, A11.
- SHARA, M. M., SAFFER, R. A. & LIVIO, M. (1997) The First Direct Measurement of the Mass of a Blue Straggler in the Core of a Globular Cluster: BSS 19 in 47 Tucanae. *ApJ*, **489**, L59.
- SHU, F. H., ADAMS, F. C. & LIZANO, S. (1987) Star formation in molecular clouds - Observation and theory. *ARA&A*, **25**, 23–81.
- SILVERMAN, J. M. & FILIPPENKO, A. V. (2008) On IC 10 X-1, the Most Massive Known Stellar-Mass Black Hole. *ApJ*, **678**, L17–L20.
- SMITH, W. & MISSEN, R. (1982) *Chemical reaction equilibrium analysis: theory and algorithms*. Wiley series in chemical engineering, Wiley.

- SPERGEL, D. N., VERDE, L., PEIRIS, H. V., KOMATSU, E., NOLTA, M. R., BENNETT, C. L., HALPERN, M., HINSHAW, G. ET AL. (2003) First-Year Wilkinson Microwave Anisotropy Probe (WMAP) Observations: Determination of Cosmological Parameters. *ApJS*, **148**, 175–194.
- STANEVA, A., SPASSOVA, N. & GOLEV, V. (1996) The ellipticities of globular clusters in the Andromeda galaxy. *A&AS*, **116**, 447–461.
- STECHEER, T. P. (1965) Interstellar Extinction in the Ultraviolet. *ApJ*, **142**, 1683.
- STETSON, P. B. (1987) DAOPHOT - A computer program for crowded-field stellar photometry. *PASP*, **99**, 191–222.
- STETSON, P. B., VANDENBERG, D. A. & BOLTE, M. (1996) The Relative Ages of Galactic Globular Clusters. *PASP*, **108**, 560.
- SUGIMOTO, D. & BETTWIESER, E. (1983) Post-collapse evolution of globular clusters. *MNRAS*, **204**, 19P–22P.
- SUNTZEFF, N. (1993) The Chemical Homogeneity of Stars in Galactic Globular Clusters. In *The Globular Cluster-Galaxy Connection*, edited by G. H. Smith & J. P. Brodie, vol. 48 of *Astronomical Society of the Pacific Conference Series*.
- SUNTZEFF, N. B. & KRAFT, R. P. (1996) The Abundance Spread Among Giants and Subgiants in the Globular Cluster Omega Centauri. *AJ*, **111**, 1913.
- TAKEDA, Y., SATO, B. & MURATA, D. (2008) Stellar Parameters and Elemental Abundances of Late-G Giants. *PASJ*, **60**, 781–.
- TRAGER, S. C., KING, I. R. & DJORGOVSKI, S. (1995) Catalogue of Galactic globular-cluster surface-brightness profiles. *AJ*, **109**, 218–241.
- URNSHEK, D. A., BOHLIN, R. C., WILLIAMSON, II, R. L., LUPIE, O. L., KOORNNEEF, J. & MORGAN, D. H. (1990) An atlas of Hubble Space Telescope photometric, spectrophotometric, and polarimetric calibration objects. *AJ*, **99**, 1243–1261.
- VACCA, W. D., CUSHING, M. C. & RAYNER, J. T. (2003) A Method of Correcting Near-Infrared Spectra for Telluric Absorption. *PASP*, **115**, 389–409.
- VALDES, F., GUPTA, R., ROSE, J. A., SINGH, H. P. & BELL, D. J. (2004) The Indo-US Library of Coudé Feed Stellar Spectra. *ApJS*, **152**, 251–259.
- VAN DEN BERGH, S. (1970) Extra-galactic Distance Scale. *Nature*, **225**, 503–505.
- VAN DEN BOSCH, F. C., JAFFE, W. & VAN DER MAREL, R. P. (1998) Nuclear stellar discs in early-type galaxies. I - HST and WHT observations. *MNRAS*, **293**, 343.
- VAN DER MAREL, R. P. & ANDERSON, J. (2010) New Limits on an Intermediate-Mass Black Hole in Omega Centauri. II. Dynamical Models. *ApJ*, **710**, 1063–1088.

- VAN DER MAREL, R. P. & FRANX, M. (1993) A new method for the identification of non-Gaussian line profiles in elliptical galaxies. *ApJ*, **407**, 525–539.
- VANDENBERG, D. A., BOLTE, M. & STETSON, P. B. (1990) Measuring age differences among globular clusters having similar metallicities - A new method and first results. *AJ*, **100**, 445–468.
- VENTURA, P., D'ANTONA, F., MAZZITELLI, I. & GRATTON, R. (2001) Predictions for Self-Pollution in Globular Cluster Stars. *ApJ*, **550**, L65–L69.
- VERGELY, J.-L., FERRERO, R. F., EGRET, D. & KOEPPEN, J. (1998) The interstellar extinction in the solar neighbourhood. I. Statistical approach. *A&A*, **340**, 543–555.
- VERNET, J., DEKKER, H., D'ODORICO, S., KAPER, L., KJAERGAARD, P., HAMMER, F., RANDICH, S., ZERBI, F. ET AL. (2011) X-shooter, the new wide band intermediate resolution spectrograph at the ESO Very Large Telescope. *A&A*, **536**, A105.
- VESPERINI, E., MCMILLAN, S. L. W., D'ANTONA, F. & D'ERCOLE, A. (2010) The Fraction of Globular Cluster Second-generation Stars in the Galactic Halo. *ApJ*, **718**, L112–L116.
- VITENSE, E. (1953) Die Wasserstoffkonvektionszone der Sonne. Mit 11 Textabbildungen. *ZAp*, **32**, 135.
- VOIGT, H.-H. (1991) *Abriss der Astronomie*. Spektrum Akademischer Verlag.
- WEBSTER, B. L. & MURDIN, P. (1972) Cygnus X-1-a Spectroscopic Binary with a Heavy Companion? *Nature*, **235**, 37–38.
- WENDE, S., REINERS, A. & LUDWIG, H.-G. (2009) 3D simulations of M star atmosphere velocities and their influence on molecular FeH lines. *A&A*, **508**, 1429–1442.
- WHITE, R. E. & SHAWL, S. J. (1987) Axial ratios and orientations for 100 Galactic globular star clusters. *ApJ*, **317**, 246–263.
- WITTE, S., HELLING, C., BARMAN, T., HEIDRICH, N. & HAUSCHILD, P. H. (2011) Dust in brown dwarfs and extra-solar planets. III. Testing synthetic spectra on observations. *A&A*, **529**, A44.
- YONG, D. & GRUNDAHL, F. (2008) An Abundance Analysis of Bright Giants in the Globular Cluster NGC 1851. *ApJ*, **672**, L29–L32.

## Abbreviations

<b>A&amp;A</b>	Astronomy and Astrophysics
<b>A&amp;AS</b>	Astronomy and Astrophysics, Supplement
<b>AJ</b>	Astronomical Journal
<b>ARA&amp;A</b>	Annual Review of Astronomy and Astrophysics
<b>ApJ</b>	Astrophysical Journal
<b>ApJS</b>	Astrophysical Journal, Supplement
<b>JRASC</b>	Journal of the Royal Astronomical Society Canada
<b>MNRAS</b>	Monthly Notices of the Royal Astronomical Society
<b>PASJ</b>	Publications of the Astronomical Society Japan
<b>PASP</b>	Publications of the Astronomical Society Pacific
<b>ZAp</b>	Zeitschrift fuer Astrophysik



# Appendix A

## List of galactic globular clusters

Table A.1 lists some properties (taken from Harris, 1996) for all known galactic globular clusters. Marked in grey are those cluster that have been surveyed by Anderson et al. (2008). The columns are:

1. ID of cluster.
2. Alternative name for cluster.
3. Right ascension.
4. Declination.
5. Integrated V magnitude of the cluster.
6. Distance  $d$  to cluster in pc.
7. Metallicity.
8. Core radius  $r_c$  in arcmin.
9. Half-light radius  $r_h$  in arcmin.
10. King-model central concentration,  $c = \log(r_t/r_c)$ ; a 'c' denotes a core-collapsed cluster.
11. Heliocentric radial velocity  $v_r$  in km/s.
12. Velocity dispersion  $\sigma_v$  in km/s.
13. Median relaxation time  $t_r(r_h)$ , in log(years).
14. Ellipticity  $e = 1 - (b/a)$ .

ID	Name	RA	Dec	V	d	[Fe/H]	$r_c$	$r_h$	c	$v_r$	$\sigma_v$	$\log(t_h)$	$\epsilon$
(1)	(2)	(3)	(4)	(5)	(6)	(7)	(8)	(9)	(10)	(11)	(12)	(13)	(14)
1636-283	ESO452-SC11	16 39	-28 23	12.00	8.3	-1.50	0.50	0.50	1.00			7.87	
2MS-GC01	2MASS-GC01	18 08	-19 49	27.74	3.6		0.85	1.65	0.85			8.43	
2MS-GC02	2MASS-GC02	18 09	-20 46	24.60	4.9	-1.08	0.55	0.55	0.95	-238.0±36.0		7.72	
AM 1	E 1	03 55	-49 36	15.72	123.3	-1.70	0.17	0.41	1.36	116.0±20.0		9.61	
AM 4		13 56	-27 10	15.88	32.2	-1.30	0.41	0.43	0.70			8.32	
AtP 2		19 28	-30 21	12.30	28.6	-1.75	1.19	1.77	0.88	115.0±10.0		9.70	
BH 176		15 39	-50 03	14.00	18.9	0.00	0.90	0.90	0.85			8.79	
BH 261	AL 3	18 14	-28 38	11.00	6.5	-1.30	0.40	0.55	1.00			7.80	0.03
Djorg 1		17 47	-33 03	13.60	13.7	-1.51	0.50	1.59	1.50			0.00	
Djorg 2	ESO456-SC38	18 01	-27 49	9.90	6.3	-0.65	0.33	1.05	1.50	-362.4±3.6		0.00	
E 3		09 20	-77 16	11.35	8.1	-0.83	1.87	2.10	0.75			8.80	
ESO-SC06	ESO-SC06	18 09	-46 25	12.00	21.4	-1.80	0.60	1.05	0.90			9.10	
Eridanus		04 24	-21 11	14.70	90.1	-1.43	0.25	0.46	1.10	-23.6±2.1		9.54	
FSR 1735		16 52	-47 03	12.90	9.8		0.39	0.34	0.56			8.11	
GLIMPSE01		18 48	-01 29	22.24	4.2		0.59	0.65	1.37			7.89	
GLIMPSE02		18 18	-16 58		5.5	-0.33	0.70		1.33				
HP 1	BH 229	17 31	-29 58	11.59	8.2	-1.00	0.03	3.10	2.50	45.8±0.7		9.44	
IC 1257		17 27	-07 05	13.10	25.0	-1.70	0.25	1.40	1.55	-140.2±2.1		9.60	
IC 1276	Pal 7	18 10	-07 12	10.34	5.4	-0.75	1.01	2.38	1.33	155.7±1.3		9.03	
IC 4499		15 00	-82 12	9.76	18.8	-1.53	0.84	1.71	1.21	31.5±0.2	2.5±0.5	9.73	0.08
Ko 1		11 59	+12 15	17.10	48.3		0.33	0.26	0.50			8.62	
Ko 2		07 58	+26 15	17.60	34.7		0.25	0.21	0.50			7.70	
Liller 1		17 33	-33 23	16.77	8.2	-0.33	0.06		2.30	52.0±15.0		0.00	
Lynga 7	BH184	16 11	-55 19	10.18	8.0	-1.01	0.90	1.20	0.95	8.0±5.0		8.83	
NGC 104	47 Tuc	00 24	-72 04	3.95	4.5	-0.72	0.36	3.17	2.07	-18.0±0.1	11.0±0.3	9.55	0.09
NGC 1261		03 12	-55 12	8.29	16.3	-1.27	0.35	0.68	1.16	68.2±4.6		9.12	0.07
NGC 1851		05 14	-40 02	7.14	12.1	-1.18	0.09	0.51	1.86	320.5±0.6	10.4±0.5	8.82	0.05
NGC 1904	M 79	05 24	-24 31	7.73	12.9	-1.60	0.16	0.65	1.70	205.8±0.4	5.3±0.4	8.95	0.01
NGC 2298		06 48	-36 00	9.29	10.8	-1.92	0.31	0.98	1.38	148.9±1.2		8.84	0.08
NGC 2419		07 38	+38 52	10.41	82.6	-2.15	0.32	0.89	1.37	-20.2±0.5	4.0±0.6	10.63	0.03
NGC 2808		09 12	-64 51	6.20	9.6	-1.14	0.25	0.80	1.56	101.6±0.7	13.4±1.2	9.15	0.12
NGC 2888		00 52	-26 34	8.09	8.9	-1.32	1.35	2.23	0.99	-45.4±0.2	2.9±0.3	9.32	
NGC 3201		10 17	-46 24	6.75	4.9	-1.59	1.30	3.10	1.29	494.0±0.2	5.0±0.2	9.27	0.12
NGC 362		01 03	-70 50	6.40	8.6	-1.26	0.18	0.82	1.76	223.5±0.5	6.4±0.3	8.93	0.01



ID	Name	RA	Dec	V	d	[Fe/H]	$r_c$	$r_h$	c	$v_r$	$\sigma_v$	$\log(t_f)$	$\epsilon$
(1)	(2)	(3)	(4)	(5)	(6)	(7)	(8)	(9)	(10)	(11)	(12)	(13)	(14)
NGC 4147		12 10	+18 32	10.32	19.3	-1.80	0.09	0.48	1.83	183.2±0.7	2.6±0.7	8.74	0.08
NGC 4372		12 25	-72 39	7.24	5.8	-2.17	1.75	3.91	1.30	72.3±1.2		9.59	0.15
NGC 4590	M 68	12 39	-26 44	7.84	10.3	-2.23	0.58	1.51	1.41	-94.7±0.2	2.5±0.4	9.27	0.05
NGC 4833		12 59	-70 52	6.91	6.6	-1.85	1.00	2.41	1.25	200.2±1.2		9.42	0.07
NGC 5024	M 53	13 12	+18 10	7.61	17.9	-2.10	0.35	1.31	1.72	-62.9±0.3	4.4±0.9	9.76	0.01
NGC 5053		13 16	+17 42	9.47	17.4	-2.27	2.08	2.61	0.74	44.0±0.4	1.4±0.2	9.87	0.21
NGC 5139	omega Cen	13 26	-47 28	3.68	5.2	-1.53	2.37	5.00	1.31	232.1±0.1	16.8±0.3	10.09	0.17
NGC 5272	M 3	13 42	+28 22	6.19	10.2	-1.50	0.37	2.31	1.89	-147.6±0.2	5.5±0.3	9.79	0.04
NGC 5286		13 46	-51 22	7.34	11.7	-1.69	0.28	0.73	1.41	57.4±1.5	8.1±1.0	9.11	0.12
NGC 5466		14 05	+28 32	9.04	16.0	-1.98	1.43	2.30	1.04	110.7±0.2	1.7±0.2	9.76	0.11
NGC 5634		14 29	-05 58	9.47	25.2	-1.88	0.09	0.86	2.07	-45.1±6.6		9.54	0.02
NGC 5694		14 39	-26 32	10.17	35.0	-1.98	0.06	0.40	1.89	-140.3±0.8	5.8±0.8	9.27	0.04
NGC 5824		15 03	-33 04	9.09	32.1	-1.91	0.06	0.45	1.98	-27.5±1.5	11.6±0.5	9.47	0.03
NGC 5897		15 17	-21 00	8.53	12.5	-1.90	1.40	2.06	0.86	101.5±1.0		9.57	0.08
NGC 5904	M 5	15 18	+02 04	5.65	7.5	-1.29	0.44	1.77	1.73	53.2±0.4	5.5±0.4	9.41	0.14
NGC 5927		15 28	-50 40	8.01	7.7	-0.49	0.42	1.10	1.60	-107.5±0.9		8.94	0.04
NGC 5946		15 35	-50 39	9.61	10.6	-1.29	0.08	0.89	2.50	128.4±1.8	4.0±2.9	8.91	0.16
NGC 5986		15 46	-37 47	7.52	10.4	-1.59	0.47	0.98	1.23	88.9±3.7		9.18	0.06
NGC 6093	M 80	16 17	-22 58	7.33	10.0	-1.75	0.15	0.61	1.68	8.1±1.5	12.4±0.6	8.80	0.00
NGC 6101		16 25	-72 12	9.16	15.4	-1.98	0.97	1.05	0.80	361.4±1.7		9.22	0.05
NGC 6121	M 4	16 23	-26 31	5.63	2.2	-1.16	1.16	4.33	1.65	70.7±0.2	4.0±0.2	8.93	0.00
NGC 6139		16 27	-38 50	8.99	10.1	-1.65	0.15	0.85	1.86	6.7±6.0		9.05	0.05
NGC 6144		16 27	-26 01	9.01	8.9	-1.76	0.94	1.63	1.55	193.8±0.6		9.14	0.25
NGC 6171	M 107	16 32	-13 03	7.93	6.4	-1.02	0.56	1.73	1.53	-34.1±0.3	4.1±0.3	9.00	0.02
NGC 6205	M 13	16 41	+36 27	5.78	7.1	-1.53	0.62	1.69	1.53	-244.2±0.2	7.1±0.4	9.30	0.11
NGC 6218	M 12	16 47	-01 56	6.70	4.8	-1.37	0.79	1.77	1.34	-41.4±0.2	4.5±0.4	8.87	0.04
NGC 6229		16 46	+47 31	9.39	30.5	-1.47	0.12	0.36	1.50	-154.2±7.6		9.15	0.05
NGC 6235		16 53	-22 10	9.97	11.5	-1.28	0.33	1.00	1.53	87.3±3.4		8.89	0.13
NGC 6254	M 10	16 57	-04 06	6.60	4.4	-1.56	0.77	1.95	1.38	75.2±0.7	6.6±0.8	8.90	0.00
NGC 6256		16 59	-37 07	11.29	10.3	-1.02	0.02	0.86	2.50	-101.4±1.9	6.6±2.6	8.86	0.01
NGC 6266	M 62	17 01	-30 06	6.45	6.8	-1.18	0.22	0.92	1.71	-70.1±1.4	14.3±0.4	8.98	0.01
NGC 6273	M 19	17 02	-26 16	6.77	8.8	-1.74	0.43	1.32	1.53	135.0±4.1		9.38	0.27
NGC 6284		17 04	-24 45	8.83	15.3	-1.26	0.07	0.66	2.50	27.5±1.7	6.3±0.9	9.09	0.03
NGC 6287		17 05	-22 42	9.35	9.4	-2.10	0.29	0.74	1.38	-288.7±3.5		8.75	0.13

ID	Name	RA	Dec	V	d	[Fe/H]	$r_c$	$r_h$	c	$v_r$	$\sigma_v$	$\log(t_h)$	$\epsilon$	
(1)	(2)	(3)	(4)	(5)	(6)	(7)	(8)	(9)	(10)	(11)	(12)	(13)	(14)	
NGC 6293		17 10	-26 34	8.22	9.5	-1.99	0.05	0.89	2.50	c	-146.2±1.7	7.7±1.3	8.94	0.03
NGC 6304		17 14	-29 27	8.22	5.9	-0.45	0.21	1.42	1.80		-107.3±3.6	8.85	0.02	8.85
NGC 6316		17 16	-28 08	8.43	10.4	-0.45	0.17	0.65	1.65		71.4±8.9	8.89	0.04	8.89
NGC 6325		17 17	-23 45	10.33	7.8	-1.25	0.03	0.63	2.50	c	29.8±1.8	5.9±1.3	8.45	0.12
NGC 6333	M 9	17 19	-18 30	7.72	7.9	-1.77	0.45	0.96	1.25		229.1±7.0	8.90	0.04	8.90
NGC 6341	M 92	17 17	+43 08	6.44	8.3	-2.31	0.26	1.02	1.68		-120.0±0.1	6.0±0.4	9.02	0.10
NGC 6342		17 21	-19 35	9.66	8.5	-0.55	0.05	0.73	2.50	c	115.7±1.4	5.2±2.1	8.51	0.18
NGC 6352		17 25	-48 25	7.96	5.6	-0.64	0.83	2.05	1.10		-137.0±1.1	8.92	0.07	8.92
NGC 6355		17 23	-26 21	9.14	9.2	-1.37	0.05	0.88	2.50	c	-176.9±7.1	8.96		8.96
NGC 6356		17 23	-17 48	8.25	15.1	-0.40	0.24	0.81	1.59		27.0±4.3	9.30	0.03	9.30
NGC 6362		17 31	-67 02	7.73	7.6	-0.99	1.13	2.05	1.09		-13.1±0.6	2.8±0.4	9.20	0.07
NGC 6366		17 27	-05 04	9.20	3.5	-0.59	2.17	2.92	0.74		-122.2±0.5	1.3±0.5	8.73	0.16
NGC 6380	Ton 1	17 34	-39 04	11.31	10.9	-0.75	0.34	0.74	1.55	c	-3.6±2.5	8.86	0.01	8.86
NGC 6388		17 36	-44 44	6.72	9.9	-0.55	0.12	0.52	1.75		80.1±0.8	18.9±0.8	8.90	0.01
NGC 6397		17 40	-53 40	5.73	2.3	-2.02	0.05	2.90	2.50	c	18.8±0.1	4.5±0.2	8.60	0.07
NGC 6401		17 38	-23 54	9.45	10.6	-1.02	0.25	1.91	1.69		-65.0±8.6	9.53	0.15	9.53
NGC 6402	M 14	17 37	-03 14	7.59	9.3	-1.28	0.79	1.30	0.99		-66.1±1.8	9.39	0.11	9.39
NGC 6426		17 44	+03 10	11.01	20.6	-2.15	0.26	0.92	1.70		-162.0±23.0	9.28	0.15	9.28
NGC 6440		17 48	-20 21	9.20	8.5	-0.36	0.14	0.48	1.62		-76.6±2.7	8.62	0.01	8.62
NGC 6441		17 50	-37 03	7.15	11.6	-0.46	0.13	0.57	1.74		16.5±1.0	18.0±0.2	9.09	0.02
NGC 6453		17 50	-34 35	10.08	11.6	-1.50	0.05	0.44	2.50	c	-83.7±8.3	8.52	0.09	8.52
NGC 6496		17 59	-44 15	8.54	11.3	-0.46	0.95	1.02	0.70		-112.7±5.7	9.04	0.16	9.04
NGC 6517		18 01	-08 57	10.23	10.6	-1.23	0.06	0.50	1.82		-39.6±8.0	8.72	0.06	8.72
NGC 6522		18 03	-30 02	8.27	7.7	-1.34	0.05	1.00	2.50	c	-21.1±3.4	6.7±0.7	8.86	0.06
NGC 6528		18 04	-30 03	9.60	7.9	-0.11	0.13	0.38	1.50		206.6±1.4	8.06	0.11	8.06
NGC 6535		18 03	-00 17	10.47	6.8	-1.79	0.36	0.85	1.33		-215.1±0.5	2.4±0.5	8.20	0.08
NGC 6539		18 04	-07 35	9.33	7.8	-0.63	0.38	1.70	1.74		31.0±1.7	9.32	0.08	9.32
NGC 6540	Djorg 3	18 06	-27 45	9.30	5.3	-1.35	0.03	0.03	2.50		-17.7±1.4	0.00	0.00	0.00
NGC 6541		18 08	-43 42	6.30	7.5	-1.81	0.18	1.06	1.86	c	-158.7±2.3	8.2±2.1	9.03	0.12
NGC 6544		18 07	-24 59	7.77	3.0	-1.40	0.05	1.21	1.63	c	-27.3±3.9	8.24	0.22	8.24
NGC 6553		18 09	-25 54	8.06	6.0	-0.18	0.53	1.03	1.16		-3.2±1.5	8.72	0.17	8.72
NGC 6558		18 10	-31 45	9.26	7.4	-1.32	0.03	2.15	2.50	c	-197.2±1.5	3.1±0.9	9.12	0.17
NGC 6569		18 13	-31 49	8.55	10.9	-0.76	0.35	0.80	1.31		-28.1±5.6	9.05	0.00	9.05
NGC 6584		18 18	-52 12	8.27	13.5	-1.50	0.26	0.73	1.47		222.9±15.0	9.02		9.02

ID	Name	RA	Dec	V	d	[Fe/H]	$r_c$	$r_h$	c	$v_r$	$\sigma_v$	$\log(t_H)$	$\epsilon$
(1)	(2)	(3)	(4)	(5)	(6)	(7)	(8)	(9)	(10)	(11)	(12)	(13)	(14)
NGC 6624		18 23	-30 21	7.87	7.9	-0.44	0.06	0.82	2.50	c	53.9±0.6	8.71	0.06
NGC 6626	M 28	18 24	-24 52	6.79	5.5	-1.32	0.24	1.97	1.67		17.0±1.0	9.17	0.16
NGC 6637	M 69	18 31	-32 20	7.64	8.8	-0.64	0.33	0.84	1.38		39.9±2.8	8.82	0.01
NGC 6638		18 30	-25 29	9.02	9.4	-0.95	0.22	0.51	1.33		18.1±3.9	8.46	0.01
NGC 6642		18 31	-23 28	9.13	8.1	-1.26	0.10	0.73	1.99	c	-57.2±5.4	8.52	0.03
NGC 6652		18 35	-32 59	8.62	10.0	-0.81	0.10	0.48	1.80		-111.7±5.8	8.39	0.20
NGC 6656	M 22	18 36	-23 54	5.10	3.2	-1.70	1.33	3.36	1.38		146.3±0.2	9.23	0.14
NGC 6681	M 70	18 43	-32 17	7.87	9.0	-1.62	0.03	0.71	2.50	c	220.3±0.9	8.65	0.01
NGC 6712		18 53	-08 42	8.10	6.9	-1.02	0.76	1.33	1.05		-107.6±0.5	8.95	0.11
NGC 6715	M 54	18 55	-30 28	7.60	26.5	-1.49	0.09	0.82	2.04		141.3±0.3	9.93	0.06
NGC 6717	Pal 9	18 55	-22 42	9.28	7.1	-1.26	0.08	0.68	2.07		22.8±3.4	8.22	0.01
NGC 6723		18 59	-36 37	7.01	8.7	-1.10	0.83	1.53	1.11	c	-94.5±3.6	9.24	0.00
NGC 6749		19 05	+01 54	12.44	7.9	-1.60	0.62	1.10	0.79		-61.7±2.9	8.78	0.04
NGC 6752		19 10	-59 59	5.40	4.0	-1.54	0.17	1.91	2.50	c	-26.7±0.2	8.87	0.04
NGC 6760		19 11	+01 01	8.88	7.4	-0.40	0.34	1.27	1.65		-27.5±6.3	9.01	0.04
NGC 6779	M 56	19 16	+30 11	8.27	9.4	-1.98	0.44	1.10	1.38		-135.6±0.9	9.01	0.03
NGC 6809	M 55	19 39	-30 57	6.32	5.4	-1.94	1.80	2.83	0.93		174.7±0.3	9.29	0.02
NGC 6838	M 71	19 53	+18 46	8.19	4.0	-0.78	0.63	1.67	1.15		-22.8±0.2	8.43	0.00
NGC 6864	M 75	20 06	-21 55	8.52	20.9	-1.29	0.09	0.46	1.80		-189.3±3.6	10.3±1.5	0.07
NGC 6934		20 34	+07 24	8.83	15.6	-1.47	0.22	0.69	1.53		-411.4±1.6	9.04	0.01
NGC 6981	M 72	20 53	-12 32	9.27	17.0	-1.42	0.46	0.93	1.21		-345.0±3.7	9.23	0.02
NGC 7006		21 01	+16 11	10.56	41.2	-1.52	0.17	0.44	1.41		-384.1±0.4	9.42	0.01
NGC 7078	M 15	21 29	+12 10	6.20	10.4	-2.37	0.14	1.00	2.29	c	-107.0±0.2	9.32	0.05
NGC 7089	M 2	21 33	-00 49	6.47	11.5	-1.65	0.32	1.06	1.59		-5.3±2.0	9.40	0.11
NGC 7099	M 30	21 40	-23 10	7.19	8.1	-2.27	0.06	1.03	2.50	c	-184.2±0.2	8.88	0.01
NGC 7492		23 08	-15 36	11.29	26.3	-1.78	0.86	1.15	0.72		-177.5±0.6	9.44	0.24
Pal 1		03 33	+79 34	13.18	11.1	-0.65	0.01	0.46	2.57		-82.8±3.3	7.76	0.22
Pal 10		19 18	+18 34	13.22	5.9	-0.10	0.81	0.99	0.58		-31.7±0.4	8.37	0.00
Pal 11		19 45	-08 00	9.80	13.4	-0.40	1.19	1.46	0.57		-68.0±10.0	9.34	0.00
Pal 12		21 46	-21 15	11.99	19.0	-0.85	0.02	1.72	2.98		27.8±1.5	9.28	0.00
Pal 13		23 06	+12 46	13.47	26.0	-1.88	0.48	0.36	0.66		0.9±0.3	8.35	0.00
Pal 14	AvdB	16 11	+14 57	14.74	76.5	-1.62	0.82	1.22	0.80		0.4±0.1	10.02	0.00
Pal 15		16 59	-00 32	14.00	45.1	-2.07	1.20	1.10	0.60		68.9±1.1	9.72	0.00
Pal 2		04 46	+31 22	13.04	27.2	-1.42	0.17	0.50	1.53		-133.0±57.0	9.28	0.05

ID	Name	RA	Dec	V	d	[Fe/H]	$r_c$	$r_h$	c	$v_r$	$\sigma_v$	$\log(t_h)$	$\epsilon$
(1)	(2)	(3)	(4)	(5)	(6)	(7)	(8)	(9)	(10)	(11)	(12)	(13)	(14)
Pal3		10 05	+00 04	14.26	92.5	-1.63	0.41	0.65	0.99	83.4±8.4		9.88	
Pal4		11 29	+28 58	14.20	108.7	-1.41	0.33	0.51	0.93	74.5±2.1		9.42	
Pal5		15 16	-00 06	11.75	23.2	-1.41	2.29	2.73	0.52	58.7±0.2	1.1±0.2	9.82	
Pal6		17 43	-26 13	11.55	5.8	-0.91	0.66	1.20	1.10	181.0±2.8		8.64	
Pal8		18 41	-19 49	11.02	12.8	-0.37	0.56	0.58	1.53	43.0±15.0		8.47	
Pyxis		09 07	-37 13	12.90	39.4	-1.20				34.3±1.9			
Rup 106		12 38	-51 09	10.90	21.2	-1.68	1.00	1.05	0.70	-44.0±3.0		9.34	
Terzan 1	HP 2	17 35	-30 28	15.90	6.7	-1.03	0.04	3.82	2.50	114.0±14.0		9.12	
Terzan 10		18 03	-26 04	14.90	5.8	-1.00	0.90	1.55	0.75			8.74	
Terzan 12		18 12	-22 44	15.63	4.8	-0.50	0.83	0.75	0.57	94.1±1.5		7.78	
Terzan 2	HP 3	17 27	-30 48	14.29	7.5	-0.69	0.03	1.52	2.50	109.0±15.0		8.82	
Terzan 3		16 28	-35 21	12.00	8.2	-0.74	1.18	1.25	0.70	-136.3±0.7		8.57	
Terzan 4	HP 4	17 30	-31 35	16.00	7.2	-1.41	0.90	1.85	0.90	-50.0±2.9		8.70	
Terzan 5	Terzan 11	17 48	-24 46	13.85	6.9	-0.23	0.16	0.72	1.62	-93.0±2.0		8.53	
Terzan 6	HP 5	17 50	-31 16	13.85	6.8	-0.56	0.05	0.44	2.50	126.0±15.0		8.22	
Terzan 7		19 17	-34 39	12.00	22.8	-0.32	0.49	0.77	0.93	166.0±4.0		8.96	
Terzan 8		19 41	-33 59	12.40	26.3	-2.16	1.00	0.95	0.60	130.0±8.0		9.21	
Terzan 9		18 01	-26 50	16.00	7.1	-1.05	0.03	0.78	2.50	59.0±10.0		8.00	
Ton 2	Pismis 26	17 36	-38 33	12.24	8.2	-0.70	0.54	1.30	1.30	-184.4±2.2		8.82	
UKS 1		17 54	-24 08	17.29	7.8	-0.64	0.15		2.10	57.0±6.0		0.00	
Whiting 1		02 02	-03 15	15.03	30.1	-0.70	0.25	0.22	0.55	-130.6±1.8		7.93	

**Table A.1:** List of galactic globular clusters from Harris (1996). Marked in grey are those cluster that have been surveyed by Anderson et al. (2008).

# Appendix B

## Tools in the *pyphoenix* package

### B.1 `phxadd`

#### Syntax

```
phxadd <grid> <Teff> <logg> <FeH> [extra...]
```

The *phxadd* script adds a new model with the given  $T_{\text{eff}}$ ,  $\log(g)$  and  $[Fe/H]$  to the specified grid. Extra parameters (like e. g. alpha element abundance) can be added in form of multiple key=value pairs. Of special interest is the extra parameter *Source*, which can be set to the name of an existing model that will be used as input for the calculation of the new one.

#### Example

```
phxadd PHOENIX-ACES-AGSS-COND-2011 5778 4.44 0.0 Alpha=0.3 Source=sun
```

Adds a new model with  $T_{\text{eff}}=5778$  K,  $\log(g)=4.44$ ,  $[Fe/H]=0.0$  and  $[\alpha/Fe]=0.3$  to the grid *PHOENIX-ACES-AGSS-COND-2011*. It will not be calculated from scratch, but another model with the name *sun* will be used.

### B.2 `phxaddextra`

#### Syntax

```
phxaddextra <name> <templateVar> <defaultValue> <visible>
```

Adds a new extra parameter to the database with a given name. *templateVar* is the name of the variable as it appears in the *PHOENIX* template (enclosed in  $\{\$. . .\}$ )

and *defaultValue* is its default value. If *visible* is 1, the name and value of the variable show up in the name of the model, unless the value is equal to the default value. After creating a new extra parameter, it can be used for example in calls to *phxadd* or *phxch*.

### Example

```
phxaddextra Alpha MODEL_ALPHA 0.0 1
```

Adds the variable for the alpha element abundance to the database as it has been used for calculating the new library of spectra.

## B.3 phxch

### Syntax

```
phxch <model> <changes...>
```

Applies the given changes in form of key=value pairs to a given model. Interesting might e. g. be the possibility to continue the calculation of a model by setting `Error=0` and `Source=<model>`.

### Example

```
phxch sun Priority=100 Teff=5778
```

Changes the priority of a model called *sun* to 100 and its effective temperature to 5778 K.

## B.4 phxstatus

### Syntax

```
phxstatus [model]
```

Without parameters, *phxstatus* prints a list of currently running jobs. If the name of a single model is given, the output contains information about this model.

# Appendix C

## Tools in the *spexxy* package

### C.1 `spexxyCheckGrid`

#### Syntax

```
spexxyCheckGrid [-h] [-g string] [-d]
```

The name of the grid to check (-g) defaults to *HiResFITS*, so it does only need to be specified in the rare occasions of checking another grid. The parameter -d tells the script to remove files from the disk that do not have corresponding spectra in the database. This tool can also be used for filtering unwanted spectra, e. g. at the moment all NLTE spectra are removed from the database when calling it.

### C.2 `spexxyConvertPhxGrid`

#### Syntax

```
spexxyConvertPhxGrid [-h] -i dir [-g string] -o dir [-f]
```

Converts a grid of *PHOENIX* output files into a grid of FITS files (see Section 3.3.1). The tool has two required parameters: the input directory (-i) containing the grid in *PHOENIX* format and the output directory (-o) to write the final FITS files into. The default output grid is called *HiResFits*. The other two parameters define the name of the grid to convert (-g), which is usually *PHOENIX-ACES-AGSS-COND-2011*, and a switch for forcing the tool to overwrite existing spectra (-f). If not specified, spectra, which have already been converted, will be skipped.

## C.3 *spexxyConvolveGrid*

### Syntax

```
spexxyConvolveGrid [-h] [-i name] -o name -w val val val
                    [-f fwhm | -v file] [-n] [-l] [-c] [-a]
```

The grid that we want to convolve is given with `-i`, which defaults to *HiResFITS*, if none is specified. The results are written to a new grid with the name provided by `-o`. The wavelength range of the convolved spectra can be specified by `-w`, which expects three values for start, end and step size of the wavelength grid. Either a FWHM of a Gaussian kernel (`-f`) or a file containing a LSF (`-v`) can be provided for the convolution. If `-c` is given, the convolution is done on a logarithmic scale, and `-l` creates output spectra on a logarithmic scale. In case of the latter, the values specified for both `-w` and `-f` are supposed to be logarithmic as well. With `-a` the spectra are converted to air wavelengths and `-n` skips spectra that are already present in the output grid. Details are given in Section 3.3.4.

### Example

```
spexxyConvolveGrid -o A1FITS -w 3000 10000 0.1 -f 1.0 -n
```

Creates our standard grid with 1 Å resolution on a wavelength grid with a step size of 0.1 Å. For this, we keep the vacuum wavelengths from the *PHOENIX* output.

```
spexxyConvolveGrid -o MuseFITS -w 4550 9400 0.32 -f 2.4 -n -a -i A1FITS
```

For even lower resolved spectra, it is a lot faster to use another input grid than the default *HiResFITS*, which can be done by using the `-i` parameter. Since the convolution kernel is a Gaussian, its new FWHM can easily be calculated as  $\text{FWHM}' = \sqrt{\text{FWHM}^2 - 1.0^2}$ . So for calculating the *MUSE* grid from the *A1FITS* grid, the FWHM would be 2.4.

## C.4 *spexxyExtractGrid*

### Syntax

```
spexxyExtractGrid [-h] -d name [name ...]
                  [-v name=value [name=value ...]] [-s int] [-i file]
                  [-o file] [-g string] [-p file]
```

The script *spexxyExtractGrid* extracts given dimensions from an existing grid and writes them into a new file (see Section 3.3.3). Most important are the `-i` and `-o` parameters, which specify the filenames of the input and the output databases. An arbitrary number of dimensions to extract can be given following `-d`. For those dimensions that are not to be extracted, default values must be specified using `-v` in form



of name=value pairs. The dimensions given for both combined must exactly match the dimensions in the input grid, i. e. every dimension needs to be taken care of. The parameter `-s` can be used with the value 0 in order to extract only models, which have failed to converge. If only parts of the parameter range are required, a file containing valid values for  $T_{\text{eff}}$  and  $\log(g)$  can be specified using `-g`.

### Example

```
spexxyExtractGrid -i input.db -d Teff logg FeH -v Alpha=0. -o output.db
```

Extracts the first three dimensions  $T_{\text{eff}}$ ,  $\log(g)$  [ $Fe/H$ ] from a grid, while fixing the fourth and last one to  $[\alpha/Fe] = 0$ .

```
spexxyExtractGrid -d Teff logg FeH Alpha Mg -o grid.db
spexxyExtractGrid -d Teff logg FeH Alpha Mg -s 0 -o failed.db
```

Extracts two list of spectra: all successfully converged spectra are written into *grid.db*, while all failed models are put in *failed.db*.

## C.5 *spexxyFillGridHoles*

### Syntax

```
spexxyFillGridHoles [-f] [-g <string>]
```

This tool creates a new directory  $\$SPEXXYPATH/<gridname>\_INTERP$ , where it puts all the interpolated spectra from the grid given by the parameter `-g` (see Section 3.3.2). If a spectrum already exists there, it is only recreated, if the parameter `-f` is specified. Finally, the successfully interpolated spectra are copied to the regular directory of the grid.

## C.6 *spexxyFitBinary*

### Syntax

```
spexxyFitBinary [-d <dir>] [-c <coeffs>] [--iVrad2 <vrad>] [--iVrad1
<vrad>] [--iTeff <Teff>] [--iLogg <log(g)>] [--iFeH
<[Fe/H]>] [--iAlpha <[alpha/Fe]>] [-m] [-p]
<spectra> ...
```

Tries to fit LOSVDs and stellar parameters for two components for a given list of spectra (see Section 4.8). The initial guesses for  $T_{\text{eff}}$  (`--iTeff`),  $\log(g)$  (`--iLogg`),  $[Fe/H]$  (`--iFeh`) and  $[\alpha/Fe]$  (`--iAlpha`) are used for both components, while a radial velocity can be specified for each (`--iVrad1`, `--iVrad2`). The number of coefficients for the continuum can be given via `-c`.

## C.7 spexxyFitElements

### Syntax

```
spexxyFitElements [-t <threshold>] <spectra> ...
```

Fits the abundances of the alpha elements Mg, Si, Ca and Ti in the given spectra as discussed in Section 4.11. Another threshold value than the default 0.005 can be specified using the `-t` parameter.

## C.8 spexxyFitLosvd

### Syntax

```
spexxyFitLosvd [-d <dir>] [-c <coeffs>] [--rSigma <sigma>] [--rVrad
<vrad>] [--iSigma <sigma>] [--iVrad <vrad>] [-t
<template>] <spectra> ...
```

Fits a line-of-sight velocity distribution (see Section 4.6) to a list of spectra against a template that must be specified using the `-t` parameter. Together with the LOSVD, a continuum is fitted, for which the number of polynomials can be given by `-c`. Ranges and initial guesses for both the line broadening  $\sigma$  and the radial velocity  $v$  can be specified using `--rSigma/--iSigma` and `--rVrad/--iVrad` respectively. The results are written back to the FITS files in a binary table extension called *LOSVD*.

### Example

```
spexxyFitLosvd -c 50 -t template.fits spec1.fits spec2.fits
```

Fits the two spectra *spec1.fits* and *spec2.fits* against the template *template.fits*.

## C.9 spexxyFitParams

### Syntax

```
spexxyFitParams [-g <grid>] [-d <dir>] [-c <coeffs>]
[--fixLoggGuess] [--rSigma <sigma>] [--rVrad <vrad>]
[--rTeff <Teff>] [--rLogg <log(g)>] [--rFeH <[Fe/H]>]
[--rAlpha <[alpha/Fe]>] [--iSigma <sigma>] [--iVrad
<vrad>] [--iTeff <Teff>] [--iLogg <log(g)>] [--iFeH
<[Fe/H]>] [--iAlpha <[alpha/Fe]>] [-f] [--ipcache] [-m]
[-p] <spectra> ...
```

Fits a set of given spectra as described in Section 4.10.2. The initial guesses are taken from the command line specified by the parameters starting with `--i` (e.g. `--iTeff`), unless they are specified in a binary table called *GUESS* in the FITS file containing the spectra. Ranges for the parameters can be given (`--r*` with comma separated lower and upper limit), otherwise they are taken from the grid file specified by `-g`. `--fixLoggGuess` fixes the surface gravity to the guess in the FITS file, if present. The number of coefficients for the multiplicative polynomial (i. e. the continuum) can be defined using `-c`. Spectra files with valid results are ignored, if `-f` is not specified. Results are written back to the FITS files in binary tables called *PARAMS* and *LOSVD*, while the continuum and its coefficients are put in *CONTINUUM* and *CONTCOEFFS* respectively.

### Example

```
spexxyFitParams -g MuseFITS/gridParams --rLogg 4.44,4.44 --iTeff 5778 -c 20
spec1.fits spec2.fits
```

Fits the two spectra *spec1.fits* and *spec2.fits* against the *MuseFITS* grid. For both, the surface gravity is fixed to 4.44 and the initial guess for the effective temperature is set to 5 778 K. The number of coefficients for the continuum is 20.

## C.10 *spexxyGridDerivs*

### Syntax

```
spexxyGridDerivs [-g <string>]
```

Calculates 2nd derivatives for use with the spline interpolator (see Section 3.3.5). *spexxyGridDerivs* creates a new directory `$SPEXXYPATH/<gridname>_DERIVS`, where it puts files with the same names as the original spectra but containing the second derivatives instead of the flux. The method used for the calculations has been explained in detail in Section 4.4.2.

## C.11 *spexxyImportIsochroneCMD*

### Syntax

```
spexxyImportIsochroneCMD [-h] [-d dir] -i file [-x distance] -f filters
[filters ...] [-r filter] [-e EB-V]
```

Imports an isochrone from Marigo et al. (2008) (see Section 4.3), which can then be used by *spexxyLSF* (see Section C.14). It expects an isochrone file (`-i`) and a distance *d*

(*-x*, in kpc) in which to place the objects, which is used to calculate the apparent magnitudes  $m$  from the absolute magnitudes  $M$  using  $m = 5 \log d + M$ . The list of filters that we want to extract from the isochrone is specified using *-f*. Since stellar parameters are given in the file, starting from a given filter (*-r*) there is the possibility of recalculating the magnitudes of the other filters using *PHOENIX* spectra. Furthermore, an extinction (*-e*) can be specified, which is applied to the magnitudes. For obvious reasons, this is only possible, if the B and V filter magnitudes alone are requested or if we let them be recalculated using *PHOENIX* spectra. The result is stored in the file *isochrone* in the given directory (*-d*), which defaults to *.spexxy/*.

## C.12 *spexxyInterpolate*

### Syntax

```
spexxyInterpolate {-x <list>|-f <file>} [-v] [-p] [-s] [-g <string>]
                  [-o <string>]
```

Interpolates a spectrum from a grid (see Section 3.3.3) specified via *-g*. In order to get a spline interpolated spectrum, the parameter *-s* can be added – the default behaviour is linear interpolation. When using splines, a grid containing the second derivatives must be present in  $\$SPEXXYPATH/$ *<gridname>\_DERIVS*, which is created automatically when using *spexxyGridDerivs* from Section 3.3.5. The parameters of the interpolated spectra can be specified in two different ways. If only one spectrum is required, the *-x* parameter can be used, which accepts a comma-separated list of parameters. For the default grid *<gridname>/gridParams* those would be  $T_{\text{eff}}$ ,  $\log(g)$ ,  $[Fe/H]$  and  $[\alpha/Fe]$ . Alternatively a file containing a table of parameters can be given with *-f*.

The interpolated spectra are written to files, for which the names are defined by *-o*. If only a single spectrum is interpolated, this must be set to the full filename, otherwise only a prefix is specified and the spectra are enumerated consecutively – unless filenames are given in the file specified by *-f*. If the parameter *-p* is present, every interpolated spectrum is plotted to the screen.

### Example

```
spexxyInterpolate -g MuseFITS/gridParams -s -x 5778,4.37,0,0 -o sun.fits
```

Interpolates a sun-like star from the *MUSE* grid using spline interpolation and writes it to a file named *sun.fits*.

## C.13 *spexxyIsoFit*

### Syntax

```
spexxyIsoFit [-d <dir>] [-i <F814W>] [-v <F606W>] -m <filename>
             <spectra> ...
```

Estimates stellar parameters for a star by comparing its colour and magnitude with an isochrone (see Section 4.3). The spectra that *spexxyFitIso* expects as parameters are not actually loaded but their filenames are a reference to the file containing the measured magnitudes (-m) only, which has to be a table of filenames and magnitudes. In both the isochrone (read from *.spexxy/isochrone* as created by *spexxyImportIsochroneCMD*) and the magnitude file, the two filters specified by -v and -i must be present. After the fit, an additional FITS extension called *GUESS* is added to the spectra files containing a binary table with the results for  $T_{\text{eff}}$ ,  $\log(g)$  and  $[Fe/H]$ .

## C.14 *spexxyLSF*

### Syntax

```
spexxyLSF -m <filename> -o <filename>
```

Fit the difference of the LSF between a model spectrum (-m) and an observation (-o) as discussed in Section 4.7.

## C.15 *spexxyTellurics*

### Syntax

```
spexxyTellurics [-d <dir>] [-s <filename>] [-f]
                <spectra> ...
```

Extracts tellurics from a standard star spectrum and removes them from observation. If a standard star is given by the -s parameter, it creates a new telluric correction spectrum as described in Section 4.2, whereupon an existing spectrum is only overwritten, if explicitly requested by the user (-f). The program then corrects all spectra specified at the command line and saves the results in a new FITS extension called *TELLDIV* within the original file.



# Acknowledgements

A whole bunch of people have helped me creating this thesis in one way or another. I would like to thank all of you for your support and for making my return to Göttingen a real pleasure. However, as I know myself, most presumably I forgot to mention some of you in the following lines, so I hope you will forgive me for this.

First, I want to thank my supervisor Stefan Dreizler, who encouraged me to start my PhD in the first place. In 2008 I was working in Cape Town at the SAAO and had already abandoned the idea of returning to research. But when Stefan's offer for a PhD position came in, it didn't take long for me to decide. He supported me over the whole time and believed in me and my work even when I did not. Thank you for that! My gratitude also goes to Rick Hessman, who always helped me with problems and allowed me to gain some insight in the work of the two MONET telescopes including visits to both, although of course the trip to MONET/N only brought us to Augsburg, where it still stood in its assembly hall. At one visit to MONET/S I managed to break the roof – sorry for that! On our last trip to Sutherland we cleaned the mirror and I spent hour after hour sitting in the Karoo desert and writing on this thesis. The Chapter about globular clusters really should get one of those stickers they put on all of their products: “Proudly South African”. I also want to thank Rick for spell-checking this thesis. I met the last member of my thesis committee, Martin Roth, in Potsdam a couple of weeks after starting my PhD work. He is a fountain of enthusiasm and strongly supported both my work and our science case in all the *MUSE* meetings that we had over the last couple of years. I want to thank him for being the co-referee for this thesis.

An outside view on this thesis came from Sonja Schuh: she found mistakes in the text no one else had and a simple “Why?” written next to a paragraph created endless hours of work for me, consisting of rewriting the text in order to include an answer to that question. I hope that I managed to do that properly! Sonja, thanks for all the support that you gave me, although you were busy enough with your little girl.

I started this thesis with a quote from Sheldon Cooper from the TV show *The Big Bang Theory*. Most physicists have to agree that we all know at least one Sheldon. One of mine is Markus Hundertmark, although he lacks the social awkwardness required for a perfect resemblance. But no matter what you ask Markus, he knows the answer. I'm still abusing him as my personal Wikipedia although he is not in Göttingen anymore. Markus, thanks for all your help and for your friendship. A lot of input for this

thesis, especially in the last couple of weeks, came from Potsdam in person of Sebastian Kamann. He helped me significantly with the analysis of his PMAS data and with the preparation of *MUSE* observations. We also conducted the first *MUSE* dry run for the globular clusters science case together. Thanks Sebastian and good luck with your PhD thesis!

Creating a new library of synthetic spectra hit me quite unprepared – I had never done anything like that before. All the more I would like to thank everybody, who helped me getting everything to work, especially Peter Hauschildt, Derek Homeier, Sebastian Wende - von Berg and Ansgar Reiners. I think we accomplished something great here! Furthermore, my gratitude goes to the *MUSE* team, including but not limited to Roland Bacon, Lutz Wisotzki, Peter Weilbacher and Harald Nicklas. Special thanks go to Philippe Prugniel, who literally kicked my ass during one of my visits to Lyon, which got me thinking about other ways of fitting stellar spectra and resulted in methods similar to his, which are presented in this thesis.

During my time at the Southern African Large Telescope (SALT) in Cape Town I met a lot of fantastic people and today I call many of them my friends. Some of them particularly encouraged me to return to University and start my PhD, especially David Buckley, Petri Vaisanen, Alexei Knyazev, Nicola Loaring and Christian Hettlage. Thanks to all of you, but also to the rest of the SALT crew, to Phil and Anne Charles, the IT crowd, the 'cleaning ladies' and all the families from site. It was a great time and I miss it, but I believe that I had a good reason to leave.

I would like to thank the girls from our secretary, especially Klaudia Wolters and Melanie Hüttenmeister, who I bothered with questions more than once.

All the calculations for the new *PHOENIX* grid have been done at the GWDG – thanks for making this possible and for all the support. My gratitudes also go to the guys from the *ACS Survey for Galactic Globular Cluster*. I have never met you, but without your work our planned *MUSE* observations would be a lot more difficult or even impossible. I think I referenced your publications about a hundred times in this thesis – that should count for something. I also want to thank Evan Kirby, whom I met in Baltimore and who provided some M5 spectra for testing. Unfortunately, the results did not make it into this thesis.

Finally, my gratitudes go to my parents for enabling me to go to University in the first place. I want to thank my girlfriend Svetlana Knyazeva, who supported me with all her heart, especially during the last couple of weeks.



# Curriculum Vitae

Dipl.-Phys. Tim-Oliver Husser  
Am Papenberg 5e  
37075 Göttingen

Geburtstag: 29.05.1981  
Geburtsort: Melle  
Staatsangehörigkeit: Deutsch

---

08/1987 – 07/1991	Grundschule Eicken-Bruche, Melle
08/1991 – 07/1993	Orientierungsstufe Melle
08/1993 – 07/2000	Gymnasium Melle
26.06.2000	Allgemeine Hochschulreife
10/2001 – 11/2006	Physikstudium (Georg-August-Universität Göttingen)
18.07.2003	Vordiplom Physik (Georg-August-Universität Göttingen)
09.11.2006	Diplom Physik (Georg-August-Universität Göttingen)
01/2007 – 04/2007	Southern African Large Telescope (SALT) in Kapstadt, Südafrika
05/2007 – 07/2007	International Max Planck Research School (IMPRS) am MPI für Sonnensystemforschung in Katlenburg-Lindau
09/2007 – 12/2008	Southern African Large Telescope (SALT) in Kapstadt, Südafrika
01/2009 – 07/2012	Promotionsstudent (Georg-August-Universität Göttingen)

**G**lobular clusters are gravitationally bound collections of hundreds of thousands of stars that are almost as old as the Universe itself. Although they have been studied for hundreds of years, their formation and evolution is not yet fully understood. We want to find answers to some of the major questions by investing a large amount of observing time with MUSE, the upcoming 2nd generation instrument for ESO's Very Large Telescope. In this thesis I discuss the current state of research on globular clusters as well as the possibilities of this new instrument. Numerical methods for the analysis of MUSE data are presented, including a comprehensive library of synthetic spectra that has been created just for this purpose. The application of these methods to both synthetic and real data is discussed with particular emphasis on a „dry run“ that has been conducted for MUSE. Finally, a potential program for the observation of globular clusters is presented.



ISBN: 978-3-86395-092-7

Universitätsverlag Göttingen